UNIVERSITÀ DEGLI STUDI DI PAVIA

DIPARTIMENTO DI INGEGNERIA
INDUSTRIALE E DELL'INFORMAZIONE

DOTTORATO DI RICERCA IN
INGEGNERIA ELETTRONICA, INFORMATICA ED ELETTRICA

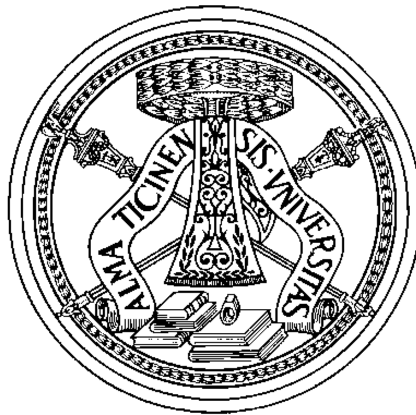

Study and characterization of Silicon-based photonic components

PhD candidate:
Riccardo Marchetti

Supervisor:
Prof. Paolo Minzioni

CICLO XXX A.A. 2016-2017

Contents

Introduction 1

1 Silicon Photonics 5

1.1 Optical properties of Silicon 5

1.2 Silicon Photonics: an historical retrospective 9

1.3 The Silicon-on-Insulator Platform 10

1.3.1 SOI wafers fabrication 11

1.3.2 SOI waveguides 12

1.3.3 SOI waveguides fabrication 13

1.4 Building blocks and applications 14

1.5 FABULOUS Project 14

1.5.1 FABULOUS network architecture 15

1.5.2 ONU structure 17

2 Optical coupling in Silicon Photonics chips 21

2.1 Optical coupling strategies 21

2.2 Diffractive grating coupler 23

2.2.1 Grating coupler theory 23

2.2.2 Uniform SOI grating couplers: performances and limitations 27

2.2.3 Advanced grating coupler designs 32

2.3 Development of a highly-efficient 1D-GC 35

2.3.1 Grating design and simulation 35

2.3.2 Device fabrication 44

2.3.3 Apodized GC experimental characterization 45

2.4 Polarization insensitive grating coupler 49

2.4.1 Design of a highly-efficient polarization-diversity 2D-GC 53

2.4.2 Device fabrication 57

2.4.3 Polarization-diversity 2D-GC experimental characterization 60

3 Reduced-height SOI waveguide 71

3.1 Propagation loss in SOI waveguides 71

3.2 100-nm high WG: Modal analysis 73
3.3 100-nm high WG: Propagation loss measurements 75
3.4 100-nm high WG: Group velocity dispersion measurements 78
4 Silicon optical resonators for WDM filtering 87
4.1 Wavelength-selective Silicon Photonics devices 87
4.1.1 Silicon waveguide Bragg gratings 87
4.1.2 Silicon micro-ring resonators 90
4.2 Design of Si-integrated filters for project Fabulous 93
4.2.1 WDM filters requirements 94
4.2.2 Waveguide geometries and resonator topologies 95
4.2.3 Evaluation of the coupling coefficients 97
4.2.4 Coupling coefficients for ring structures 101
4.2.5 Coupling coefficients for racetrack structures 106
4.2.6 Final configurations selected for the first fabrication 108
4.3 Fabrication procedure 111
4.4 Experimental characterization 112
4.4.1 Linear characterization 112
4.4.2 Non-linear effects characterization 117
4.5 Improved design for 2nd generation integrated filters 121
4.6 Experimental characterization of 2nd generation filters 125
4.7 Stand-alone packaged device 134
5 Hybridly integrated III-V on Si semiconductor optical amplifiers 137
5.1 Current approaches for light generation and amplification in Silicon Photonics 137
5.2 III-V on Si SOAs for FABULOUS Project 142
5.3 Packaged SOA experimental characterization 143
Conclusions 151
Appendix A 155
Appendix B 159
Bibliography 161

Introduction

The world of telecommunications has been rapidly evolving in the recent years, pushed by the tremendous growth of internet data flows and by the steadily increasing spread of mobile devices and cloud services. To get the picture of the situation, it can be considered that, in 2016, the global IP traffic was 1.2 ZB per year (zettabyte = 10^{21} byte), and according to *Cisco* forecasts, it will reach 3.3 ZB per year by 2021. Numbers become even more shocking when we consider global data centers traffic, which is expected to reach 15.3 ZB per year by 2020. The consequent ever increasing demand of bandwidth required to satisfy these extremely high data traffic volumes, is starting to expose the limits of standard electronic transmissions using copper interconnects, which cannot scale with the data rate, because of their frequency dependent loss. At 10 Gbps for example, the reach distance of a standard copper cable assembly is about 7 m, whereas that of a copper backplane is only about 1 m, and these distances are going to shrink as data rates rise. Optical interconnects, due to their intrinsic high bandwidth, can represent a solid alternative to copper for short-medium reach, such as rack-to-rack or board-to-board connections into data centers and, indeed, they are already a reality in high-performance data centers networks. Optical communications based on fibre-connected discrete devices, date back to the late 1970s and are nowadays a very mature technology. However, one of the main limitations of these standard optical components is that they are usually implemented using different base-materials (often “exotic” and expensive materials) and require very different and highly specialized fabrication processes, according to their specific application, thus resulting in low-volume fabrication and high-cost components. Silicon Photonics instead, represents an ideal platform for the integration of different optical functions on a single photonic chip, enabling high-volume manufacturing at low fabrication costs. Silicon in fact, besides being the fundamental element of the microelectronics industry, also possesses very interesting optical properties, and allows to fabricate integrated photonic components exploiting the same fabrications processes and facilities used for the development of CMOS components. Due to its great potential and flexibility, Silicon Photonics has drawn attention from many scientific groups and companies worldwide, and has been deeply studied and investigated for more than a decade. Currently Silicon Photonics has successfully managed to move from the Lab to the Industry, as Silicon-based transceiver modules have already been commercialized by companies such as *Intel* and *Luxtera*, and has found many applications besides data centers interconnects, such as coherent long-reach communications, nano-optomechanics, bio-sensing, imaging, LIDAR application, and many others. Despite all the recent great advances, there are still some main issues which deserve to be addressed and furtherly studied, in order to increase the performances of Silicon-based photonic integrated chips. Improvements in lithography and fabrication processes for example, have allowed to scale down integrated optical waveguides dimensions to the sub-micrometer range, with an obvious

beneficial effect for on-chip dense integration. On the other hand, however, this has raised the problem of how to reduce the high propagation losses of such small-sized waveguides, which are mainly due to side-wall roughness, without excessively complicating the fabrication process, and how to achieve efficient optical coupling with standard single mode fibres, overcoming the problem of mode-size mismatch between fibres and Si-waveguides. Another great open issue of Silicon Photonics, is the implementation of integrated laser sources and optical amplifier, which is made particularly hard because of the indirect-bandgap nature of Silicon. Hybrid integration of III-V semiconductor materials on Silicon, is widely regarded as the most promising solution to this problem, but, however, many step forwards are still required in order to achieve efficient devices that can be reliably mass-manufactured. This thesis work has been carried out targeting all of these issues, and with the specific objective of designing and characterizing high-performance Si-based optical components, such as grating couplers, waveguides, WDM filters, and integrated SOAs, conceived to be implemented in an integrated optical network unit for an innovative type of passive optical access network. In particular, the thesis is organized as follows:

1. Chapter 1 will give a general overview of the Silicon Photonics field, describing Silicon optical properties, and how they can be exploited for the implementation of optical devices. The SOI platform will be described, and some of the possible applications will be introduced. The second part of the Chapter will instead focus of the description of the FP7 European Project Fabulous, in which context this thesis work has been carried out. The proposed network architecture will be described, as well as the optical components required for the integration of the optical network unit.

2. Chapter 2 will analyze the problem of optical coupling between optical fibres and integrated silicon waveguides, focusing, in particular, on the diffractive grating coupler approach. The Chapter is divided in two sections. The first section will address the topic of one-dimensional grating couplers optimized for a single state of polarization of light: at first, the performances and limitations of uniform grating couplers will be described, and, after that, the design, fabrication and experimental characterization of a highly-efficient mirrorless apodized grating coupler will be reported. The second part of the Chapter will instead focus on polarization-insensitive two-dimensional grating couplers. After a brief review of the possible solutions previously reported in the scientific literature, the design and experimental characterization of an optimized polarization-diversity two-dimensional grating coupler, conceived for implementation in the FABULOUS optical network unit, will be reported.

3. Chapter 3 will focus on the problem of side-wall roughness induced propagation losses in SOI strip waveguides having sub-micrometer dimensions. At

first, the loss performances of standard SOI waveguides will be described, as well as the fabrication techniques reported in literature for propagation loss reduction. After that, a new type of reduced-height SOI waveguide, fabricated by means of CMOS-compatible processes, will be proposed, and a complete characterization in terms of modal properties, propagation loss and group velocity dispersion will be reported.

4. Chapter 4 will be centered on wavelength selective Si-based optical components. After a brief introduction on the possible approaches for implementing integrated optical filters, the main section of the Chapter will describe the design and characterization of Silicon micro-ring based filters, conceived for implementation in the FABULOUS optical network unit. The filters are implemented using both standard waveguides as well as the reduced height waveguides described in Chapter 3, and are designed targeting low insertion losses and WDM compatible spectral properties.

5. Chapter 5 will finally focus on the problem of developing optical sources and amplifiers in a Silicon platform. The possible techniques for achieving hybrid integration of III-V semiconductor materials on Silicon will be firstly described. After that, the characterization of the CW properties of an innovative hybridly-integrated SOA, fabricated by *III-V Lab*, will be reported; the maximum performances achievable by the device will be outlined, as well as the limitations induced by fabrication and packaging imperfections.

Most of the work reported in this thesis has been carried out in the Photonic Integrated Lab of the University of Pavia, under the supervision of Prof. Paolo Minzioni. The work regarding the development of a highly-efficient apodized one-dimensional grating coupler has instead been carried out during a 6 months exchange period at the Optoelectronics Research Centre (ORC) of the University of Southampton, under the supervision of Prof. Periklis Petropoulos and Dr. Cosimo Lacava.

1 Silicon Photonics

This Chapter will give a brief introduction to the field of Silicon Photonics, describing Silicon optical properties and how Silicon (often indicated as “Si” in the following) can be used as a base material for the development of integrated optical devices. Some of the possible applications of Si-Photonics will be introduced: among them a special attention will be dedicated to the EU-funded (FP7) FABULOUS Project, aiming to develop an innovative Passive Optical Network (PON) architecture based on the use of a Si-integrated Optical Network Unit (Si-ONU). The network architecture will be described, paying particular attention to both the SI-ONU structure and the network “upstream” direction, as they constitute the most important and innovative feature of the project.

The results obtained from theoretical and experimental investigations of some of the Si-ONU components are reported in this Thesis, and they will be accurately described in the following Chapters.

1.1 Optical properties of Silicon

Thanks to its excellent electronic properties, Silicon has undoubtedly established as the fundamental base material in the field of microelectronics. Nevertheless, Silicon also owns very interesting optical properties, which makes it a legitimate candidate for the implementation of Si-based optical devices. Silicon bandgap structure, at a temperature T of 300 K, is shown in Fig.1(left). The band-gap energy value is equal to 1.12 eV (about 1100 nm), thus meaning that, as it can be seen in Fig.1(right), the optical absorption is very high in the visible spectrum region (allowing Silicon to be used as an efficient material for photodetection in the visible region), and practically negligible in the optical fibre transparency windows (1.3 - 1.5 µm, roughly corresponding to 0.825-0.950 eV).

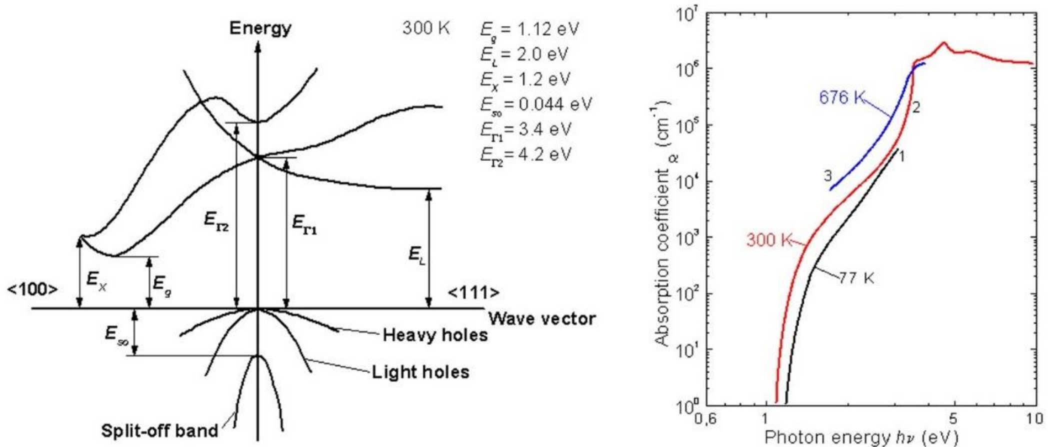

Figure 1: (left) Band structure of Silicon. (right) Silicon absorption coefficient [cm^{-1}] as a function of photon energy [eV], at 77 K and 300 K [1], and at 676 K [2].

As it can be seen in Fig. 1(left), bulk silicon shows an indirect band-gap structure, meaning that the bottom of the conduction band and the top of the valence band are not located at the same point in the Brillouin zone. As the photons carry negligible momentum, the participation of a lattice phonon is thus required in order to allow radiative recombination of an electron and a hole across the band-gap, thus making it a second-order process. The radiative recombination lifetime lies in the ms range and is definitely long if compared to that of non-radiative recombination processes, such as Auger recombination or recombination at bulk or surface defects (which is in the order of a few ns), thus dropping the radiative quantum efficiency to values as low as 10^{-4} % to 10^{-5} %. Quantum efficiency can be slightly improved by using high purity material, in order to reduce the density of bulk and surface non-radiative recombination centers, or by enhancing the radiative recombination process. Room-temperature photoluminescence has been for example demonstrated making use of porous silicon [3], Erbium doped crystalline Silicon [4] or Silicon quantum dots dispersed in a Silicon Dioxide matrix [5]. Nevertheless, despite more than two decades of investigations, lasing action in a Silicon based material has not been demonstrated yet. For this reason, most of the interest from both the scientific and industrial communities is now focused on Si-integrated optical sources achieved by the hybrid integration of III-V materials on a Silicon substrate (which will be discussed in Chapter 5). Silicon refractive index measurements are reported, as a function of photon energy [6], in Fig.2.

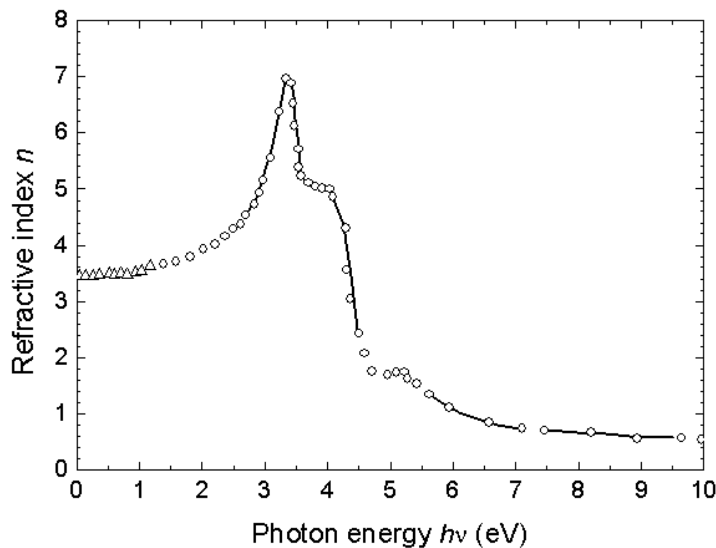

Figure 2: Refractive index of Silicon as a function of the photon energy [6].

As it can be seen in Fig.2, Si refractive index n_{Si} is equal to about 3.47 in the telecom wavelength window (1.3 - 1.5 µm/0.825-0.950 eV). If used in combination with materials with lower refractive index, such as Silicon Dioxide (n_{SiO2}= 1.44), Silicon allows to obtain optical guiding structures with very high index contrast, thus enabling tight optical confinement and sub-µm waveguide dimensions.

Bulk Silicon exhibits a centro-symmetric structure, which prohibits a dipolar second-order non-linear susceptibility $\chi^{(2)}$ (with the exception of the small contribution from the surface, where the material crystalline structure is naturally broken), and thus makes it impossible to exploit the Pockels effect in order to vary the refractive index and obtain optical modulation, as it is usually accomplished, for example, in Lithium-Niobate light modulators. Recently however, it has been shown that tensile strain can induce a non-negligible $\chi^{(2)}$ effect in Silicon waveguides: in [7] for example, it has been shown that the deposition of a 150 nm thick Si_3N_4 over-layer on top of a Si waveguide can induce a $\chi^{(2)}$ value of about 20±10 pm/V, while in [8] an induced $\chi^{(2)}$ value of 122 pm/V was reported.

Other two physical mechanisms can be conveniently exploited to tune the Si refractive index: the thermo-optic effect and the plasma-dispersion effect. The index variation due to local temperature change can be expressed as [9]:

$$\frac{dn}{dT} = 1.86 \cdot 10^{-4}\ K^{-1} \tag{1}$$

This effect can be quite strong in magnitude, as the experimental results reported in [9] show, for example, that a π phase variation of the propagating light can be obtained over a 500 µm long device when applying a power of only 10 mW (corresponding to a temperature variation of about 7 °C and an index variation of $1.3 \cdot 10^{-3}$). However thermal processes are inherently slow and therefore they do not represent an optimal choice for achieving fast light modulation; on the other hand, they can be beneficially exploited for the fine-tuning of the resonant frequency of ring-based integrated filters, as it will be discussed in Chapter 4. Plasma-dispersion effect instead relates to the variation of Si refractive index, both in its real and imaginary part, induced by a variation of the concentration of free electrons and holes. This effect can be described by the Drude-Lorentz model, where the variation of the absorption coefficient α (i.e. the imaginary part of the refractive index) and of the real refractive index n, are expressed as a function of the electron carrier density N_e and hole carrier density N_h:

$$\Delta\alpha = \frac{e^3\lambda_0^2}{4\pi^2c^3\varepsilon_0 n}\left(\frac{\Delta N_e}{\mu_e(m_{ce}^*)^2} + \frac{\Delta N_h}{\mu_h(m_{ch}^*)^2}\right) \tag{2}$$

$$\Delta n = \frac{-e^2\lambda_0^2}{8\pi^2c^2\varepsilon_0 n}\left(\frac{\Delta N_e}{m_{ce}^*} + \frac{\Delta N_h}{m_{ch}^*}\right) \tag{3}$$

Where e is the electronic charge, λ_0 is the optical wavelength, c is the speed of light, ε_0 is the free space permittivity, n is the refractive index of the unperturbed crystalline Silicon, m_{ce}^* and m_{ch}^* are the conductivity effective masses of electrons and holes respectively, and μ_e and μ_h are the mobilities of electrons and holes respectively.

An experimental characterization of the index variation for different values of N_e and N_h at the central wavelength λ_0 of 1550 nm was carried out by Soref et al. in [10]. Interestingly they showed that experimental results had a very good match with Drude-Lorentz equations only for what regards electrons concentration, while for hole concentrations a $(\Delta N_h)^{0.8}$ dependency was observed. Plasma-dispersion effect allows achieving fast optical modulation, and it is practically employed in most of the Si-based light modulator.

Despite having a negligible second-order non-linear susceptibility $\chi^{(2)}$, Silicon exhibits a great third-order non-linear susceptibility $\chi^{(3)}$, whose effects cannot be neglected when the intensity I of the light propagating in the Si-waveguide is sufficiently high. The real part of $\chi^{(3)}$ is responsible for the Kerr effect, which produces self-phase modulation (SPM), cross-phase modulation (XPM) and for-wave-mixing (FWM), while the imaginary part of $\chi^{(3)}$ is instead responsible of the phenomenon of two photon absorption (TPA), which can be extremely relevant in Si-structures. The Kerr effect can be generally described by a non-linear refractive index:

$$n(I) = n + n_2 I \tag{4}$$

This introduces an intensity-dependent term to the phase ϕ accumulated by the optical beam during propagation:

$$n_2 = \frac{3\chi_{Re}^{(3)}}{4\varepsilon_0 c n^2} \tag{5}$$

$$\frac{d\phi}{dz} = \frac{2\pi}{\lambda_0} n_2 I \tag{6}$$

When a single signal propagates along the waveguide, the non-linear phase variation phenomenon is referred as SPM. In this case, if the propagating signal is an optical pulse, the time-dependent intensity profile leads to a variation of the instantaneous frequency of the pulse (chirp), thus causing the generation of new frequencies and leading to pulse spectral broadening [11].

On the other side, when two signals with different wavelengths are propagating into the waveguide, two additional Kerr-based non-linear phenomena can take place: XPM and FWM [12]. In XPM a high intensity beam at λ_P (usually referred as *pump*) can induce a strong non-linear phase change over a lower intensity beam at λ_S (usually referred as *signal*). In FWM instead, starting from the pump and the signal beams, a new optical beam (usually referred as *idler*) can be generated at a new frequency $\nu_I = 2\nu_P - \nu_S$, provided that a phase-matching condition is satisfied.

Considering the nonlinear absorption term, TPA is originated by the simultaneous absorption of two photons having energy larger than half of the Silicon energy band-

gap (i.e. when $\lambda < 2200$ nm and thus relevant when standard telecom-wavelengths are used) and it is usually described by the TPA coefficient β, whose expression is given in Eq.(7). When the light intensity I of an optical beam propagating in a Si waveguide is sufficiently high, TPA results in a non-linear intensity dependent loss mechanism, as expressed by Eq.(8).

$$\beta = \frac{3\chi_{Im}^{(3)}}{\varepsilon_0 c n^2 \lambda} \tag{7}$$

$$\frac{dI}{dz} = -\beta I^2 \tag{8}$$

Kerr non-linear effects are usually to be avoided in Wavelength Division Multiplexing (WDM) systems, as they can negatively affect the system performances (as it will be showed in Chapter 3). However, they can be effectively exploited for the implementation of Si-based all-optical modulators and switches [13, 14, 15], logic gates [16] and wavelength converters [17].

1.2 Silicon Photonics: an historical retrospective

The first pioneering work regarding the possibility to use Silicon as an optical material dates back to the 1980-s, by Soref et al. [18]. In that work the first silicon rib-channels waveguides, as well as the first 2x2 integrated power splitter (a scheme of the device proposed in [18] is shown in Fig.3), were demonstrated.

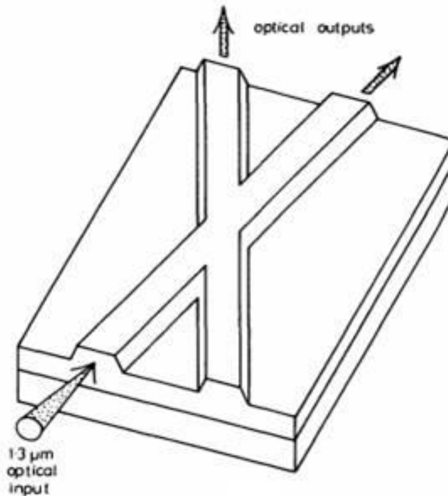

Figure 3: Schematic of the 2x2 power splitter based on the use of Si-on-Si rib waveguides, proposed by Soref et al. in [18].

The employed technology was based on the use of a Silicon-on-Silicon platform. The waveguide layer was lightly doped (n or p) while the substrate was heavily doped (n^+ or p^+): the large concentrations of carriers in the substrate leads to a refractive index

decrease of the substrate with respect to the lightly doped layer, because of the free-carrier dispersion effect, thus allowing to achieve an optical guiding effect. The refractive index contrast obtained with this technique was anyway small ($\Delta n \approx 10^{-2}$), so that waveguides with very large geometrical dimensions (width ≈ 10 µm) had to be implemented. Si-on-Si optical waveguides also exhibited a very high propagation loss, which was reported to be 15 dB/cm at $\lambda = 1.3$ µm.

The first intuition regarding the possibility of integrating different optical and electronic components on a single Silicon chip, and the consequent advantages, dates back to the work of Abstreiter, published in 1992 [19]. One year later, Soref extended the original idea, proposing the concept of a Silicon "superchip" (see Fig.4) including a number of different components: heterostructure transistor circuits, conventional integrated circuits, laser diodes, optical amplifiers, fast external modulators, waveguides, switches, couplers, fast photodetectors, facet reflectors for 90° waveguide bends, splitters, combiners, and V-grooves for aligning and coupling various optical fibres to waveguides facets [20].

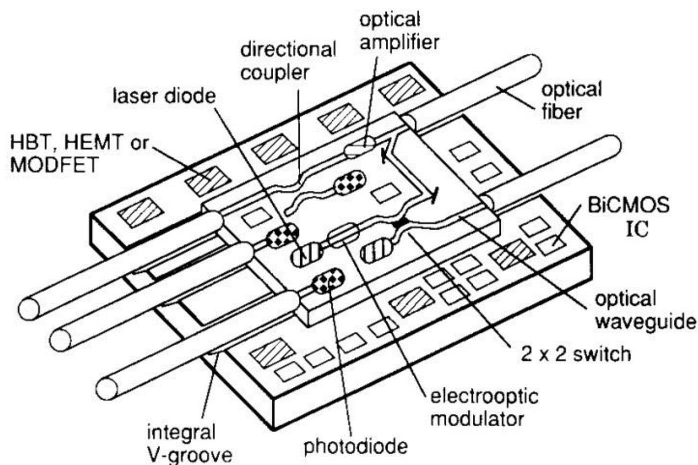

Figure 4: Schematic of the Silicon "superchip" proposed by Soref [20].

1.3 The Silicon-on-Insulator Platform

The true turning point for the field of Silicon-based integrated optics is represented by the advent of Silicon-on-Insulator (SOI) wafers at the end of the 1980-s. SOI wafers are composed by a crystalline Silicon layer, separated from a conventional Silicon substrate by means of a thin layer of Silicon Dioxide (SiO_2, commonly indicated as silica). This technology was initially developed for the microelectronics industry, as it allowed to insulate the electronics components implemented in the top Si layer from the bottom Si substrate, thus allowing to overcome the problem of parasitic capacities. However, this technology turned out to be very useful also for the implementation of integrated optical waveguides: the strong refractive index contrast between Si and SiO_2 (as previously pointed out in paragraph 1.1), and between Si and air, allows in fact to achieve vertical confinement of light in the SOI top Si layer. The first types of SOI wafers

were fabricated using a process called SIMOX, which made use of oxygen-ion implantation to define the buried oxide layer (BOX) into a Silicon substrate. SIMOX SOI wafers were characterized by a typical BOX thickness ≈ 0.4 µm, and a top Si thickness ≈ 0.3 µm [21], and were successfully employed for the integration of optical waveguides [22].

1.3.1 SOI wafers fabrication

Currently the most commonly employed SOI wafers are the UNIBOND wafers, fabricated by the French company SOITEC using the Smart-Cut^{TM} technology [23]. A schematic representation of the Smart-Cut^{TM} process is reported in Fig.5.

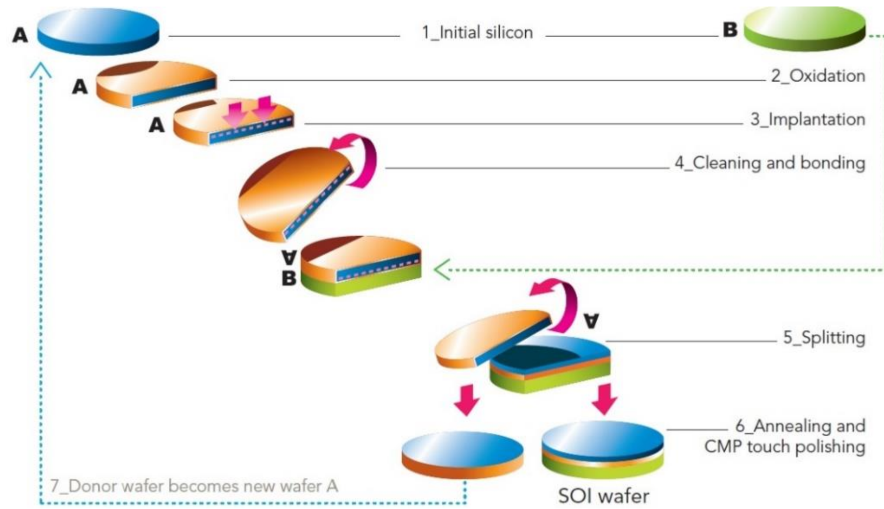

Figure 5: Schematic representation of the required fabrication process to produce a UNIBOND SOI wafer using Smart-Cut^{TM} technology [24].

The process begins with two initial native Silicon wafers, labeled as A and B in Fig.5. Wafer A is capped with a SiO_2 layer by a thermal-oxidation process (performed in a high-temperature environment with high oxygen concentration), in order to create the buried-oxide layer. An implantation process using hydrogen ions is then performed over wafer A, to create a weakened layer just below the surface of the oxidized coating. After that, wafer A is flipped onto the non-oxidized wafer B (by means of hydrophilic bonding at room temperature), and a first medium-temperature (400-600 °C) annealing process is performed, so that a thin heavily damaged layer appears at the depth of the maximum hydrogen ions concentration. Wafer A is then cleaved in correspondence of the weakened layer obtaining, as a result, the SOI wafer and the remainder of wafer A, which can be used as a starting wafer for a new cycle. Finally, the obtained SOI wafer undergoes a second high-temperature annealing process (about 1100 °C), to remove radiation defects in the Si layer and to strengthen the chemical bonds between the buried-oxide and the Si substrate, followed by a Chemical Mechanical Polishing (CMP) of the top Si layer surface.

UNIBOND SOI wafers are usually fabricated with a diameter of 200 mm or 300 mm (8 or 12 inches). Thickness of the BOX, which can be controlled by the duration of the thermal-oxidation process, usually varies from 0.7 µm to 3 µm, while the thickness of the Si layer, which is determined by the depth of the implanted hydrogen ions, usually varies from 0.1 µm to 0.5 µm.

All of the Si-based components which will be described in the next Chapters, were fabricated starting from commercially available SOITEC wafers obtained by UNIBOND technology.

1.3.2 SOI waveguides

While the optical confinement in the vertical direction is achieved by the intrinsic structure of SOI wafers, etching processes can be used to achieve optical confinement also in the horizontal direction, thus implementing an optical waveguide. Different types of waveguide geometry can be implemented, as shown in Fig.6.

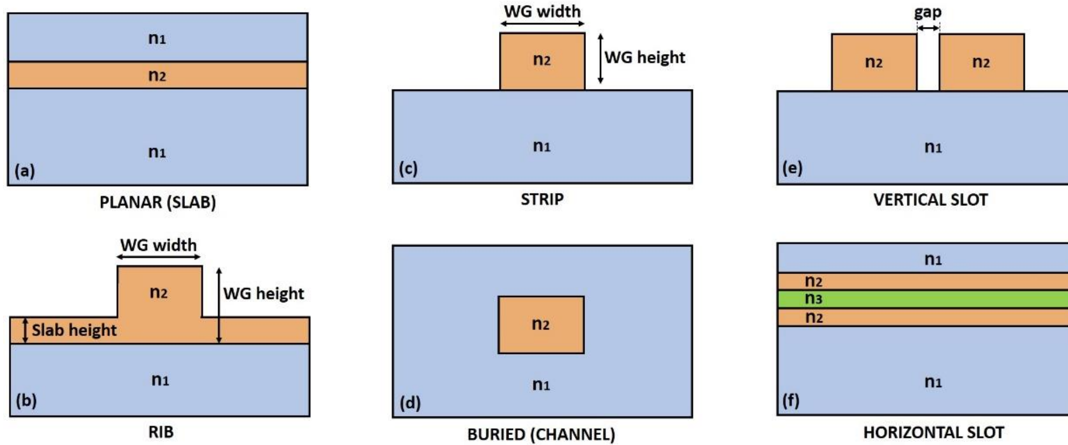

Figure 6: Basic waveguide geometries fabricated in SOI wafers. For Silicon n_2 = 3.47, for Silicon Dioxide n_1 = 1.44.

The first types of waveguide to be implemented and studied were planar waveguides (see Fig.6(a)) [25] and large rib waveguides with micrometric dimensions (see Fig.6(b)) [26, 27]. Over the years, thanks to the improvement of the fabrication technologies and with the goal of achieving dense optical integration, the scientific interest shifted towards waveguides with reduced dimensions, so that both small rib waveguides [28] and strip (see Fig.6(c)) or channel waveguide (see Fig.6(d): a channel waveguide is basically a strip waveguide not exposed to air, but coated by a top oxide layer, TOX) were investigated [29, 30]. Another type of SOI waveguide structure, called slot waveguide, was proposed in 2004 [31, 32]. In the vertical configuration (see Fig.6(e)), a slot waveguide is created by bringing two strip waveguides in very close proximity with each other (the gap value is 50 nm in [31]), so that, due to the discontinuity of the electric field at the interface between two different optical media, the optical field can be enhanced and confined in the low refractive index gap region. A horizontal slot waveguide can also be implemented, (See Fig.6(f)), by sandwiching a low refractive

index material between two Silicon slabs. Slot structures have been successfully exploited for implementing waveguides with improved Kerr non-linear properties while reducing carriers and TPA, such as in [33], where a vertical slot configuration was adopted using organic polymer as the low refractive index material, or in [34], where a horizontal slot configuration was employed using Silicon nanocrystals as the low refractive index material.

1.3.3 SOI waveguides fabrication

Waveguide structures are fabricated starting from SOI wafers, using the same fabrication processes typical of the CMOS (Complementary Metal Oxide Semiconductor) Industry. For transferring the desired pattern into the wafer two principal lithographic techniques can be used: Deep-UV Lithography, or Electron Beam Lithography (EBL). In both cases, as a first step, a sensitive polymer or a sensitized resin is spin-coated over the wafer, to be used as photoresist exposed to a source of radiation. Photoresist can be positive-tone, meaning that the exposed regions dissolve when attacked by a photoresist developer while the un-exposed regions remain unaffected, or negative-tone, where the situation is reversed. In Deep-UV Lithography, the resist is selectively exposed to a Deep-UV light source through a mask, where the pattern is delineated by chromium lines on a transparent fused-quartz substrate. Excimer lasers are usually used as light sources, such as krypton fluoride lasers at $\lambda = 248$ nm or argon fluoride lasers at $\lambda = 193$ nm. Deep-UV Lithography is a fast technique, as it allows patterning a large portion of the SOI wafer in a single exposure, but its resolution is limited by the wavelength of the employed source, because of diffraction. In EBL instead, a collimated beam of electrons is directly scanned over the wafer (without the need of a mask) in order to selectively expose the desired portions of the resist. Although being a process slower than Deep-UV Lithography, EBL allows to define very small features, as the ultimate resolution is only set by electrons scattering effects (the so called "proximity effect"). When using, for example, the ZEP-520 resist, (which is one of the most commonly employed EBL resists) the minimum pattern resolution is about 60 nm [35]. Once the resist has been patterned and developed, dry etching techniques are used to transfer the pattern from the sample surface into the Silicon layer, using the un-developed resist portion as an etching mask. The most commonly employed techniques are Reactive Ion Etching (RIE), and Inductively Coupled Plasma - Reactive Ion Etching (ICP-RIE). In RIE technique, a single RF power generator is used to generate and accelerate a plasma of active gas species (sulfur hexafluoride is often used) in the chamber containing the wafer: thanks to the combined effect of chemical and physical interaction of the accelerated ions with the wafer, the undesired material can be removed, obtaining both strong anisotropic profiles (which are required to define the waveguide vertical sidewalls) and good selectivity between the mask layer and the un-masked Silicon. ICP-RIE is basically very similar to standard RIE technique, with the exception that two different RF power generators are used to separately generate and accelerate the plasma respectively, so that the ion energy and the ion density can

be controlled in a separate way. After the etching process the obtained Silicon waveguides can be left exposed to air, or they can be coated with a protective Silicon Dioxide layer, which is usually deposited by means of Chemical Vapor Deposition (CVD) techniques [36].

Beside Silicon, many other CMOS-compatible materials can be integrated in a SOI platform using standard fabrication processes, in order to implement additional optical functions. Germanium can for example be deposited by means of Reduced Pressure - Chemical Vapor Deposition (RP-CVD) [37, 38], for implementing photodetectors and waveguides for non-linear applications, as well as Silicon Nitride, which can be deposited by means of Plasma Enhanced - Chemical Vapor Deposition (PE-CVD) [39], and can be used, for instance, for implementing low-loss TPA-free optical waveguides.

1.4 Building blocks and applications

As it is clear from the discussion in the previous paragraph, one of the main advantages of Si-Photonics is the possibility to implement optical components exploiting the well-established fabrication processes typical of the CMOS industry, thus allowing to reduce the devices dimensions (and consequently the power consumption) and paving the way for on-chip dense optical integration.

Using Silicon waveguides as a basic elements, many different optical components can be implemented, such as grating couplers [40] or edge-couplers [41] for light coupling from optical fibres to the waveguides, directional couplers [42] and Y-branches [43] for splitting and recombining light into different waveguides, distribute Bragg gratings [44], and arrayed waveguide gratings (AWG) [45]. Interferometric structures such as Mach-Zehnder interferometers [15, 46] or ring resonators [47] have been demonstrated too, and phase variations due to carrier effects in such structures have been successfully exploited for the implementation of optical modulators [48, 49].

The most straightforward application for Silicon Photonics is that of data communications, both for high-bandwidth short-reach communications (such as in data-centers) and for long-reach coherent communications (such as, for example, in access networks). Silicon integrated optical components can be however employed for a huge number of other possible applications, such as bio-sensing [50, 51] and Raman spectroscopy [52], LIDAR systems [53], optical gyroscopes [54], microwave photonics [55], imaging [56], and many others.

1.5 FABULOUS Project

An example of the advantages enabled by applying Si-Photonics technologies to optical communications is represented by the EU-funded (FP7) research project FABULOUS (FDMA Access By Using Low-cost Optical network Units in Silicon photon-

ics). The final goal of the FABULOUS project was to develop and test a new architecture for access-network PONs, based on the realization of a highly integrated Si-ONU with a low final cost for the customer.

1.5.1 FABULOUS network architecture

The network architecture proposed by the FABLOUS project was designed so as to meet the requirements of Next Generation PON (NG-PON2), standardized by ITU-T as G.989 [57], such as:

i. Compatibility with legacy infrastructure, (the already installed pure-splitter based PON network), thus requiring the ability to support a maximum Optical Distribution Network (ODN) loss value of 31 dB without any amplification stage along the path.
ii. An aggregate capacity of more than 40 Gbps per each fibre coming out of the OLT, with every fibre capable of serving from 64 to 1000 different users.
iii. An average data rate of 1 Gbps per user for the downstream (DS) traffic, and a data rate in the range from 500 Mbps to 1 Gbps per user for upstream (US) traffic.
iv. A passive reach of at least 20 km, even if 40 km would be preferred.
v. Low power consumption (in order to meet the EU directives regarding "green" and sustainable ICT).

The FABULOUS network is based on two different hierarchic levels of modulation, as it can be seen in Fig.7, where a schematic of the proposed network architecture is shown.

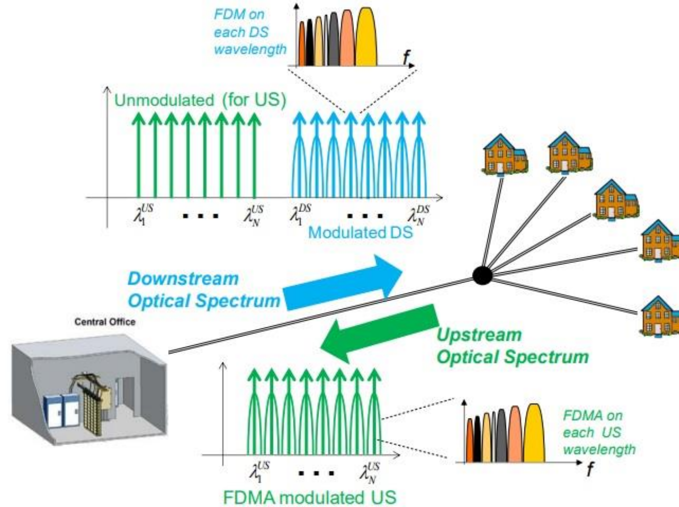

Figure 7: Schematic of the Fabulous network architecture [58].

At the optical level, a Wavelength Division Multiplexing (WDM) scheme is adopted, which allows to increase the transmission capacity per single fibre. At the electric level,

Frequency Division Multiplexing (FDM) and Frequency-Division Multiple Access (FDMA) are used to modulate the single optical carriers, in order to respectively generate the downstream and upstream data-flows.
The use of FDMA for the upstream data modulation provides significant improvements with respect to more traditional time-domain approaches, such as Time and Wavelength Division Multiplexing (TWDM), which is one of the multiplexing options available in standard G.989 [57]. In fact, while in time-domain solutions all the ONUs have to work at the full wavelength speed, FDMA allows the ONUs to access their individual portion of the available electrical spectrum, thus running at the single user baud-rate. This greatly relaxes the electrical hardware requirements for each ONU device, and it also makes easier to apply Digital Signal Processing (DSP), Forward Error Correction (FEC) and equalization.

The network is "passive", meaning that all the laser sources are placed in the Optical Line Terminal (OLT) located at the central office (CO), and not at the user side (thus helping to reduce the complexity of the ONU and hence its cost). The OLT sends to the different ONUs not only the downstream traffic, but also a set of continuous wave (CW) signals. Each ONU then filters a particular CW wavelength, modulate it, and send it back to the OLT with its state of polarization rotated by 90° with respect to the incoming radiation, thus acting as a reflective Faraday rotator. The upstream modulated signal is therefore orthogonal to the respective CW seed, and the orthogonality condition is preserved in every point of the network. This feature allows the OLT to perform simple single-polarization homodyne coherent detection of the upstream signal (as it is shown in Fig.8), using a single optical source for generating both the local oscillator and the CW seed. The polarization rotation scheme adopted for the US signal is also beneficial for reducing the penalty induced by spurious reflections, which is one of the common problems of reflective PONs.

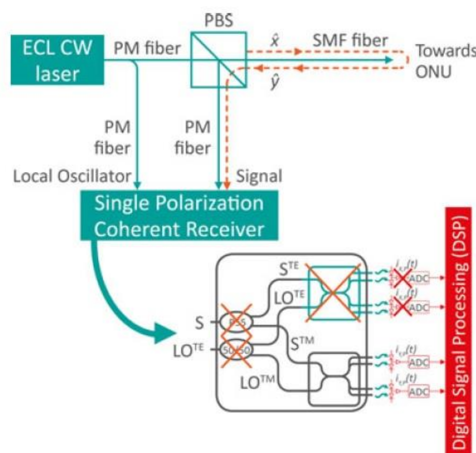

Figure 8: Schematic of single-polarization homodyne detection of the upstream data-flow performed at the network OLT. The lower part of the Figure shows a comparison with a standard dual-polarization coherent detection scheme, where all the components that can be avoided thanks to use of single-polarization are barred [59].

1.5.2 ONU structure

As previously mentioned, the main innovation of FABULOUS Project resides in the technique employed for the generation of the US signal, based on the use of polarization-rotating reflective ONUs.

All the required optical devices were integrated on a Si-Photonics platform allowing great component miniaturization and the realization of a single-PIC ONU. Compared to the case of optical devices implemented with discrete components, Si-based optical chips allow reducing both the power consumption, thanks to the reduced device footprint, and the final ONU market-price, as Si-Photonics relies on the high-volume manufacturing processes typical of the CMOS industry. It is for example expected that, assuming a production volume of 1 million pieces per year, the final market-price of the ONU would probably be less than 100$, in which most of the costs would be related to the optical packaging [60].

Silicon Photonics theoretically allows for a complete integration of the photonic components and their related driving electronic circuitry on the same chip, thus bringing the optical functions at the transistor level. As an example, such an integration has already been demonstrated by US Company *Luxtera* in [61], whose photonic and electronic components are integrated on the same die, to implement a QSFP (Quad Small Form-factor Pluggable) 4x10-Gb/s active optical cable interconnect.

For the FABULOUS Project instead, a flip-chip technique was used: the Electronic Integrated Circuit (EIC) and the PIC are electrically and thermally connected by means of 484 discrete copper micro-pillars with reduced parasitic capacities. The pillars have a 25 µm diameter, and are formed by Cu electro-plating of the under-bump metal-pads on the PIC and EIC, followed by the deposition of a lead-free Sn-Ag-Cu solder-cap [62]. An image of one of the Fabulous flip-chipped ONU is shown in Fig.9, together with a microscope image of the solder flip-chip bond between a couple of copper pillar on the PIC and EIC.

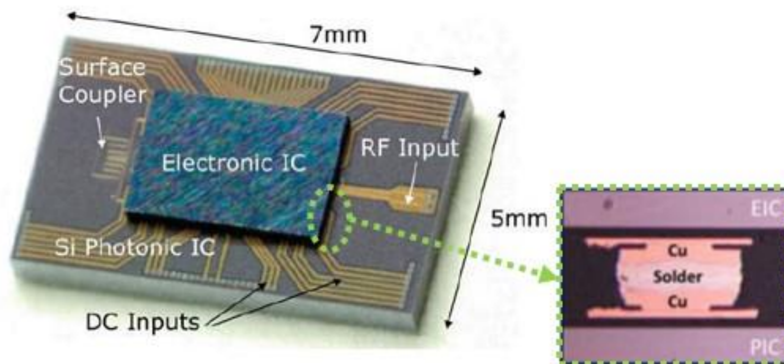

Figure 9: Photograph of the FABULOUS ONU silicon chip, showing the EIC flip-chipped over the PIC. The insert is a microscope image of a solder-reflow bond between a pair of copper micro-pillars on the PIC and the EIC [62, 63].

A schematic of the optical components integrated in the PIC for the generation of the US signal is shown in Fig.10.

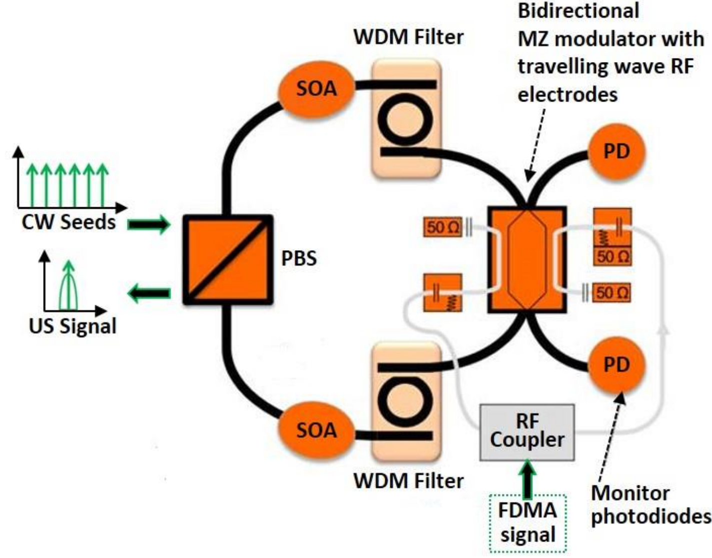

Figure 10: Schematic Representation of the optical components integrated in the silicon PIC of the ONU for the generation of the US traffic.

The un-modulated signal (made of different CW seeds) is sent by the OLT and, after travelling across the ODN, reaches the ONU with an arbitrary state of polarization. Here the light coming out of a standard single-mode fibre (SMF) is coupled to the optical chip by means of a two-dimensional diffractive grating coupler (2D-GC) implemented as a photonic crystal. The input 2D-GC also acts as a polarization beam splitter (PBS), allowing to separate the incoming signal into its two different orthogonal polarization, and coupling each of them to the fundamental TE mode of two outgoing integrated silicon waveguides. This architecture brings two main benefits: all the optical components located downstream of the 2D-GC need to be optimized only for a single state of polarization, and the functioning of the ONU itself turns to be independent from the input state of polarization, as this only affects the ratio between the amount of optical power coupled to the two waveguides, but not the overall quantity of optical power coupled to the ONU. The problem of achieving efficient coupling between optical fibre and photonic integrated circuits is discussed in Chapter 2, where a detailed description of the 2D-GCs implemented for FABULOUS Project is given.

After being separated by the 2D-GC, the two components of the input signal are filtered by means of a pair of integrated micro-ring based WDM filters, thus allowing the ONU to select a single wavelength for the generation of the upstream signal. The micro-ring filters are electrically tunable, meaning that their resonance frequency can be finely tuned by current injection. This adds a useful grade of flexibility to the ONU, as the wavelength used for the US transmission can be dynamically changed according

to the network requirements. A detailed discussion of the design and experimental characterization of the FABULOUS integrated filters is given in Chapter 4.

Although the ONU architecture should be in theory implemented using passive components only, it is however necessary to include some amplification stage, in order to guarantee a minimum level of optical power for the upstream signal relayed from the ONU to the OLT. This is achieved by hybrid-integration of a pair of Semiconductor Optical Amplifiers (SOAs) on the two symmetric branches of the ONU, immediately before the WDM filters. A detailed description of the experimental characterization of one of the FABULOUS SOA (hybridly integrated on a Silicon substrate and packaged as a stand-alone device) is given in Chapter 5.

After being amplified and filtered, the two components of the input CW seed impinge with different propagation directions, respectively clockwise and counter-clockwise with respect to Fig.10, on a bidirectional Mach-Zehnder Modulator (MZM), where the FDMA signal is applied to achieve the modulation of the US signal. After passing through the MZM the two modulated components recombine themselves at the 2D-GC, thus reversing the splitting of the input signal; if the two branches of the MZM exhibit a π phase difference, the overall "reflected" signal, after recombination at the grating coupler, shows a state of polarization orthogonal to that of the original CW seed, thus implementing a reflective Faraday rotator [64]. The MZM is made of a reversed-bias p-n junction, thus exploiting the mechanism of carrier-depletion in order to vary the waveguide refractive index. The active regions are 3 mm long on both arms of the modulator, and travelling wave (TW) phase modulation is implemented, applying the same microwave driving signal in opposite directions on the two electrodes. A first fabricated generation of the MZM device exhibited a $V_\pi \cdot L_\pi$ of 4 V·cm, a propagation loss of 1 dB/mm, and an electro/optical bandwidth of 20 GHz when applying a bias voltage of -1 V [65]; a second generation of the MZM was then developed, showing an improved $V_\pi \cdot L_\pi$ of 2 V·cm, thus achieving a V_π of 7 V [62].

As it can be seen in Fig.10, also a pair of Germanium photo detectors is included in the ONU architecture. They are used as monitors for controlling the MZM biasing, thus having a very relaxed bandwidth requirement (< 1 MHz). For this reason, the photo detectors are monolithically integrated on the PIC exploiting well established and already demonstrated fabrication techniques (see for example [37]), without any particular achievement beyond the state of the art.

2 Optical coupling in Silicon Photonics chips

One of the main issue related to the use of Silicon nanowires with sub-micrometer dimension, is that of achieving efficient coupling with standard single-mode fibres. This Chapter will focus on fibre-to-chip optical coupling strategies, based on the use of diffractive grating couplers. The different solutions already reported in scientific literature for achieving efficient coupling, either polarization sensitive or insensitive, will be analyzed. After that, the original results of the scientific research carried out during the PhD activity will be discussed. They include the complete development (simulation, design, fabrication and experimental characterization) of a highly-efficient apodized 1-D grating coupler, and the design and experimental characterization of test-structures for evaluating the performances of an optimized 2-D grating coupler, which had been previously simulated by other researchers in the *Physics Department* of the *University of Pavia*. The activity regarding the development of an efficient 1-D grating coupler has been carried out during a 6 months exchange period at the *Optoelectronics Research Center (ORC)* of the *University of Southampton*, and the activity results have been reported in [66] and currently submitted for publication in *Nature-Scientific Reports*. The activity results regarding the 2-D grating coupler have instead been reported in [67].

2.1 Optical coupling strategies

As already discussed in the previous Chapter, Silicon is a poor material for optical signal generation, and therefore, unless a III-V optical source is hybridly integrated over the Si substrate, light has to be generated from an external optical source and then coupled to the Si chip. The easiest and most practical way of bringing light to a chip is by means of standard single-mode optical fibres (SMFs). Unfortunately, the cross-sectional area of an optical fibre core with a 9 µm diameter is almost 600 times bigger than the modal effective area of a SOI waveguide (standard cross-section 500x220 nm), thus preventing to achieve direct coupling with a reasonable level of insertion loss. To overcome this issue, two main strategies have been extensively studied in the scientific and industrial community:

i. Edge coupling (horizontal coupling)
ii. Diffractive grating coupling (vertical coupling)

In edge coupling, also known as end fire coupling, an inverse taper is fabricated on a SOI waveguide at the edge of the chip, meaning that the waveguide width is tapered down to a very small value in order to expand the waveguide evanescent field mode profile, which can then be coupled to a lensed fibre with reduced mode-field diameter (MFD). To allow modal expansion not only in the in-plane, but also in the out-of-plane direction, the inverse-taper structure can be coated with an additional overlay made of polymer [68] or silicon-rich oxide (SiOx) [41], whose refractive index can be

tailored in order to match that of an optical fibre, by controlling the amount of silicon nano-crystals dispersed in the oxide matrix. A schematic of a typical edge coupling structure is shown in Fig.11.

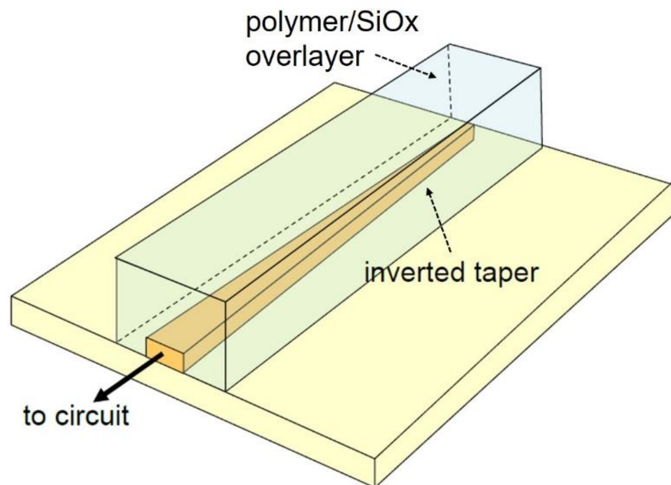

Figure 11: Schematic of a standard edge coupling configuration for coupling light between a SOI waveguide and a tapered single mode fibre.

Edge coupling allows to obtain very high coupling efficiencies (> -1 dB) for both TE and TM light polarization over a large spectral bandwidth (1 dB bandwidth $\geq$ 100 nm). In [41] for example, a silicon strip waveguide having a thickness of 220 nm and initial width of 500 nm, is linearly tapered down to 80 nm over a length of 300 µm, by means of 193-nm deep UV (DUV) Lithography and reactive ion etching (RIE) techniques, demonstrating a coupling efficiency as high as -0.25 dB at a wavelength of 1550 nm for both TE and TM polarizations, when a lensed fibre having MFD equal to 3 µm is used.

Recently, M. Papes et al. [69] also demonstrated the possibility to achieve efficient edge coupling using cleaved SMFs with a 10.4 µm MFD, instead of high numerical-aperture (NA) lensed fibres. This is accomplished by increasing the upper cladding refractive index near the chip facet with the deposition of a stack of subwavelength thick Si_3N_4 layers, demonstrating a coupling efficiency of -0.42 dB for the TE mode at 1550 nm.

Despite its great performances in term of high coupling efficiency, polarization insensitivity and high operational bandwidth, the edge coupling approach requires very complicated fabrications processes in order to be practically implemented, such as high-quality chip facets polishing and the deposition of anti-reflection coatings. Moreover, the necessity to use expensive lensed fibres and the poor tolerance to fibre misalignments (1-dB tolerance $\leq$ 1 µm), makes edge coupling hardly compatible with already-existing standard photonic packaging techniques.

2.2 Diffractive grating coupler

A possible alternative solution to the optical coupling problem is then represented by vertically coupled diffractive grating structures. Grating couplers, compared to edge couplers, are generally cheaper to fabricate, as they do not require complicated post-processing, they show better tolerance to fibre misalignments and can also be put anywhere on the Si chip: this allows for greater flexibility in the design stage, and also allows for wafer-level automated testing.

2.2.1 Grating coupler theory

A waveguide diffractive (uniform) grating coupler is obtained when the waveguide refractive index profile is varied according to a periodic pattern in one or more dimensions. If the refractive index is changed only along the direction of light propagation, a one-dimensional grating coupler is obtained (1D-GC), whereas if the refractive index is varied also along the width of the waveguide, a two-dimensional grating coupler (2D-GC) is obtained. 1D-GCs will be analyzed first, while 2D-GCs will be discussed in Paragraph 2.4.

The physical behavior of a diffractive grating can be described in terms of the Bragg condition, which defines the relation between the wave-vector of the incident optical beam, and the wave-vectors of the diffracted beams. Assuming to have a 1D grating (where the index variation is taken to be on the z axis), placed between two materials with refractive index equal to n_1 and n_2, the Bragg equation can be expressed as:

$$\boldsymbol{k_{m,z}} = \boldsymbol{k_{u,z}} + m\boldsymbol{K} \tag{9}$$

Where m is the diffraction order, $\boldsymbol{k_{u,z}}$ is the z axis component of the wave-vector of the undiffracted beam $\boldsymbol{k_u}$, $\boldsymbol{k_{m,z}}$ is the z axis component of the wave-vector of mth diffracted order $\boldsymbol{k_m}$, and $\boldsymbol{K}$ is a vector lying in the $\hat{\boldsymbol{z}}$ direction which describes the grating according to the following expression:

$$|\boldsymbol{K}| = \frac{2\pi}{\Lambda} \tag{10}$$

Where Λ is the grating period. The magnitude of the wave-vectors $\boldsymbol{k_u}$ and $\boldsymbol{k_m}$ can be expressed as:

$$|\boldsymbol{k_{u,m}}| = \frac{2\pi}{\lambda} n_1 \quad \textit{in material } 1 \qquad |\boldsymbol{k_{u,m}}| = \frac{2\pi}{\lambda} n_2 \quad (\textit{in material } 2) \tag{11}$$

Being λ the wavelength of the incident optical beam. The Bragg condition expressed by Eq.(9) basically represents a phase-matching condition along the z axis for the beams diffracted by the grating. It derives from the electric field boundary condition

at the interface between two media having different refractive index, requiring the tangential components to be continuous.
An intuitive way to represent the Bragg condition expressed by Eq.(9) is by means of a wave-vector diagram, as it can be seen in Fig.12.

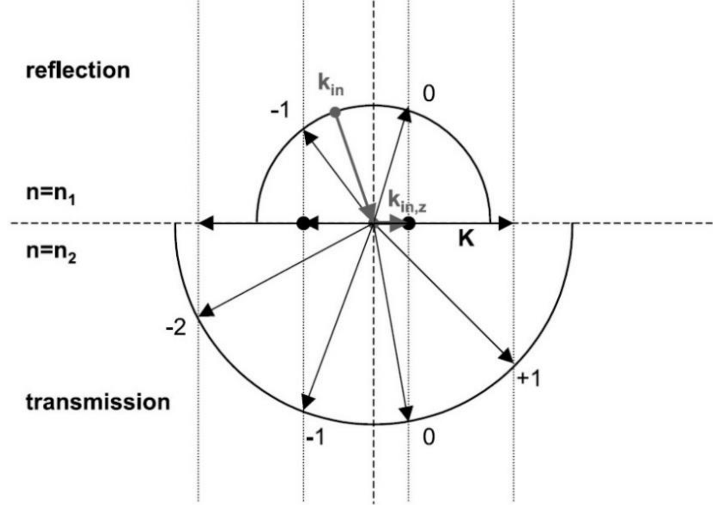

Figure 12: Wave-vector diagram representing the Bragg condition for diffracted beams from a grating.

The wave-vector diagram of Fig.12 represents a situation in which a beam travelling with wave-vector $\boldsymbol{k_{in}}$, is incident on a grating located at the interface between two media having refractive indexes respectively equal to n_1 and n_2. Concentric circles are used in the diagram, where the radius of each circle represents the magnitude of the wave-vector $\boldsymbol{k}$ in the corresponding medium. The grating is ideally located in the center of the diagram. The undiffracted reflected and transmitted beams (corresponding to a diffraction order m equal to 0) are governed by the well-known Snell equations:

$$\theta_r = \theta_i \tag{12}$$

$$n_2 sin(\theta_t) = n_1 sin(\theta_i) \tag{13}$$

Where θ_i, θ_r, and θ_t are respectively the incidence, the reflection and the transmission angle. The mth order diffracted beam can be graphically constructed by adding m times the grating vector $\boldsymbol{K}$ to the z axis component of the undiffracted beam (which is equal to the z axis component of the incoming beam, because of Snell law), and then by tracing vertical lines from the end point of the resulting vector, perpendicularly to the interface of the two circles. If the vertical line crosses the wave-vector circle, the mth order diffracted beam can physically exist, with its ray starting at the center of the circles and ending at the intersection point, whereas if no intersection happens, the diffracted beam cannot physically exist.

For a waveguide grating coupler, a similar wave-vector diagram approach can be considered, by substituting the incident beam with a waveguide guided mode characterized by its propagation constant β, which can be expressed as:

$$\beta = \frac{2\pi}{\lambda} n_{eff} \tag{14}$$

Where n_{eff} is the effective refractive index of the waveguide grating. The Bragg condition can therefore be rewritten as:

$$\boldsymbol{k_{m,z}} = \beta + m\boldsymbol{K} \tag{15}$$

Were the magnitude of wave-vectors $\boldsymbol{k_{m,z}}$ and $\boldsymbol{K}$ can again be expressed according to Eq.(10) and Eq.(11). Two situations are of particular interest, according to the ratio between the grating period Λ and the optical wavelength λ, as showed in Fig.13. In Fig.13(left) Λ is exactly equal to λ/n_{eff} (i.e. the optical wavelength inside the grating): in this configuration the first order diffracted mode is vertically emitted out of the grating, and it can be therefore coupled to an optical fibre, but the second order diffracted mode is reflected back to the waveguide. This configuration, also known as resonant configuration, is usually not employed in practice, unless some strategy to suppress the reflect contribution is adopted. This can be done, for example, by implementing a partially reflecting mirror before the grating [70], as shown in Fig.14. In Fig.13(right) instead, Λ is bigger than λ/n_{eff}, and therefore the first order diffracted mode is emitted with its direction slightly detuned from the vertical axis, while the second order in-waveguide reflection contribution is suppressed. This the configuration that is mostly adopted for designing waveguide grating couplers.

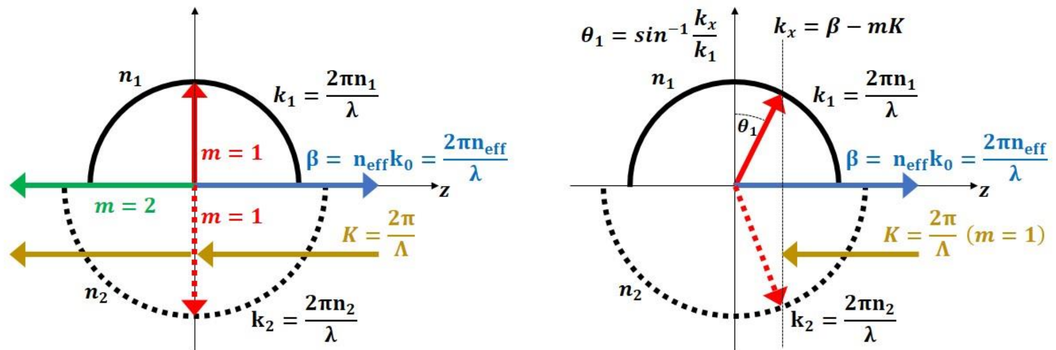

Figure 13: Wave-vectors diagrams of waveguide grating couplers in resonant configuration (left) and detuned configuration (right).

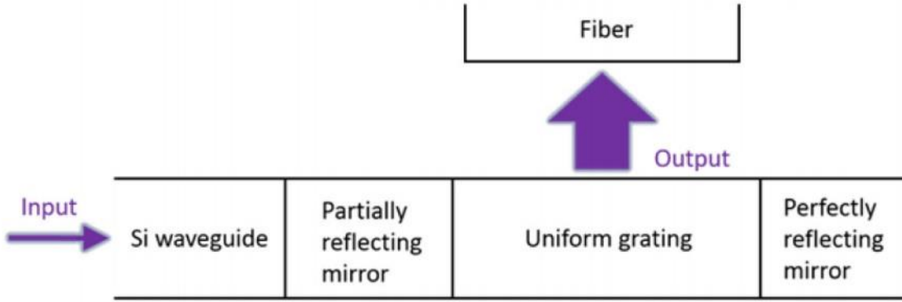

Figure 14: example of a resonant grating coupler, where a partially reflecting mirror is put before the grating to suppress the in-waveguide second order diffracted contribution [70].

If we take into consideration the first order diffraction angle θ_1 in the detuned configuration, the Bragg condition of Eq.(15) can be reformulated as:

$$n_{eff} - n_1 \cdot sin\,\theta_1 = \frac{\lambda}{\Lambda} \tag{16}$$

By taking a deeper look at Eq.(16), two main aspects must be highlighted:

i. The Bragg condition shows a strong dependence on the optical wavelength λ, meaning that operational bandwidth of a grating coupler will be definitely lower than that of an edge-coupler.

ii. For both the resonant and the detuned configurations, there are two first order diffracted contributions, one emitted upwards, and the second one downwards. This means that for a grating coupler implemented in a SOI waveguide, part of the optical power incident on the grating will be lost in the substrate.

It is also important to notice that the Bragg condition is strictly valid only for infinite grating structures and for small index variations. For a finite structure, diffraction will not occur at a single discrete k-vector, but at a range of k-vectors around the one predicted by the Bragg condition.

2.2.2 Uniform SOI grating couplers: performances and limitations

A cross-sectional schematic of a standard 1D uniform grating coupler implemented in a SOI platform is given in Fig.15, where the k-vector of the waveguide mode is assumed to lie on the z axis.

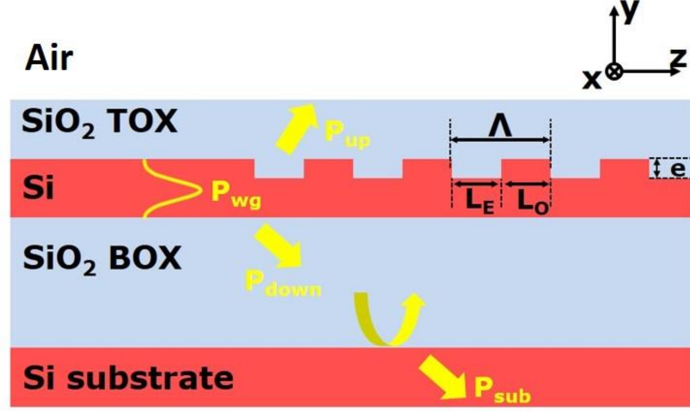

Figure 15: Cross-sectional schematic of a uniform GC implemented in SOI technology.

The periodic index variation is obtained by partially etching the Si waveguide with an etch depth e, thus defining etched trenches with length L_E and un-etched teeth with length L_O. The period Λ is simply defined as the length of each scattering unit, thus being:

$$\Lambda = L_E + L_O \tag{17}$$

While the grating fill-factor (FF) can be defined as the ratio between the un-etched tooth L_O and the grating period Λ:

$$FF = \frac{L_O}{\Lambda} = \frac{L_O}{L_O + L_E} \tag{18}$$

The grating effective refractive index n_{eff} can be expressed as:

$$n_{eff} = FF \cdot n_O + (1 - FF) \cdot n_E \tag{19}$$

Where n_O and n_E respectively define the effective refractive index of the grating un-etched tooth, and of the etched trench. The resulting grating n_{eff} is therefore influenced both by the choice of the FF, and by the chosen value of e, as in increase in etch depth will lead in a reduction of n_E.
The grating structure can be exposed to air, or it can be coated with a Silicon Dioxide top cladding (top oxide, TOX).

Assuming the grating to work in an output configuration (thus with an input wave-guided mode coupled to an optical fibre, according to the wave-vector diagram description reported in the previous paragraph), three main parameters can be defined which describe the grating performances:

i. Directionality: the ratio between the optical power diffracted upwards (P_{up}), and the input optical power of the wave-guided mode (P_{wg}).
ii. Reflectivity: the ratio between the optical power reflected back into the waveguide from the grating, and the input optical power of the wave-guided mode (P_{wg}). Reflectivity is always present, even in detuned grating configurations, because of the refractive index contrast between the Si waveguide and the grating section. It should be minimized as it can cause parasitic Fabry-Perot oscillations.
iii. Coupling efficiency (CE): the ratio between the optical power coupled to the fundamental mode of the optical fibre, and the input optical power of the wave-guided mode (P_{wg}). Thanks to the reciprocity theorem, which can be proven based on Maxwell's equations [71], and can be applied to linear open systems (systems where energy can leak away) [72] such as a Silicon grating, the grating CE remains the same both in output configuration (from the waveguide to the fibre) and in input configuration (from the fibre to the waveguide).

The diffraction angle θ_1 of a uniform GC at a specific central wavelength λ, can be tuned by an accurate choice of the geometrical parameters Λ, e, and FF, accordingly to the Bragg condition (see Eq.(16)). When dealing with a standard SOI platform, having a 220 nm thick Si layer and a 2 µm thick BOX, the maximum CE is usually achieved for shallow etching levels ($e \approx 70$ nm) and FF values close to 0.5, and it is limited to values $< 60\%$. This can be seen in Fig.16 and in Fig.17, where the CE of a uniform GC (obtained by means of 2D-FDTD simulations) is reported, as a function of the optical wavelength, for different values of e and FF, assuming to have TE light polarization (along the x direction, with reference to Fig.15). The grating period Λ is set to be 634 nm, so as to obtain a diffraction angle θ equal to 14.5° for a central wavelength of 1550 nm. It is also very important to notice that 1D-GC are strongly sensitive to polarization; as TE and TM polarized waveguide modes exhibit very different values of effective refractive index, a 1D-GC optimized for TE light polarization will suppress light in the opposite polarization, as shown in Fig.18.

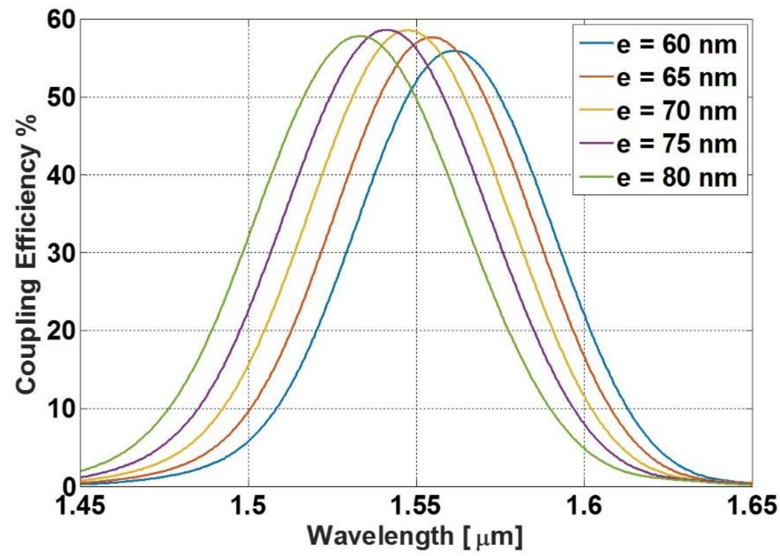

Figure 16: CE for a uniform GC implemented in standard SOI platform (Si thickness = 220 nm, BOX thickness = 2 µm), with a grating period $\Lambda = 634$ nm, and $FF = 0.5$. CE is reported as a function of optical wavelength λ for different values of etching depth e, ranging from 60 nm to 80 nm.

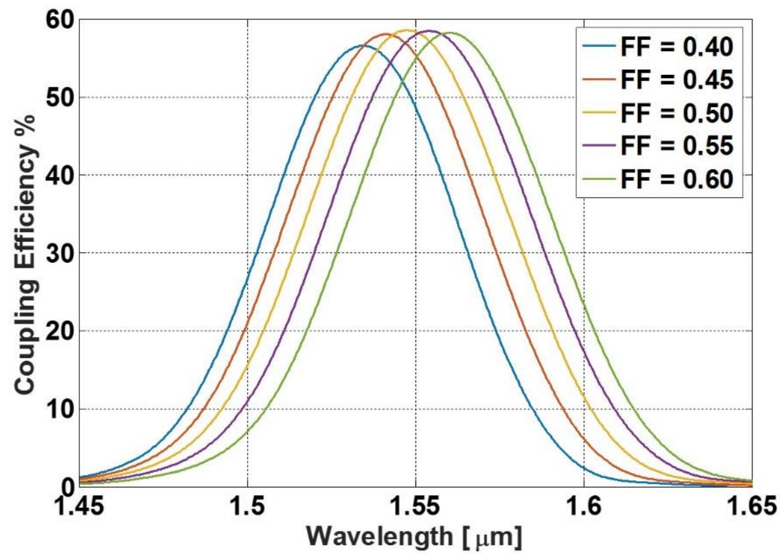

Figure 17: CE for a uniform GC implemented in standard SOI platform (Si thickness = 220 nm, BOX thickness = 2 µm), with a grating period $\Lambda = 634$ nm, and $e = 70$ nm. CE is reported as a function of optical wavelength λ for different values of fill-factor FF, ranging from 0.4 to 0.6.

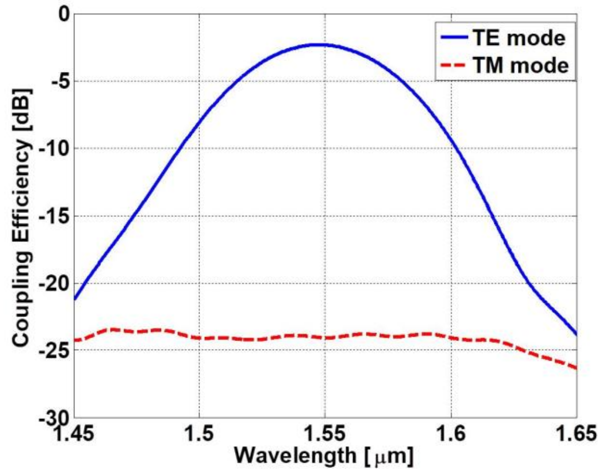

Figure 18: Coupling efficiency of a TE-optimized 1D-GC as a function of optical wavelength for TE light polarization (blue trace) and for TM light polarization (red trace).

It is also important to keep in mind that the Bragg condition is strictly valid only for small index variations. When a high level of etching depth e is used to design the grating, thus involving a strong refractive index contrast between the etched trench and the un-etched tooth, the "actual" grating central diffraction wavelength will slightly differ from the theoretical one predicted by the Bragg condition, for a given set of Λ, e, and FF values. This can be seen, for example, in Fig.19, where the central wavelength obtained by means of 2D-FDTD simulations is plotted, as a function of the etching depth e, for uniform GCs implemented in 220 nm Si-thick SOI (at each level of e, the period value Λ is chosen, in Fig.19, in order to have a nominal central wavelength of 1550 nm and a diffraction angle θ_1 of 14.5°). In specific situations where high etching levels are required, this problem can be overcome by simply setting the nominal central wavelength λ to a value slightly bigger than the required one.

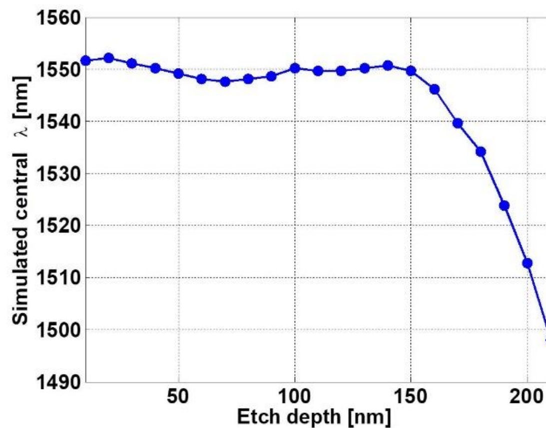

Figure 19: Simulated central wavelength of uniform GCs as a function of etch depth. For each etch depth level e, the grating period Λ is set in order to have a nominal central wavelength of 1550 nm and a diffraction angle of θ of 14.5°.

The low CE of standard uniform GCs can be explained in terms of poor directionality, and poor mode-matching between the radiated field distribution and the Gaussian field distribution of the fundamental mode of a SMF.
For what regards directionality, a considerable part of the optical power incident on the grating is diffracted downwards, as it has already been mentioned in the previous paragraph. In an ideally perfectly symmetrical situation, assuming infinitely extending BOX and TOX and full-etching of the Si layer, the 1st order upwards and downwards diffracted modes would have the same intensity, thus clipping the maximum achievable CE to values < 50%. In practical SOI implementations, part of the power diffracted downwards is reflected at the interface between the BOX and the Si Substrate, thus allowing to increase directionality and, consequently, the maximum achievable CE. The buried oxide layer thickness has a strong influence on the resulting directionality, as the maximum value is achieved when the reflected contribution is in phase with the upwards diffracted field. However, this parameter cannot be optimized in the grating design stage, if not by choosing the most appropriate SOI wafer from the ones commercially available. Some of the technique which have been used in literature to increase GC directionality will be described in the next paragraph.
For what concerns the mode matching issue instead, the normalized power density profile radiated from a uniform GC implemented in 220 nm Si-thick SOI, assuming a 70 nm deep etching depth, is shown in Fig.20.

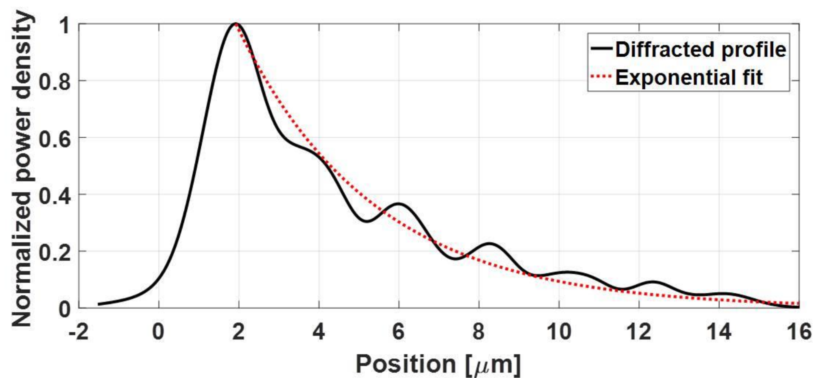

Figure 20: Normalized power density profile of the diffracted mode from a uniform GC, implemented in 220 nm Si-thick SOI platform with a 70 nm deep etch.

As it can be seen in Fig.20, in uniform GCs most of the optical power P is radiated in the initial section of the grating, and then an exponentially decaying trend is observed, which can be expressed as:

$$P(z) = P_0 \, e^{-2\alpha z} \tag{20}$$

Where α is the grating coupling strength ($\alpha \approx 0.146$ μm^{-1} for the example of Fig.20), whose value varies as a function of e and FF, as it can be seen, for example, in Fig.21, where the normalized power density profiles of the diffracted mode is reported, for 220 nm Si-thick SOI gratings, having e equal to 70 nm, and FF ranging from 0.5 to 0.8.

As the fundamental mode of SMF is characterized by a Gaussian distribution, with a MFD of 10.4 µm, the grating-fibre mode overlapping is however quite poor (usually < 80% [73]), thus affecting the resulting CE.

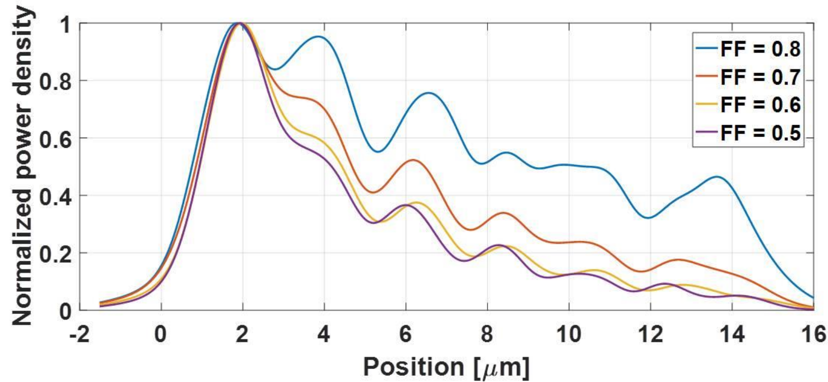

Figure 21: Normalized power density profile of the diffracted mode from uniform GCs, implemented in 220 nm Si-thick SOI platform with a 70 nm deep etch, and FF ranging from 0.5 to 0.8.

2.2.3 Advanced grating coupler designs

Many different approaches have been proposed in the scientific literature in order to improve the performances of SOI grating couplers. Grating directionality, for example, can be greatly increased by embedding a mirror in between the BOX layer and the Si substrate. In [74] for example, a back-reflector is implemented as a Distributed Bragg Reflector (DBR), using a stack of amorphous-Si/SiO_2 layers with $\lambda/4$ thickness, and demonstrating a CE of 69.5%. A schematic of the grating structure proposed in [74] is reported in Fig.22.

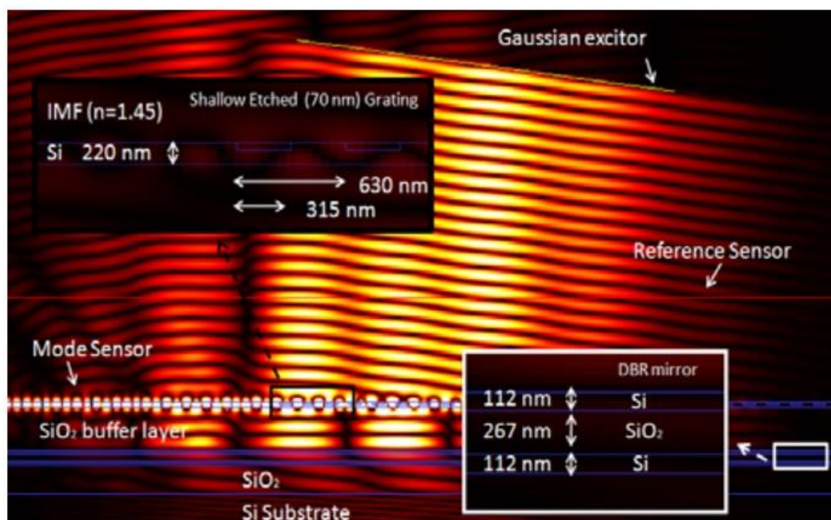

Figure 22: Uniform GC with embedded DBR mirror [74].

Alternatively, the back-reflector can also be implemented as a metallic mirror, made of aluminum [75, 76] or gold [77]. It must be mentioned that, when implementing a grating back-reflector, the performance improvement comes at the expense of a greatly increased fabrication complexity, which may involve the use of non-CMOS compatible materials (such as aluminum or gold, which may induce metal contamination issues) or the use of complicated and expensive processes, such as multi-layer deposition [74], adhesive bonding [76] or backside etching at the wafer substrate [75].

Another interesting technique for improving the grating directionality is based on the deposition of a poly-Si layer over the grating structure [78, 79]. The additional layer allows to increase the grating refractive index contrast, and its thickness is carefully chosen in order to set constructive interference between the field components radiated by each scattering element of the grating. A schematic cross-section of the grating design proposed in [79] is given in Fig.23; thanks to this approach an experimental coupling efficiency of -1.6 dB has been demonstrated. Recently Yang et al. [80] also demonstrated the possibility to deposit a 230 nm high Germanium over-layer on a 220 nm Si-thick SOI grating. The high Ge refractive index (n_{Ge}= 4.28 at λ = 1550 nm) allows a great directionality increase, while the layer thickness is kept enough small to reduce the absorption loss (which is calculated to be 0.2 dB), thus achieving a theoretical CE of 1.2 dB.

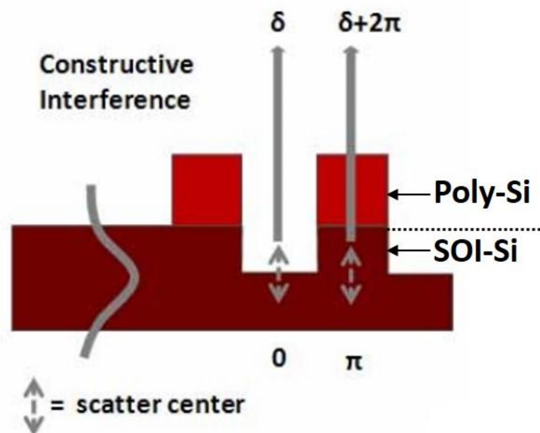

Figure 23: Schematic of a 220 nm Si-thick SOI grating coupler, with a 160 nm thick amorphous-Si overlay [79].

As it has previously been mentioned, one of the main limitation of uniform GCs is the modal mismatch between the radiated field distribution (which is characterized by an exponential decay) and the SMF Gaussian mode distribution. This problem can be mitigated by employing non-uniform (also known as apodized) grating structure, meaning that the effective refractive index of each grating scattering unit is varied along the direction of light propagation into the grating, so as to tailor the distribution of the diffracted optical power, thus achieving a better matching with the fibre Gauss-

ian mode. The effective index variation can be obtained either by using multiple etching depths to define the grating trenches, as reported in [81, 82] (an approach that can strongly complicate the fabrication process as it requires multiple etching steps), or by varying the fill-factor FF or the length Λ of each grating radiative element, in order to obtain the desired radiated field profile, while using a unique etching depth all over the grating structure. In the second case, different techniques can be employed to optimize the apodized grating structure; one possibility is, for example, represented by the use of numerical techniques, such as genetic algorithms, which can however be very computationally intensive and time-consuming, as, in this case, the lengths L_E and L_O of the etched and non-etched portions of each grating scattering unit have to be optimized individually. A genetic algorithm has for example been used in [75], to optimize the performances of a GC implemented in a 260 nm Si-thick SOI platform with 3 µm thick BOX, demonstrating, also thanks to the use of an embedded back-reflector, an experimental CE of -0.62 dB, which is the current record value for SOI 1D-GCs. An alternative approach to define the grating apodization curve, relies on theoretically calculating the ideal grating coupling strength distribution $\alpha(z)$ along the grating direction, required to obtain an output Gaussian distribution $G(z)$ [40, 83]. This is accomplished by imposing that:

$$\frac{dP(z)}{dz} = -2\alpha(z)P(z) = -G^2(z) \tag{21}$$

Obtaining, as a result, the following expression for $\alpha \ z$:

$$\alpha(z) = \frac{G^2(z)}{2\left(1 - \int_0^z G^2(t)\,dt\right)} \tag{22}$$

Once the ideal $\alpha(z)$ distribution is obtained, the coupling strength α of each scattering unit is individually tuned by varying its FF, in order to fit the theoretical distribution. In [40, 83], this is done assuming that the coupling coefficient α of a single scattering unit with a given FF, remains strictly the same both in a uniform and in a non-uniform configuration, thus performing simulations over uniform GC structures with different FF to obtain the relationship between α and FF. It is also important to mention that, with this approach, the etching depth e is not optimized together with the apodization profile, but it is instead chosen a priori, accordingly to etching depth level that maximize directionality in the corresponding uniform GC configuration. Finally, another apodization approach is based on linearly chirping the grating FF along the direction of light propagation, while keeping the length of each scattering unit Λ fixed to a unique value, as it happens in uniform configurations. This technique is for example applied in [84] and [85], while in [86] a linearly chirped grating configuration is used as a starting point for a subsequent genetic algorithm based numerical optimization.

2.3 Development of a highly-efficient 1D-GC

2.3.1 Grating design and simulation

Starting from the basic structure of a uniform GC, we decided to improve the CE by introducing a linear apodization on the grating *FF*, using an approach similar to that of [84, 85]. As it has already been discussed in the previous paragraph, a linear variation of the *FF* value along the grating brings two positive effects on the grating performances: the amount of optical power radiated by the first elements of the grating is reduced, and the optical impedance matching between the waveguide and the grating section is improved, thus allowing to reduce the problem of back-reflections into the waveguide [86]. The equation used to apodize the grating can then be expressed as:

$$FF = FF_0 - R \cdot z \tag{23}$$

where FF_0 is the initial fill-factor of the first radiative unit, R is the linear apodization factor and z is the distance of each radiative unit from the starting point of the grating. A cross-sectional schematic of the grating is shown in Fig.24.

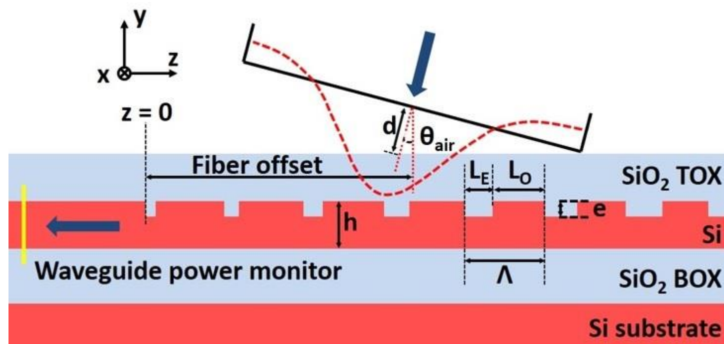

Figure 24: Cross-sectional schematic and simulation layout of a non-uniform GC in a SOI wafer, based on a linear apodization of the grating *FF*.

It is important to underline that Eq.(23) only describes the evolution of *FF* along the grating, but does not impose any limitation on the length Λ of the single scattering units, which still remains a free parameter. In most of the works reported in the scientific literature about linearly-apodized GCs, Λ is considered to be constant along the whole grating [84, 85, 86]. This assumption prevents the Bragg condition (expressed by Eq.(16)) from being simultaneously satisfied by all of the grating elements: in fact, as *FF* is varied along the grating, the effective index n_{eff} of each radiative unit changes consequently (see Eq.(19)), and thus the Bragg condition is satisfied only at a specific point of the grating but not along the whole structure. To alleviate this, we decided to design a GC with a linear apodization of *FF* and a value of Λ that was varied along the structure, so as to satisfy the Bragg condition along the whole grating. If we reformulate the Bragg condition as:

$$n_{eff} - sin\,\theta_{air} = \frac{\lambda}{\Lambda} \tag{24}$$

Where the diffraction angle θ_1 in the TOX has been replaced with the diffraction angle in air θ_{air}, accordingly to Snell equation, we can then combine Eq.(24) with Eq.(18-19), which define the grating FF and n_{eff}, and with Eq.(23), which describes the grating apodization, in order to derive an explicit formulation for the length $L_{E,i}$ and $L_{O,i}$ of the etched and un-etched portion of the ith grating scattering unit:

$$L_{O,i} = \frac{\lambda(FF_0 - R \cdot z_i)}{(FF_0 - R \cdot z_i)(n_O - sin\,\theta_{air}) + (1 - FF_0 + R \cdot z_i)(n_E - sin\,\theta_{air})} \tag{25}$$

$$L_{E,i} = \frac{\lambda(1 - FF_0 + R \cdot z_i)}{(FF_0 - R \cdot z_i)(n_O - sin\,\theta_{air}) + (1 - FF_0 + R \cdot z_i)(n_E - sin\,\theta_{air})} \tag{26}$$

Where the distance z_i of the $\mathrm{i^{th}}$ grating scattering unit from the origin of the grating can be written as:

$$z_i = \sum_{j=0}^{i-1} L_{O,j} + L_{E,j} \tag{27}$$

As it can be seen from Eq.(25) and Eq.(26), knowledge of the effective refractive indices n_E and n_O of the etched trenches and un-etched teeth respectively, is required in order to determine $L_{O,i}$ and $L_{E,i}$. While e is a constant value, as it only depends on the height h of the native Si layer of the SOI wafer, n_E varies as a function of the etch depth e. Both n_O and n_E values were extracted from mode simulations, performed using *MODE Soultions*™ commercial software from *Lumerical Inc.,* of slab waveguides having height respectively equal to h and $h - e$, and width equal to 12 µm. The employed software makes use of a finite difference algorithm to mesh the waveguide geometry, and then formulates the Maxwell's equation as a matrix eigenvalue problem which is solved by applying sparse matrix technique; more details about the numerical simulation method can be found in [87]. The simulated values of n_E as a function of e, assuming $h = 260$ nm, are reported in Fig.25.

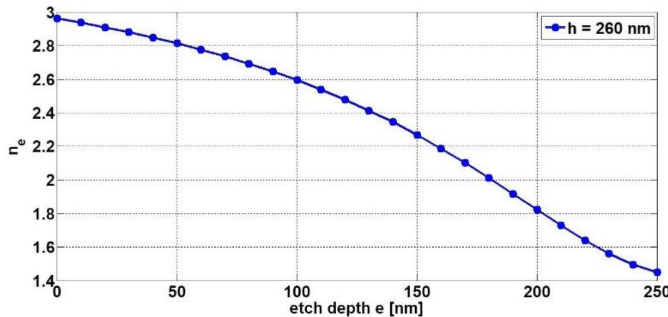

Figure 25: Effective index n_E of the grating teeth as a function of the etch depth e.

Using the obtained values of n_E and n_O, we calculated the length of the teeth L_O and trenches L_E of each radiative unit to optimize the CE for a beam with $\lambda = 1550$ nm and an angle of incidence θ_{air} of 14.5°. In Fig.26 a schematic representation of the difference between our linear apodization scheme and the standard approach based on the use of a fixed Λ is reported.

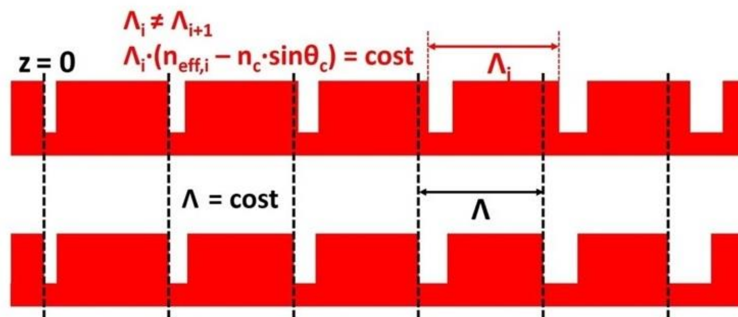

Figure 26: Cross-sectional schematic of the proposed linearly apodized GC (top) compared to that of a linearly apodized grating with fixed period Λ (bottom).

It is worth noting that using the proposed approach, and considering the standard situation where the thickness of the Si layer (h) and BOX layer are imposed by the choice of a particular SOI wafer, only two grating parameters have to be optimized: the etch depth e and the linear apodization factor R; this allows for a much simpler design procedure with respect to genetic-algorithms-based techniques, where the lengths of the etched and un-etched portions of each radiative unit are individually specified, and it also allows for an increased physical understanding. Regarding the choice of the initial fill-factor FF_0 in our design, it has been shown that increasing FF_0 results in an improvement of the grating CE [85], as a FF increase leads to a reduction of the corresponding coupling strength α (see for example Fig.21), which should ideally be zero in the first section of the grating. Unfortunately, the value producing the highest CE ($FF_0 = 0.95$ [85]) would require a minimum grating feature not generally available with the fabrication processes available to us, which imply a minimum feature size of about 60 nm. We therefore set FF_0 to 0.9, which corresponded to a value of $L_E = 60$ nm for the first trench.

After that, we performed a campaign of fully-vectorial two-dimensional (2D) FDTD simulations using *FDTD Solutions*™ commercial software from *Lumerical Inc.*, in order to find the optimum values of etch depth e and linear apodization factor R that maximize the grating CE, for the structure shown in Fig.24. FDTD is a finite-difference time-domain algorithm for simulating wave propagation into optical media, which is commonly and extensively used in the field of Silicon Photonics, as it allows for an exact numerical calculation of Maxwell's equations. Being a time-domain simulator, FDTD algorithms simulate the propagation of a short pulse of light (usually ten to hundreds of femtosecond long), which is composed by a broad spectrum of wavelength

components, thus allowing, with a single simulation run, to obtain information about the optical system response on a wide spectrum. The FDTD algorithm can be generally applied to three-dimensional (3D) optical systems, even if this can lead to very long and computationally-intensive simulations. As 1D-GCs can be considered to be symmetrical optical systems, since no index variation occurs in the transverse direction (the x direction, with reference to Fig.24), 2D simulations can be conveniently employed to assess the grating CE, as they allow for less computational memory and simulation time with respect to 3D simulations.

We took into consideration two different types of SOI wafer, both having a 2 µm high buried-oxide layer (BOX), and with a native Si layer of respectively 220 and 260 nm. A top-oxide layer (TOX) was included in the layout, with a layer height of 720 nm for the 220 nm SOI wafer, and 680 nm for the 260 nm SOI wafer, assuming the grating trenches to be completely filled by the TOX SiO_2, and considering no index-matching fluid between the TOX and the fibre. A conformal mesh algorithm was employed in order to guarantee the simulation accuracy. The refractive index of both Si and SiO_2 were calculated following the data reported by Palik [88]: therefore, the refractive indices at the design wavelength of 1550 nm are n_{Si} =3.48 and n_{SiO2} =1.44.

In order to evaluate the CE, we simulated the grating as an in-coupling device, thus coupling light from a SMF into the fundamental mode of the SOI waveguide by means of the grating. The fibre source was simulated as a Gaussian profile emitter, characterized by a MFD of 10.4 µm, and the light wave-vector was tilted by θ_{air} = 14.5° with respect to the vertical direction (which corresponds, because of Snell law, to θ_c = 10° in the TOX), in order to prevent back-reflections into the fibre. Considering that SMFs have a 125 µm thick cladding, and that, in practical situations, the fibre end-point is assumed to be just touching the surface of the chip, the light coming out of the fibre has to propagate for a stand-off distance $d = 125/2 \cdot \tan\theta_{air} \approx 16.1$ µm, before reaching the TOX. To take into consideration this effect, we included the stand-off distance d in the mathematical definition of the Gaussian source so that, being the numerical aperture NA of the fibre equal to 0.14, the Gaussian mode impinged on the grating with a MFD of about 10.8 µm. The electric field of the Gaussian beam was polarized along the x direction with reference to Fig.24, so that the incoming light could be coupled to the fundamental TE mode of the integrated waveguide. A frequency-domain power monitor, positioned along the Si waveguide at a 10 µm distance from the grating, was used to measure the amount of optical power coupled to the waveguide. The CE of different grating configurations was calculated while simultaneously sweeping both the etch depth e, by 10 nm steps, and the linear apodization factor R, by 0.0025 µm^{-1} steps. For every grating configuration, the offset of the fibre mode from the starting point of the grating was optimized too. An example of the simulation results is shown, for the 260 nm SOI platform, in Fig.27, where a contour plot of peak coupling efficiency at the central wavelength of 1550 nm, as a function of parameters e and R, is built from simulation data.

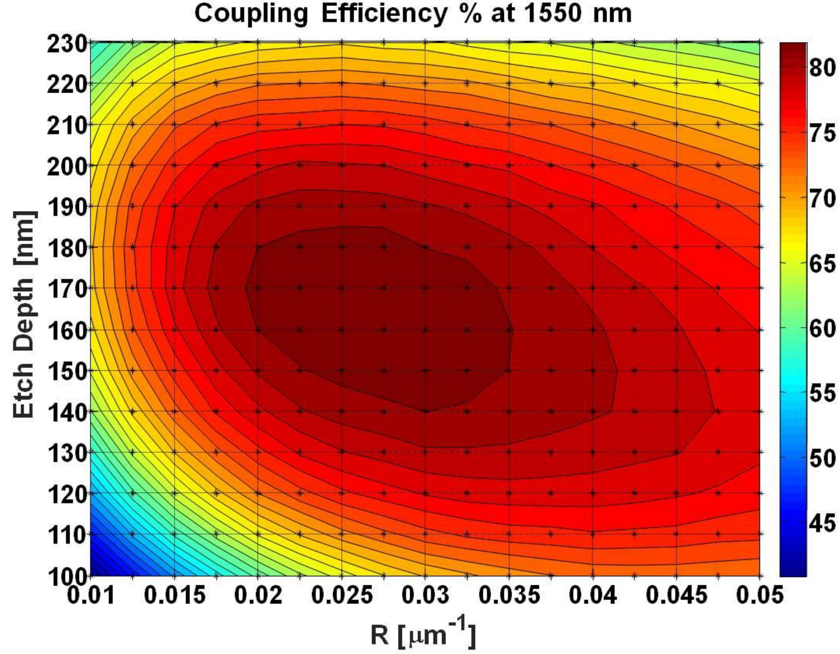

Figure 27: Contour plot of the peak CE at $\lambda = 1550$ nm of the linearly apodized GC realized in 260 nm SOI platform, as a function of etch depth e and of the linear apodization factor R.

From Fig.27 it can be seen that, starting from an etch depth of 100 nm, the maximum coupling efficiency is found to be 73% when the apodization factor R is equal to 0.0425 μm^{-1}; increasing the etch depth while reducing R yields a strong improvement of the CE, which reaches a maximum of 83% (-0.8 dB) for $e = 160$ nm and $R = 0.025$ μm^{-1}. If the etch depth is further increased, the CE starts to reduce, recording a value of 68% for $e = 230$ nm and $R = 0.025$ μm^{-1}. It is also interesting to note that the simulated CE is higher than 80% for a wide range of (e;R) combinations, thus showing a good tolerance of the prosed grating device to small variations in the fabrication process. The same procedure used for the design of the apodized GC based on the 260 nm SOI platform, was also applied to the 220 nm SOI platform, achieving a maximum CE of 70% (-1.6 dB) for $e = 110$ nm and $R = 0.0275$ μm^{-1}. The maximum CE achieved at the central wavelength of 1550 nm, as a function of the etch depth, for each of the two analyzed SOI platforms, is reported in Fig.28. It can be seen that by using a SOI platform with a thicker Si layer it is possible to obtain a higher CE, as already reported in other works [86], and that deep etching levels (110 nm and 160 nm for the 220 nm and 260 nm SOI platforms, respectively) are required to obtain the maximum CE.

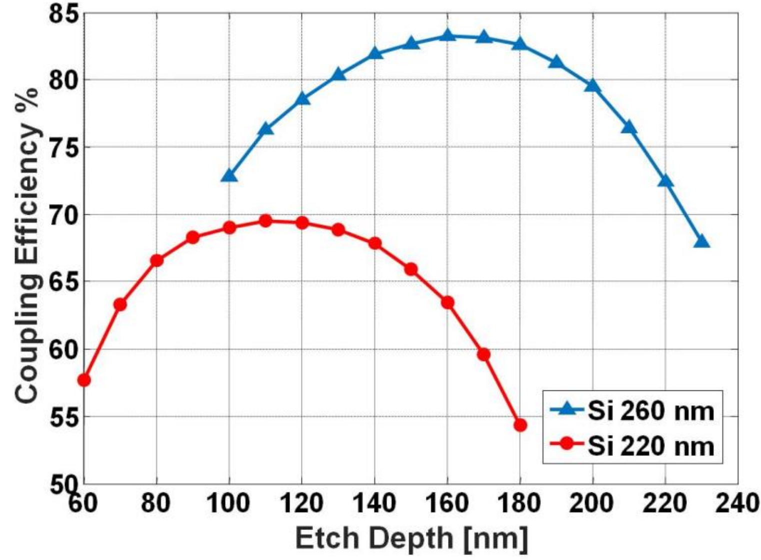

Figure 28: Maximum CE at the central wavelength of 1550 nm for the linearly apodized GC based on 220 nm SOI (red plot) and 260 nm (blue plot).

To complete the analysis, we then simulated the grating as an out-coupling device. To do that, we set a fundamental-mode (TE polarized) waveguide source in the SOI waveguide, a frequency-domain power-monitor immediately above the TOX to assess the grating directionality and a second frequency-domain power-monitor inside the Si-layer to assess the grating reflectivity by measuring the amount of optical power reflected back into the waveguide, as shown in Fig.29.

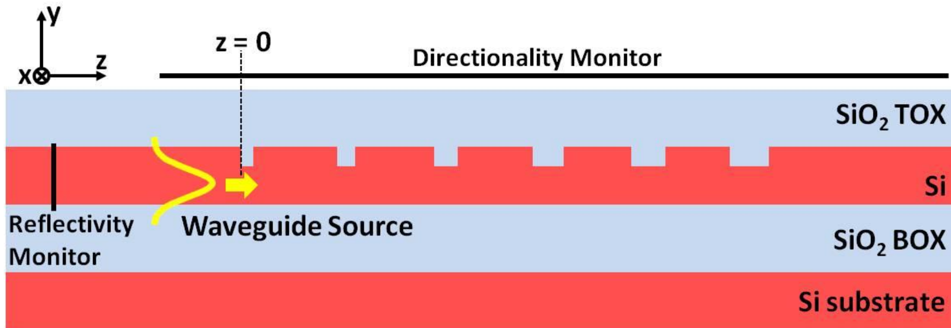

Figure 29: Cross-sectional schematic and simulation layout used to assess the directionality and reflectivity of uniforms and apodized GC.

The analysis was carried out for the 260 nm Si-thick SOI platform, comparing the performances at $\lambda = 1550$ nm of our apodized design to that of uniform gratings having a constant $FF = 0.5$, realized in the same platform and having the same TOX height. Directionality results are shown, as a function of etch depth e, in Fig.30, while the results of reflectivity simulations are reported in Fig.31.

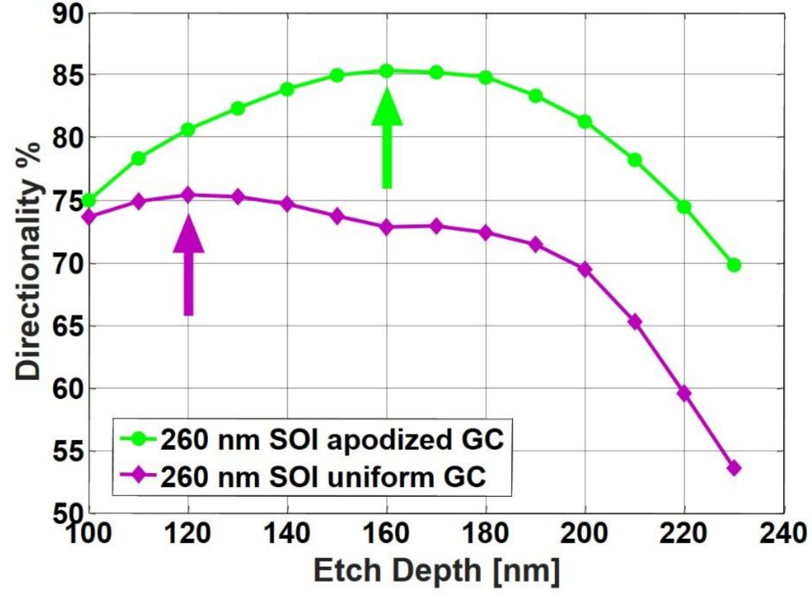

Figure 30: GC directionality at $\lambda = 1550$ nm as a function of e for the proposed linearly-apodized GC (green curve) and for a uniform GC (purple curve) with constant $FF = 0.5$. The arrows indicate the maximum directionality achievable in each structure.

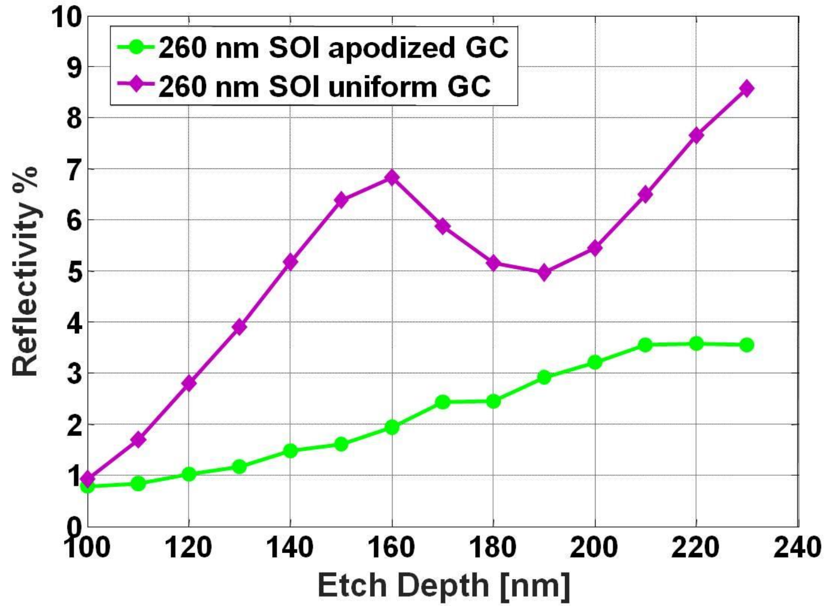

Figure 31: GC reflectivity at $\lambda = 1550$ nm as a function of e for the proposed linearly-apodized GC (green curve) and for a uniform GC (purple curve) with constant $FF = 0.5$.

From Fig.30 it can be noticed that the maximum directionality achievable by the proposed apodized GC is equal to 85%, almost 10% better than the maximum directionality achievable when employing a uniform design. Since TOX and BOX values were kept constant in the apodized and uniform configurations, this shows that the proposed apodization profile allows to significantly improve GC directionality.

It is also worth noting that the optimum values of etching depths (which are indicated with arrows in Fig.30) are different when considering a uniform GC rather than the apodized one. This demonstrates that, in order to properly optimize the GC performances, the apodization profile and the etching depth must be simultaneously optimized. This aspect, as previously mentioned, was not taken into consideration in previous works, such as in [83, 84, 85], where the optimum etch depth e for the apodized grating is chosen to be the same value which maximizes the directionality of the uniform design, thus leading to a reduced directionality and CE. With reference to Fig.30 for example, it can be clearly observed that choosing an e value of 120 nm (the value which maximizes the directionality of the uniform design) for our apodized grating, would have left to a directionality value of less than 81%.

Regarding the reflectivity simulation results, reported in Fig.31, it can be seen that the proposed apodization strategy allows to achieve a significant reduction of the GC reflectivity with respect to the uniform case. Furthermore, it also suggests that the big difference in the identification of the optimal etch-depth between uniform and apodized GC could be related to large reflectivity increase observed in the uniform GC around 160 nm.

It is also interesting to notice that the difference between the calculated values of directionality and CE is only about 2% for the proposed apodized GC at 160 nm deep etch. This means that the chosen apodization profile is very efficient in matching the radiated mode field profile with the Gaussian profile of a SMF, as it can be seen in Fig.32, where the normalized power density profile radiated from the proposed grating is reported.

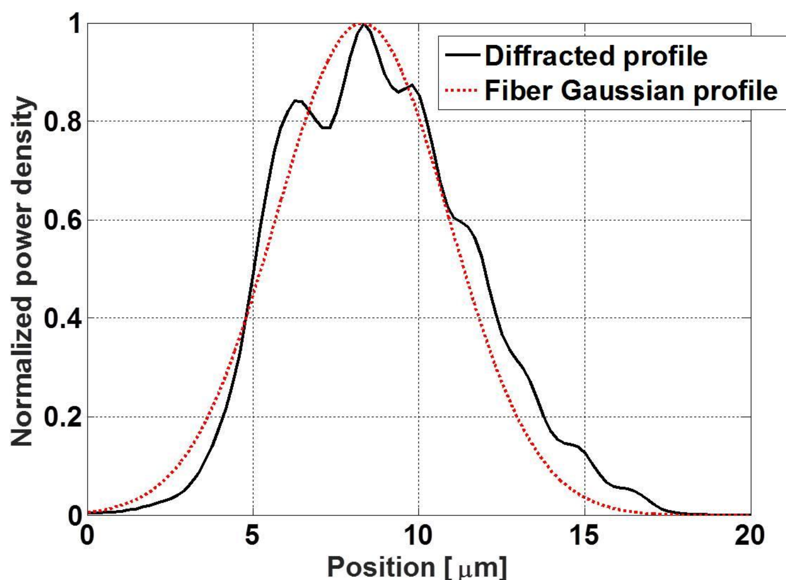

Figure 32: Normalized power density profile, radiated from the optimized apodized grating at 160 nm deep etch, as a function of the position along the length of the grating.

In Tab.1 a comparison between our results and the previous works reported in literature is given. It can be seen that our design strategy allowed to achieve for the first time a CE better than -1 dB, employing a SOI wafer with Si thickness < 340 nm (thus allowing for the implementation of single-mode waveguides) and without the use of any back-reflectors.

Si [nm]	**Description**	**CE_T [dB]**	**CE_E [dB]**	**Ref.**
220	Genetic algorithm	-2.15	-	[40]
220	Poly-Si overlay	-1.08	-	[78]
220	Poly-Si overlay	-	-1.6	[79]
220	Ge overlay	-1.2		[80]
220	Linear apodization	-2.6	-2.7	[84]
220	Genetic algorithm	-1.9		[86]
220	*Back-reflector (Au)*	*-1.43*	*-1.61*	[77]
220	*Back-reflector (DBR)*	*-0.36*		[40]
220	*Back-reflector (DBR)*	*-0.86*	*-1.58*	[74]
220	**Linear apodization**	**-1.6**	**-**	*
250	Fully-etched PhC	-1.8	-1.74	[89]
250	Lag effect in etching	-1.31	-1.9	[82]
N.D.	two etching depths	-1.2		[81]
250	Linear apodization	-2.3	-2.7	[85]
250	*Back-reflector (Al)*	*-0.26*	*-0.62*	[75]
250	*Back-reflector (Al)*	*-0.43*	*-0.58*	[76]
260	Genetic algorithm	-1.0	-	[86]
260	**Linear apodization**	**-0.8**	**-0.9**	*
340	200-nm deep etching	-0.8	-1.2	[83]
340	Genetic algorithm	-0.5	-	[86]

Table 1: Summary of the theoretical (CE_T) and experimental (CE_E) coupling efficiencies for different GC reported in the literature. Results are ordered with respect to the thickness of the Silicon layer. Devices that required the use of a back reflector are reported in *italic*, while those relative to the proposed design technique are shown in **bold**. All the results are reported with the number of significant figures given by the authors. For the grating structure reported in [81] the thickness of the employed Si layer is not explicitly reported.

A direct comparison with [84] and [85], in which constant-Λ linear-apodization gratings were employed, shows that our design approach achieves a CE improvement of at least 1 dB. Furthermore, our results also show a non-negligible CE improvement with respect to results reported in [86], where a constant-Λ linear-apodization design was used as the starting configuration for a GA based refinement, thus highlighting the importance of allowing Λ to vary. We also applied our design strategy to a SOI wafer with 340 nm-thickness Si-layer, in order to compare our apodization technique to that reported in [83], obtaining a CE of 85% (-0.7 dB), for $e = 210$ nm and $R = 0.0425$. The obtained CE is slightly higher than that reported in [83] (CE = 83%; -0.8

dB), where the fill-factor (FF) apodization, as already discussed in paragraph 2.2.3, is implemented in such a way to fit the theoretical scattering coefficient α distribution required to produce a Gaussian-shaped beam profile. The improvement achieved using the proposed design strategy can be explained considering two aspects:

i) only minor differences are present between the FF apodization curve reported in [83] and a linear apodization

ii) identifying the optimal etch depth and the single-element scattering coefficient in uniform GC does not guarantee obtaining the optimal CE, as previously shown (see Fig.30).

2.3.2 Device fabrication

Based on the previous analysis we decided to fabricate the apodized GC design yielding the highest CE in a 260 nm Si-thick SOI platform (e = 160 nm, FF_0= 0.9, R = 0.025 µm^{-1}). The grating width (along the x direction of Fig.24) was set to 12 µm, in order to properly accommodate the fibre Gaussian mode, while the length of the device was 14.847 µm, comprehending 24 scattering units. The length of each grating tooth L_O and trench L_E is reported in Tab.2.

Period	L_E[nm]	L_O[nm]	Period	L_E[nm]	L_O[nm]	Period	L_E[nm]	L_O[nm]
1	60	540	9	138	484	17	225	422
2	69	533	10	148	477	18	237	413
3	79	526	11	159	469	19	249	405
4	88	520	12	170	461	20	261	396
5	98	513	13	180	454	21	273	387
6	108	506	14	191	446	22	286	378
7	118	498	15	203	438	23	298	369
8	128	491	16	214	430	24	311	//

Table 2: Optimal trench and tooth width obtained from the optimization of the apodized GC in 260 nm SOI platform, having FF_0= 0.9 and R = 0.025 µm^{-1}.

To assess the grating CE, we designed a test structure composed of two apodized GCs, connected by a 5.2 mm long single mode rib waveguide. The rib width was set to 500 nm, while its height was set to be the same as the grating etching depth e, so that a single etch process could be used to define the test structure. The waveguides were connected to the gratings by 500 µm long linear tapers, in order to adiabatically expand the dimension of the guided optical mode. In order to separate the loss contribution due to beam coupling from that originated by waveguide propagation loss, an additional set of 5 waveguides was designed, with increasing length at 5 mm step. Electron Beam Lithography (E-beam) was used to define the sample pattern and Inductively-coupled plasma (ICP) Reactive-ion etching (RIE) was employed to define the final structures. As s final step, a protective TOX layer was deposited over the patterned SOI wafer, by means of plasma enhanced chemical vapor deposition

(PECVD). Four different chips were fabricated, each of them containing two test structures, and the set of waveguides for propagation loss assessment. A schematic representation of the test structure used for the apodized grating CE is given in Fig.33(top), while in Fig.33(bottom) a cross-sectional representation of the employed single mode rib waveguide is shown. An optical micrograph of the fabricated apodized GC is shown in Fig.34.

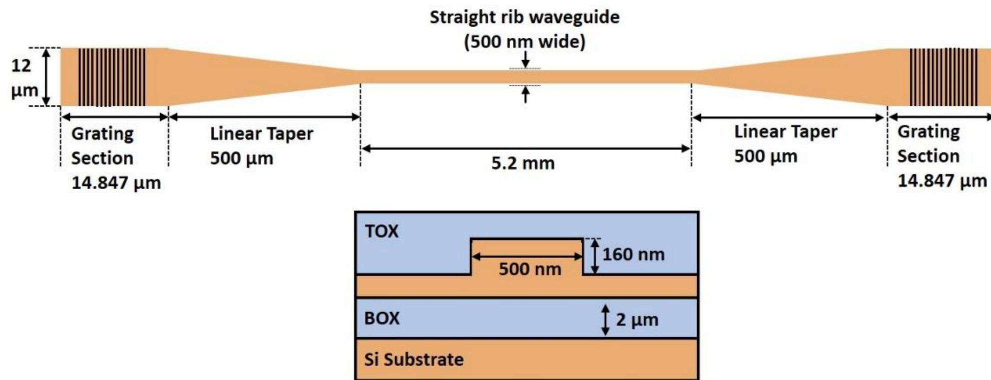

Figure 33: (top) Schematic representation of the test structure designed for the apodized grating CE measurement. (bottom) Cross-section of the single mode rib waveguide connecting the pair of GCs.

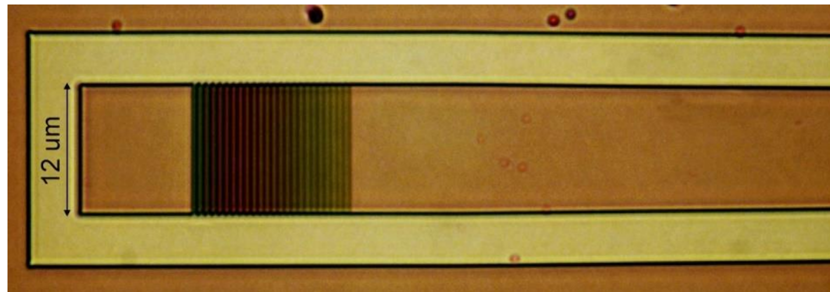

Figure 34: Optical micrograph of one of the fabricated apodized GC.

2.3.3 Apodized GC experimental characterization

The experimental characterization was carried out by means of a vertical coupling scheme, using polarization maintaining (PM) single mode fibres mounted on triaxial piezo-actuated stages. The fibres were tilted by 14.5° with respect to the vertical direction (as it was supposed in the design stage) and carefully oriented so that TE light polarization could be injected into the gratings. The employed optical source was a PM external cavity laser (ECL), tunable from 1523 to 1600 nm at 5 pm steps, while the output optical power collected from the test structures was measured by means of a power meter. The grating CE was obtained by subtracting the waveguide propaga-

tion loss from the measured fibre-to-fibre transmission and dividing by two (thus assuming that the input and output coupling losses could be considered equal, thanks to the reciprocity theorem). The measured CE as a function of wavelength is shown, together with the 2D-FDTD simulation result, in Fig.35 and Fig.36, for the two best performing chips, while a summary of the measured coupling efficiencies for all of the analyzed devices is given in Tab.3.

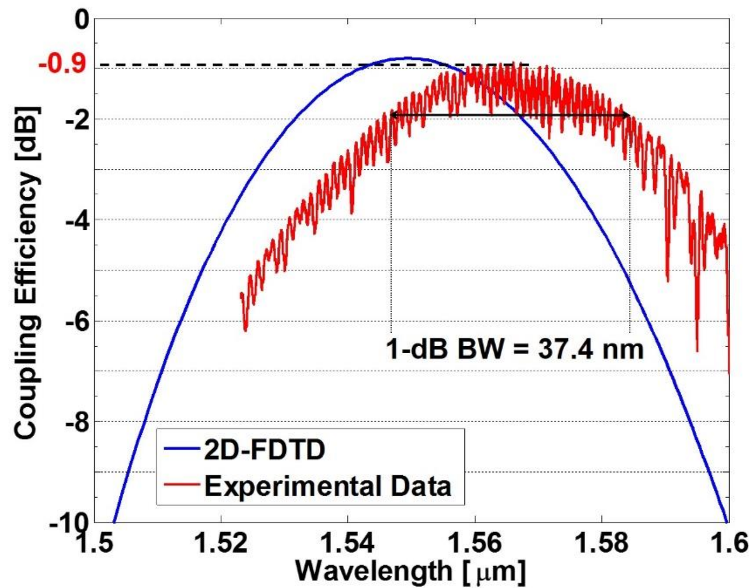

Figure 35: Experimental CE of the grating belonging to chip 2 (red trace) together with the FDTD simulated CE; the maximum CE is -0.9 dB and the 1-dB BW is 37.4 nm.

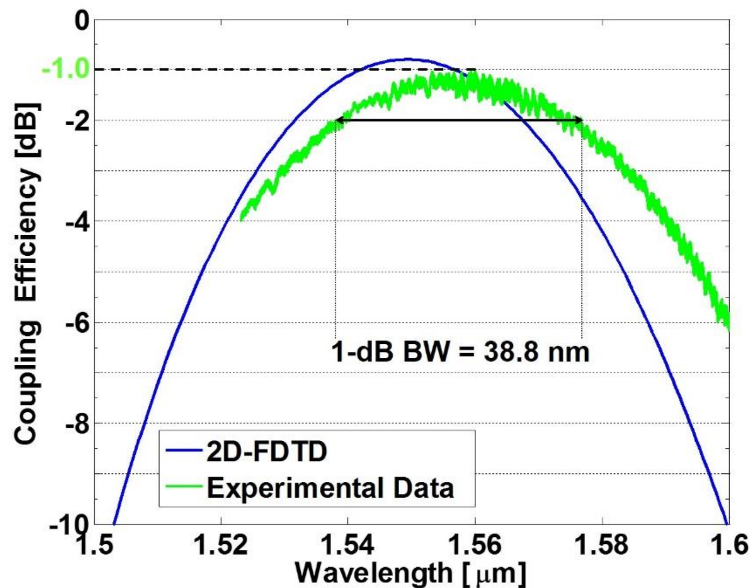

Figure 36: Experimental CE of the grating belonging to chip 1 (green trace) together with the FDTD simulated CE; the maximum CE is -1.0 dB and the 1-dB BW is 38.8 nm.

	Chip 1		Chip 2		Chip 3		Chip 4	
Struct.	**CE**[dB]	**BW**[nm]	**CE**[dB]	**BW**[nm]	**CE**[dB]	**BW**[nm]	**CE**[dB]	**BW**[nm]
1	1.0	38.4	1.0	39.8	1.4	37.8	1.2	39.4
2	1.0	38.8	0.9	37.4	1.4	39.8	1.3	39.3
Prop. Loss	3.1 [dB/cm]		3.3 [dB/cm]		3.0 [dB/cm]		4.5 [dB/cm]	

Table 3: Summary of the fabricated gratings coupling efficiency and 1-dB bandwidth, and waveguide propagation loss, for all of the measured chips.

As it can be seen from Tab.3, we measured an average CE of -1.1 dB, and a maximum CE of -0.9 dB; these results are in very good agreement with the simulated CE values (-0.8 dB, i.e. 83%), thus indicating a good consistency in the fabrication process. The discrepancy between the simulated -1 dB bandwidth of 32.8 nm and the experimental derived one, with an average value of 38.8 nm and a maximum value of 39.8, can be explained by small fabrication imperfections and variations over the wafer, such as variation in the actual etch depth or in the uniformity of the deposited TOX layer. The peak wavelength variation of the measured spectra (the central wavelength is 1566 nm in Fig.35 and 1560 nm in Fig.36) with respect to the nominal central wavelength of 1550 nm, can be explained again by fabrication imperfections, as well as inevitable experimental errors in setting the fibres angle-of-incidence (AOI). It is anyway important to underline that the grating transmission spectrum can be easily tuned to the nominal central wavelength by simply modifying the fibres AOI, without any additional losses, as it is shown in Fig.37(left), where the transmission spectrum of the apodized grating coupler belonging to chip 1, is plotted as a function of wavelength, for different fibres AOI values, ranging from 11° to 16°.

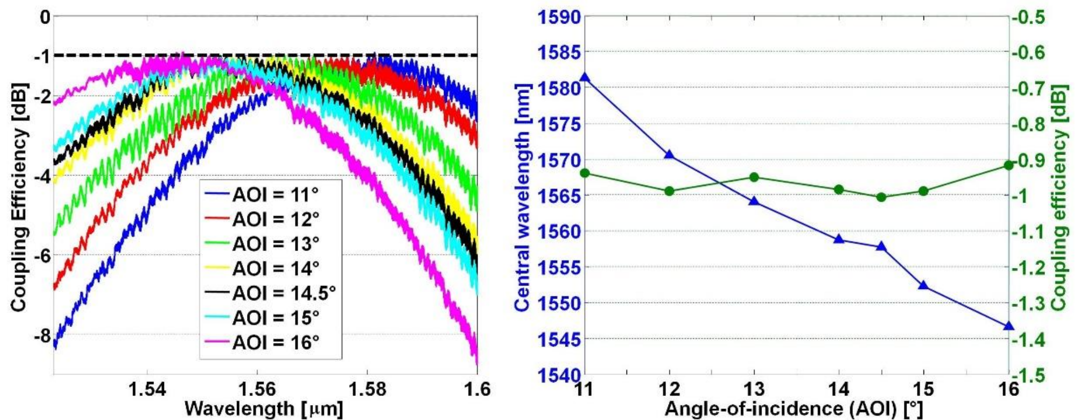

Figure 37: (left) Transmission spectra of the apodized grating as a function of wavelength, for different fibre AOI. (right) Central wavelength of the apodized grating transmission spectra and maximum coupling efficiency as a function of the fibre AOI.

From Fig.37(right), where the spectra central wavelengths and the maximum CEs are reported as a function of the AOI, it can be seen that an increase of the AOI leads to a blue-shift of the grating transmission spectrum, which shifts from 1581 nm to 1546

nm with a rate of about 6.6 nm/°, but no significant trend is observed in the measured maximum coupling efficiency, which is always comprised between -0.9 dB and -1.0 dB.

Taking a deeper look at the experimental grating transmission spectra, the presence of a parasitic amplitude ripple can be observed, with an amplitude of about 0.4 dB in Fig.35 and about 0.8 dB in Fig.36, at the central coupling wavelength. We believe that this ripple, rather than being originated by the residual grating reflectivity, which should be equal to about 2% (see Fig.31), might instead be caused by spurious reflections taking place at the linear taper connecting the grating to the single mode waveguide. The period of the ripple is in fact very close to 1 nm, and, assuming a reasonable average refractive index of the taper of about 2.8, this would correspond to a cavity length of about 450 µm, which is compatible with the actual taper length. The value of the ripple period also allows to exclude the possibility of a parasitic cavity originated by the residual grating reflectivity, taking place between the two gratings, as the single mode waveguide is 5.2 mm long, or between the grating and the fibre, which would imply a cavity length < 20 µm. In order to make sure that the interaction between the non-optimized taper and the grating would not lead to an unexpected spectral redistribution of the transmission efficiency, thus constructively boosting the apparent transmission at certain wavelengths, and destructively suppressing the apparent transmission at intermediate wavelengths, we decided to perform a new set of 2D-FDTD simulations, including the effect of the taper reflections. This could basically allow us to understand if the "true" grating CE would correspond to the maximum or average values of the experimentally observed ripple. To do that, we simulated the optimum grating structure, according to the simulation layout reported in Fig.38, inserting a 100 nm wide trench in the Si waveguide, at a distance of 500 µm from the end of the grating section. The transmitted optical power was then collected by a frequency-domain power monitor, positioned along the Si waveguide at a 10 µm distance from the trench.

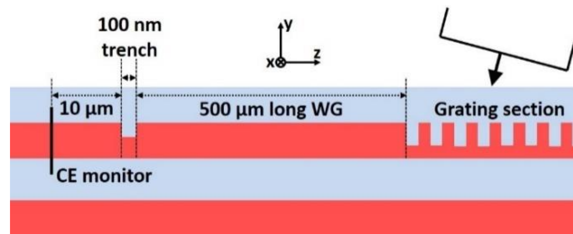

Figure 38: Cross-sectional schematic and simulation layout used to evaluate the impact of a back-reflecting element (the 100-nm wide trench) on the measured CE.

The 100 nm wide waveguide trench can be considered as a modelized representation of the distributed reflections taking place in the linear taper, and different amount of back-reflections can be simulated by simply varying the trench etching depth. The simulations results are shown in Fig.39, where the blue curve represents the unperturbed situation (corresponding to a 0% etching depth of the trench) while the yellow and purple curves correspond respectively to 40% and 60% etching depth of the trench.

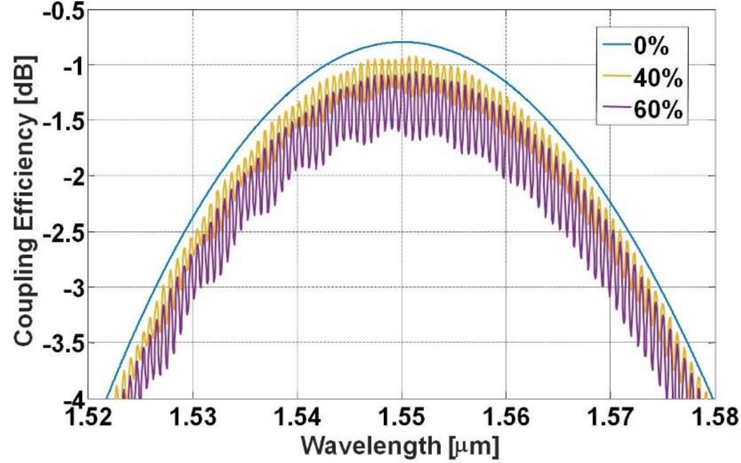

Figure 39: 2D-FDTD simulation of the optimum grating transmission, when a 100 nm wide trench is inserted in the Si waveguide at a distance of 500 µm from the end of the grating section, at different etching percentage. The blue curve represents the unperturbed case, while the yellow and purple curves correspond to hole etching percentages of respectively 40% and 60%.

As expected, an increase of the trench etching percentage leads to an increase of the reflection coefficient, thus increasing the amplitude of the ripple and reducing the average CE. It is anyway interesting to notice that the peaks of the ripple never exceed the threshold set by the CE of the unperturbed grating, meaning that maximum experimentally derived CEs of the analyzed sample can be conveniently taken in correspondence of one of the maxima of the parasitic oscillation.

Finally, it can be useful to compare our experimental results to that of other grating couplers, as reported in Tab.1. It can be seen that the coupling efficiency we measured is better than [84] and [85] (2.7 dB), where a similar linear apodization of the grating *FF* is applied, using respectively 220 nm and 250 nm Si-thick SOI wafers, and it is also better than [83] (1.2 dB), where a 340 nm Si-thick SOI wafer is adopted. Our result is also quite close the record value of -0.62 dB reported in [75], which is achieved using a 250 nm Si-thick SOI wafer in addition to an Al back-reflector. This proves that a very high coupling efficiency, below the -1 dB threshold, can be obtained even without the use of any back-reflector, thus making the fabrication process much simpler.

2.4 Polarization insensitive grating coupler

As it has been previously described in Paragraph 2.2, one of the main limitations of the 1D grating coupler approach, is that CE can only be optimized for a single state of polarization of the transmitted light, whereas CE for the orthogonal polarization can be more than one order of magnitude smaller (see for example Fig.18). Also the linearly apodized GC described in the previous paragraph shows very high CE only for TE light polarization. Different solutions have been in proposed in the scientific

literature in order to try to implement a polarization insensitive 1D-GC. In [90] for example, two non-uniform GC structures are proposed: the first one is obtained by the geometrical intersection of two uniform GC structures, respectively optimized for TE and TM light polarization, while the second one is obtained by the geometrical union of the same TE and TM uniform designs. A schematic of the design strategy reported in [90] is shown in Fig.40.

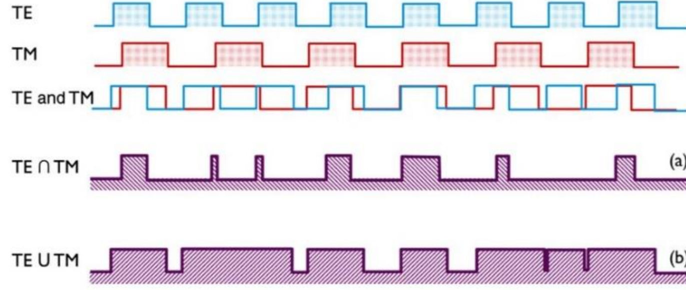

Figure 40: Schematic of the designed strategy proposed in [90] for obtaining a polarization insensitive 1D-GC. Grating (a) is obtained by the geometrical intersection of two different uniform GCs, having a grating period optimized for TE and TM light polarization respectively. Grating (b) is obtained by the union of the same two uniform GCs.

The design technique proposed in [90] was implemented in a standard SOI platform (220 nm Si thickness, 2 µm BOX thickness) and allowed to demonstrate a theoretical CE of -6.9 dB for the intersection grating, when performing a shallow 60 nm deep etch, and a CE of -5.4 dB for the union grating, when performing a 100 nm deep etch. The theoretical polarization-dependent loss (PDL), which is defined as the difference between the TE mode CE and the TM mode CE, was theoretically assessed to be 0.57 dB for the intersection grating and 0.5 dB for the union grating. A proof-of-concept sample of the intersection grating was also fabricated, demonstrating an experimental CE of -7.8 dB for the TE mode, and a CE of -8.0 dB for the TM mode at the central wavelength of 1550 nm.

Better performances in terms of average CE were reported in [91], were a uniform 1D-GC is used to couple TE and TM light polarizations in opposite directions into two SOI waveguides, as shown in Fig.41.

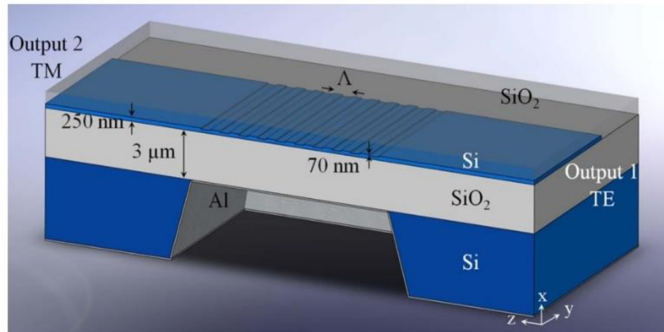

Figure 41: 3D cross-section of the grating coupler proposed in [91].

The grating coupler proposed in [91] is based on the same SOI platform used in [75], with a 250 nm Si layer thickness, a 3 µm BOX thickness, and the addition of an Al back-reflector, deposited underneath the BOX layer by etching the Si substrate. The proposed GC theoretically allows to achieve a TE mode CE of -0.7 dB and a TM mode CE of -1.1 dB; however, the maximum CE values are reported, for the two orthogonal polarizations, at the different positions of the optical fibre with respect to the grating. When the position of the fibre is fixed, as it practically happens when packaging a PIC, the theoretical CE drops to -3.1 dB (-3.8 dB from experimental measurements) for both polarizations.

Another possibility to implement a polarization insensitive 1D-GC, is to employ a SOI platform with a very thick Si layer which allows the propagation of both TE and TM first order modes. In [92] for example, a 400 nm thick Si layer is used and, thanks to a proper choice of the grating period Λ, a uniform GC is demonstrated which is able to simultaneously couple to the second diffraction order (m = 2) of TE_0 mode, and the first diffraction order (m = 1) of TM_1 mode, with a CE better than -3 dB for both states of polarization. However, it is important to underline that the adoption of this type of technique requires all the other integrated optical components (such as waveguides, filters, modulators, etc.) to be optimized for multi-modal operation, which is definitely not trivial.

A completely different approach to achieve polarization insensitive coupling, is to implement a two-dimensional refractive index variation by etching the SOI waveguide with round-shaped or square-shaped holes, thus obtaining a two-dimensional grating-coupler (2D-GC), also known as photonic crystal. Two main different strategies can be used to implement a 2D-GC, as shown in Fig.42.

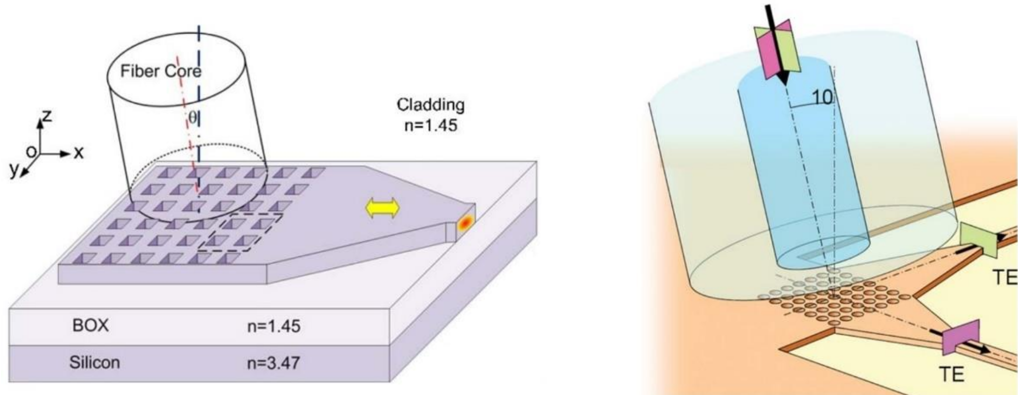

Figure 42: (left) 2D-GC based on the use of sub-wavelength structures. The two orthogonal polarization states of fibre light are respectively coupled to the TE and TM modes of a unique SOI waveguide [93]. (right) 2D-GC based on a polarization diversity approach. The two orthogonal polarization states of fibre light are respectively coupled to the TE mode of two separate SOI waveguides [94].

In Fig.42(left) the technique proposed in [93] is shown. In this case the refractive index variation along the transverse direction (the y direction with reference to Fig.42(left)), is implemented in order to engineer the grating effective refractive index n_{eff} experienced by light propagating in the x direction. In fact, by properly choosing the period Λ_y and the FF_y along the y direction, a situation can be achieved where the resulting n_{eff} is exactly the same for both TE and TM polarizations, which can therefore be effectively coupled to the same output SOI waveguide. From an operation principle point of view, this type of grating can be considered very similar to a standard 1D-GC where the low-index grating section, rather than being implemented as a "trench", is instead implemented as a sub-wavelength structure [95]. The grating structure proposed in [93] allows to achieve a theoretical CE of about 40% for both TE and TM modes, which can be improved up to 64% if a bottom DBR reflector is included. The second approach shown in Fig.42(right), where a polarization-diversity 2D-GC is implemented, is instead based on a different principle of operation. The 2D-GC in this case is made of a uniform matrix of etched cylinders, which is basically obtained as the notional superimposition of two orthogonally oriented 1D-GCs. This allows the grating to couple the two orthogonal state of polarizations of light coming from a fibre, into the fundamental TE mode of a pair of silicon waveguides, where each state of polarization is coupled to a different waveguide. This 2-D grating structure, therefore, at the same time performs the function of a fibre–chip interface, a polarization splitter and polarization rotator [94]. Compared to the sub-wavelength structure technique proposed in [93], polarization-diversity approach requires to double all the optical components to be integrated on the PIC, but has the fundamental advantage that the optical components must be optimized only for TE mode operation. The first example of a polarization-diversity 2D-GC was demonstrated in [96], using a SOI platform with 220 nm Si thickness and 1 µm BOX thickness, and achieving a coupling efficiency of approximatively 20% at the central wavelength of 1550 nm. Other 2D-GC devices implemented in standard SOI platforms (Si thickness = 200 nm, BOX thickness = 2 µm) were reported in [97] with a CE of 21%, in [98] with a CE of 27% and in [99] with a CE of 39% (at the central wavelength 1520 nm). Polarization diversity 2D-GCs can also be implemented by adopting more complex lattice schematic for the photonic crystal, such as in [100] (see Fig.43), where each element of the lattice is composed by 5 etched cylinders.

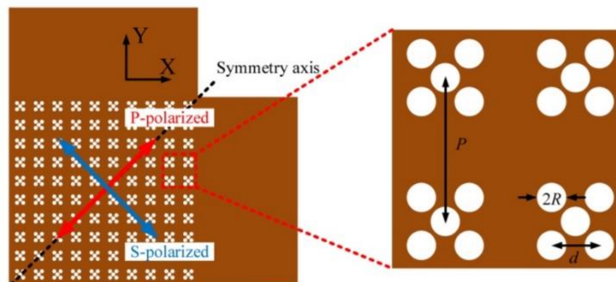

Figure 43: Top-view of the 2D-GC structure proposed in [100].

2.4.1 Design of a highly-efficient polarization-diversity 2D-GC

The reason for the low performances of the polarization-diversity 2D-GCs proposed in the scientific literature, is that their design has been mostly carried out by extending and generalizing the results of 2D-FDTD simulations. Although these types of simulations can conveniently describe the behavior of simple 1D-GCs, they are not suitable for an accurate description of 3D finite systems such as photonic crystals, thus making it impossible to assess what the ultimate theoretical CE of a 2D-GC may actually be. The effect of the etch depth variation on the 2D-GC coupling efficiency, for example, has never been deeply investigated, and therefore most of the previous works [97, 98, 99] makes use of a shallow 70 nm deep etch (which is the optimum value for uniform 1D-GC in 220 nm SOI), assuming that this might be also the optimum value for the 2D-GC scenario.

To overcome this limitation, a complete set of fully-vectorial 3D-FDTD simulations was performed, in order to optimize all the geometrical parameters of a uniform 2D-GC and achieve the maximum possible CE. A complete and detailed description of the simulation methodology can be found in [101], while a description of the optimized grating structure and of the experimental results can be found in [67]. This work was carried out as a part of the FABULOUS Project (see Paragraph 1.5), with the objective of developing a highly-efficient and polarization insensitive grating coupler for the Silicon-based ONU. The project target was to obtain a CE better than -4dB at 1550nm and a 1 dB bandwidth of at least 30nm, while remaining compatible with the materials and fabrication process-flow of the FABULOUS project. A schematic of the proposed 2D-GC structure is shown in Fig.44.

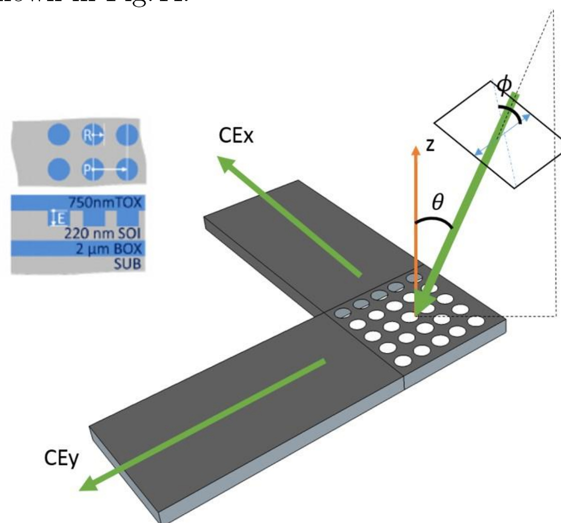

Figure 44: Schematic representation of the analyzed uniform 2D-GC structure. The inset shows the three variables (E = etch-depth, R = hole-radius, and P = grating-pitch) used to optimize the coupler response at 1550nm. The material cross-section, consisting of a top-oxide layer (TOX), a patterned silicon-on-oxide layer (SOI), the buried-oxide layer (BOX), and the silicon substrate (SUB), is also shown [67].

The 2D-GC was implemented in a 220 nm Si-thick SOI platform, with a 2 µm thick BOX layer, assuming a 750 nm cladding TOX deposited over the grating. The device was simulated in in-coupling configuration, thus placing an optical fibre source tilted by $\theta = 15°$ with respect to the normal-incident axis (z axis in Fig.44), lying in the plane that bisects the two output waveguide (i.e. the plane that is normal incident to the grating plane and at 45° with respect to both x and y axis). The optical mode was implemented as a Gaussian source, centered at $\lambda = 1550$ nm, and with a MFD of 10.4 µm. The amount of optical power coupled to the fundamental TE mode of the two grating waveguide is respectively defined by CE_x and CE_y so that the global coupling efficiency CE_T can be defined as:

$$CE_T = CE_x + CE_y \tag{28}$$

Simulations were carried out considering a 15 µm x 15 µm x 5 µm simulation volume which fully surrounds the grating region, and an integrated conformal mesh algorithm was adopted, so as to increase the simulation mesh spatial resolutions in the regions were strong refractive index variations occurs. The three investigated GC geometrical parameters, as shown in the inset of Fig.44, were: the etching depth E, the hole radius R, and the grating pith P, defined as the distance between the centers of two consecutive holes. Some simulations results can be seen in Fig.45 and in Fig.46, where the polarization angle ϕ of the incoming light is assumed to be equal to 45°, so that the CE_x contribution can be considered to be negligible in Eq.(28) [101].

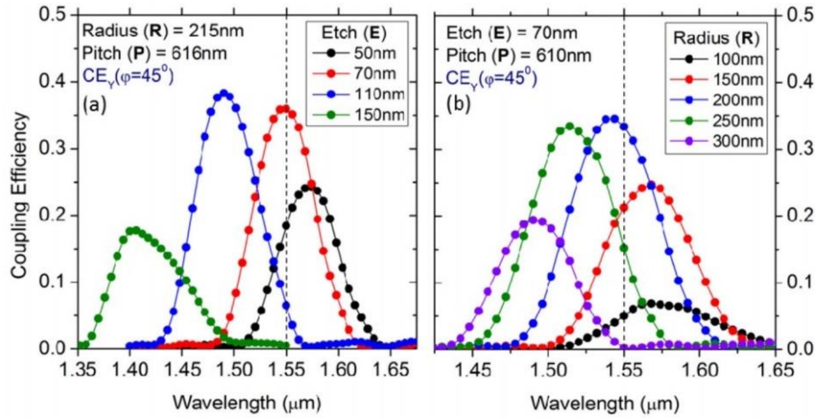

Figure 45: (left) Transmission spectra of different 2D-GC configuration with fixed radius R and pitch P, for different values of the etch depth E [101]. (right) Transmission spectra of different 2D-GC configuration with fixed E and P, for different values of R [101].

In Fig.45(left) it can be seen that, when considering a 2D-GC with fixed R and P, an etch depth increase leads to a CE variation and to a blue-shift of the transmission spectrum. A similar situation is depicted in Fig.45(right), where P and E were kept fixed, while R was swept from 100 nm to 300 nm. In order to properly center the transmission spectrum at the desired central wavelength of 1550 nm, the grating radius

and pitch must be changed simultaneously, as it shown in Fig.46, where the transmission spectra and the maximum CEs are reported as a function of the R/P ratio, for a fixed etch depth of 70 nm.

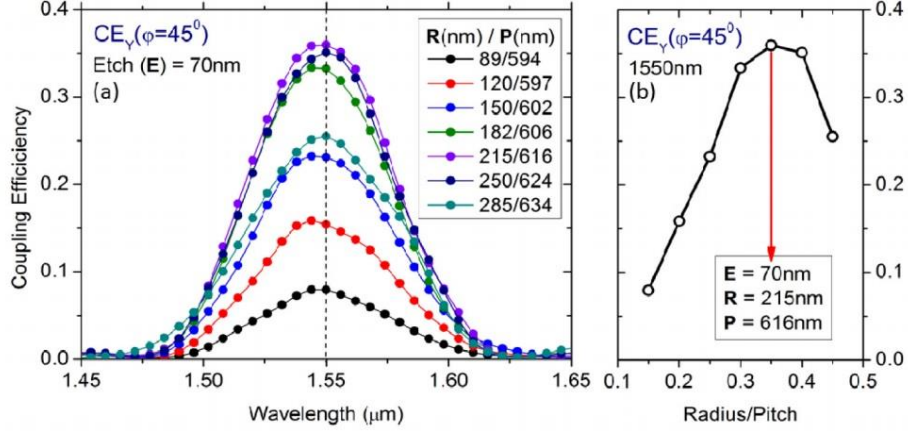

Figure 46: (left) Transmission spectra of different 2D-GC configuration, having fixed etch depth ($E = 70$ nm), and different R/P ratio [101]. (right) Maximum CE as a function of the R/P ratio for $E = 70$ nm [101].

From Fig.46 it can be seen that, when performing a 70 nm deep etch, the maximum achievable CE is equal to 37% (-4.3 dB), for $R = 215$ nm and $P = 616$ nm. This CE value is similar to the one reported in [99], where a 70 nm deep etch is also used. However, if the same procedure is repeated for different values of the etching depth E, a contour plot can be built, which shows CE at the central wavelength of 1550 nm for all the possible combinations of E, R, and P values, as reported in Fig.47.

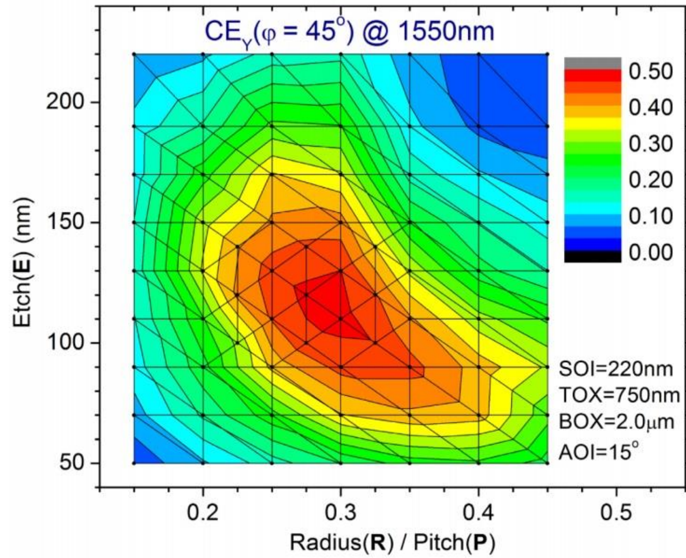

Figure 47: Contour plot of the maximum CE achievable in a uniform 2D-GC as a function of E and the R/P ratio [101].

From Fig.47, it can be seen that a maximum CE of 48% (-3.2 dB) can be achieved when E = 120 nm, P = 630 nm and R = 179 nm. This clearly shows that deeper etching levels, with respect to the 70 nm shallow etch employed in [97, 98, 99], are required in order to achieve maximum CE. The 1 dB bandwidth for the optimum 2D-GC structure is about 37 nm. In Fig.48 and in Fig.49 the effect of deviations from the nominal values of hole radius R and etch depth E on the resulting CE and central wavelength is shown.

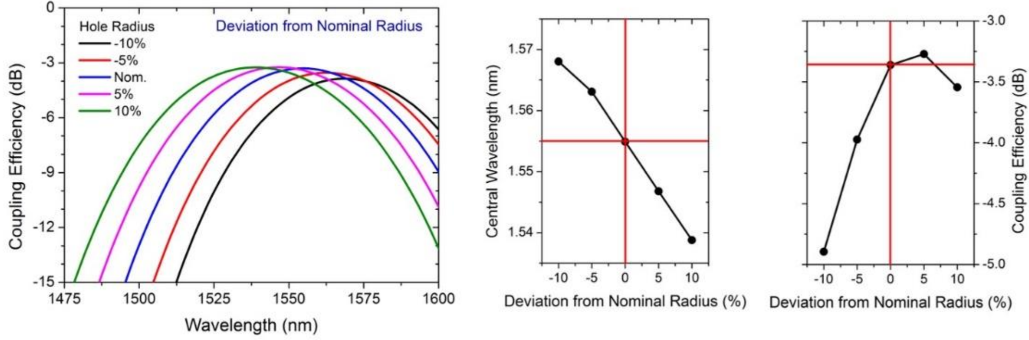

Figure 48: Effect of hole radius R variations on the 2D-GC coupling efficiency and central wavelength.

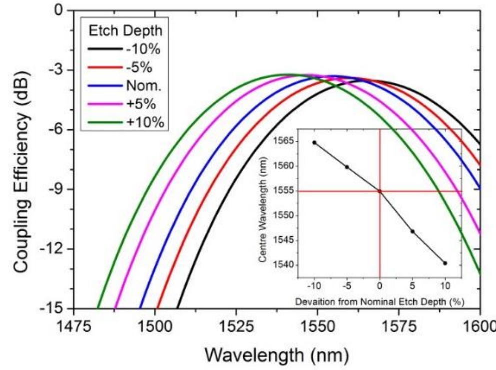

Figure 49: Effect of the etch depth E variations on the 2D-GC coupling efficiency and central wavelength.

From Fig.48, it can be seen that a variation of + 10nm/-10nm in the etch depth results in a CE variation of + 1%/-2% and a wavelength shift of -12nm/+10nm. In Fig.49 instead, it is shown that a variation of + 10nm/-10nm in the hole radius results in a CE change of $-3\%/+1\%$, and a wavelength shift of + 10nm/-10nm.

Finally, for what regards the dependency of the 2D-GC performances on the state of polarization of the input light, simulation results show that when ϕ is rotated by 90°, CE_y drops from 47% to 0.6% thus resulting in a polarization extinction ratio (PER) of -19 dB. The overall coupling efficiency CE_T however, only varies between 45% (-3.5 dB) and 51% (-2.9 dB) when the input polarization angle ϕ experience a full

360° sweep, meaning that maximum theoretical PDL of the optimum 2D-GC is equal to -0.6 dB.

The final parameters of the optimized 2D-GC structure are summarized in Tab.4.

Si-thickness (*S*)	220 nm
BOX thickness	2 µm
Etch depth (*E*)	120 nm
Pitch (*P*)	630 nm
Radius (*R*)	179 nm
CE_T	-3.2 dB (47%)
PDL	-0.6 dB
Footprint	12 µm x 12 µm (20 x 20 holes)

Table 4: Summary of the design parameters of the optimized 2D-GC structure.

An additional set of 3D-FDTD simulations were performed in order to assess the modal-profile and Poynting-vector of light coupled from the 2D-GC into the Si slab. An example of these simulation results is shown in Fig.50. It can be seen that light propagates with an offset of 3.7° from the axis of the grating coupler, due to the non-zero angle of incidence between the input fibre-mode and the surface-normal of the coupler. The optimum angle between the two arms of the grating-coupler should therefore be equal to 82.6° (90° – 2 × 3.7°). Simulation results also show that, after ≈50 µm of propagation in the Si slab, the coupled mode recovers a single-mode-like profile, as it can be seen in the inset of Fig.50.

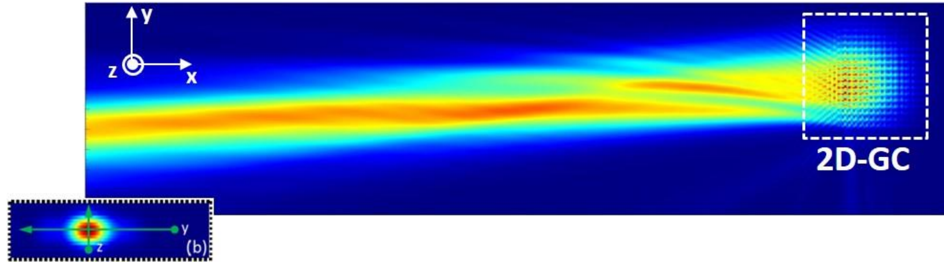

Figure 50: Non-orthogonal projection of coupled light into the SOI slab, with a 3.2° offset of the propagating mode, with respect to the axes of the coupler. The inset is a contour plot of the coupled mode at a distance of 68 µm from the edge of the 2D-GC.

2.4.2 Device fabrication

The device was fabricated by CEA-Leti foundry starting from a commercial SOI wafer composed of a 2 µm thick Buried Oxide Layer (BOX) covered by a 220 nm thick crystalline Silicon layer. The Si layer was patterned by means of a backend compatible 193 nm Deep UV lithography machine, which defined both the waveguide and grating

patterns. A first etching step was then performed to define the grating coupler final device, employing an etching depth of 120 nm. After a deposition of a silica hard mask a second etching steps was done down to the BOX (etch depth 220 nm) to define the Si-nanowire vertical pattern. A 750 nm Top Oxide layer (TOX) was finally deposited on the wafer acting as protective layer and giving more mechanical stability to the final sample [67].

On each fabricated sample chip, different test structures were included in order to assess the 2D-GC performances. Here is a short list and description:

1. The 1st test structure was composed by a pair of 2D-GCs connected by means of linear tapers to a standard 500 nm x 220 nm SOI strip waveguide. The taper overcomes the modal mismatch between the light coupled by the 2D-GC and the single-mode (SM) waveguide. The length of the taper was chosen to be 170 µm, in order to adiabatically adjust the mode dimensions (the simulated efficiency of the linear taper was calculated to be 91%), while the length of the SM waveguides was set to 1 mm. The angle between the axes of the tapers was set to be equal to 82.6°, thus taking into account the offset angle of propagation of light coupled from the 2D-GC. A schematic of test structures #1 is shown in Fig.51.

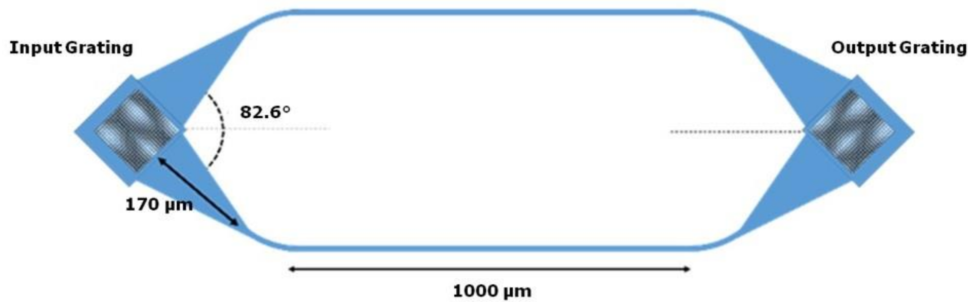

Figure 51: Schematic representation of test structures #1.

2. The 2nd test structure consisted of a 2D-GC connected to a pair of 1D-GC using tapers and SM waveguides. This structure is used to measure the PER of the 2D grating coupler. A schematic of test structures #2 is shown in Fig.52.

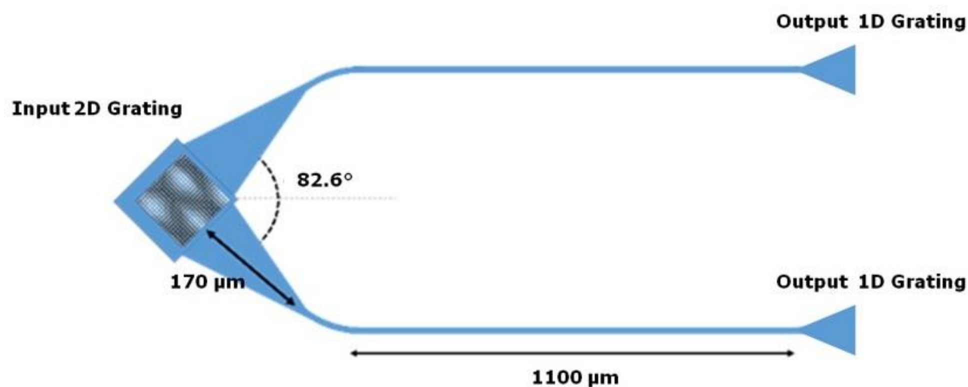

Figure 52: Schematic representation of test structures #2.

As the performances of the 1D-GCs were not an important parameter in this context, a focusing uniform grating configuration was employed, as shown in Fig.53. The outer radius of the 1D-GC was set to 36.56 μm, with an angular aperture of 30°. The grating had a uniform period Λ = 680 nm with FF = 0.5, while the etching depth was set to be 120 nm, so that a single etching process could be employed to define both the 2D-GCs and the 1D-GCs. The length of the first etched tranche was slightly narrowed, (150 nm instead of 340 nm) in order to provide a better effective index matching between the SOI waveguide and the grating section.

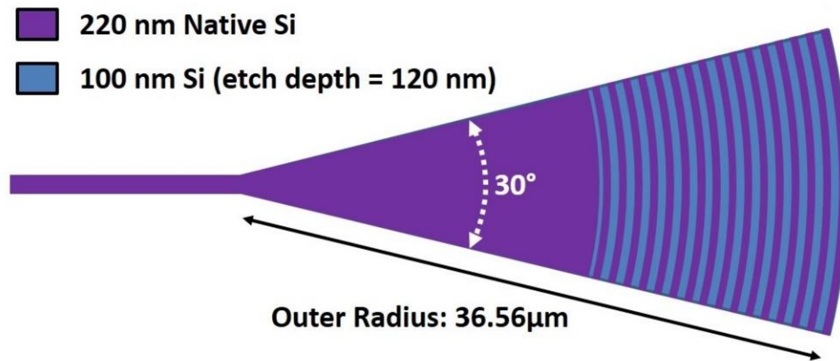

Figure 53: Schematic top-view of the focusing uniform 1D-GC employed in test structures #2.

3. The 3rd test structure was composed by a pair of 2D-GCs connected by a 12 μm wide multi-mode (MM) waveguide, having length equal to 1.2 mm. The purpose of this structure was to directly evaluate the CE of the pair of 2D-GCs, without including the taper-loss. A schematic of test structures #3 is shown in Fig.54.

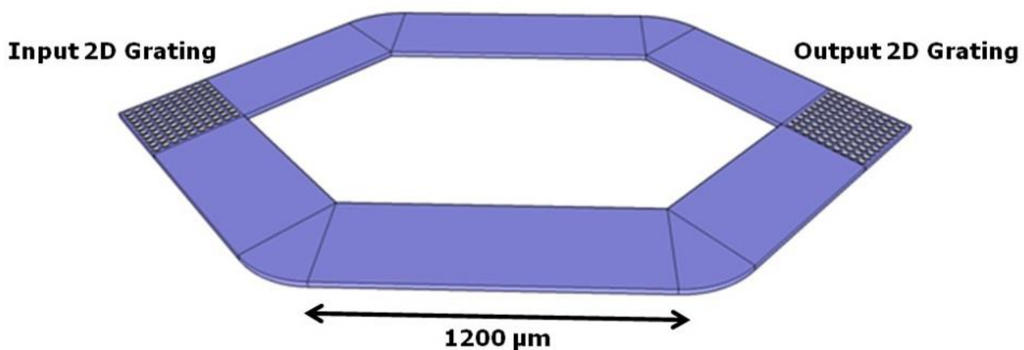

Figure 54: Schematic representation of test structures #3.

4. The 4th test structure consisted of a 2D-GC connected to a pair of output 2D-GCs using two branches of 12 μm wide MM waveguide. This structure was used to evaluate the CE of a single 2D-GC, without taper-losses in a non-interferometric structure. A schematic of test structures #4 is shown in Fig.55.

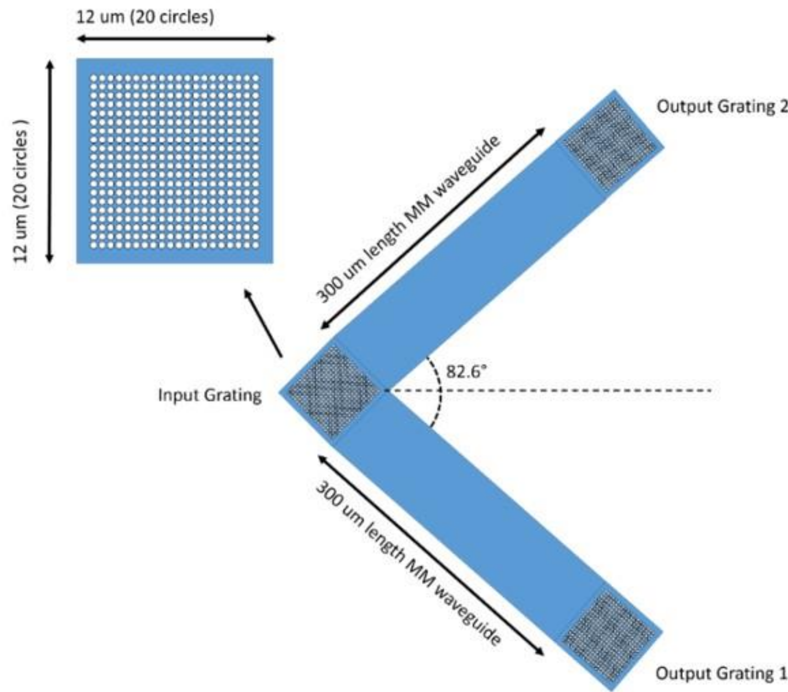

Figure 55: Schematic representation of test structures #4.

2.4.3 Polarization-diversity 2D-GC experimental characterization

The set-up used for the experimental characterization of the 2D-GC test structures is shown in Fig.56.

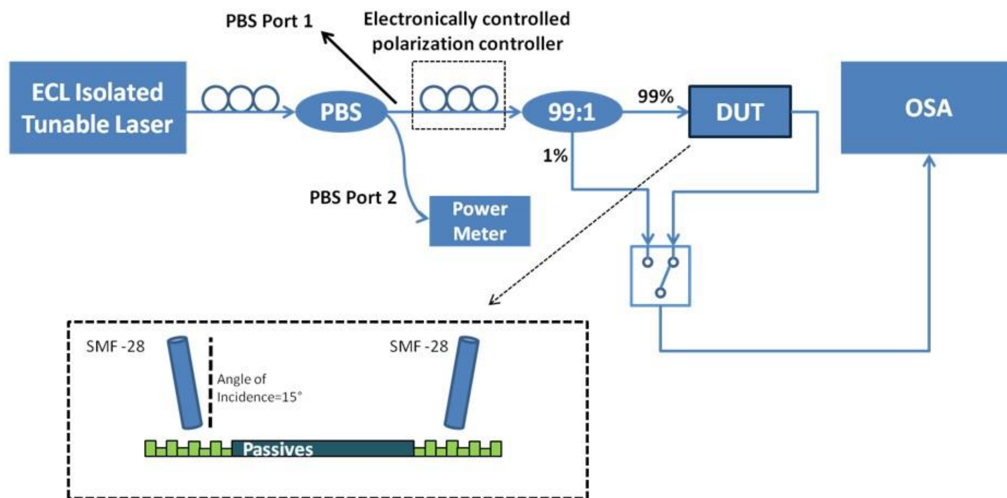

Figure 56: Experimental setup employed for the characterization of 2D-GC test structures. ECL: External Cavity Laser, DUT: Device Under Test, OSA: Optical Spectrum Analyzer.

An external cavity semiconductor tunable laser operating in the extended telecommunication bandwidth (λ = 1500-1590 nm) was coupled to a Polarization Beam Splitter (PBS) input. The polarization was then controlled at the PBS output port 1, by an electronic fibre-based polarization controller, which allows to generate every state

of polarization across the Poincare sphere. PBS port 2 was instead connected to a power meter; by minimizing the power level at this port, it is possible to maximize the power sent on the desired polarization at the PBS port 1. A fibre coupler is then used to tap the 1% of the light, while the remaining 99% is sent to the Device Under Test (DUT) by means of a vertical coupling scheme (see Fig.56 inset), using standard Corning SM-28 single mode fibres, both aligned on the top of the chip with a fixed AOI with respect to the sample vertical direction. The 1% is sent to an optical switch (MEMS activated), allowing us to carefully measure the optical beam power, both at the input and at the output of the experimental setup, using the same OSA, thus avoiding possible mis-calibration issues. For this reason, also the output fibre was connected to the optical switch.

The first set of measurement was carried out to assess CE on test structures #1, without using any index-matching fluid between fibre and sample; the AOI was set to be 15° (as from design specifications). The measured fibre-to-fibre transmission is given in Fig.57.

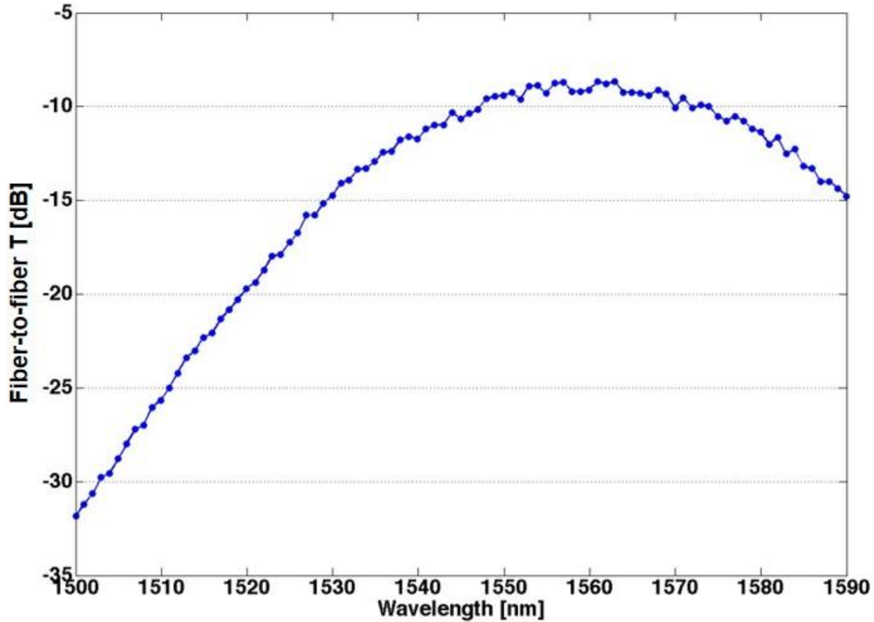

Figure 57: Fibre-to-fibre transmission measured without index-matching on test structure #1. Maximum CE = -8.9 dB.

As it can be seen from Fig.57, the maximum measured fibre-to-fibre transmission (which also includes the loss contributions due to the linear tapers and waveguide propagation) is equal to -8.9 dB, centered at 1562 nm. By subtracting the waveguide loss (measured in a different characterization experiment), the CE of the single 2D grating coupler is determined to be equal to -4.4 dB. Fibre-to-fibre transmission was also measured for different AOI, to estimate the loss-penalty into the taper due to launching at the wrong angle (see Fig.58). A fibre-to-fibre penalty of more than -2 dB

was measured for an angle deviation of 4°, implying a single 2D-GC loss increase of more than 1 dB (see Fig.59(left)). This happens because an AOI variation leads to a variation of the offset propagation angle in the grating plane of coupled light, thus increasing the taper loss (the taper direction is optimized for an offset angle of 3.7°, which is achieved for a nominal fibre AOI of 15°). As expected, when the AOI is reduced, the central wavelength red-shifts, while it blue-shifts when the AOI is increased (see Fig.59(right)).

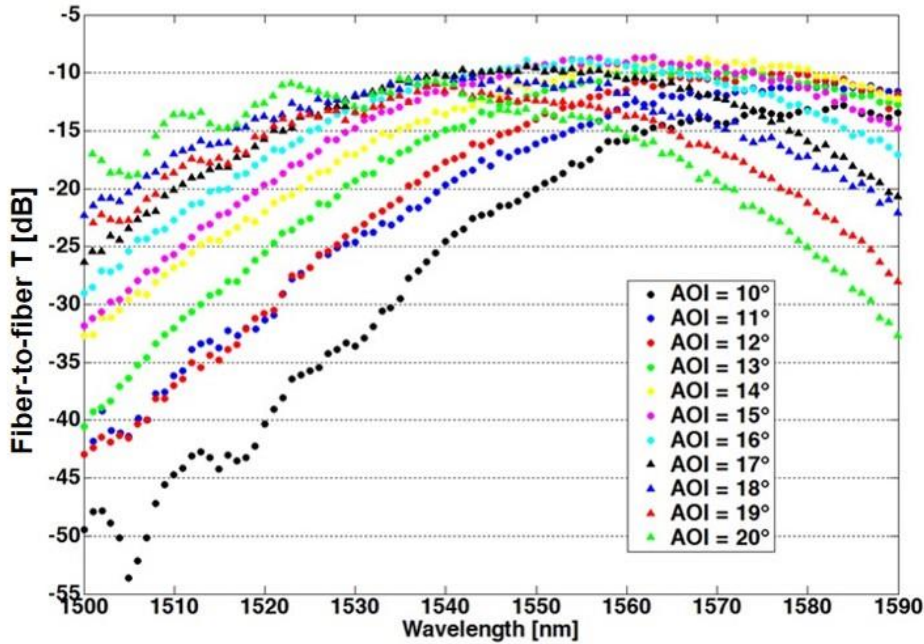

Figure 58: Fibre-to-fibre transmission measured as a function of AOI set on both input and output fibres.

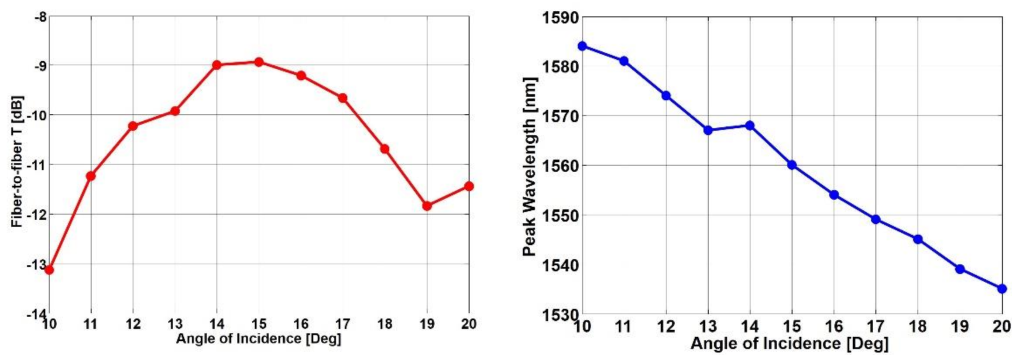

Figure 59: (left) Fibre-to-fibre transmission measured at the peak of each spectrum of Fig.58. (right) Fibre-to-fibre transmission peak wavelength for each spectrum of Fig.58.

Another important performance parameter is the bandwidth of the 2D-GC around the central wavelength. Measurements gave an average 1-dB bandwidth value of about 33 nm (as shown in Fig.60), which is relatively independent of the AOI (for

12°≤AOI≤18°), but it is slightly lower than what predicted from simulations (the simulated value was 37 nm at the design AOI = 15°).

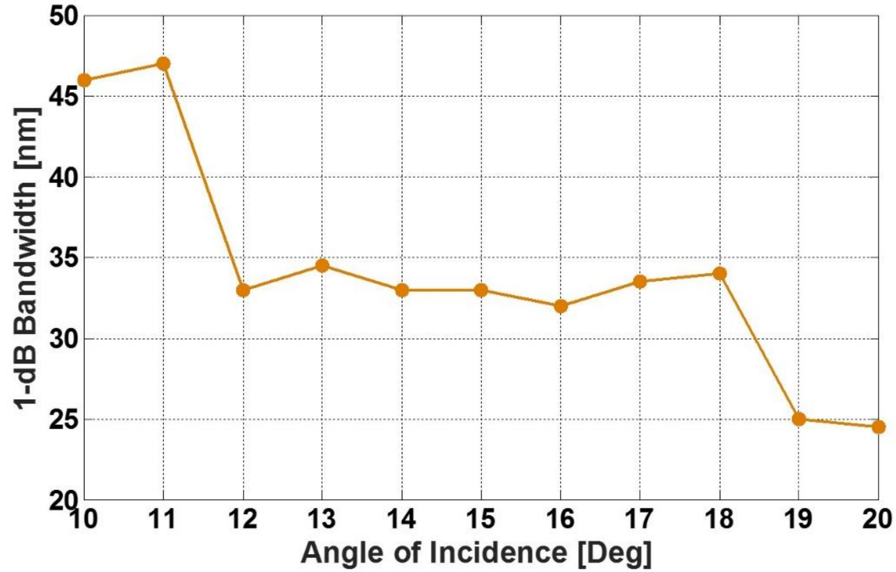

Figure 60: 1-dB bandwidth measurement results.

All the measurements were repeated on 3 different sample chips fabricated by CEA-Leti. Fig.61 shows the fibre-to-fibre transmission of test structure #1 measured at the peak wavelength, for the 3 investigated chips (each chip has two replicas of test structure #1). The maximum variation was observed on chip 1, being equal to 0.9 dB.

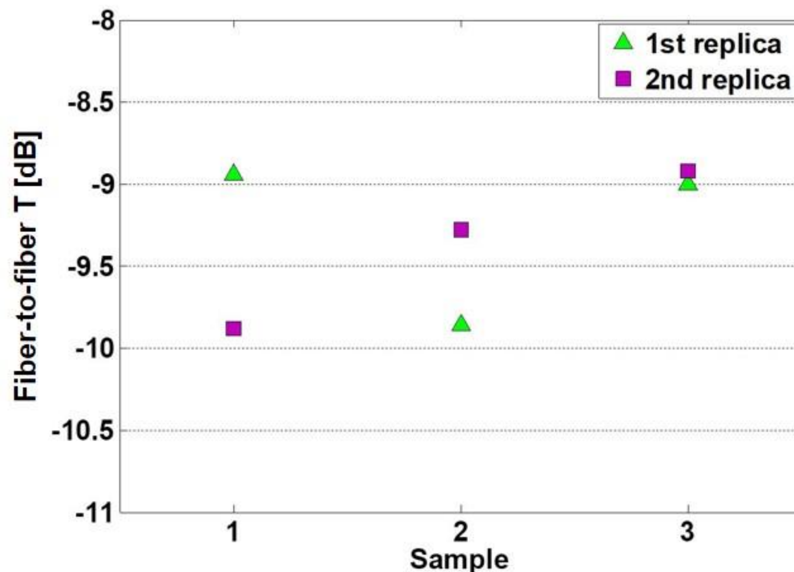

Figure 61: Fibre-to-fibre transmission measured at the peak wavelength for the 3 chips under test. Each chip includes two replicas of test structure #1.

A second set of measurements was carried out over test structure #1, in order to assess the 2D grating coupler tolerance to fibre misalignments. To do that, the input and output fibres were initially aligned, using the experimental setup previously shown in Fig.56, so as to obtain the maximum transmission and, after that, the output power from the device was recorded while shifting the position of the input fibre from maximum efficiency point in the x and y direction (in the plane of the grating coupler). The results obtained using an input laser wavelength equal to 1550 nm, are showed in Fig.62, where the color-map represents the transmission function (normalized with respect to its maximum value, and obtained by experimental data interpolation) as a function of the displacement of the input fibre in the x and y directions.

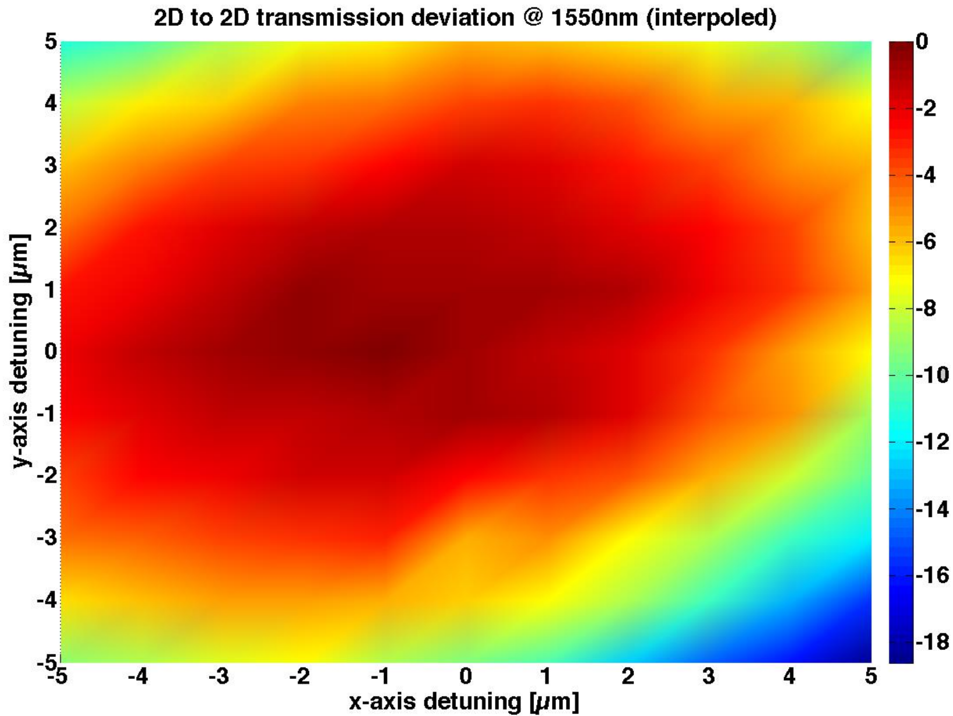

Figure 62: Fibre-to-fibre normalized transmission measured at $\lambda = 1550$ nm, as a function of the displacement of the input fibre in the x and y directions.

By plotting the normalized fibre-to-fibre transmission as a function of the x-direction displacement when having no y-direction displacement from the maximum (as shown in Fig.63(left)) and the normalized fibre-to-fibre transmission as a function of the y-direction displacement when having no x-direction displacement from the maximum (as shown in Figure Fig.63(right)), it is possible to evaluate the 1-dB bandwidth of the 2D-GC. The obtained values of 4.9 µm for the 1dB bandwidth in the x direction, and 3.7 µm for the 1dB bandwidth in the y direction, are slightly bigger than the values expected from simulations (which are reported in Fig.64), thus ensuring a relatively large tolerance of the device to fibre misalignments.

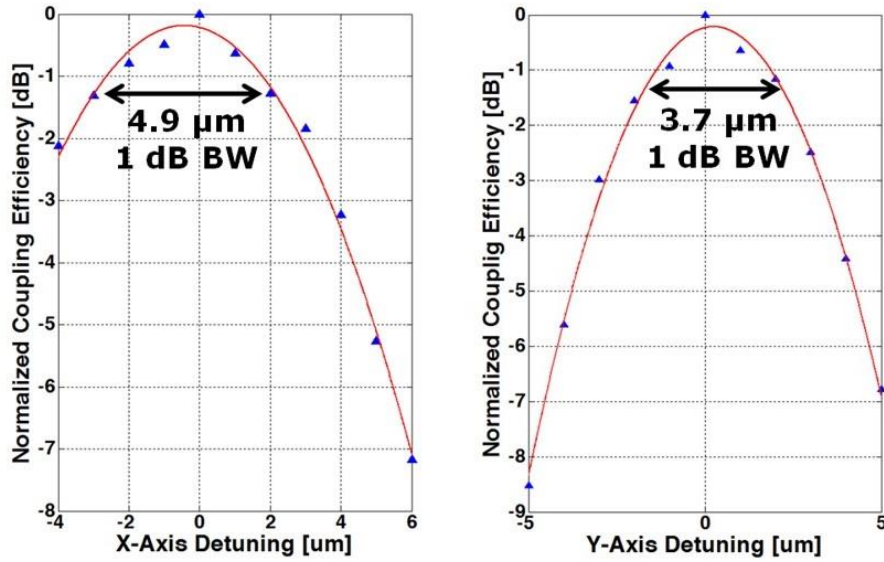

Figure 63: (left) Fibre-to-fibre normalized transmission measured at $\lambda = 1550$ nm, as a function of the displacement of the input fibre in the x direction. (right) Fibre-to-fibre normalized transmission measured at $\lambda = 1550$ nm, as a function of the displacement of the input fibre in the y direction. Blue triangles correspond to experimental data, red curve is a 2° order polynomial fit.

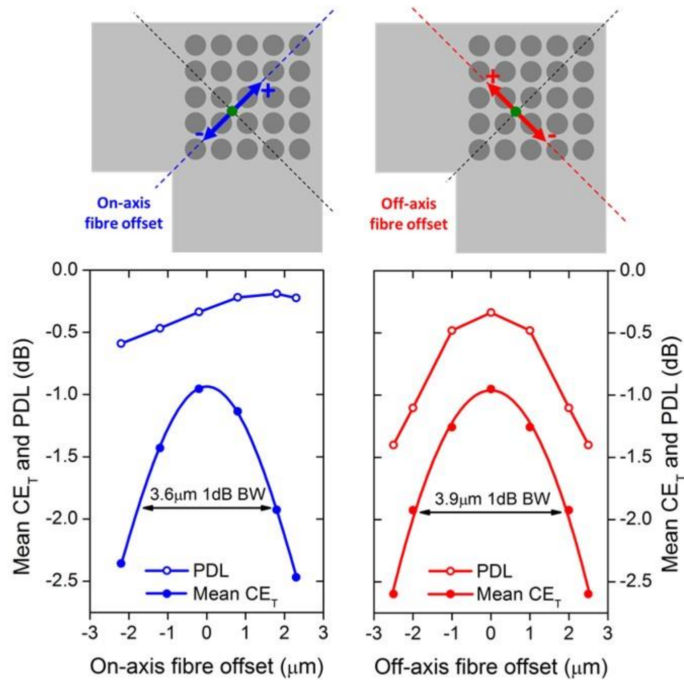

Figure 64: Simulated alignment tolerances of the 2D-GC for on-axis fibre displacements (left) and off-axis fibre displacements (right). The reported values refer to a 2D-GC simulated with the addition of a gold back-reflector, but can considered to be the nearly the same for the 2D-GC device under analysis [102].

The last measurement carried out on test structure #1, was made in order to evaluate the variation of 2D-GCs coupling efficiency when changing the polarization state of the light injected into the structure. To do that, we used the electronically controlled polarization controller, and randomly changed the polarization state of the incoming light, while aligning the input and output fibres over the 2D-GCs; the objective was to align the fibres in such a way to obtain the maximum CE, while minimizing the polarization-dependent-loss (PDL). Once the optimum alignment condition was reached, the output power was recorded as a function of time, while the polarization state of the input light was randomly changed, so that the variation of the output power represents the PDL. Results of this measurement, for λ equal to 1550 nm, are shown in Fig.65, where it can be seen that the PDL value is about 0.88 dB (the recorded value must be divided by two, as two 2D-GCs were included in test structure #1). It is clearly evident that there's a discrepancy between the PDL measured value and the one expected from simulations. This can be explained by small fabrication asymmetries, whose effect can be strongly increased if the azimuthal angle of the fibre differs from the optimum one (41.3°), as shown in Fig.66, or if the sample under measurement is tilted or moved from the optimum position.

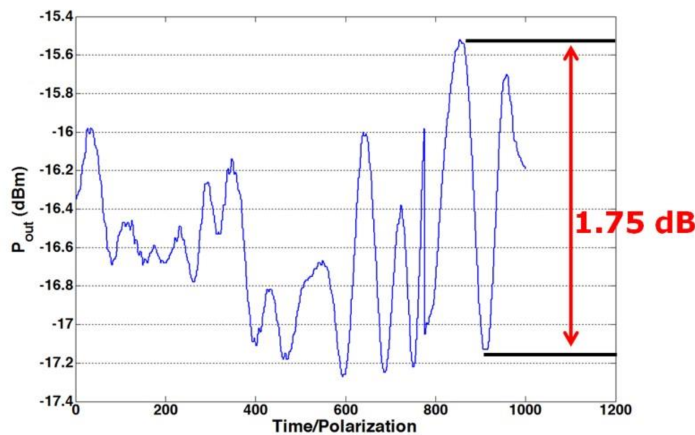

Figure 65: Output power from test structure #1, while changing the input light polarization state; the power variation represents the PDL.

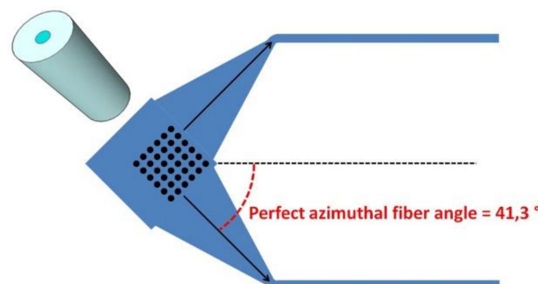

Figure 66: Schematic representation of the input 2D Grating Coupler of test structure #1; The optimum azimuthal angle at which the input fibre must be coupled with respect to the 2D-GC in order to minimize the PDL is shown.

In order to assess the Polarization Extinction Ratio (PER) of 2D-GCs connected to SM waveguides by means of modal tapers, test structure #2 (schematically represented in Fig.67) was used. To perform the measurement, we first optimized the fibre alignment maximizing the output signal at port 2, then minimized it by changing the polarization state of the input signal and acquired the output spectrum al port 2. We then moved the output fibre to port 1, without changing the polarization of the input, and acquired the output spectrum. The difference between the maximum values of the two acquired spectrum at the central coupling wavelength, assuming that the coupling loss introduced by the 1D-GC can be considered equal on both the output ports, represent the PER. The experimental results are shown in Fig.68, where it can be seen that the measured PER value of 24.9 dB proves the excellent performances of the proposed device as a PBS.

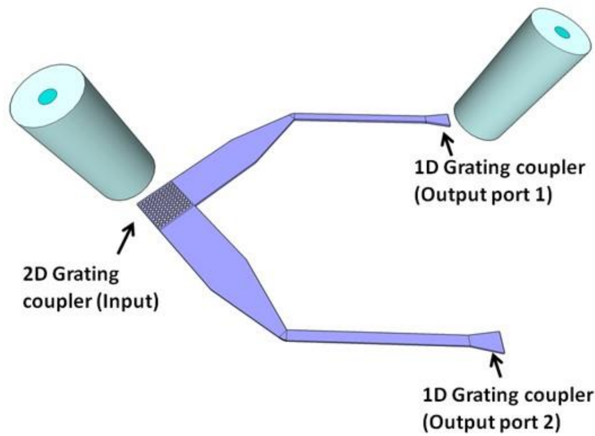

Figure 67: Schematic representation of test structure #2, designed for PER measurement.

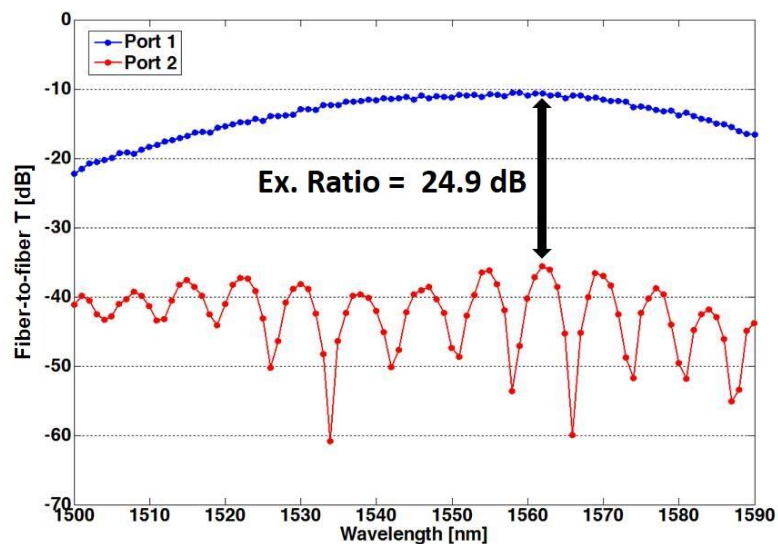

Figure 68: PER measurement results.

The CE was then measured in test structure #3, having a closed-loop structure with MM waveguides. Results are shown in Fig.69, where a maximum fibre-to-fibre transmission of -12.6 dB centered at 1555 nm is reported. Unexpectedly this value results to be extremely low, especially if compered to CE values reported from measurements carried out on test structure #1. The reason for this discrepancy might be found in a MM-mixing introduced by the bend in the MM waveguides, which re-distributes the coupled mode from the 2D-GC across the many possible modes in the MM waveguide, creating hot- and cold-spots not considered in the simulated design.

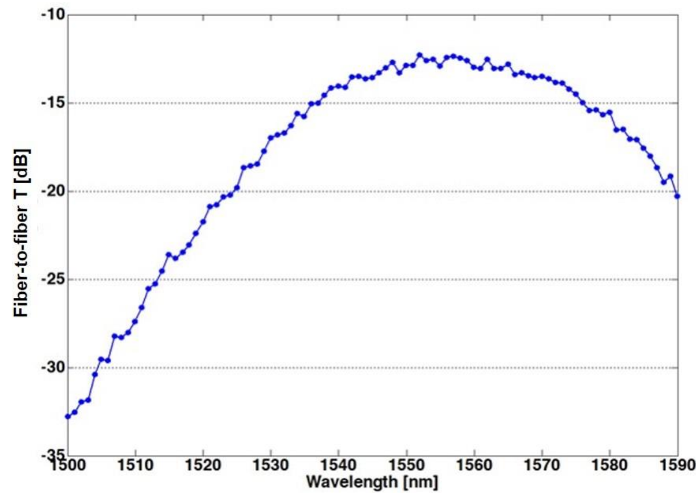

Figure 69: Fibre-to-fibre transmission measured on test structure #3.

The best results in term of CE were found for test structures #4, were an input 2D-GC is connected by means of two straight MM waveguides to two different output 2D-GCs. Using a measuring procedure similar to the one used for test structure #2, both the CE and the PER can be assessed. Measurements results are shown in Fig.70.

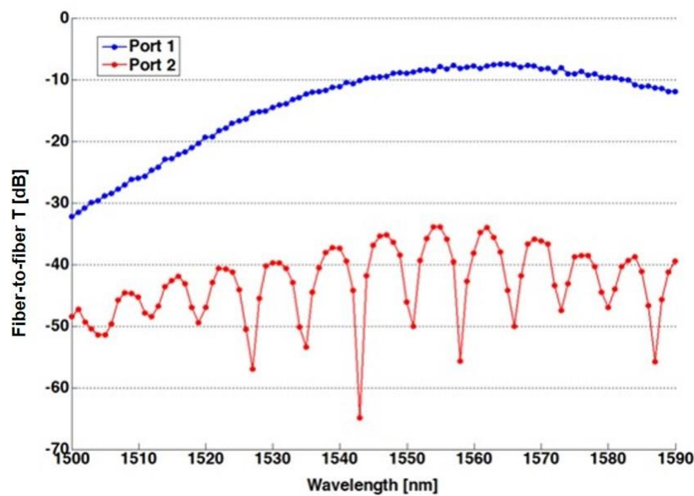

Figure 70: Fibre-to-fibre transmission measured on the two output ports of test structure #4.

From Fig.70, it can be seen that a maximum fibre-to-fibre transmission of -7.5 dB at the wavelength of 1554 nm was achieved. By assuming that the MM waveguide propagation losses are negligible, thus allowing to obtain a worst-case evaluation of the 2D-GC losses as all the waveguide losses are therefore included in the grating coupling losses, the CE of a single 2D-GC can be found as the half of the fibre-to-fibre transmission, thus obtaining a CE value of -3.75 dB. From Fig.70, it can also be noted that the measured extinction ratio (≈ 25 dB) confirms the results reported in Fig.68.

In order to evaluate the propagation loss of the SM waveguides fabricated by CEA-Leti, we included 3 test-spirals on all of the analyzed chips. The spirals were all fabricated using 500 x 220 nm standard waveguides (the same ones used for 2D-GC test structures #1 and #2) using standard 1D-GCs (the same couplers already described in Fig.53) for optical coupling. As the 3 spirals have different total lengths, by measuring their fibre-to-fibre transmissions, it was possible to extract the propagation loss, as shown in Fig.71, where the propagation loss (expressed in dB/cm) was measured at λ equal to 1550 nm, for all of the 3 analyzed chips.

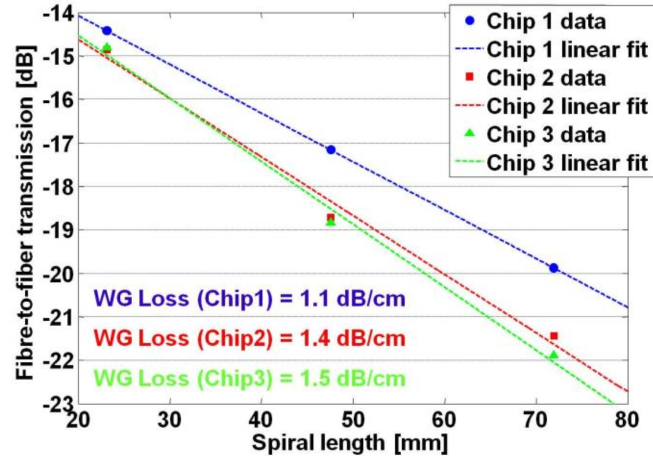

Figure 71: SM waveguides propagation losses measured on all of the 3 analyzed chips.

As a concluding remark, the measured CE for the taper-less 2D-GCs definitely fulfills the FABULOUS Project specifications, which required CE > -4 dB. Also the measured polarization exaction ratio, which is about 24.9 dB (for 2D-GCs implemented both with and without the taper), completely satisfies the project requirement of having a PER better than 20 dB. The discrepancy between the experimental CE of taper-less 2D-GCs (-3.75 dB) and the theoretically obtained one (-3.2 dB), can probably be attributed to small variations of the fabricated samples with respect to the nominal design, originated by fabrication imperfections (such as a non-complete etch of the grating holes). For what regards the tapered structures instead, the difference in the experimental results obtained with and without taper, indicates that the latter introduces a considerable additional loss of 0.65 dB (the simulated taper loss was 0.41 dB). Further optimization of the taper design is therefore required for improving the 2D-

GC performances. It is however very important to mention that this is the first time that a CE better than -4 dB for a fully CMOS-compatible 2D-GC is experimentally demonstrated, using a 220 nm Si-thick SOI platform. The previous best result was obtained by *Ghent University/IMEC*, where a 2D-GC was fabricated from a standard SOI wafer using a 70 nm deep etch, and having CE equal to -4 dB [99], while, more recently, a 2D-GC implemented in 220 nm Si-thick SOI was experimentally demonstrated, measuring a maximum CE of -1.8 dB at the central wavelength of 1550 nm [103]. This last result however, was obtained by flip-chip bonding of a partially etched 2D-GC (cladded with benzocyclobutene, BCB) on a carrier wafer, and by using an embedded gold back-reflector, thus employing a non-fully CMOS-compatible fabrication technique.

3 Reduced-height SOI waveguide

After facing the problem of the fibre-to-chip optical coupling in Chapter 2, this chapter will deal with the most fundamental component in Silicon Photonics: the optical waveguide. At first, the problem of propagation loss in SOI waveguides will be described and, after that, a new SOI platform based on reduced height waveguides will be introduced. Reduced height waveguides will be described in terms of modal properties, propagation loss and group velocity dispersion. The work regarding group velocity dispersion has been published on *Optics Express*, and can be found in [46].

3.1 Propagation loss in SOI waveguides

As it has already been pointed out in the previous chapters, optical waveguides represent the basic building block for every integrated optical circuit. Silicon-on-Insulator based strip waveguides allow achieving very tight optical confinement (thanks to the high refractive index contrast between Silicon, having $n_{Si} = 3.47$, and Silicon Dioxide, having $n_{SiO2} = 1.44$), thus allowing to design optical components with bending radii in the order of a few µm. For standard SOI waveguides the height of the waveguides (which corresponds to the thickness of the native SOI Si layer) is usually chosen in the range from 200 nm to 250 nm, while the typical width usually varies between 400 nm and 500 nm [30, 45, 29]. Since Silicon exhibits negligible absorption in the telecom wavelength window, the main contribution to waveguide propagation losses is given by the interaction of the guided optical mode with the side-wall roughness. In standard SOI waveguides, having a width/height ratio > 1, the fundamental optical mode is quasi-TE polarized, meaning that the direction of the electric field E is normal to the lateral core/cladding interface. As the normal components of the displacement vector D ($D = \varepsilon E$) most be continuous at the interface between two media having different index of refraction, this leads to a strong discontinuity of the electric field at the sidewall, thus enhancing its interaction with the roughness. An opposite situation is instead experienced by the quasi-TM polarized modes, where the E-field discontinuity takes place at the top and bottom surfaces of the Si core. The effect of the sidewall roughness on the waveguides scattering loss has been modeled and analytically studied by Paine and Lacey [104]. The formula derived in [104] (reported in Eq.(29)), which is based on the previous work by Marcuse [105], allows to derive a maximum value of scattering loss α_{max}, by knowing the root-mean square σ and the correlation length L_c of the surface roughness distribution, according to:

$$\alpha_{max} = \frac{\sigma^2 \kappa}{k_0 d^4 n_1} \tag{29}$$

Where k_0 is the light wavevector in vacuum, d is the half-width of the waveguide Si core, and n_1 is the effective refractive index of a Si slab waveguide having the same thickness as the considered waveguide. The factor κ, as described in [104], takes into

account both the chosen waveguide geometry and the statistical distribution of the roughness, which can have different shape (such as Gaussian, exponential, etc.), and is characterized by its own correlation length L_c. In most practical implementations however, κ can be approximated to 1. Eq.(29) shows that the scattering loss is greatly increased by reducing the waveguide width, as α_{max} is inversely proportional to the fourth power of d. For example, a surface roughness of only 5 nm would generate a scattering loss of about 60 dB/cm when considering a Si strip waveguide having width equal to 400 nm and height equal to 200 nm [106]. Scattering loss is also extremely dependent on the etching technique used to fabricate the waveguide, which has a strong influence on the root-mean square of the roughness distribution. For strip waveguides fabricated using standard reactive-ion etching technique, the propagation loss values reported in literature usually vary between 2.4 dB/cm [107] and 3.6 dB/cm [29]. Advanced fabrication processes can also be employed to reduce the waveguide scattering loss, such as side-wall roughness smoothing by thermal oxidation [108], which allows to obtain propagation losses as low as 0.8 dB/cm, or the use of Si selective oxidation instead of etching to define the waveguide geometry [109], which allowed to demonstrate an ultra-low propagation loss of 0.3 dB/cm at λ = 1550 nm. A cross-sectional representation of an etch-less Si waveguide and the distribution of its fundamental TE mode is shown in Fig.72, as reported in [109].

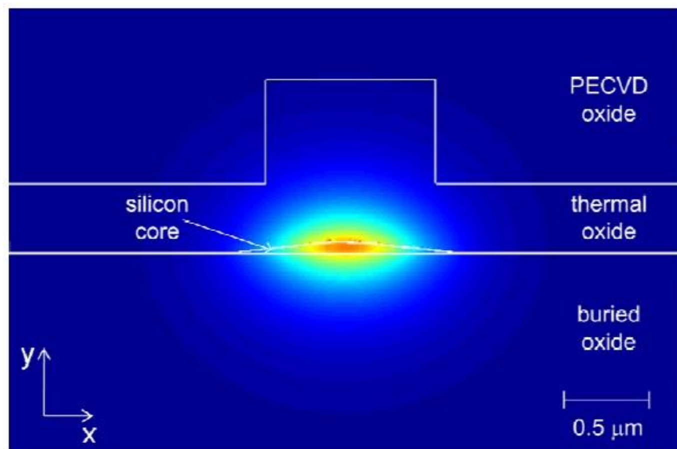

Figure 72: TE mode profile of a 1 µm wide Si etch-less waveguide [109].

When dealing with SOI waveguides fabricated using standard processes however, the scattering loss can be reduced by optimizing the waveguide geometry. Barwicz et al. [110] for example, showed that using SOI waveguides having reduced height with respect to the 220 nm standard thickness of the commonly employed SOI wafers, allows to theoretically reduce the propagation loss of nearly an order of magnitude, thanks to the lower overlap of the optical mode with the vertical sidewalls. Using this approach, Si waveguides having height equal to 106 nm and width equal to 600 nm were demonstrated in [111] for the implementation of integrated tunable filters; the waveguides were fabricated starting from a SOI wafer with 3 µm of buried oxide and

220 nm of native Si, using calibrated steam oxidation and fluorhydric acid (HF) stripping for reducing the Si layer thickness.

Due to their promising performances in terms of scattering loss reduction, we decided to perform a complete experimental characterization, which is currently lacking in the scientific literature, of reduced height waveguides. Whereas the waveguide described in [111] are obtained using complicated and expensive fabrication processes, we used a standard RIE etching process to lower the waveguide height from 220 nm to 100nm.

3.2 100-nm high WG: Modal analysis

The first step we performed was to carry out a modal analysis of reduced height waveguides, in order to identify the width-range which allows to achieve single mode propagation, thus avoiding eventual modal conversion phenomena that may act as an additional source of losses [112]. To do that, we performed effective index simulations, using *MODE Soultions*™, for Si waveguides having height equal to 100 nm, and width varying from 100 nm to 1 µm, at 20 nm steps. Si waveguides were considered to be fully surrounded by Silicon Dioxide, thus including a TOX layer. Si refractive index n_{Si} and SiO_2 refractive index n_{SiO2} were assumed to be equal to 3.48 and 1.44 respectively, at the wavelength of 1550 nm. Simulation results are reported in Fig.73, where the effective refractive index of the first 3 waveguide modes is reported as a function of the waveguide width.

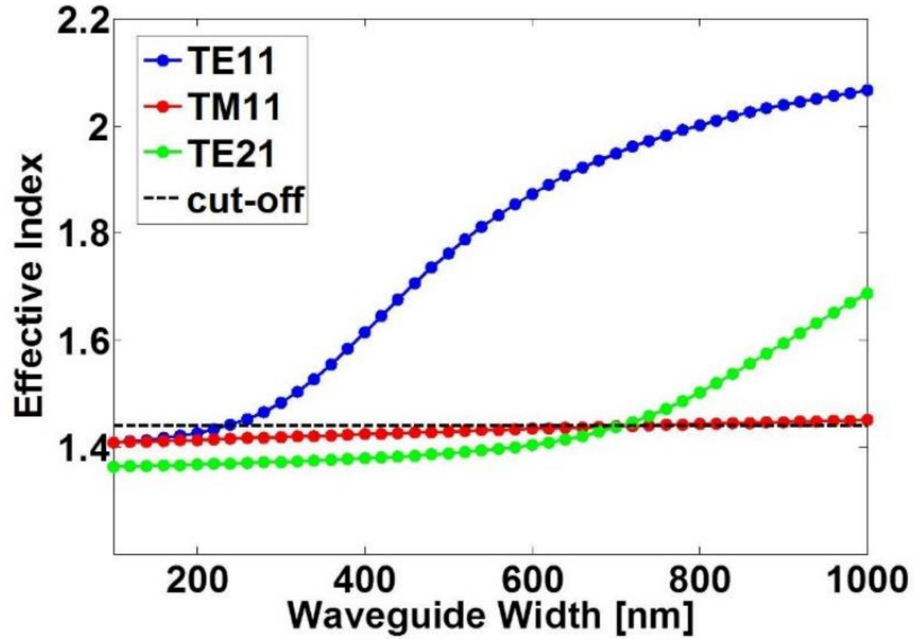

Figure 73: Simulation of the effective index of the first 3 modes of a 100 nm high waveguide at $\lambda = 1550$ nm, as a function of the waveguide width [46].

As it can be seen from Fig.73, when the width of the 100 nm high Si waveguides is comprised in the 300 nm - 700 nm range, only the propagation of the fundamental TE mode is allowed, so that the waveguide operates in single-mode regime. When the waveguide width is increased beyond 700 nm, also the second order TE mode starts to be supported (as its effective refractive index becomes greater than the threshold set by refractive index of the cladding SiO_2). However, in the 700 nm - 800 nm width range, the second order TE mode will be only barely guided and will therefore experience very high propagation losses, so that the waveguide can still be considered almost as single mode. In Fig.74 a schematic of two lowered height waveguide cross-sections having width equal to 500 and 800 nm, superimposed with the distribution of the power density, is shown, together with the schematic of a standard 500×220 nm strip waveguide as a comparison.

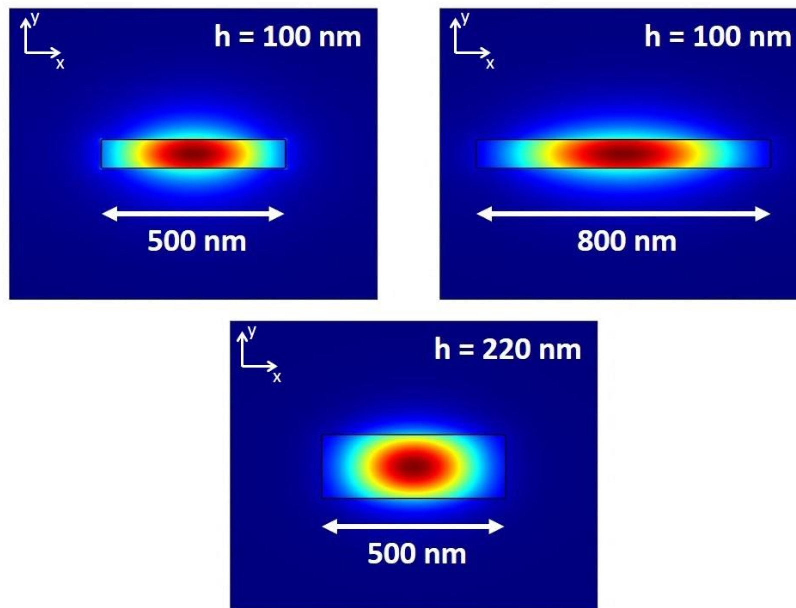

Figure 74: Optical power distribution in the transverse section of lowered-height and standard waveguides. The black line represents the physical cross-section of the waveguide, while the beam propagates perpendicularly to the sheet surface.

From Fig.73, it can also be seen that the effective refractive index of 100 nm high Si waveguide at $\lambda = 1550$ nm is much lower than that of standard 500x220 nm waveguides, having $n_{eff} = 2.4$, meaning that the optical mode is much less confined in the Si core, and more spread in the SiO_2 cladding. This can be clearly seen in Fig.75, where the normalized electric field amplitude of the fundamental TE mode is plotted, as a function of the position along the x axis (according to the reference system of Fig.74), for two Si waveguides having width equal to 500 nm, and separated by a 250 nm wide gap. The E-field amplitude is plotted for both the cases of standard height waveguides (220 nm, black trace) and reduced height waveguides (100 nm, red trace).

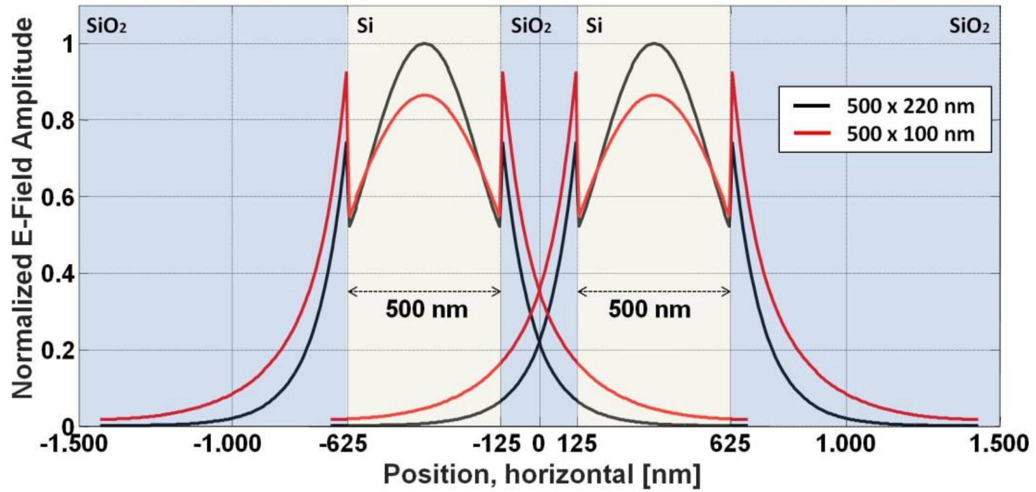

Figure 75: Normalized E-field amplitude plot as a function of horizontal position, for the TE fundamental mode of two optical waveguides. The waveguides are 500 nm wide, and placed at a distance of 250 nm from each other. The black plot corresponds to 220 nm high waveguides, while red plot corresponds to 100 nm high waveguides.

3.3 100-nm high WG: Propagation loss measurements

To assess the scattering loss properties of reduced height waveguides, we designed 3 set of test waveguides, each set including 5 different types of waveguide. Regarding the waveguides included in each set, the first one was a standard 500×220 nm waveguide, while the four remaining waveguides were height-reduced structures (height = 100 nm) having width respectively equal to 500 nm, 600 nm, 700 nm and 825 nm. The different sets were composed by waveguides with different lengths (5.1 mm, 7 mm, 10 mm for standard waveguides, and 4.7 mm, 6.6 mm, 9.6 mm for lowered height waveguides) with a fixed number of 90° curves (8 curves per waveguide having radius equal to 10 µm for standard waveguide and 40 µm for lowered height waveguides). At the input/output of each waveguide, standard 1D-GC were designed (the same type of grating previously described in Fig.53), in order to couple light by means of standard single mode fibres. Propagation loss value can be obtained by performing a linear fit of the measured the fibre-to-fibre transmissions of waveguides with different lengths, using an approach similar to that previously reported in Fig.71 in Chapter 2.

The samples were fabricated at CEA-Leti Si-photonics foundry, starting from 200 mm SOI wafers, with a 2 µm thick buried oxide layer and a 220 nm thick silicon layer. The optical waveguides were patterned using 193-nm DUV lithography and two different inductively-coupled-plasma reactive-ion etching processes (ICP RIE): the first process, with an etch depth of 120 nm, was used to define the grating coupler and to lower the waveguides height from 220 nm to 100 nm, whereas the second, with a full-etch depth of 220 nm, was used to define the lateral edges of both standard and lowered-height strip waveguides [46].

The experimental setup used for propagation loss measurements is reported in Fig.76.

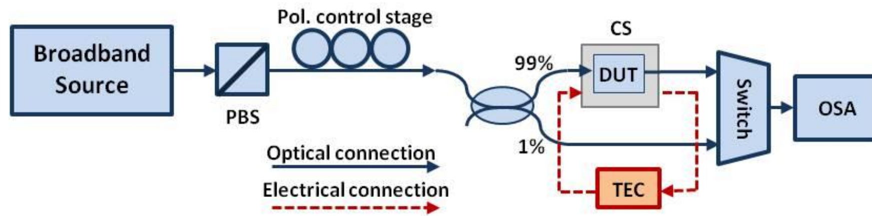

Figure 76: Experimental setup used for propagation loss measurement of fabricated waveguides. PBS: Polarization Beam Splitter, DUT: Device Under Test, TEC: Thermoelectric Cooler, OSA: Optical Spectrum Analyzer.

As an optical source, the broadband ASE (amplified spontaneous emission) emission from an erbium-doped fibre amplifier (EDFA) was used. The optical beam was sent to a polarization-beam-splitter (PBS), in order to get a linearly polarized output, and then to a fibre polarization control stage, as the implemented 1D-GCs were designed for TE light polarization. A 99/1 fibre power splitter was then used: 1% of the incoming light was taken a monitor of the input power, while the remaining 99% was coupled to the sample under measurement. Finally, the output light from the chip was sent to an optical spectrum analyzer (OSA), using a resolution of 0.01 nm, together with the input power monitor, by means of a MEMS optical switch. A feedback control loop was used in order to detect and stabilize the temperature of the sample, which was set to be 20 °C.

An example of the transmission spectra acquired on the three standard waveguides (500x220 nm) with different lengths is shown in Fig.77. It can be noticed the presence of a totally unexpected "high frequency" ripple in the transmission spectra, as well as the presence of different "notches" having a non-constant spectral separation. This is probably due to a high level of side-wall roughness on the fabricated waveguides, which generates many back-reflection hot-spots along the waveguides length. Therefore, in order to achieve useful results, the transmission spectra were smoothed with a moving average technique, in a 15 nm wide wavelength window centered around 1550 nm, as shown in the inset of Fig.77. Propagation losses were then calculated for each acquired wavelength in the smoothing-window, and the obtained values were then averaged between etch others, in order to obtain a final estimation of the propagation loss at 1550 nm. Similar spectra were obtained for the reduced height waveguides, and the same smoothing technique was applied for calculating the propagation losses. Unfortunately however, many of the fabricated reduced-height waveguides were systematically not working; this allowed to obtain reliable results only for 3 of the 5 waveguide geometries implemented (500 x 220 nm, 500 x 100 nm, 825 x 100 nm). The obtained results, for two different analyzed chips, are reported in Tab.5.

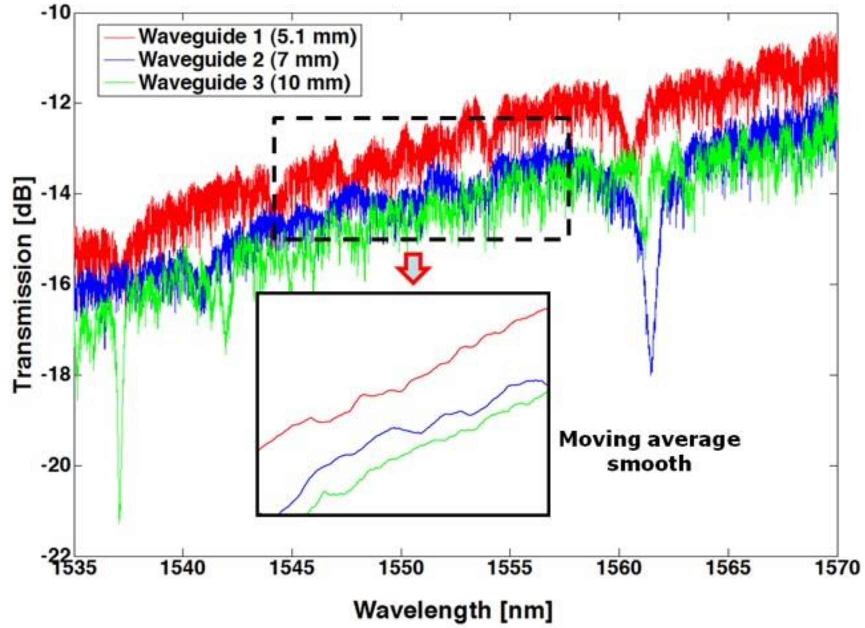

Figure 77: Fibre-to-fibre transmission spectra of three 500 x 220 nm standard waveguides having length respectively equal to 5.1, 7, and 10 mm. The region where moving average smooth was applied is highlighted.

Waveguide geometry (width x height) [nm]	**500 x 220**	**500 x 100**	**825 x 100**
Loss [dB/cm] chip #1	2.9	2.6	1.7
Loss [dB/cm] chip #2	3.0	2.4	2.0

Table 5: Waveguide propagation loss for 3 different waveguide geometries, measured for 2 different chips.

From Tab.5, it can be noticed that the propagation loss values obtained for standard SOI waveguides (500x220 nm) are definitely higher than the ones reported in Chapter 2 (see Fig.71), where the same waveguide geometry was implemented in a different fabrication run. This points out how difficult it can be to control the actual size of waveguides side-wall roughness, where even small variations in the fabrication process can lead to big variations in the resulting propagation loss. However, when taking into account the results obtained in a single fabrication run, as reported in Tab.5, it can clearly be seen that the use of reduced height waveguides effectively allows to reduce propagation losses, if compared to the standard geometry. As expected, the best results for reduced height waveguides are obtained by increasing the waveguide width (in accordance with Eq.29); when using the 825x100 nm geometry propagation losses are improved by more than 1 dB/cm with respect to standard waveguides.

3.4 100-nm high WG: Group velocity dispersion measurements

Beside characterizing the scattering loss of reduce height waveguides, we also decided to study their properties in terms of group index and group velocity dispersion. For application such as χ_3 based non-linear optics for example, an accurate knowledge of the waveguide dispersion is an indispensable prerequisite for determining the non-linear system phase-matching bandwidth. While an experimental characterization of the group velocity dispersion of channel waveguides implemented in standard 220 nm Si-thick SOI platform [113] or in platforms with thicker Si layers [114, 115] has already been carried out, no experimental data are available in the scientific literature for reduced height waveguides.

In order to measure the waveguide group index at different wavelengths, we designed a set of Mach-Zehnder interferometers (MZI), using different 100-nm high waveguides, having width equal to 500, 600, 700 and 800 nm respectively. We also added a MZI structure implemented using a standard 500x220 nm waveguide, so that we could compare our results with those already published in literature [113]. A schematic of the implemented Mach-Zehnder interferometer is shown in Fig.78.

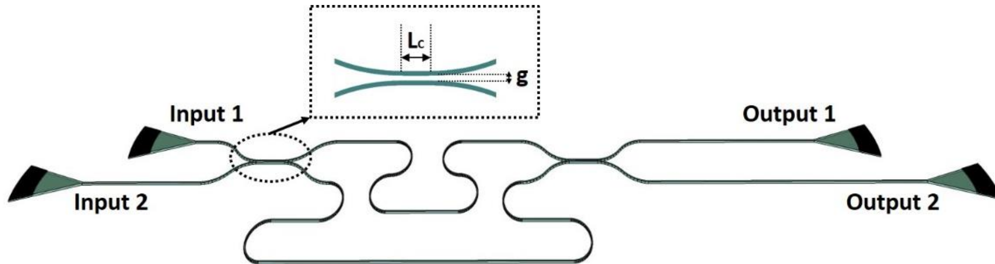

Figure 78: Schematic of the MZI structure used to measure waveguide dispersion.

The input and output ports of the MZI were implemented using the same 1D-GCs employed for the waveguides designed for propagation loss assessment (See Fig.53). The coupling sections of the MZI were instead implemented as directional couplers, as it can be seen in the inset of Fig.78. A directional coupler simply consists of two parallel waveguides, which are brought in close proximity; thanks to the evanescent field coupling, the optical power propagating in one of the input waveguides can be split into two separate output waveguides and, symmetrically, two different signals at the input of the coupler can be combined at the output. The power cross-coupling ratio of a directional coupler can be obtained using Coupled Mode Theory (CMT) [116, 117], and can be expressed as:

$$\kappa^2 = \frac{P_{cross}}{P_0} = sin^2(C \cdot L_C) \tag{30}$$

Where P_0 is the input optical power, P_{cross} is the optical power coupled across the directional coupler, L_C is the length of the straight portion of the directional coupler, and C is the coupling coefficient. Assuming the directional coupler to be lossless, a similar equation can be found for the direct-coupling ratio t^2, by replacing the sine function of Eq.(30) with a cosine function. For what regards the coupling coefficient C, it can be derived using the Eigenmode Expansion Method (EME), which is based on the numerical calculation of the refractive indexes of the first two eigenmodes (also known as the "symmetrical" and the "anti-symmetrical" supermodes) of the system composed by the two coupled optical waveguides. It can be found that the coupling coefficient C is exponentially dependent on the gap g between the two waveguides, as expressed by:

$$C = B \cdot e^{-A \cdot g} \tag{31}$$

Where A and B are factors which depend on the waveguide geometry and on the optical wavelength λ. In order to relax the fabrication tolerances, we decided to fix the value of g to 300 nm for our MZI structures, and we then performed 3D-FDTD simulations (using *FDTD Solutions*™ software) in order to calculate the coupling-length L_C required to achieve a 50% power splitting at $\lambda = 1550$ nm, for all of the implemented waveguide geometries. The implemented directional coupler simulation layout is shown in Fig.79(left), while the simulation results for a 500x100 nm waveguide geometry are shown in Fig.79(right), where the cross-coupling power ratio κ^2 is reported as a function of L_C, at 5 µm steps, and the expected sinusoidal trend can be observed. The final L_C values for all of the considered waveguide geometries, obtained by simulations with smaller L_C steps, are reported in Tab.6. Interestingly, it can be noticed that, thanks to the lower modal confinement of reduced height waveguides (which had already been described in Fig.75), smaller coupling lengths are required to achieve a 50% power splitting ratio, with respect to standard 500x220 nm waveguides.

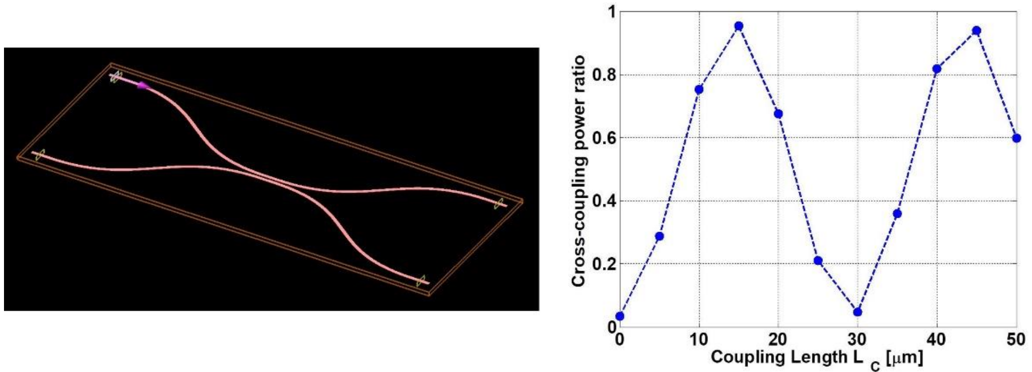

Figure 79: (left) 3D-FDTD simulation layout of a directional coupler. (right) Simulated cross-coupling power ratio for a directional coupler implemented with 500x100 nm waveguides, as a function of the coupling length L_C. L_C was varied at 5 µm steps.

WG cross-section [nm x nm]	500x100	600x100	700x100	800x100	500x220
Coupling length L_C [µm]	7.3	14.3	25.8	42.1	41.6

Table 6: 3D-FDTD simulated optimum coupling lengths L_C for implementing a directional coupler with 50% splitting ratio, both using reduced height waveguides (height = 100 nm, width = 500, 600, 700, 800 nm) and standard waveguides (height = 220 nm, width = 500 nm).

MZIs were designed to be unbalanced, meaning that a significant phase difference is accumulated between the guided modes propagating in the two arms of the structure, which then undergo constructive or destructive interference at the output direction coupler. Consequently, as the accumulated phase difference is obviously wavelength-dependent, the transmission function of the MZI exhibits a cosine-like interference pattern, whose free spectral range (FSR) can be expressed as:

$$FSR = \frac{c}{n_g \Delta L} \tag{32}$$

Where c is the speed of light in vacuum, n_g is the waveguide group index, and ΔL is the length difference between the two arms of the MZI. In order to obtain a suitable FSR, were designed two different structure, having ΔL respectively equal to 50 µm and 100 µm, for each different type of waveguide.
The samples were fabricated on the same chips carrying the waveguides designed for propagation loss assessment, which have been described in the previous paragraph. The experimental setup used for the MZIs measurement is shown in Fig.80: it is basically the same setup previously described in Fig.76, where, as an optical source, the EDFA had been replaced with an external cavity laser, tunable from 1475 to 1590 nm and providing a maximum output power of 8 dBm and a line-width < 100 kHz. An optical micrograph of the fabricated MZIs, vertically coupled by means of 1D-GCs, is shown in Fig.81.

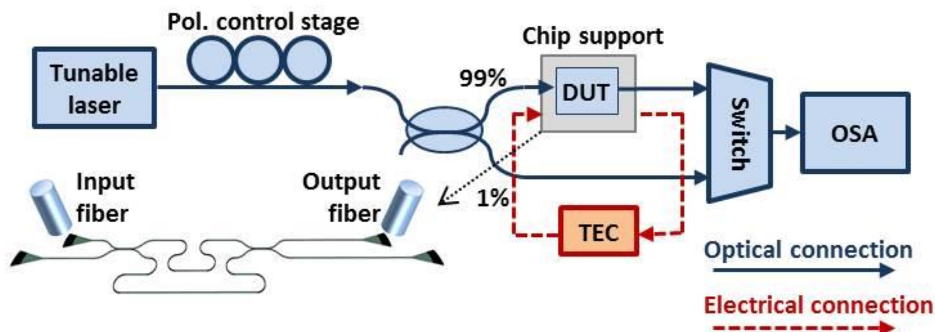

Figure 80: Experimental setup used to measure waveguides dispersion. DUT: Device Under Test, TEC: Thermoelectric Cooler, OSA: Optical Spectrum Analyzer [46].

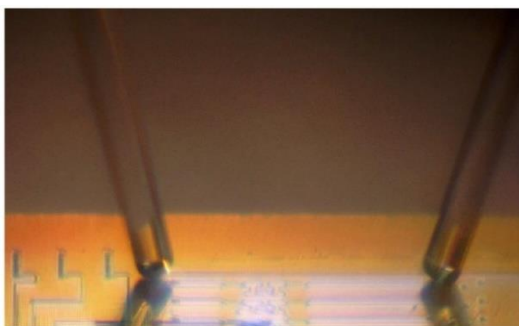

Figure 81: Optical micrograph of a fabricated sample carrying different MZI structures. Standard single mode fibres vertically coupled to 1D-GCs were used to couple light in and out from the chip.

Using the experimental set-up shown in Fig.80, measurements were carried out by exploiting a 2-step procedure. As a first step the MZIs transfer function was acquired while sweeping the laser wavelength over its entire excursion range (1475 nm-1590 nm) with a 50 pm step. The relatively low wavelength-resolution allows to limit the required measurement-time, thus improving the measurement stability, but it is anyway enough accurate to allow to clearly extract the spectral ranges corresponding to the different transmission minima. The second acquisition was then performed by sweeping the laser wavelength with a 1-pm resolution over a 100 pm wide wavelength range centered around each of the previously identified minima. This procedure allows a precise identification the spectral position of the transmission minima with the best possible resolution (which is basically limited by the minimum sweeping step allowed by the chosen optical source) on a wide wavelength range, without requiring excessive time. As an example, the experimental transmission function of one of the MZI, implemented using 600x100 nm waveguides and with $\Delta L = 100$ µm, is shown, as a function of the optical wavelength λ, in Fig.82.

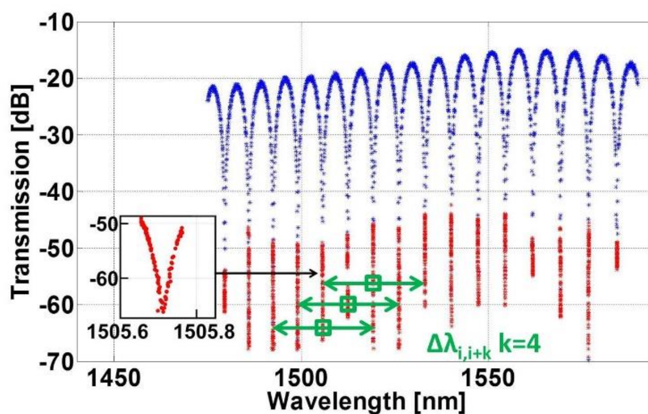

Figure 82: Example of the acquired experimental data, measured on the MZI implemented with 600x100 nm waveguides, and having $\Delta L = 100$ µm. The blue dots represent the 50 pm resolution data while the red dots represent the 1 pm resolution data. The green arrows represent the wavelength windows considered (4 FSR) for the group index and dispersion calculation [46].

Once the spectral position of the minima in the transmission function is known, the waveguide group index n_g can be calculated over each free-spectral-range (FSR) window. To do that, we can start by expressing the waveguide effective refractive index n_{eff} using a first order Taylor series expansion, as reported in the following equation:

$$n_{eff}(\lambda_2) = n_{eff}(\lambda_1) + (\lambda_2 - \lambda_1) \left. \frac{dn_{eff}}{d\lambda} \right|_{\lambda_1} \tag{33}$$

Where λ_1 and λ_2 are the wavelengths corresponding to two consecutive minima. If we than recall that the destructive interference condition for the MZI transmission function minima requires the phase shift accumulated by light propagating over the unbalance length ΔL to be an odd multiple of π, as expressed by:

$$\frac{2\pi}{\lambda_i} n_{eff}(\lambda_i)\Delta L = (2m_i + 1)\,\pi \qquad m_i \in N \tag{34}$$

We can then combine Eq.(33) and Eq.(34) to express n_{eff} as:

$$n_{eff}(\lambda_i) = \frac{\lambda_1 \lambda_2}{\Delta L(\lambda_2 - \lambda_1)} + \lambda_1 \left. \frac{dn_{eff}}{d\lambda} \right|_{\lambda_1} \tag{35}$$

Finally, if we consider that the waveguide group index is defined as:

$$n_g = n_{eff} - \lambda \frac{dn_{eff}}{d\lambda} \tag{36}$$

We can combine Eq.(35) and Eq.(36) to express n_g as a function of λ_1, λ_2 and ΔL:

$$n_g = \frac{\lambda_1 \lambda_2}{\Delta L(\lambda_2 - \lambda_1)} \tag{37}$$

The n_g values obtained using Eq.(37) represent an average value of the waveguide group index in the spectral window comprised between two adjacent minima wavelengths λ_1 and λ_2. Once n_g is experimentally characterized, group velocity dispersion parameter D, can be derived, using the following equation:

$$D = \frac{1}{c} \cdot \left(\frac{dn_g}{d\lambda} \right) \tag{38}$$

In order to get reliable results for the dispersion calculation, n_g has to be measured with very high accuracy. In [113] light intensity $I(\lambda)$ is used to evaluate the waveguide group index for each wavelength point of the measured transmission spectrum; unfortunately, this technique could not be applied in our case, as an amplitude ripple, originated by residual gratings reflections, was superimposed to the transmission spec-

trum and it would have introduced a significant noise in the n_g calculation. We therefore decided to apply a moving-average technique: to do that, starting from the experimental transmission spectra, we calculated the group indexes n_g values by applying Eq.(37) not between two consecutive minima λ_1 and λ_2, but between two minima λ_i and λ_{i+k} separated by a k number of FSR, were k is a positive integer. Using this approach, n_g is still calculated at each wavelength corresponding to transmission minima, but its value is now obtained as an average over a k number of FSR [46].

An example of the wavelength windows $\Delta\lambda_{i,i+k}$ used for n_g calculation can be seen, marked by green arrows, in Fig.82, where k is equal to 4. From Eq.(37) it can be noticed that, as the error in determining λ_i and λ_{i+k} is imposed by the resolution of the laser source sweep (1 pm in our case), an increase of $\Delta\lambda_{i,i+k}$ will result in a reduction of the error in the n_g calculation.

Unfortunately, the MZIs implemented using 700x100 nm and 800x100 nm waveguides and having $\Delta L = 100$ µm, were systematically not working on all of the fabricated samples, due to fabrication imperfections. Therefore, for the 700x100 nm and 800x100 nm waveguide geometries, the n_g calculation was carried using the transmission spectra acquired from the MZIs having $\Delta L = 50$ µm, while, for the remaining waveguide geometries, the MZIs having $\Delta L = 100$ µm were considered.

The experimentally derived group index values are reported, together with the values predicted by means of modal simulations (performed using *MODE Solutions*™ software), in Fig.83, for the MZI implemented with standard height waveguide, and in Fig.84 for the MZI implemented with reduced height waveguides.

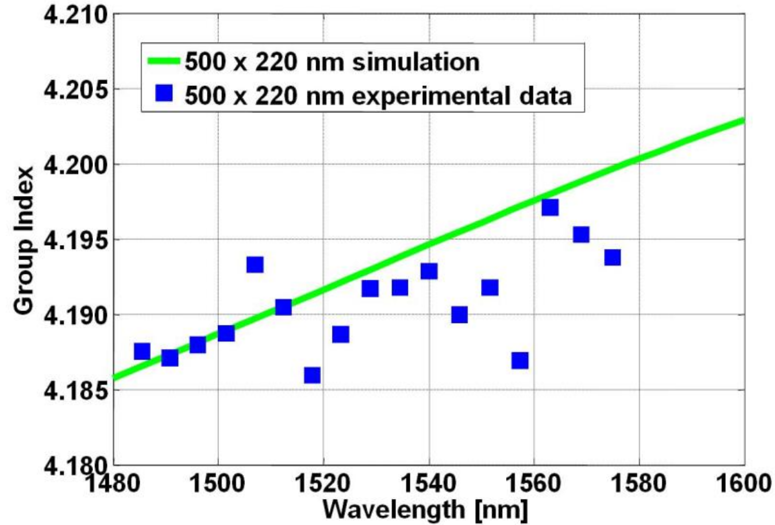

Figure 83: Experimentally derived (blue squares) group index values for standard 500x220 nm waveguides, and values predicted from simulations (green line) [46].

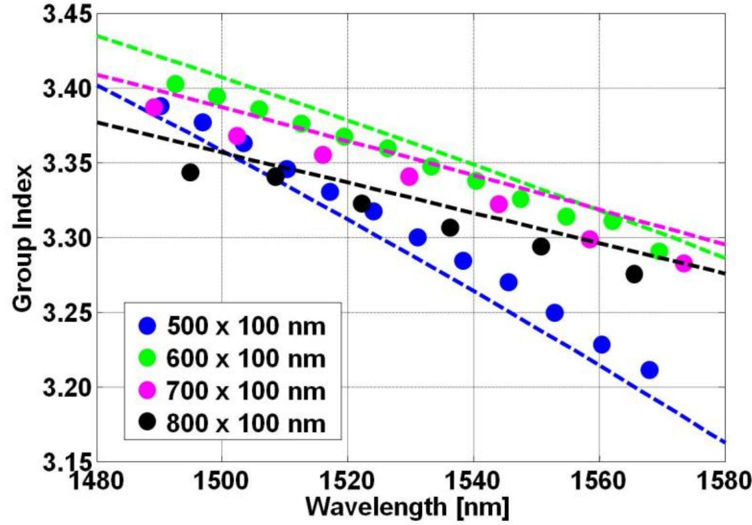

Figure 84: Experimentally derived (dots) group index values for 100 nm high waveguides, and values predicted from simulations (dashed lines) [46].

After having calculated n_g at different wavelengths and for each analyzed waveguide geometry, the data points were fitted with a second order polynomial function; if the group index fitting functions are derived with respect to the optical wavelength λ, as reported in Eq.(38), a linear expression can be obtained for representing the dependency of the group-velocity dispersion parameter D over λ.

The experimentally derived dispersion curves for the different waveguide geometries are plotted in Fig.85, together with the dispersion curves obtained by modal simulations.

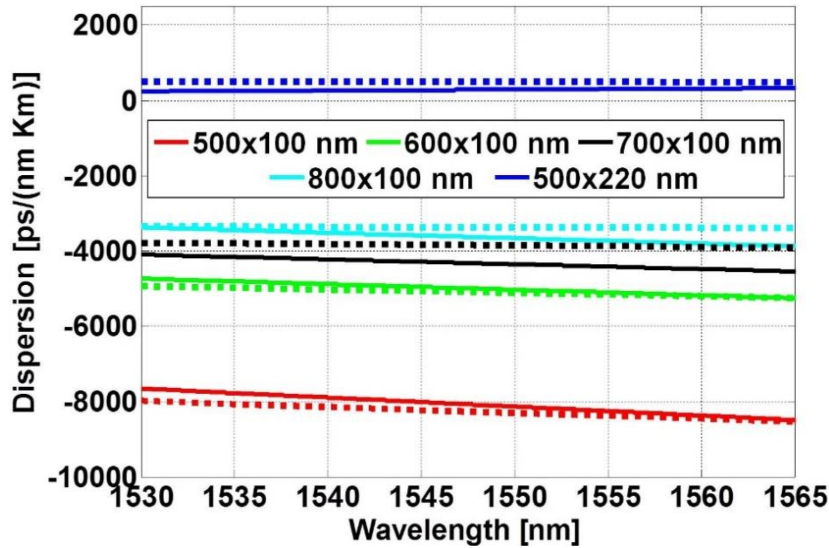

Figure 85: Dispersion curves of the analyzed waveguides in the C-band. Solid lines represent the experimentally derived curves, while dashed lines represent those derived by numerical simulations [46].

It is worth noting (see Fig.86) that the dispersion dependency on the waveguide width obtained experimentally perfectly matches that expected by simulations. It can be seen that the experimental D values are in good agreement with the theoretical model, the maximum discrepancy being equal to about $\pm$500 ps/(nm·km) for $\lambda = 1550$ nm. It should also be mentioned that the difference between the experimentally and theoretically derived D values could be also due to a non-perfect fabrication process, leading to small variations in the etching depth ($\pm$4% with the employed process) or to non-ideal sidewalls verticality.

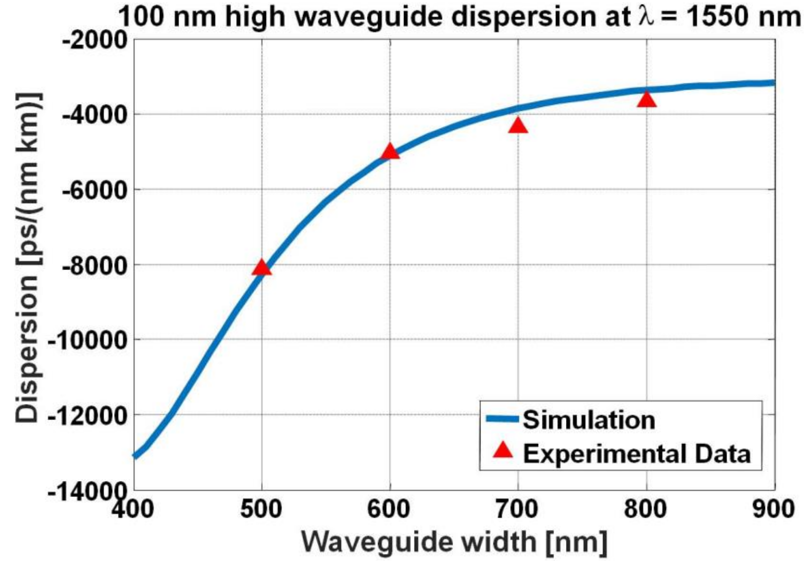

Figure 86: Dispersion at λ = 1550 nm as a function of waveguide width, for 100-nm high waveguides. Red triangles represent experimentally derived D values, whereas the blue trace represents D values obtained from modal simulations [46].

Standard waveguides (500x220 nm) exhibit an anomalous $D \approx 290$ ps/(nm·km), which is in line with the simulated value $D \approx 490$ ps/(nm·km) and with the values previously reported in literature [113]. For what regards the 100 nm high waveguides instead, it can be seen that they show anomalous dispersion. The impact of the waveguide dispersion can be significantly reduced when the waveguide width is increased from 500 to 800 nm, as D varies from $\approx$ -8130 ps/(nm·km) to $\approx$ -3900 ps/(nm·km). The very high anomalous dispersion value D reported for the 800x100 nm waveguides, which is almost ten times bigger than the intrinsic material dispersion (D_{mat} = -830 ps/(nm·km)), meaning that the waveguide dispersion term is the dominating one, suggests that reduced-height SOI waveguides could be effectively employed as platform for implementing low-loss integrated devices for the compensation of the normal dispersion of standard optical fibre networks.

4 Silicon optical resonators for WDM filtering

This chapter will describe the development of a low-loss integrated WDM filter targeting the project FABULOUS specifications. At first, the two most popular choice for implementing Silicon-based wavelength-selective optical components will be described: waveguide Bragg gratings and micro-ring resonators. After that, the design, fabrication and experimental characterization of tunable ring-resonators, implemented using different filter topologies and waveguide geometries, are going to be deeply analyzed. The integrated filter development has been reported in [118, 119], whereas the non-linear measurements carried out on the filters has been reported in [120, 121]. The contribution of the candidate during the PhD activity concerns the experimental characterization of both the 1st and 2nd generation devices, and the optimization of the design of the 2nd generation devices.

4.1 Wavelength-selective Silicon Photonics devices

Wavelength selective optical devices are extremely important components for Silicon Photonics, especially for WDM telecom applications, where high-finesse filters are required in order to extract a single wavelength signal from a grid of closely spaced signals at different wavelengths. Currently, the two most popular approaches for the implementation of a Silicon-based optical filter are waveguide Bragg gratings and micro-ring resonators.

4.1.1 Silicon waveguide Bragg gratings

Waveguide Bragg grating are structures where a periodic modulation of the effective refractive index of the waveguide is obtained along the propagation direction of the guided optical mode, by periodically varying the physical dimensions of the waveguide. The first demonstration of a reflective waveguide Bragg grating integrated in a SOI platform was reported by Murphy et al. [122], where a top surface corrugation with period Λ = 223 nm was performed by a 150 nm deep etch over a 3 µm thick SOI ridge waveguide. Currently instead, the most common approach is to perform a sidewall corrugation, so that a single etch process can be used to define both the waveguide and the corrugation. A simplified top-view schematic of a sidewall corrugated waveguide Bragg grating, where a stepwise index variation is assumed, is shown in Fig.87.

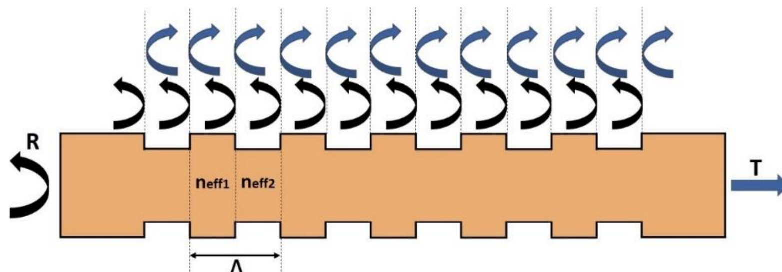

Figure 87: Schematic top-view of Silicon waveguide Bragg grating with sidewall corrugation.

As it can be seen in Fig.87, at each interface between the un-etched portion (characterized by n_{eff1}) and the etched portion (characterized by n_{eff2}) of the Silicon waveguide, part of the travelling light is reflected, while the remaining part is transmitted, with the relative phase of the reflected signal being determined by the grating period Λ and by the optical wavelength λ. As the refractive index is periodically modulated, this results in multiple distributed reflection contributions, which only interfere constructively around the central wavelength (also known as Bragg wavelength), which can be expressed as:

$$\lambda_B = 2\Lambda n_{eff} \tag{39}$$

Where n_{eff} is the average grating refractive index. In practical implementations, the sidewall corrugation is usually obtained as a sinusoidal width profile variation, having uniform period [123], or by using more complex width profiles, such as in [124], where the width variation profile is defined by the superimposition of multiple sinusoidal functions having different periods, so that multiple values of λ_B can be obtained.

One very important parameter to define the Bragg grating properties is the coupling coefficient κ, which can be interpreted as the amount of reflection per unit of length. The κ parameter can be calculated, according to the specific structure, using different techniques, such as Coupled-Mode Theory (CMT), Fresnel equations in the "plane-wave approximation" or FDTD simulations. In the case of a stepwise effective index variation, using the Fresnel equations based approach, the κ coefficient can be expressed as [125]:

$$\kappa = \frac{2\Delta n}{\lambda_B} = \frac{\Delta n}{\Lambda n_{eff}} \tag{40}$$

Where $\Delta n = n_{eff1} - n_{eff2}$. If a sinusoidal effective index variation is instead taken into account, the κ coefficient can be expressed as:

$$\kappa = \frac{\pi \Delta n}{2\lambda_B} = \frac{\pi \Delta n}{4\Lambda n_{eff}} \tag{41}$$

Starting from the κ coefficient, two important parameters which describe the Bragg grating performances can be defined, being the peak power reflectivity R_{peak} at the Bragg wavelength, and the bandwidth $\Delta\lambda$, defined as the bandwidth between the first nulls around the Bragg wavelength. R_{peak} and $\Delta\lambda$ can be respectively expressed as:

$$R_{peak} = tanh^2(\kappa L) \tag{42}$$

$$\Delta\lambda = \frac{\lambda_B^2}{\pi n_g} \sqrt{\kappa^2 + \left(\frac{\pi}{L}\right)^2} \tag{43}$$

Where n_g is the group index and L is the length of the Bragg grating. From Eq.(42) and Eq.(43) it can be seen that relatively long structures (in the order of hundreds of µm) are usually required in order to achieve high peak reflectivity and low bandwidth, thus leading to integrated devices with relatively high foot-print. From Eq.(43) it can also be observed that small values of κ, and therefore according to Eq.(41), small values of corrugation amplitude (which results in a reduced Δn), are required in order to achieve bandwidth $\Delta\lambda$ values smaller than 1 nm, thus suitable for WDM applications with a 100 GHz channel spacing. When employing strip waveguides, the lowest experimentally demonstrated $\Delta\lambda$ bandwidth has been reported to be 0.8 nm [126] by implementing a side-wall corrugation with 10 nm amplitude and using 193-nm DUV Lithography for the fabrication. It is important to remark that such a small geometrical feature is definitely close to the ultimate resolution limit achievable using optical lithography, thus making the final performances of the device extremely sensitive to small fabrication variations in different runs. The same device proposed in [126] for example, yielded a $\Delta\lambda$ bandwidth value of 1.56 nm [44] when being fabricated by the same research group and in the same foundry (IMEC), but in a different fabrication run. In order to achieve low $\Delta\lambda$ bandwidth with bigger corrugation amplitude values (thus relaxing fabrication tolerances), rib waveguides can be used, where the corrugation can be performed both on the rib or on the slab of the waveguide: in [44] for example, a $\Delta\lambda$ value as low as 0.43 nm has been experimentally demonstrated, implementing the Bragg grating on the waveguide slab with a corrugation amplitude of 40 nm. The device layout implemented in [44] in order to collect the reflection from the Bragg grating is shown in Fig.88. Grating couplers are integrated for fibre-coupling, connected to 500 nm wide strip waveguides for optical routing. The waveguide Bragg grating is implemented in a rib waveguide, connected to the strip waveguides by means of double-layer linear tapers, and a Y-branch splitter is used to separate the input signal from the reflected one. It is important to notice that, with the structure proposed in Fig.88, even assuming a theoretically optimized Bragg grating peak power reflectivity $R_{peak} = 1$, the insertion loss between the signals collected at the Transmission port and at the Reflection port will always be > 3 dB, due to the power splitting ratio of the Y-branch coupler.

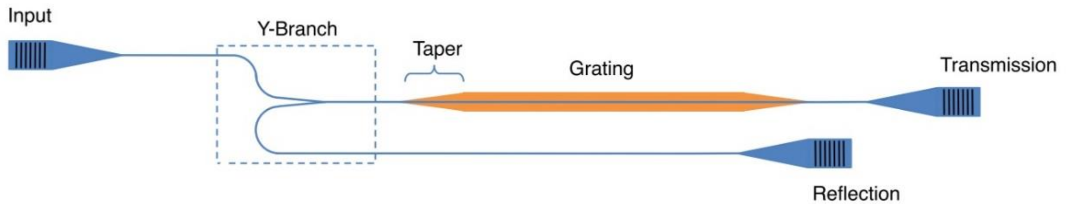

Figure 88: Schematic top-view of the Bragg grating filter proposed in [44].

Another different approach for obtaining very narrow bandwidths is based on the use of phase-shifted waveguide Bragg grating. When a phase-shift is inserted in the middle of a uniform Bragg grating (which, as previously described, is characterized by a transmission stop-band), a cavity is generated, and a very narrow Lorentzian line shape appears in the middle of the transmission stop-band. In [127] for example, using a quarter-wave phase shift, a narrow transmission line of 15 pm was experimentally demonstrated.

4.1.2 Silicon micro-ring resonators

A micro-ring resonator is generally formed by a looped optical waveguide, which can be accessed by a specific coupling mechanism. The simplest implementation of a micro-ring ring resonator is the so-called "all-pass" configuration, where a straight silicon waveguide (usually referred as the "bus" waveguide) is coupled, by means of a directional coupler, to a resonator which can have a circular shape (see Fig.89(a)) or a racetrack shape (see Fig.89(b)). In the first case the resonator is ideally point-coupled to the waveguide, whereas in the second configuration the coupling length of the directional coupler is increased thanks to the straight section of the racetrack.

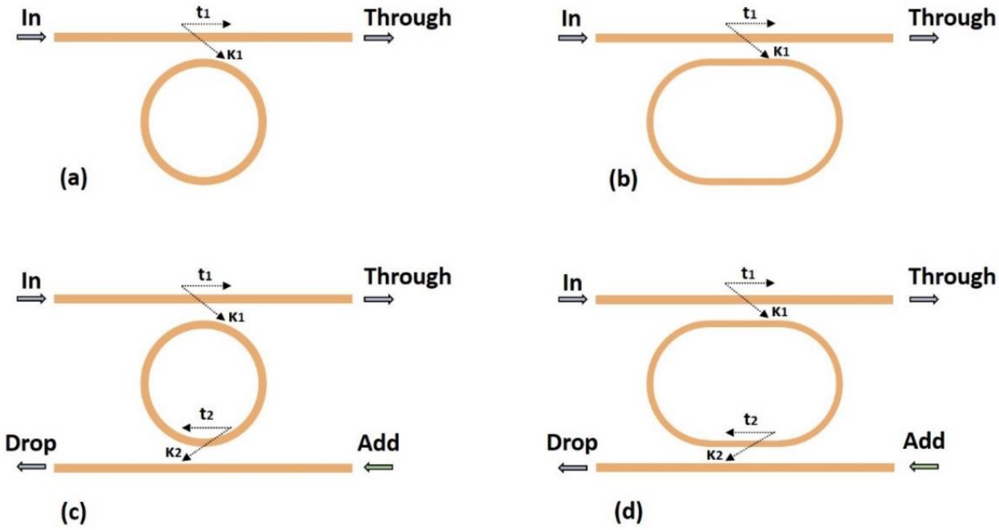

Figure 89: Different configurations of micro-ring resonators. (a) All-pass configuration with ring-shaped resonator. (b) All-pass configuration with racetrack-shaped resonator. (c) Add/drop configuration with ring-shaped resonator. (d) Add-drop configuration with racetrack-shaped resonators. For each directional coupler t represents the straight field-coupling coefficient, while κ represents the cross field-coupling coefficient.

The roundtrip length of the resonator can be defined as:

$$L_{rt} = 2\pi R + 2L_C \tag{44}$$

Where R is the bend radius and L_C is the length of the racetrack straight section. For a ring resonator Eq.(44) can be still applied considering $L_C = 0$. When the phase accumulated by light propagating over a roundtrip length equals an integer times 2π, light in the ring constructively interferes with itself, and the cavity is in resonance. The resonance condition obviously depends upon the wavelength of light in the resonator, so that the resonance wavelengths can be expressed as:

$$\lambda_{res} = \frac{n_{eff} L_{rt}}{m}, \quad m \in N \tag{45}$$

Where n_{eff} is the effective refractive index of the resonator waveguide. If we define the straight and cross field-coupling coefficient of the directional coupler respectively as t_1 and κ_1 ($t_1^2 + k_1^2 = 1$ if we assume a loss-less directional coupler), we can express the ratio of the transmitted and incident field in the bus waveguide of an all-pass configuration, assuming continuous wave (CW) operation, as:

$$\frac{E_{pass}}{E_{in}} = e^{i(\pi+\phi)} \frac{a - t_1 e^{-i\phi}}{1 - t_1 a e^{i\phi}} \tag{46}$$

Where ϕ is the single-pass phase shift, and a is the single-pass field amplitude transmission, which relates to the resonator waveguide propagation loss. ϕ and a can be written as:

$$\phi = \frac{2\pi n_{eff} L_{rt}}{\lambda} \tag{47}$$

$$a = e^{-(\alpha L_{rt})/2} \tag{48}$$

Where α is the power attenuation coefficient. From Eq.(48) it can be seen that a tends to 0 as the propagation losses increase, while it is equal to 1 in a loss-less situation. By squaring Eq.(46) the intensity transmission function $T_{through}$ for the All-pass configuration can be found:

$$T_{through} = \left| \frac{E_{through}}{E_{in}} \right|^2 = \frac{a^2 - 2t_1 a \cos\phi + t_1^2}{1 - 2t_1 a \cos\phi + (t_1 a)^2} \tag{49}$$

For an ideally loss-less situation ($a \approx 1$) the transmission spectrum of the All-pass filter is flat and equal to 1, independently from the optical wavelength λ. If $a \neq 1$ instead, the transmission spectrum shows notches in correspondence of the resonance frequencies λ_{res}; in particular if the coupled optical power is equal to the power lost in the ring ($\kappa^2 = 1 - a^2$, or equally, $t = a$) a condition called "critical coupling" is achieved, and the transmission function drops to zero at resonance. If $t < a$ or $t > a$ instead, the resonator is said to be in an "overcoupling" or "undercoupling" regime respectively.

The spectral properties of the transmission function can be expressed in terms of the full-width at half-maximum (FWHM), which can be expressed, starting from Eq.(49), as:

$$FWHM = \frac{(1-ta)\lambda_{res}^2}{\pi n_g L_{rt}\sqrt{ta}} \tag{50}$$

The free spectral range (FSR) instead, which is defined as the wavelength separation of two consecutive resonances, can be written as:

$$FSR = \frac{\lambda^2}{n_g L_{rt}} \tag{51}$$

As it can be seen from Eq.(50)and Eq.(51) both the FWHM and the FSR depends on the waveguide group index, and are therefore strongly dependent from the resonator waveguide dispersion.

Other two parameters which can be derived from Eq.(50) and Eq.(51) in order to describe the resonator performances are the finesse and the quality factor (Q-factor). The finesse describes the sharpness of the resonances relatively to their wavelength spacing (see Eq.(52)), whereas the Q-factor describes the sharpness of the resonances relatively to their resonant wavelength value (see Eq.(53)).

$$Finesse = \frac{FSR}{FWHM} \tag{52}$$

$$Qfactor = \frac{\lambda_{res}}{FWHM} \tag{53}$$

From a physical point of view, the finesse and the Q-factor can be respectively interpreted as the numbers of round-trips completed by light travelling into the resonator and the number of completed oscillations of the optical field, before the circulating energy drops to $1/e$ of its initial value. By substituting the expressions λ_{res}, *FSR* and *FWHM* in Eq.(52) and Eq.(53), the definition of the finesse and the Q-factor can be specialized to the case of an all-pass resonator as:

$$Finesse = \frac{\pi\sqrt{ta}}{1-ta} \tag{54}$$

$$Qfactor = \frac{\pi n_g L_{rt}\sqrt{ta}}{\lambda_{res}(1-ta)} \tag{55}$$

A second different configuration is the so-called add/drop configuration, where the looped waveguide, which can be again implemented both with a ring shape (see

Fig.89(c)) or with a racetrack shape (see Fig.89(d)), is coupled to two separate bus waveguides, so that the resonating optical signal can be partially transmitted to the drop port. This micro-ring resonator configuration is particularly useful in WDM applications, as it allows a single channel to be separated and collected at the drop port, whereas all the remaining channels can be collected at the through port without being affected by the resonator. Moreover, if a signal at the resonant wavelength is injected from the add port, it can be coupled to the input bus waveguide and collected at the through port, thus being "added" to the input WDM signal.

The same equations used to define L_{rt}, ϕ, a and the FSR in the case of an all-pass configuration, can still be applied to the case of an add/drop configuration. For what regards the intensity transmission function, two different functions must be used for the through port and the drop port, which can be expressed, assuming again CW operation, as:

$$T_{through} = \left|\frac{E_{through}}{E_{in}}\right|^2 = \frac{t_2^2 a^2 - 2t_1 t_2 a \cos\phi + t_1^2}{1 - 2t_1 t_2 a \cos\phi + (t_1 t_2 a)^2} \tag{56}$$

$$T_{drop} = \left|\frac{E_{drop}}{E_{in}}\right|^2 = \frac{(1-t_1^2)(1-t_2^2)a}{1 - 2t_1 t_2 a \cos\phi + (t_1 t_2 a)^2} \tag{57}$$

Where t_1 and t_2 are the straight field-coupling coefficients for the input and output directional coupler respectively. The FWHM, the finesse and the Q-factor can also be defined for the add/drop configuration, and they can be written as:

$$FWHM = \frac{(1 - t_1 t_2 a)\lambda_{res}^2}{\pi n_g L_{rt}\sqrt{t_1 t_2 a}} \tag{58}$$

$$Finesse = \frac{\pi\sqrt{t_1 t_2 a}}{1 - t_1 t_2 a} \tag{59}$$

$$Qfactor = \frac{\pi n_g L_{rt}\sqrt{t_1 t_2 a}}{\lambda_{res}(1 - t_1 t_2 a)} \tag{60}$$

4.2 Design of Si-integrated filters for project Fabulous

As previously described in Chapter 1, in the Silicon-based ONU structure for the project FABULOUS, a pair of WDM filters was required in order to select the proper CW seed to be sent to the reflective Mach-Zehnder modulator for the generation of the Upstream data-flow. The implemented WDM filters also had to be tunable, in

order to allow the ONU to dynamically change the wavelength of operation according to the network requirements.

4.2.1 WDM filters requirements

The main project requirements for the WDM filters are reported in Tab.7.

WDM Filters Requirements	
Parameter	**Value**
Operation band	1530 - 1570 nm
Channel spacing	100 GHz
Filter bandwidth @ -20 dB	$<$ 100 GHz
Filter bandwidth @ -3 dB	$>$ 40 GHz
Insertion loss	$<$ 1 dB
Spectral uniformity of insertion loss	$<$ 1 dB
Suppression of adjacent channels	$>$ 30 dB
Suppression of non-adjacent channels	$>$ 40 dB
In-band amplitude ripple	$<$ 0.5 dB

Table 7: Project FABULOUS specifications for the integrated WDM filters.

In summary, the target was to design a filter able to select any wavelength among a grid of 16 wavelengths with a 100 GHz spacing (corresponding to 0.8 nm at the central $\lambda = 1550$ nm). This would require a tuning range of approximately 12.8 nm, obviously implying a filter FSR $\geq$ 12.8 nm. As the upstream signal was expected to be at relatively low-bit-rate, a filter bandwidth @ -3 dB of 40 GHz has been considered.

Due to the very stringent bandwidth requirement, we decided to implement the WDM filters using an add/drop ring-resonator based approach. A few critical aspects however, had to be taken into account both in the design stage and in the experimental characterization, in order to remove possible signal-distortion sources and limiting effects. The main issues were:

i. Insertion losses and adjacent channel suppression.
ii. Back-reflections from the integrated filters.
iii. Non-linear effects occurring in the filter resonant cavity.

The insertion loss is defined as the loss provided by the filter between the output of the through port and the drop port. Providing a very low insertion loss ($<$ 1dB) for the filtered channel is an essential requirement for the WDM filter. However, from a design point of view, this parameter is quite difficult to be properly evaluated using numerical simulation tools, as it is mainly related to fabrication-dependent waveguide roughness (as already pointed out in Chapter 3). One possible way to reduce the filter insertion loss is by increasing the coupling coefficient κ between the bus waveguide

and the resonator (thus lowering t), even if this comes at the expense of the out-of-band extinction. It is anyway worth underlining that, as the ONU structure envisaged the implementation of two filters on each chip (see Fig.10), the extinction requirement on adjacent channels could be made less severe in order to reduce filter insertion losses.

Back-reflections from the integrated filter are instead due to a counter-directional coupling effect [47], which is originated by the effective refractive index change experience by the radiation propagating in the coupling region, and by small perturbations of the waveguide cross-section. This effect can cause a partial power transfer from the forward-propagating beam to an undesired counter-propagating beam that travels back to the input port, thus leading to additional losses. This unwanted back-reflections could be particularly detrimental in the FABULOUS ONU structure, as they might affect the operation of the integrated SOAs (see Fig.10). Such an effect can be reduced by increasing the bus-resonator coupling coefficient, even if this solution obviously modifies the filter spectral response.

For what regards the non-linear effects, it is important to keep mind that the enhancement of the signal beam intensity inside the resonant cavity can cause a significant increase of the efficiency of the non-linear processes. As previously described in Chapter 1, Silicon exhibits a very large $\chi^{(3)}$, so that phenomena like SPM and TPA can take place in the resonator. SPM could cause a non-negligible signal spectral broadening and a modulation of the signal phases, thus affecting the filter response, whereas TPA could induce additional non-linear losses and small distortions of the signal temporal shape. Moreover the free carriers generated by TPA might also cause free-carriers effects such as free-carrier absorption (FCA, see Eq.(2)) and free-carrier dispersion (FCD, see Eq.(3)), thus leading to possible inter-symbol interference effects, as the absorption and the dispersion experienced by each pulse could be influenced by the previously transmitted bit patter.

4.2.2 Waveguide geometries and resonator topologies

As one of the main concerns in the filter realization was to reduce the device losses, the first design step was the identification of a waveguide-design able to reduce the propagation losses, which, as deeply discussed in Chapter 3, are mainly due to the lateral surface roughness produced in the etching process. In order to reduce losses, which are generally close to 3 dB/cm in standard SOI waveguides with a typical 500×220 nm cross-section, it is necessary to reduce the interaction between the optical radiation and the waveguide surface. This result could be achieved by employing two different approaches, either by using rib waveguides, where the mode is pushed deeper in the substrate, or by using high aspect ratio (width/height>5) strip waveguides where a reduced waveguide height yields a smaller interaction with the lateral surface.

According to the filter requirements, the FSR should exceed 12 nm, suggesting that the micro-resonators radius should be definitely smaller than 10 µm. Such a small value

automatically prevented the possibility to employ rib waveguides for the filters implementation, as their low lateral confinement would lead to very high curvature losses. For this reason, we decided to use only strip waveguides in the design stage, both with standard cross-section (500x220 nm) and with reduced height and high aspect ratio (800x100 nm).

For what regards the implemented cavity topology, we decided to implement both ring-based and racetrack-based resonators. The two different topologies, are reported in Fig.90, where all the important geometrical parameters are highlighted.

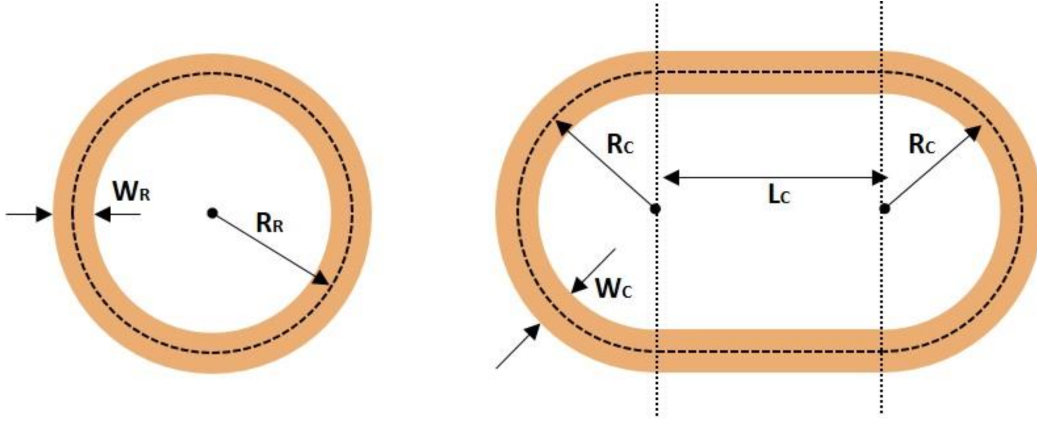

Figure 90: Schematic representation of the implemented resonators topologies. For the ring configuration, W_R and R_R respectively represent the width and the radius of the looped waveguide. For the racetrack configuration W_C is the width of the waveguide, R_C is the radius of the curved section, and L_C is the length of the straight coupling section.

By substituting the expressions of the round-trip length of the ring and racetrack in Eq.(51), the following expressions can be obtained for the FSR, for the ring and racetrack case respectively:

$$FSR_{ring} = \frac{c}{n_g \cdot 2\pi R_R} \quad (61)$$

$$FSR_{racetrack} = \frac{c}{n_g \cdot 2(\pi R_C + L_C)} \quad (62)$$

We set the FSR to be the same for the two configurations, so that a simple equation could be find in order to relate R_R and R_C to the length L_C of the racetrack coupling region:

$$L_C = \pi(R_R - R_C) \quad (63)$$

The group index value n_g for the FSR calculation in Eq.(61) and Eq.(62) was, for simplicity, assumed to be that of a standard SOI waveguide having a 500x220 nm cross-section, independently from the waveguide geometry effectively implemented in

the filter. This was obviously just a design simplification, as the group index of reduced-height waveguide is smaller than that of standard ones (see Fig.83 and Fig.84), which however did not imply any deterioration of the performances of the filters effectively implemented using 100-nm high waveguides. In fact, a group index reduction, just results in effective FSR bigger than the nominal, thus also relaxing the filter FSR specifications.

Comparing the two structures, it is clear that the racetrack resonator can provide a larger coupling with the bus waveguide, as the coupling length L_C can be increased while keeping constant the FSR. On the other hand, if L_C is increased, R_C must be reduced (and R_C is in any case lower than the corresponding R_R), and this may lead to an increase of the round-trip propagation losses. Additionally, in the racetrack configuration there is a mismatch between the optical mode in the straight and curved part, which is experienced four times in each round-trip. This yields an increase of the resonator losses and also an increase of the counter-propagating radiation component, which, as previously discussed, may cause significant problems in the Reflective-Mach Zehnder device operation.

4.2.3 Evaluation of the coupling coefficients

The first step performed to design the WDM filters was to evaluate the coupling coefficients κ required in order to satisfy the project spectral requirements. If we write the drop port transmission function (Eq.(57)) of an add/drop micro-ring resonator (see Fig.91), as a function of the cross-coupling coefficients κ_1 and κ_2, the following expression is obtained:

$$T_{drop} = \left|\frac{E_{drop}}{E_{in}}\right|^2 = \frac{\kappa_1^2\kappa_2^2}{1-2\sqrt{1-\kappa_1^2}\,\sqrt{1-\kappa_2^2}\;a\,cos\,\phi+(1-\kappa_1^2)(1-\kappa_2^2)a^2} \tag{64}$$

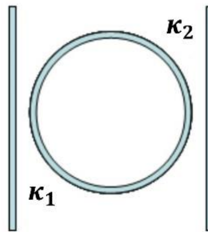

Figure 91: Basic structure of a single-resonator add/drop filter. κ_1 and κ_2 are the bus-resonator field-coupling coefficients.

Eq.(64) has been derived assuming lossless directional couplers ($\kappa^2 + t^2 = 1$) and can be applied both to ring or racetrack configurations. Using Eq.(64) it can be seen, as it is reported in Fig.92, that by simply varying the κ coefficients it is not possible to satisfy the bandwidth requirements, even considering a perfectly lossless device (a

= 1). For very low κ values in fact, the resulting 3-dB BW is too small, while, increasing κ, the 30-dB bandwidth becomes too large to satisfy the filter specifications.

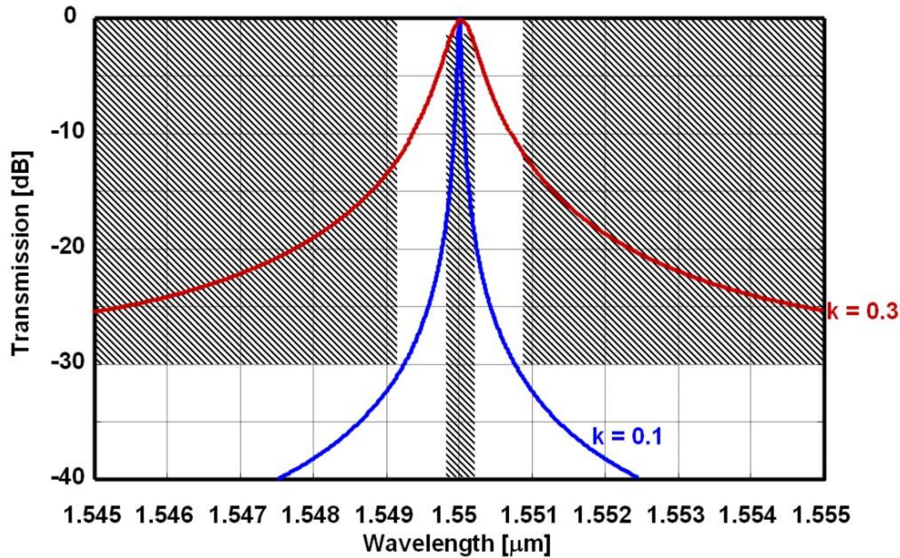

Figure 92: Single-ring filter transfer function (drop port) for two different κ values. In order to fulfill the requirements, the filter transfer function should not overlap with the grey areas.

In order to obtain a suitable transfer function, we therefore decided to exploit filters composed by more than a single resonator, obtained by cascading several ring-resonators with proper coupling coefficients. Using multiple resonators allows to obtain a transfer function shape closer to the ideal “flat top, vertical edges” shape, even if, on the other side, it can also lead to increased optical attenuation. For these reasons we decided to keep the number of cascaded elements as low as possible, and studied the transmission function properties of filters composed by 2 and 3 resonators.

A schematic representation of a 2-rings filter is given in Fig.93, where κ_1 and κ_3 are the bus-ring field-coupling coefficients, and κ_2 is the ring-ring field-coupling coefficient.

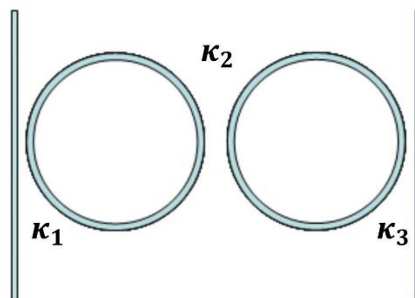

Figure 93: Basic structure of a double-resonator add/drop filter. κ_1 and κ_3 are the bus-resonator field-coupling coefficients, while κ_2 is the resonator-resonator field-coupling coefficient.

When two cascaded resonators are considered, the drop port transfer function can be expressed as:

$$T_{drop} = \left| \frac{-i\kappa_1\kappa_2\kappa_3\sqrt{F_1F_2}}{1 - t_1t_2F_1 - t_2t_3F_2 + t_1t_3F_1F_2} \right|^2 \tag{65}$$

Where the directional couplers are once again assumed to be lossless, so that:

$$t_j = \sqrt{1-\kappa_j^2} \qquad j = 1,2,3. \tag{66}$$

And the F_m parameters are used to take into account the single-pass attenuation and the single-pass phase shift in each resonator, according to:

$$F_m = a_m e^{-i\left(\frac{2\pi n_{eff} L_{rt,m}}{\lambda}\right)} \qquad m = 1,2. \tag{67}$$

Using the same approach previously described for the single-ring resonator, we varied the κ coefficients (assuming an ideal loss-less situation, $a = 1$) in order to find a suitable transfer function. In particular, setting $\kappa_1 = \kappa_3 = 0.26$ (κ_1 and κ_3 must be equal in order to obtain a symmetric filter response) and $\kappa_2 = 0.05$, the transfer function reported in Fig.94 was obtained.

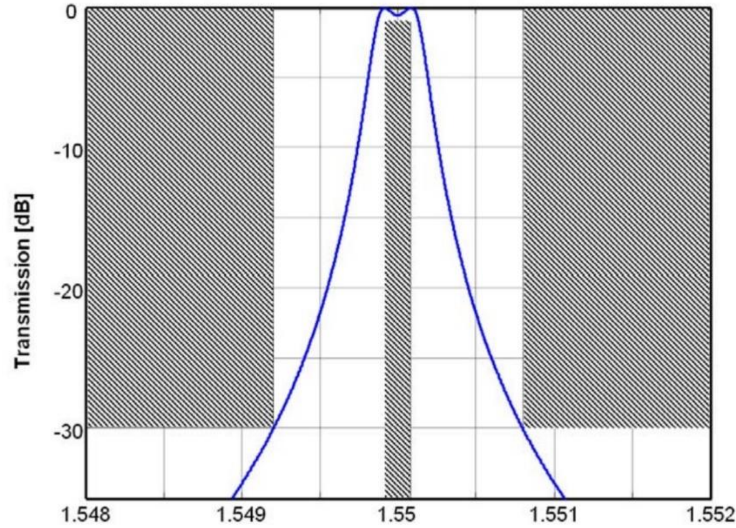

Figure 94: Double-ring filter transfer function (drop port). The filter requirements are satisfied, but with limited margin.

As it can be seen from Fig.94, the obtained double-ring filter transfer function allows to satisfy the filter requirements, but with minimal margins with respect to the required specifications. In order to further improve the spectral properties of the filter, we therefore decided to analyze the case of 3 cascaded resonators, as shown in Fig.95.

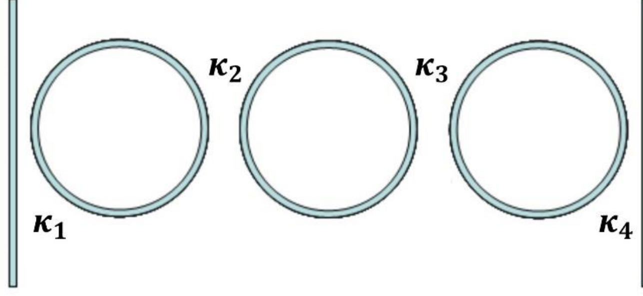

Figure 95: Basic structure of a triple-resonator add/drop filter. κ_1 and κ_4 are the bus-resonator field-coupling coefficients, while κ_2 and κ_3 are the resonator-resonator field-coupling coefficients.

For the case of a triple-resonator filer, the drop transmission function can be expressed as:

$$T_{drop} = \left| \frac{-i\kappa_1\kappa_2\kappa_3\kappa_4\sqrt{F_1F_2F_3}}{1 - t_1t_2F_1 - t_2t_3F_2 - t_3t_4F_3 - t_1t_4F_1F_2F_3 + t_1t_3F_1F_2 + t_2t_4F_2F_3 + t_1t_2t_3t_4F_1F_3} \right|^2 \quad (68)$$

Where t_j and F_m can again be expressed according to Eq.(66) and Eq.(67). We then performed again a sweep of the coupling coefficients κ, and obtained the drop port transfer function reported in Fig.96 for $\kappa_1 = \kappa_4 = 0.35$, and $\kappa_2 = \kappa_3 = 0.07$ (κ_1 and κ_4, as well as κ_2 and κ_3, must again be respectively equal to each other to achieve a symmetric spectrum).

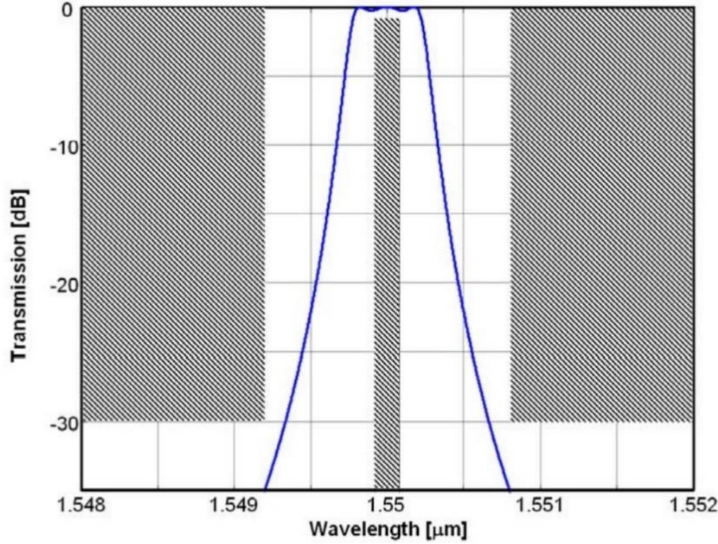

Figure 96: Triple-ring filter transfer function (drop port). The filter requirements are fully satisfied.

The previous analysis was carried out assuming a perfectly lossless device ($a = 1$). In order to take into account the impact of the expected waveguide propagation losses (≈ 3 dB/cm) we performed an additional sweep of the κ coefficients in Eq.(65) and in

Eq.(68) including the round-trip loss term. The obtained best κ values, which differ only slightly from the ones calculated in a lossless approximation, are reported in Tab.8

Optimal κ coefficients		Without losses	With losses
2 Resonators	κ_1, κ_3	0.260	0.280
	κ_2	0.050	0.050
3 resonators	κ_1, κ_4	0.350	0.400
	κ_2, κ_3	0.070	0.085

Table 8: Optimal coupling coefficients κ required to satisfy the filter bandwidth specifications, calculated for double and triple resonator configuration, assuming an ideally lossless device or a waveguide propagation loss $\approx$ 3 dB/cm.

4.2.4 Coupling coefficients for ring structures

After evaluating the coupling coefficient values required to meet the bandwidth specifications in each of the filter topology described in the previous paragraph, we then had to determine the optimal waveguide height to implement. One hand we considered standard waveguides with 220 nm height, to match the standard SOITEC Si layer thickness on the wafer, while, on the other hand, we considered waveguides with reduced height (100 nm). The first parameter under analysis was the coupling coefficient between the bus waveguide (whose width was fixed at 500 nm to allow easy integration in the R-MZ device in the ONU) and a micro-ring having radius equal to 6 µm (to respect the FSR requirement).

In Fig.97 the bus-ring power-coupling coefficient (i.e. κ^2) is reported as a function of the width of the ring waveguide, considering a bus-to-ring fixed gap of 200 nm, which corresponds to the minimum value suitable for fabrication. All the values were calculated using 3D-FDTD simulation software (*FDTD Solutions*^{TM} by *Lumerical Solutions Inc.*).

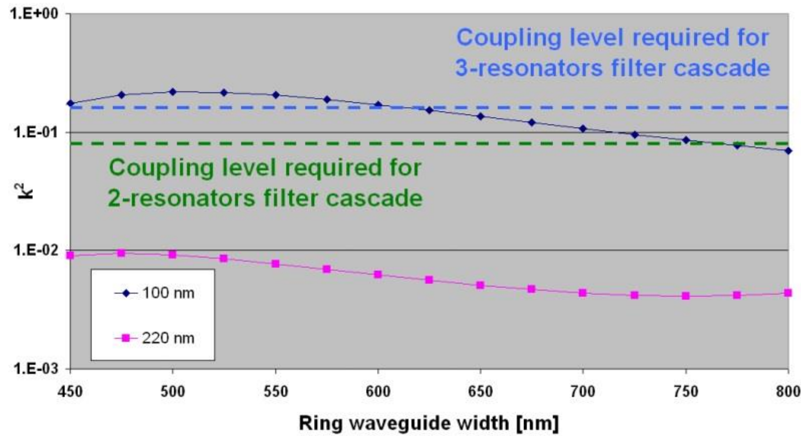

Figure 97: 3D-FDTD simulations of the power coupling coefficient (κ^2) between the bus waveguide and the ring, as a function of the ring width, in a straight-coupling configuration, assuming a fixed gap of 200 nm. κ^2 values are reported in logarithmic scale.

From Fig.97 it can be clearly seen that the use of 220 nm high waveguides does not allow to achieve a sufficient coupling between the bus and ring waveguides. In order to overcome this issue, we also considered the possibility to implement directional coupler with curved coupling regions, as shown in Fig.98(right) in order to increase the effective coupling length. In particular, we considered a 90° constant-gap coupling region, with two constant-radius 45°curves to connect the straight bus waveguide to the 90°-coupling region.

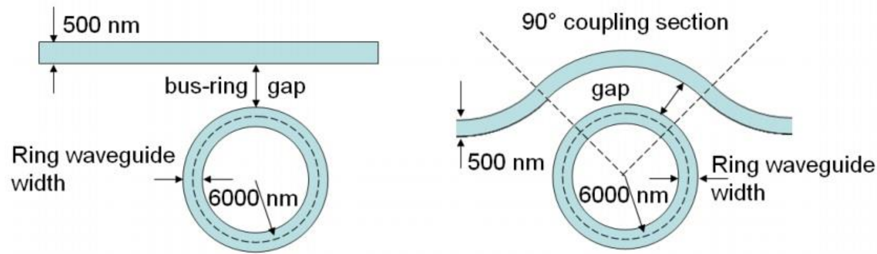

Figure 98: (left) Straight bus-ring coupling region. (right) Curved bus-ring coupling region. In both situations the analysis has been carried out considering a fixed gap of 200 nm (minimum value suitable for fabrication) and a fixed bus-waveguide width of 500nm.

Even adopting a curved-coupling scheme, the 220 nm high waveguide for the ring resonator cannot provide the required values of power-coupling coefficients, as shown in Fig.99.

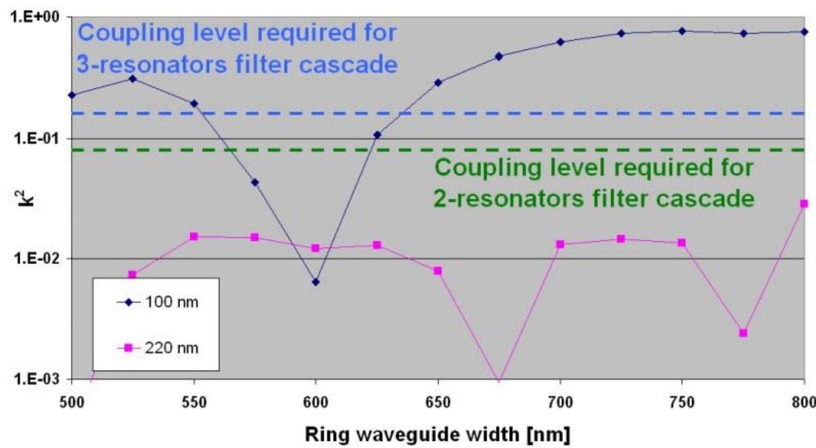

Figure 99: 3D-FDTD simulations of the power coupling coefficient (κ^2) between the bus waveguide and the ring, as a function of the ring width, in a curved-coupling configuration, assuming a fixed gap of 200 nm. κ^2 values are reported in logarithmic scale.

Considering the power-coupling curve reported in Fig.99 for 100 nm high waveguides, which is strongly non-monotonic, it is interesting to notice that the exploitation of the same width for the bus-waveguide and the ring-waveguide does not result in reaching the maximum coupling. Also, if the waveguide width is larger than 700 nm, the power-

coupling coefficient turns out to be almost independent from the waveguide width. The latter consideration suggests that the use of a curved-coupling region could be an interesting solution to increase the design tolerances when using reduced-height waveguides.

Based on this analysis we decided to implement ring-based resonators with both straight and curved coupling regions, but only considering the 100 nm high waveguides. Standard 220 nm high waveguide were instead employed for designing cascaded resonators based on a racetrack configuration, as it will be described in the next paragraph.

As a last step, we performed 3D-FDTD simulations of the power-coupling coefficient from bus-to-ring, and from ring-to-ring, as a function of both the ring waveguide width and the gap between the bus and the ring (or the gap between the cascaded rings). This was done in order to assess the optimal pair of parameters which allows to achieve the required value of κ^2 while keeping the best tolerance to gap width variations, which can be caused by imperfections in the fabrication process. We first started with the bus-ring coupling coefficient, as it is significantly larger than that required for the ring-ring coupling. The obtained results, in the case of a straight coupling section, are reported in Fig.100.

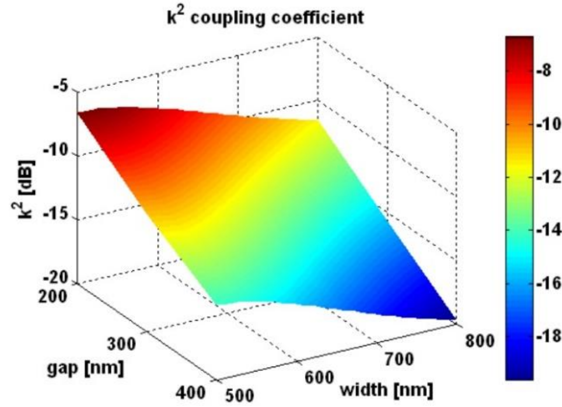

Figure 100: κ^2 surface as a function of the ring waveguide width and the bus-ring gap, when a straight coupling region is used. κ^2 values are expressed in dB.

Starting from the κ^2 surface of Fig.100, the graphs reported in Fig.101 can be derived, the left one referring to the double-ring configuration, and the right one referring to the triple-ring configuration. In each graph the green line corresponds to the gap/width combinations yielding the desired coupling, while the brown and blue lines identify the boundaries of the area where the coupling coefficient is equal to the desired value within a 0.5 dB tolerance. In order to maximize the design tolerance to small variations in the fabricated structure, we decide to use ring resonators based on waveguides with 525-nm width. As highlighted in Fig.101, this waveguide width allows to optimize the filter tolerance, and the corresponding gap between the bus waveguide and the resonator is quite large (and hence "less critical"). In particular, the bus-ring

gaps required to achieve the desired coupling coefficient were found to be respectively equal to 310 nm for the double-ring configuration, and 230 nm for the triple-ring configuration.

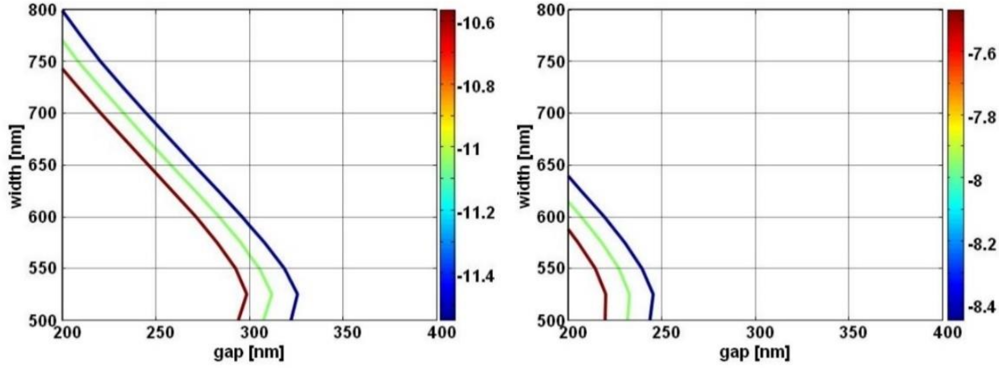

Figure 101: The green line corresponds to the gap/width combinations yielding the ideal coupling coefficient, while the region between the brown and the blue line corresponds to the gap/width combinations yielding the ideal coupling coefficient ±0.5 dB when using a straight-coupling section. Results are reported for the double-ring configuration (left) and for the triple-ring configuration (right).

We then performed the same FDTD simulations in the case of the 90°-curved constant-gap coupling region obtaining, as a result, the κ^2 surface shown in Fig.102.

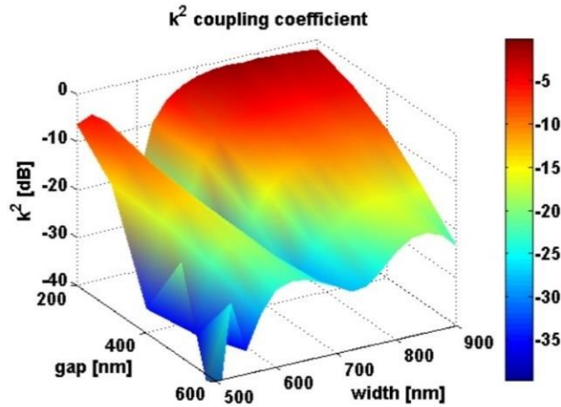

Figure 102: κ^2 surface as a function of the ring waveguide width and the bus-ring gap, when a curved coupling region is used. κ^2 values are expressed in dB.

The corresponding graphs showing the gap/width regions yielding a suitable coupling are reported in Fig.103. In this case a large “tolerance region” was obtained considering an 825-nm wide waveguide, corresponding to a bus-ring gap of 410 nm for the double-ring configuration, and of 355 nm for the triple-ring configuration. The “tolerance region” in this graph may appear smaller than the one obtained for the straight-coupling situation (see Fig.101), but it must be underlined that the two charts have different scales. Moreover, examining Fig.103, it can be noticed that a second

slightly bigger “tolerance region” could be identified for a waveguide width of 550 nm, corresponding to a bus-ring gap of 340 nm in the case of double-ring resonators, and of 260 nm in the case of triple-ring resonators. We however chose to implement ring waveguides with 825 nm width, for two main reason:

i. The corresponding optimal gap values are larger than that corresponding to a waveguide width of 550 nm, thus being less critical.
ii. Choosing an 825 nm width for the resonator waveguide also allows to improve the tolerance for the ring-to-ring coupling coefficient, as it will be explained next.

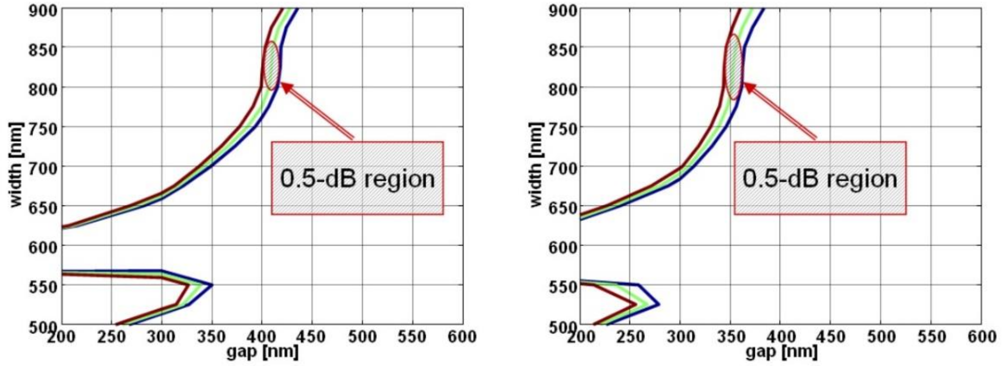

Figure 103: The green line corresponds to the gap/width combinations yielding the ideal coupling coefficient, while the region between the brown and the blue line corresponds to the gap/width combinations yielding the ideal coupling coefficient ±0.5 dB when using a curved-coupling section. Results are reported for the double-ring configuration (left) and for the triple-ring configuration (right). The red ovals show the tolerance-regions chosen for the filters design.

The last set of 3D-FDTD simulations was carried out in order to evaluate the ring-to-ring power-coupling coefficient. The resulting κ^2 surface is reported in Fig.104.

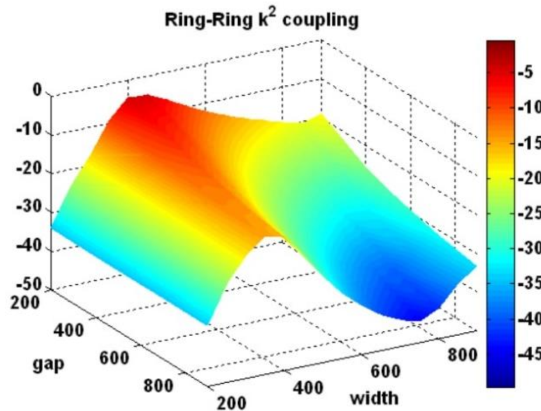

Figure 104: κ^2 surface as a function of the ring waveguide width and the ring-to-ring gap. κ^2 values are expressed in dB.

From Fig.104 the graphs of Fig.105 can be again obtained for the case of double-ring and triple-ring resonators.

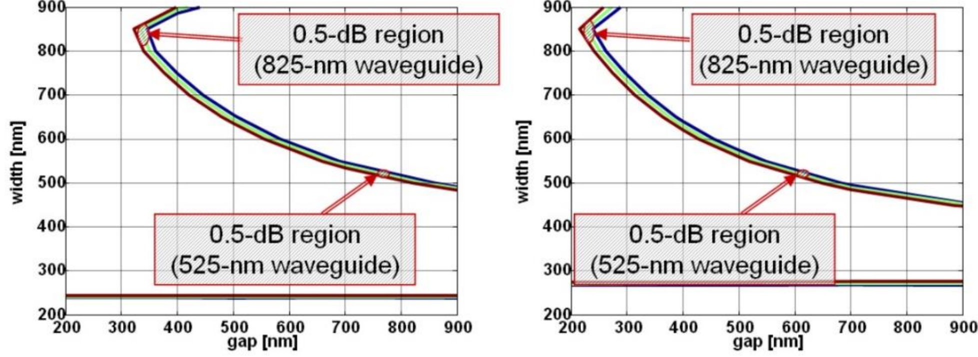

Figure 105: The green line corresponds to the gap/width combinations yielding the ideal coupling coefficient, while the region between the brown and the blue line corresponds to the gap/width combinations yielding the ideal coupling coefficient ±0.5 dB for the ring-to-ring coupling. Results are reported for the double-ring configuration (left) and for the triple-ring configuration (right). The red ovals show the tolerance-regions chosen for the filters design.

In this situation the waveguide width values have already been fixed previously, when optimizing the tolerance of the bus-ring couplers, so that the optimal gap values can be automatically obtained, being respectively equal to 755 nm and 600 nm for the double-ring configuration and the triple-ring configuration when employing a 525 nm wide ring waveguide, and to 340 nm and 240 nm for the double-ring configuration and the triple-ring configuration when employing a 825 nm wide ring waveguide. It can be noticed that the "tolerance region" is much wider when larger waveguides are used, for both the 2-ring and the 3-ring configuration (thus corroborating the previous choice of using 825 nm wide waveguides, when optimizing the curved-coupling bus-to-ring coefficient). This result suggested that the structures realized using curved bus-ring coupling-regions and larger waveguides should show a greater tolerance to possible deviation of the nominal dimension that could arise during the fabrication process.

4.2.5 Coupling coefficients for racetrack structures

As pointed out in the previous paragraph, standard 500x220 nm waveguides does not allow to achieve the required values of coupling coefficient when used in ring resonator configurations. We therefore decided to implement the standard waveguides in racetrack resonator configurations, as, by, adjusting the length L_C of the racetrack straight portion (see Fig.90), the required values of κ^2 can be obtained. For the race-track-based filter design we followed a procedure similar to the one used for the ring resonators, but with two main differences:

i. All the waveguides (both for the bus and the resonators) were to set to have a 500×220 nm cross-section.

ii. The bus-racetrack gap was set to the value of 200 nm (the minimum value suitable for fabrication), while the value of L_C yielding the correct coupling coefficient was derived, as a consequence, by means of numerical simulations.

The first step that we therefore carried out was to perform 2D-FDTD simulation of the bus-to-racetrack power-coupling coefficient as a function of the bend radius R_C. It must be recalled that we assumed the filter FSR to be fixed, thus implying that $R_C + L_C$ must always remain constant. This means that any reduction of the radius R_C results in an increase of L_C. Simulations results are reported in Fig.106.

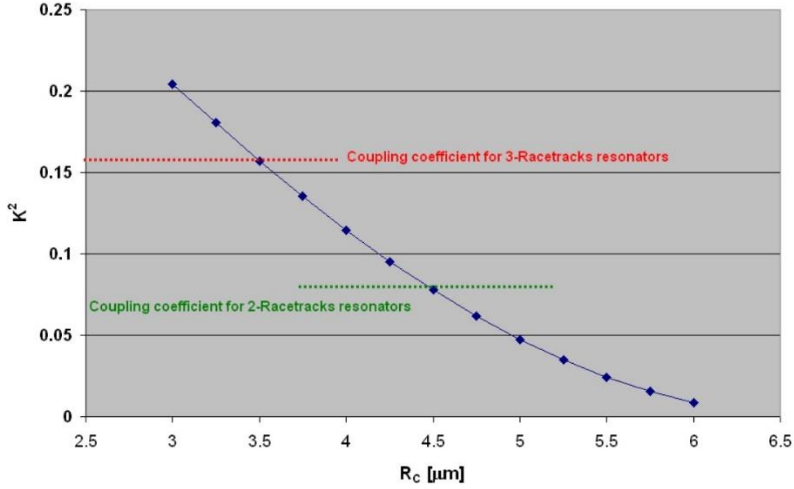

Figure 106: 3D-FDTD simulation results of the bus-to-racetrack power coupling coefficient as a function of the bend radius R_C. A fixed 200 nm bus-racetrack gap was considered.

From Fig.106 it can be seen that for racetrack resonators, different values of R_C had to be employed when considering a double-racetrack configuration or a triple-racetrack configuration, where the optimal values were found to be respectively equal to 4490 nm and 3465 nm. We point out that another possibility would have been that of taking R_C = 3465 nm for both configurations and then increase the bus-racetrack gap, for the double-racetrack filter, to reduce the coupling coefficient till the correct value was achieved. We anyway did not adopt this strategy, as the use of a smaller R_C (3465 nm instead of 4490 nm) might, in principle, increase filter losses.

We then carried out simulations in order to define the dependence of the racetrack-to-racetrack power-coupling coefficient as a function of the gap in-between them. As two different R_C values were obtained from the previous analysis in the case of double or triple-resonator, it is evident that two different coupling-vs-gap curves were required for a proper design of the filters. For the double-resonator filter, simulation results are reported in Fig.107, which shows that the correct coupling condition is achieved when the racetracks separation is equal to 415 nm. From Fig.108 instead, it can be seen that, in the case of a triple-resonator filter, the optimal racetrack separation was found to be 400 nm.

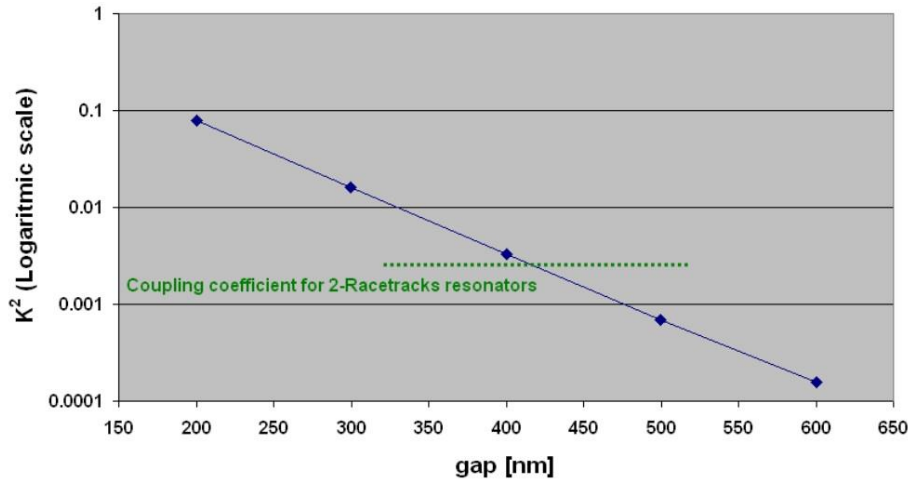

Figure 107: 2D-FDTD simulation result of the racetrack-to-racetrack power-coupling coefficient κ^2 as a function of the racetrack-to-racetrack gap, considering a double-racetrack structure with R_C fixed to 4490 nm.

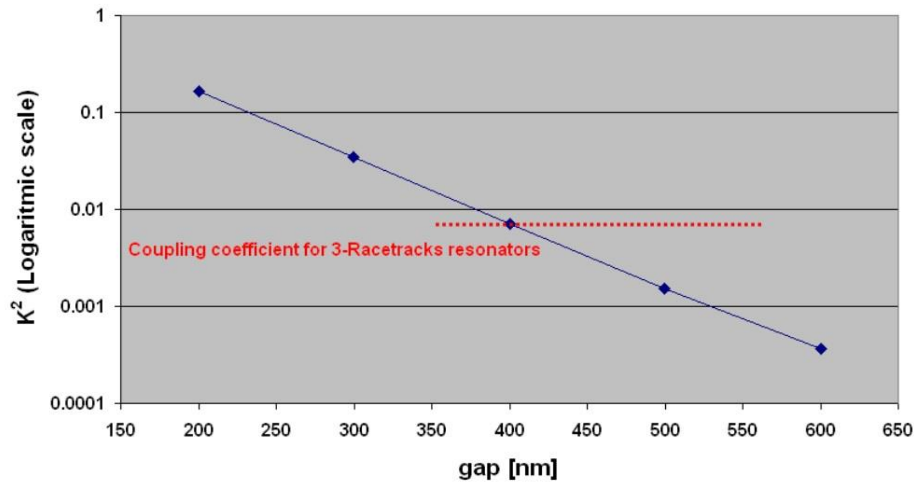

Figure 108: 2D-FDTD simulation result of the racetrack-to-racetrack power-coupling coefficient κ^2 as a function of the racetrack-to-racetrack gap, considering a triple-racetrack structure with R_C fixed to 3465 nm.

4.2.6 Final configurations selected for the first fabrication

As a result of the design activity reported in the previous two paragraphs, the following final configurations were identified for fabrication. The ring resonator configurations with straight coupling sections are showed in Fig.109, the ring resonator configurations with curved coupling sections are showed in Fig.110, while the racetrack configurations implemented using standard waveguides are shown in Fig.111.

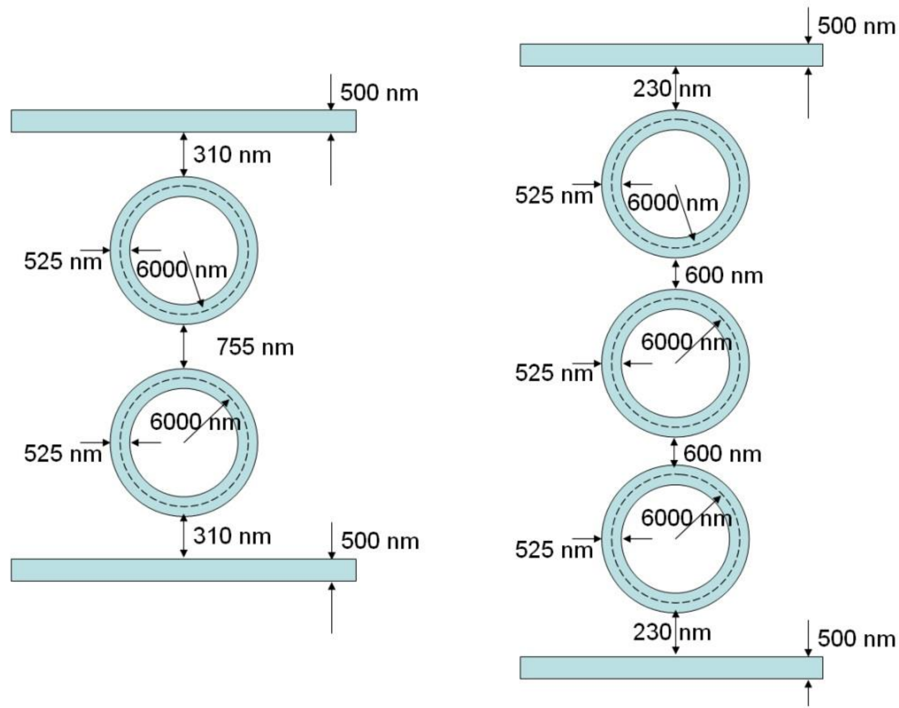

Figure 109: Schematic of the double-ring and triple-ring configurations proposed for the realization of the optical filter exploiting straight coupling and 100-nm high optical waveguides.

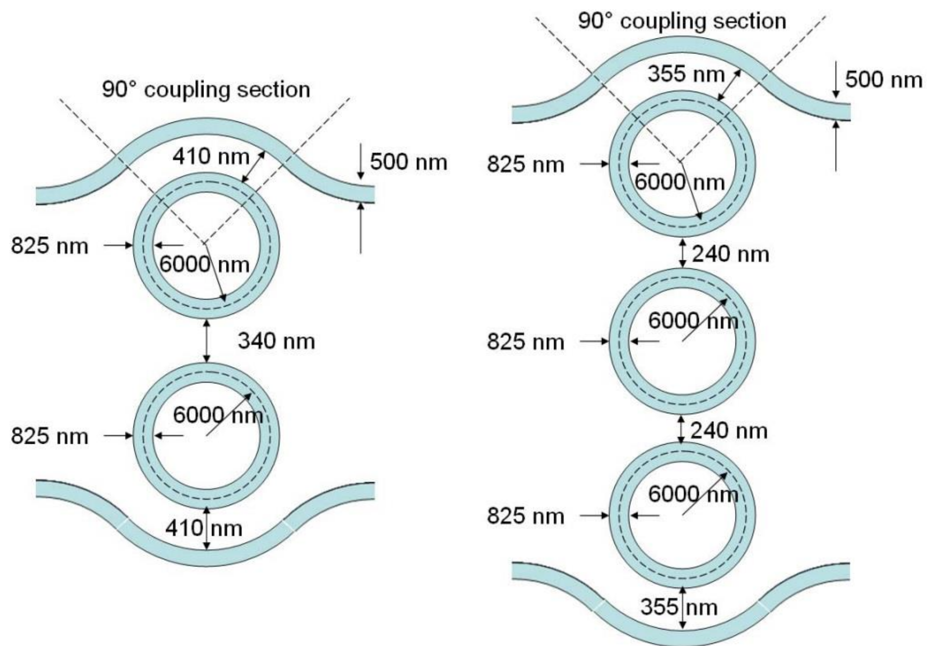

Figure 110: Schematic of the double-ring and triple-ring configurations proposed for the realization of the optical filter exploiting curved coupling and 100-nm high optical waveguides.

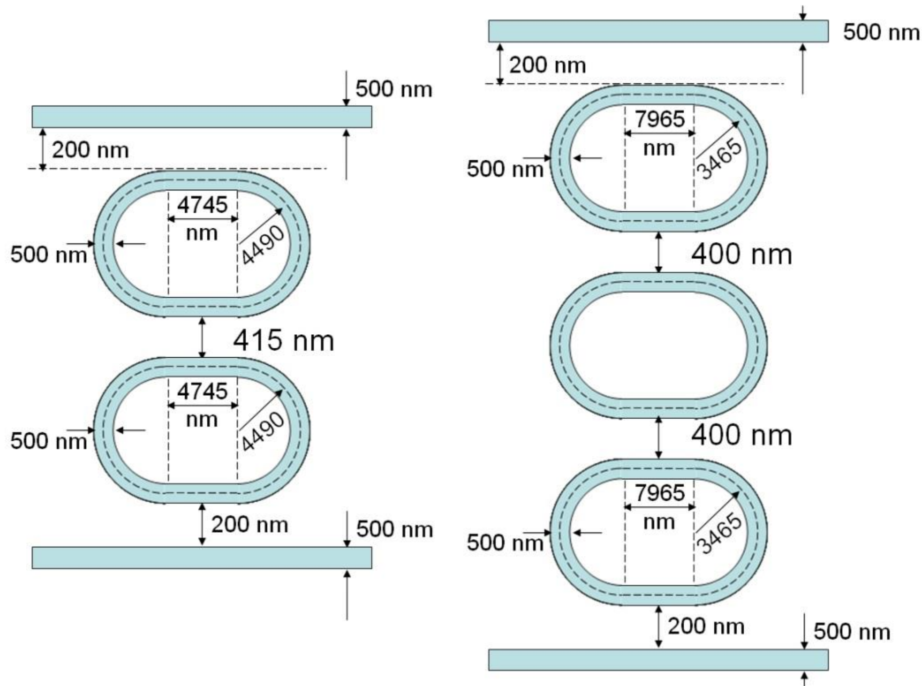

Figure 111: Schematic of the double-racetrack and triple-racetrack configurations proposed for the realization of the optical filter exploiting standard 500 × 220 nm (width × height) optical waveguides.

As previously described, the implemented filters also had to be tunable, meaning that their resonance wavelength could be varied, with a tuning range approximatively equal to the filter FSR. In order to implement this functionality, we included electrical-heating elements over each resonator of the proposed filter structures, as shown, for example, in Fig.112, where the fabrication mask of a triple-resonator filter is shown.

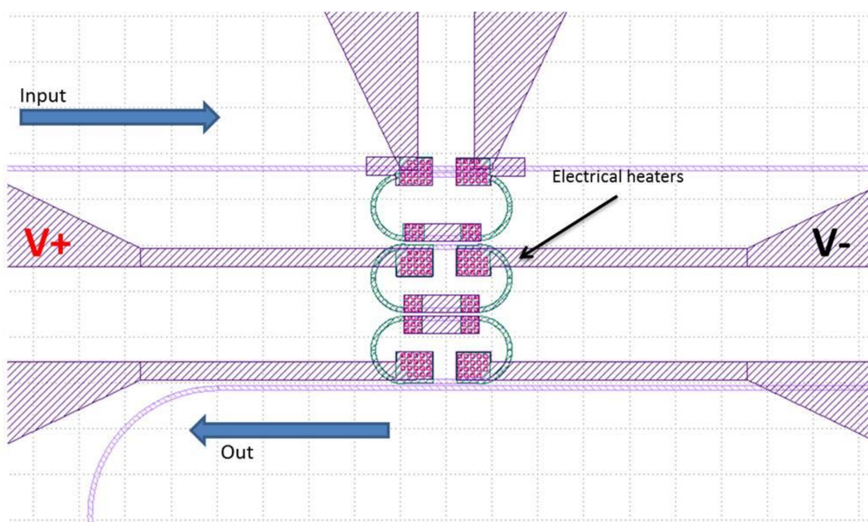

Figure 112: Triple-racetrack resonator fabrication mask. The electrical-heaters are marked in green and placed over the bent sections of each racetrack composing the filter.

By applying a voltage between the two driving electrodes (marked as V+ and V- in Fig.112) it is possible to inject a current into the electrical-heaters (made of a TiN resistive layer), thus inducing a controlled temperature variation due to the Joule effect, which results in a variation of the ring/racetrack effective refractive index, and therefore in a resonant wavelength variation. The variation rate of the resonant wavelength λ_{res} as a function that the temperature variation dT can be expressed as:

$$\frac{d\lambda_{res}}{dT} = \frac{\lambda_{res}}{n_g}\frac{dn_{eff}}{dT} = \frac{\lambda_{res}}{n_g}\frac{dn_{eff}}{dn}\frac{dn}{dT} \tag{69}$$

Where dn/dT is the thermo-optic coefficient of Silicon (see Eq.(1)). In Eq.(69) it can be seen that resonant shift also depends on n_g and dn_{eff}/dT, meaning that the resulting tuning efficiency for the implemented filters will also depend on the chosen waveguide geometry and resonator topology.

4.3 Fabrication procedure

The proposed filter devices were fabricated starting from 200 mm SOI wafers having a 220 nm thick Silicon layer and a 2 µm thick buried oxide layer. The wafers were processed with a MPW (multi-project wafer) run at the CEA-Leti Si-photonics foundry, using standard CMOS process flows. The first step for the wafer-processing was the definition of the grating couplers, by 193-nm DUV lithography, and a specific 120-nm partial etch of the Si-layer (with uniformity better than 3% on the whole wafer). This partial etch was used to both pattern the grating couplers, and to define the height of the reduced height (100 nm) strip waveguides (220nm Si-layer – 120nm Si-etch = 100 nm Si-waveguide) used to implement the ring-based filters. The grating couplers were implemented using a focusing uniform design (see Fig.53), which allows to couple light from the input optical fibre to the Silicon waveguides, either 220 nm high or 100 nm high according to the specific filter design.

The other etching process used had a depth of 220nm ± 3% (full-etch) and a uniformity of 1.5% on the whole wafer. Both the etching processes were performed using ICP-RIE: it must be highlighted that this fully CMOS-compatible etching technique is very different, as previously discussed in Chapter 3, from the strategies exploited in the past to realize height-reduced waveguides [128], which required steam oxidation of the Si layer and subsequent HF stripping.

A HDP (high density plasma) oxide cladding layer was deposited to encapsulate the waveguide, and to optically insulate the waveguide from the Ti/TiN heater used to tune the filters. The oxide layer thickness was selected to give the best trade-off between heating efficiency and optical losses. The heater consisted of a 10nm-thick layer of Ti (used for adhesion), and of a 110nm-thick TiN resistive layer that was patterned to create the thermo-optic phase shifter above the waveguide. Finally, a silicon-oxide cladding layer was deposited, and tungsten vias were added, to contact

the heater layer. This oxide layer provides optical isolations from the aluminum metallization used for electrical routing to the contact pads [118]. A schematic cross section of the full device is shown in Fig.113(left), while a top-view optical micrograph of a fabricated double-ring resonator is shown in Fig.113(right).

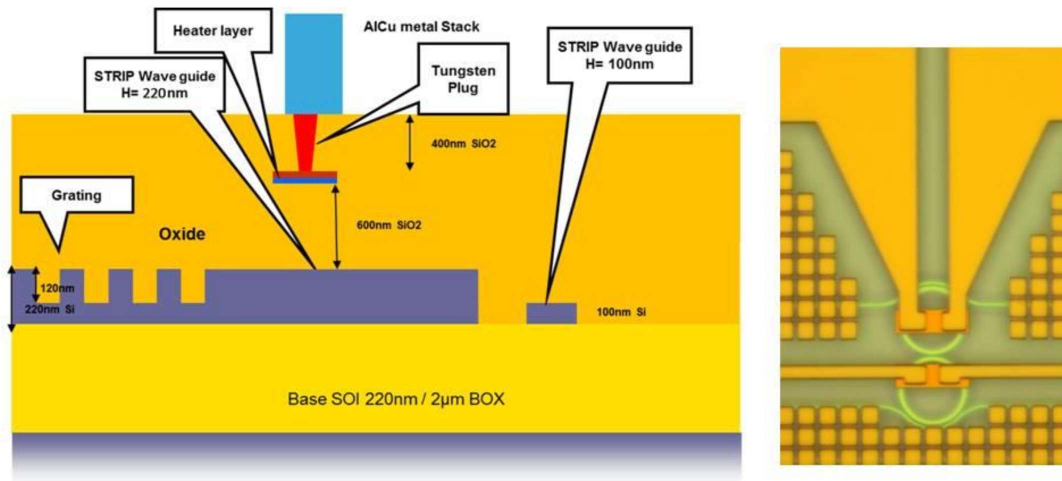

Figure 113: (left) Cross-sectional view of the fabricated chip. (right) Optical micrograph of a fabricated double-ring resonator filter [118].

4.4 Experimental characterization

The fabricated samples were then experimentally characterized, in order to assess their properties in terms of spectral characteristics, insertion loss and tuning efficiency. We also carried out measurements with high levels of input optical powers, in order to study the possible effects of non-linear effects on the filter performances.

4.4.1 Linear characterization

The experimental setup used to characterize the filters, is shown in Fig.114(left). An optical broad-band source (the ASE emission from an EDFA optical amplifier) beam was coupled into a 20 dB fibre tap coupler: the 99% of the output power was sent to the device under test (DUT), while the 1% output was used as a power input reference monitor. In order to couple the light into the Silicon chip, grating couplers were employed, with an estimated coupling loss of $\approx$ 6 dB/grating. The coupled light went through the filter, to be then coupled out by means of another GC (same spectral and loss characteristics as the input one). The output signal was finally sent to an optical spectrum analyzer (OSA) that recorded, for each measurement, the spectral response of the DUT.

In order to fine-tune the resonant wavelength of each implemented resonator, a stabilized current generator was employed, connected to a multiprobe electrical stage that allowed us to inject the desired amount of electrical current into the on-chip

electrical contacts. A microscope image of one the analyzed filter during the measurement stage, is shown in Fig.114(right), where the standard optical fibres used to vertically couple the input/output GCs (with a 10° tilting angle) and the multiprobe used to inject current in the on-chip pads can be noticed.

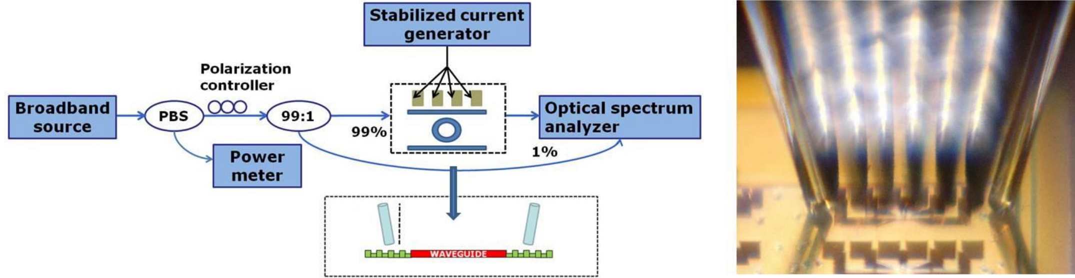

Figure 114: (left) Experimental setup used for the samples characterization. (right) Microscope image of one of the analyzed structure. Standard single mode fibres were used to vertically couple the on-chip GCs, while a multiprobe stage was used to inject current in the on-chip pads for thermal tuning.

The employed measuring procedure can be described as follows. We firstly coupled the output optical fibre to the drop port GC, while launching a low level of optical power at the input GC (to avoid the possibility of non-linear effects), and coarsely varied the amount of injected current in order to red-shift the filter resonance wavelength. After that, the injected current values were refined, in order to finely adjust the resonance wavelengths of each resonator composing the filter structure, so that the spectral shape of the drop transfer could be optimized. Once the optical spectrum at the drop port had been acquired, we moved the output optical fibre to the through port GC, where the optical spectrum was acquired while maintaining the same values of injected current which were previously set. This procedure was very critical, as any experimental mistake during the alignment of the output optical fibre (when moving from the drop to the through port) would result in a fictitious increase of the evaluated insertion loss. The procedure was then repeated for different values of the injected bias current. We found out, however, that the fabricated electrical-heater were extremely fragile and tended to break for values of injected current bigger than 10 mA: this prevented us from achieving a full FSR tuning. The acquired drop and through spectra, for each of the studied configurations, were than analyzed by means of *MATLAB* scripts, in order to evaluate the filter central wavelength, the 3-dB BW, the 20-dB BW, and the level of suppression of the adjacent WDM channels (assuming a 100 GHz spacing) at each level of injected current. The insertion loss was defined as the difference between the drop transmission at resonance, and the through transmission immediately close to the resonance. Examples of the obtained experimental results from some relevant structures are showed in the following Figures. In Fig.115-116 the acquired drop and through spectra are shown for all the configurations implemented using two cascaded resonators. In Fig.117-118 instead, the wavelength shift achievable

by current injection is reported as function of the electrical power dissipated in the electrical-heaters, whose ohmic resistance was measured to be equal to 270 Ω. The reported graphs show the experimental results obtained for the double-racetrack and triple-racetrack structures, and for the triple-ring structures implemented both using straight and curved-coupling sections. It can be seen that, as expected, the wavelength shift varies linearly with the dissipated power, so that, by applying a linear fitting procedure, the tuning efficiency coefficient [mW/nm] can be derived. Finally, in Tab.9-13 the insertion loss evaluation results and the bandwidth characteristics (3-dB BW, 20-dB BW, and left/right adjacent channel suppression) are reported for all the analyzed filter configurations.

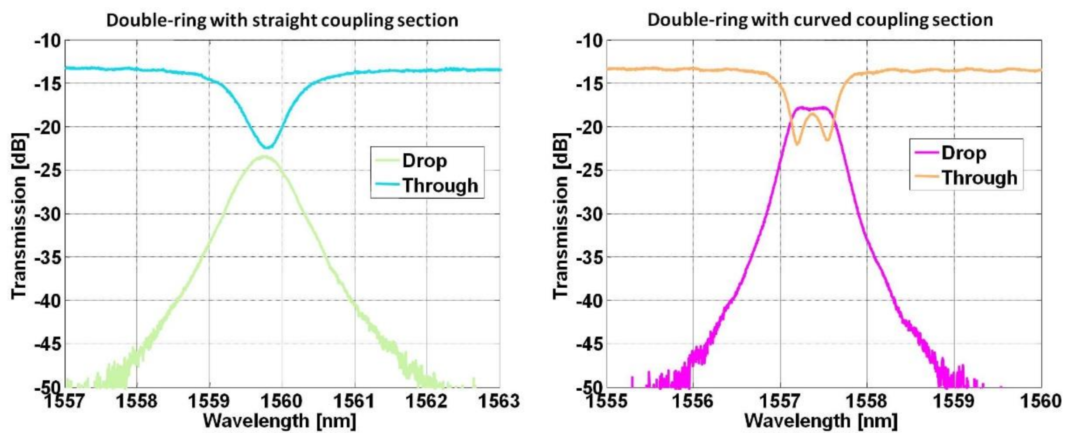

Figure 115: (left) Superimposition of the experimental drop and through transmission spectra for a double-ring filter implemented with straight coupling sections and 100 nm high waveguides. (right) Superimposition of the experimental drop and through transmission spectra for a double-ring filter implemented with curved coupling sections and 100 nm high waveguides.

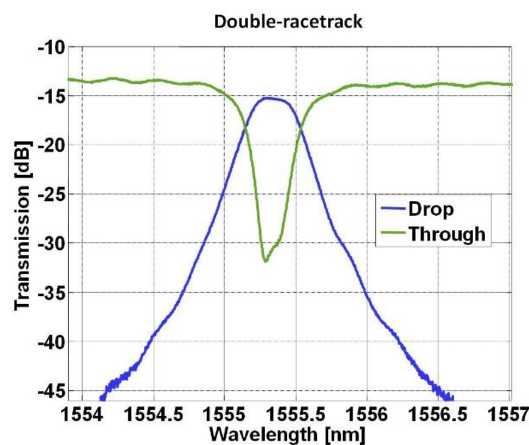

Figure 116: Superimposition of the experimental drop and through transmission spectra for a double-racetrack filter implemented with standard 220 nm high waveguides.

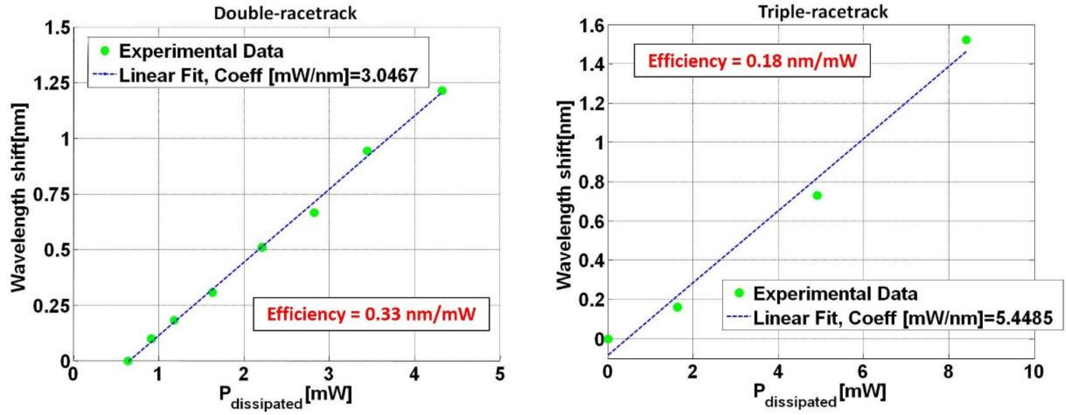

Figure 117: (left) Electrical tuning characteristic for the double-racetrack filter. (right) Electrical tuning characteristic for the triple-racetrack filter. The green circles represent the experimental data, while the blue line is the best linear fit.

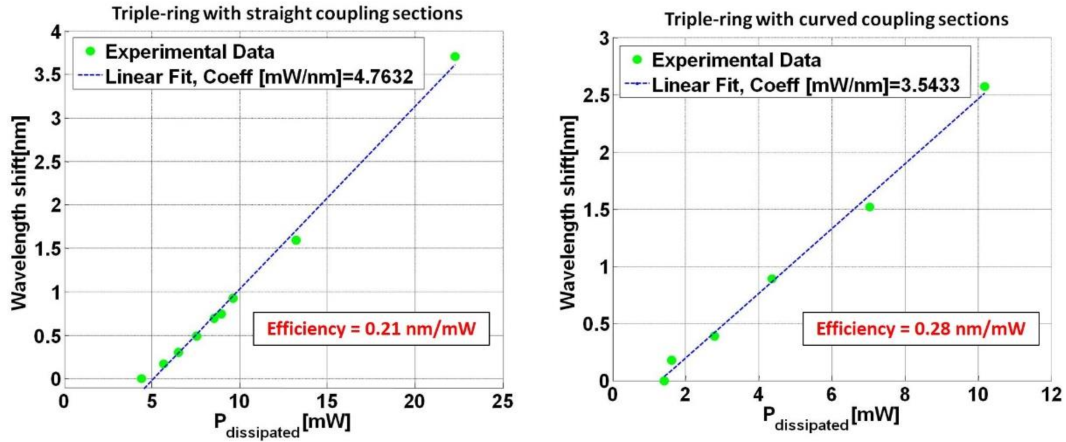

Figure 118: (left) Electrical tuning characteristic for the triple-ring filter with straight coupling section. (right) Electrical tuning characteristic for the triple-ring filter with curved coupling section. The green circles represent the experimental data, while the blue line is the best linear fit.

LOSS	Racetrack	Ring (straight c.)	Ring (curved c)
Double-filter	2.0 dB	10.6 dB	4.6 dB
Triple-filter	3.1 dB	10.0 dB	4.7 dB

Table 9: Recap of the loss between the drop channel and the through channel, for all of the analyzed filter configurations.

3-dB BW [GHz]	Racetrack	Ring (straight c.)	Ring (curved c)
Double-filter	47.1	89.3	73.7
Triple-filter	69.9	113.0	132.0

Table 10: Recap of the drop transmission 3-dB bandwidth, for all of the analyzed filter configurations.

20-dB BW [GHz]	Racetrack	Ring (straight c.)	Ring (curved c)
Double-filter	158.6	365.3	207.9
Triple-filter	165.1	323.4	261.0

Table 11: Recap of the drop transmission 20-dB bandwidth, for all of the analyzed filter configurations.

Left chan. supp. [dB]	Racetrack	Ring (straight c.)	Ring (curved c)
Double-filter	24.0	10.7	21.9
Triple-filter	27.5	8.7	14.4

Table 12: Recap of the adjacent left channel suppression, expressed in dB, for all of the analyzed filter configurations.

Right chan. supp. [dB]	Racetrack	Ring (straight c.)	Ring (curved c)
Double-filter	24.2	10.8	16.7
Triple-filter	22.9	10.5	11.7

Table 13: Recap of the adjacent right channel suppression, expressed in dB, for all of the analyzed filter configurations.

For what regards the thermo-optic shift, it can be seen from Fig.117 that the tuning efficiency is obviously reduced when increasing the number of cascade resonators, as the resonance wavelength of each resonator must be tuned individually. Comparing the wavelength shifts measured over filter with the same number of resonators and different topologies (see Fig.117-118) it can be noticed that the best performances are offered by ring resonators implemented with reduced height waveguides and curved coupling sections.

The measured values of insertion loss are quite high for all of the analyzed configurations (especially for the ring structures with straight coupling sections) and are definitely far from the specifications required for the FABULOUS project. The high insertion loss also results in a considerable broadening of the resonance peak, leading to very high values of the 20-dB BW, and therefore to a poor attenuation of the adjacent WDM channels at a 100 GHz spacing. Three possible reasons for the filters poor performances in terms of insertion loss could be identified:

i. Scattering loss due to the residual waveguide roughness.
ii. Curvature loss due to waveguide bending in the resonators.
iii. Loss in the coupling region due to the effective refractive index discontinuity.

While the first problem was out of our control, as it could be dealt only by improving the fabrication process quality at the Si-Photonics Foundry, modifications in the filters design could allow to address the second and the third problems, as it will be discussed in paragraph 4.5.

4.4.2 Non-linear effects characterization

After characterizing the filter performances in terms of insertion losses and spectral properties, we also decide to carry out measurements with high levels of input optical power, in order to assess the possible consequences of $\chi^{(3)}$-induced non-linear effects on the filters response. This evaluation was required because of the particular structure of the FABOLOUS ONU (see Fig.10), in which the upstream CW seed is amplified by two integrated SOAs, and has to pass twice trough the rings-based filters where, given the high optical power and the resonance-induced power-enhancement factor, non-linear effects can easily become relevant.

Two set of measurement were made using CW light sources: the first one aimed to investigate the changing in the spectral response of the filter, using very high value of injected power (> 2 mW), while the second one aimed to determine the variation of the insertion losses over a wider range of input power values. The first set of measurement was carried out using the same setup previously shown in Fig.114(left). In this case we used, as an optical source, the ASE emitted by an EDFA, which was filtered (using a tunable filter with 5 nm bandwidth), amplified by means of a second EDFA (in order to vary the input optical power level) and then input to the filtering structures. Dramatic changes of the filter transfer function were observed as a function of the input power, as it is shown in Fig.119, where the reported measurements were carried out over a double-racetrack configuration.

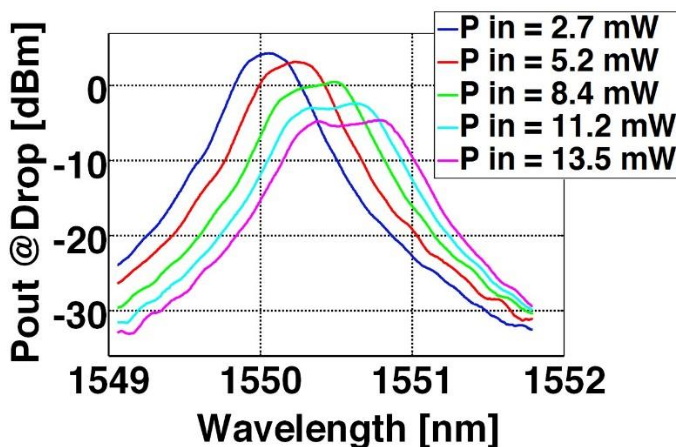

Figure 119: Example of transfer function deterioration (loss increase and band broadening) in the double racetrack filter caused by optical nonlinear effects.

As it is shown in Fig.119, the TPA effect may lead to a significant distortion of the drop transfer function:

i. It introduces additional losses on the drop channel.
ii. The free carriers generated by TPA produce a refractive index change (Free Carrier Dispersion, FCD, see Eq.(3)), thus causing an undesired shift of the

resonance wavelength of the resonators. As the wavelength shift is proportional to the square of the optical power circulating into the resonator, the wavelength shift produced in the two resonators of the filter is different, thus causing a distortion of the transmission spectrum.

The second set of measurements was carried out using a narrowband CW-laser, amplified by means of an EDFA, as the optical source. The laser wavelength was initially tuned, with low optical input power, so as to match the filter resonance, and then the output power from the drop channel was recorded as a function of the input power. The measurement results, performed on double-resonator filters, are reported in Fig.120, where all of the three possible topologies (racetracks, rings with straight coupling sections, rings with curved coupling sections) were taken into account.

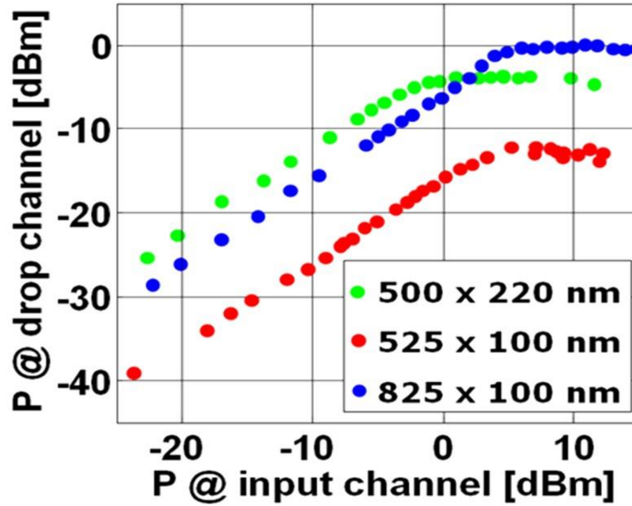

Figure 120: Curves of the output power P_{out} at the drop port as a function of the optical power P_{in}. The green trace refers to measurements carried out on double-racetrack structures, implemented using standard waveguides with a 500x220 nm cross-section. The blue trace refers to measurements carried out on double-ring structures with curved coupling sections, implemented using reduced-height waveguide with a 825x100 nm cross-section. The red trace refers to measurements carried out on double-ring structures with straight coupling sections, implemented using reduced-height waveguide with a 525x100 nm cross-section.

Fig.120 shows that, even at moderate levels of input power (P_{in}), TPA affects the device insertion losses: the output power (P_{out}) grows linearly with the P_{in} up to a certain “threshold power”. After the threshold no significant increase of P_{out} is obtained by increasing P_{in}. This phenomenon might affect the filter behavior during the US operation of the ONU, as high power levels are required for the transmission. Interestingly, reduced-height waveguides, which, as previously discussed in Chapter 3, allow a significant reduction of propagation losses, also show an higher threshold-power with respect to the standard waveguides (500×220 nm). We believe that this behavior can be related to the reduced height of the waveguide: as recombination centers are

mainly located on the waveguide surfaces, the use of a reduced-height structure allows for a faster free-carrier recombination. Indeed free-carriers travel for less than half of the length required in standard waveguides before reaching the surface.

We then performed bit-error-rate (BER) measurements of modulated signals injected in the filters having different values of input optical power, in order to assess the possible effects of TPA, FCA and FCD on inter-symbolic interference and consequently on the devices performances. To carry out the measurements we used the experimental setup reported in Fig.121.

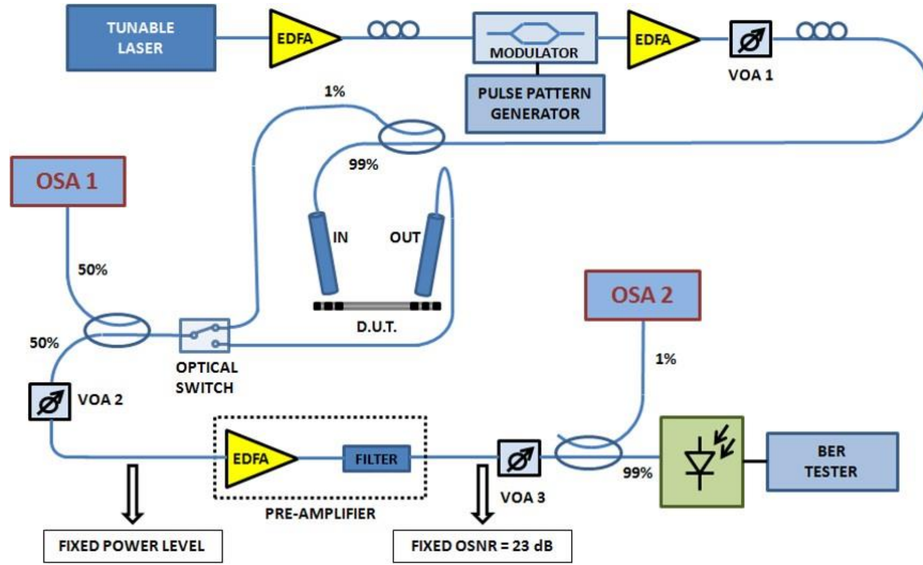

Figure 121: Set-up used for the BER measurements at the WDM filter output.

The output from a semiconductor tunable laser was sent to a $LiNbO_3$ modulator, in order to obtain a 10 Gbit/s non-return-to-zero (NRZ) modulated signal, using a pseudorandom binary sequence (PRBS) 2^{15} and 2^{31} bits long. The bitrate of the employed signal was definitely higher than the one expected for the effective FABULOUS upstream signal (which was required to be between 500 Mbit/s and 1 Gbit/s), so that the obtained results can be considered as a worst-case evaluation. The modulated signal was then fed to the integrated filters by means of the previously described vertical coupling scheme, and the BER of the output signal from the filters was measured as a function of the optical power incident on the photodiode (P_{ph}), in order to evaluate the presence of nonlinearity induced distortions. Three variable optical attenuators (VOA) were employed in the setup of Fig.121: the first was used to vary the level optical power injected into the filter, the second was used to guarantee a fixed power level before the final pre-amplifier (in order to obtain a fixed optical signal-to-noise ratio (OSNR) of 23 dB at the output of the pre-amplifier), and the third was used to vary the level of optical power arriving at the photodiode. The filters were tested by tuning the signal wavelength with the filter resonance at low power, but

without re-tuning the filters even in presence of FCD-induced detuning. An example of the measurements results, carried out on the double-ring structures with curved coupling sections, can be seen in Fig.122, where the BER curves are reported as a function of P_{ph} for different values of the input signal power, and compared to the back-to-back BER curve of the measurement setup, obtained by removing the filter.

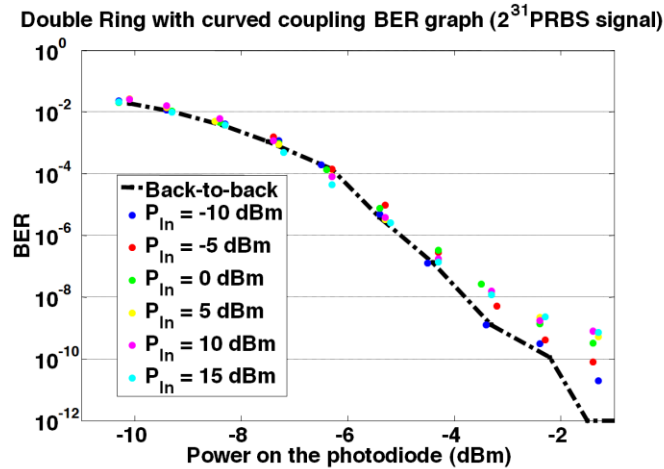

Figure 122: BER characteristics in the double-ring filter with curved coupling sections, for different values of the input power.

From Fig.122 it can be see that no significant change is present in the BER curves when varying the input optical power, thus suggesting that the filter detuning increases the filter insertion loss but prevents from excessive signal distortion. Furthermore, from Fig.123, which shows the normalized modulated signal output spectra for different values of the input power, it can be seen that no SPM-induced spectral broadening is observed, even if the filter detuning causes a distortion of the signal side-bands.

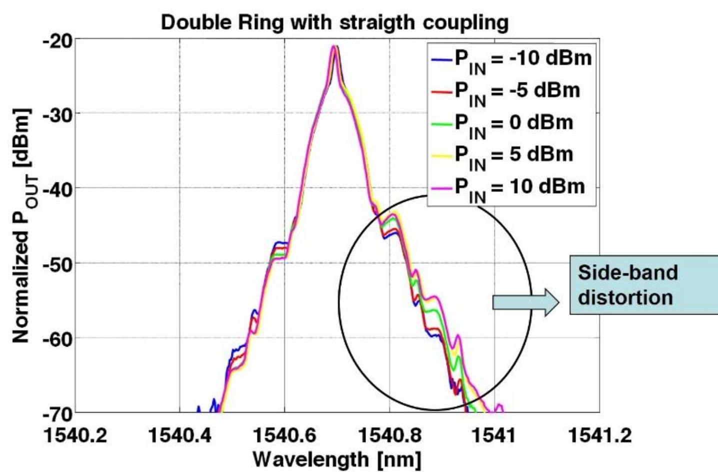

Figure 123: Drop channel output spectra in the double ring filter with straight coupling, at different values of input power.

4.5 Improved design for 2nd generation integrated filters

In order to overcome the issues that were observed thanks to the characterization of the 1st generation filters, we decide to modify the design of the 2nd generation integrated FABULOUS filters, focusing only on standard-waveguide (500×220 nm) racetrack-based filters and reduced-height waveguides (100-nm high) ring-based filters with curved coupling sections, as these were found to be the configurations offering the relatively best performances in terms of insertion loss.

For what regards the ring-based filters with curved coupling sections, in our initial design the ring radius could have been furtherly increased, while still satisfying the requirement on the minimum FSR to be implemented: in fact, due to the weaker modal confinement (as it has been previously discussed), the group index for 100-nm high waveguides is definitely lower than that of standard 220-nm high waveguides, so that, if the optical path length is kept fixed, the actual physical length of resonators based on reduced height waveguides will be bigger than that of resonators based on standard waveguides. Based on that, we decided to increase the ring radius from the original value of 6 µm, to 8.5 µm, thus expecting a significant reduction of the curvature propagation loss. It is important to underline that, in our case, the biggest impact on curvature propagation loss is not given by "pure" radiative loss originating from bending (which can be easily simulated using an FDTD approach, and resulted to be <0.01 dB/cm even for a ring radius of 6 µm), but from the scattering loss induced by side-wall roughness, as, when propagating in a curved waveguide, the optical mode is more deeply pushed against the edge of the waveguide Si-core, as it can be seen in Fig.124.

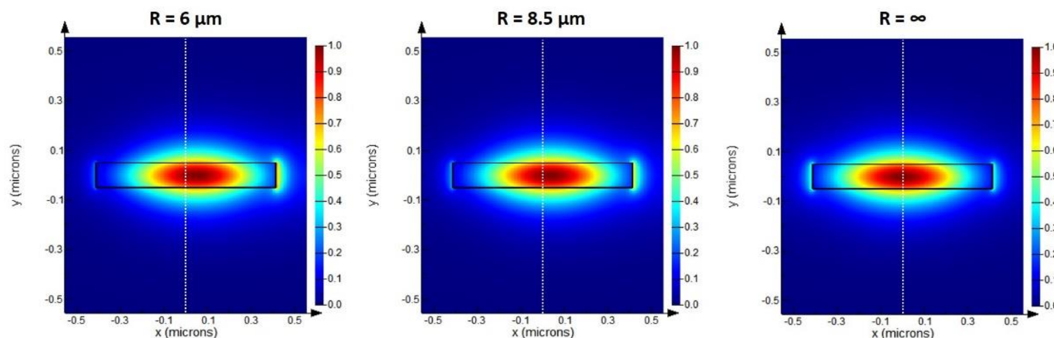

Figure 124: Modal simulation of the E-field distribution (obtained using *MODE SOLUTIONS™* software from *Lumerical Inc.*) of the fundamental TE mode of a SOI waveguide having a 825x100 nm cross-section, and radius of curvature R equal to 6 µm (left), 8.5 µm (middle) or ∞ (right). The white line indicates the middle point of the waveguide. By reducing R, the mode is pushed deeper against the waveguide edge, thus increasing the interaction with the side-wall roughness.

After setting the radius value to 8.5 µm, FDTD simulations were performed to evaluate the power-coupling coefficient κ^2 between the curved bus and the ring, as a function of both the ring waveguide width and the gap length, following the same

procedure previously employed for the design of the 1st generation filters. A first set of simulations, performed over a wide range of gap-width combination and reported in Fig.125 (where the continuous lines represent the required κ^2 coefficient (see Tab.8) for the double and triple-resonator configuration, within a $\pm$0.3 dB tolerance margin) allowed to identify 800 nm as a suitable waveguide width value, as it corresponded to bigger gap values than the ones implemented in the 1st generation. By increasing the bus-ring gap in fact, we expected to reduce the mode index contrast experienced by light propagating in the coupling region, therefore reducing the overall filter insertion loss. After that, a second set of simulations was performed over a narrower range of possible parameter combinations (790 nm $<$ width $<$ 810 nm, 425 nm $<$ gap $<$ 575 nm) and with a smaller computational mesh. Simulations results, which are showed in the inset of Fig.125 (where the dotted lines represent the optimal κ^2 values, and the continuous lines represent the tolerance interval), allowed us to identify the optimal gap values required for a waveguide with of 800 nm, which were found to be 515 nm for the double-ring configuration (with a gap increase of 28% with respect to the 1st generation) and 435 nm for the triple-ring configuration (with a gap increase of 23% with respect to the 1st generation). As a final step, after having set the waveguide width to 800 nm, FDTD simulations of the ring-to-ring power-coupling coefficient were carried out in order to find the optimal gap length (simulations results are reported in Fig.126), which was found to be 355 nm for the double-ring configuration, and 270 nm for the triple-ring configuration.

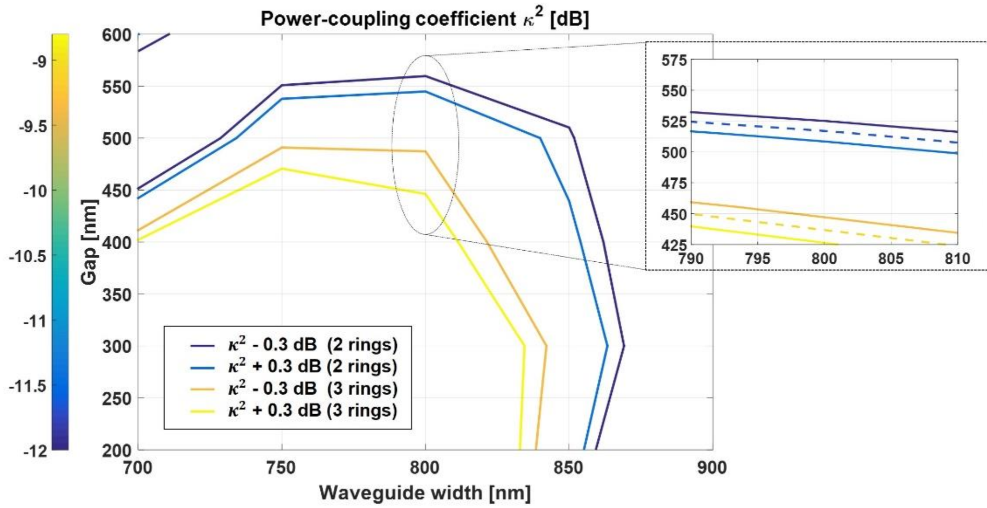

Figure 125: Contour plot of power coupling coefficient κ^2 between the curved bus and the ring obtained by means of FDTD simulations, as a function of the waveguide width and the gap length. The blue and purple continuous curves represent the optimal κ^2 value within a $\pm$ 0.3 dB tolerance region for the double-ring configuration, whereas the yellow and orange curves refer to the triple-ring configuration. The inset reports the results of FDTD simulations performed over a smaller range of parameters, using a smaller simulation mesh; the dotted lines represent the optimal κ^2 values, while the continuous lines represent the tolerance regions.

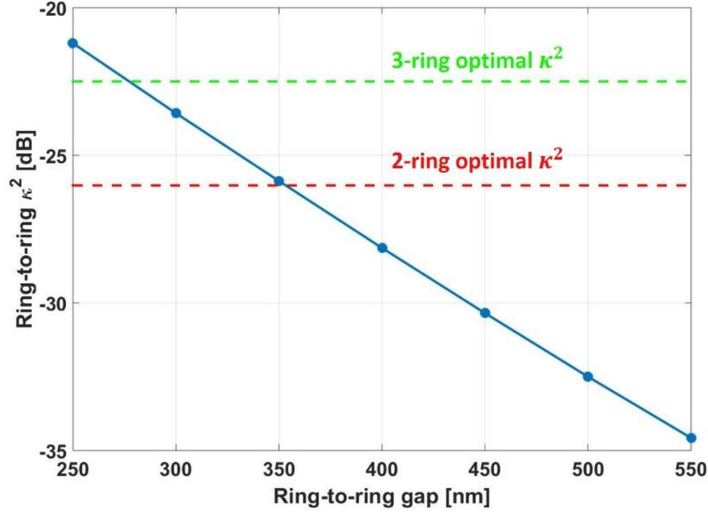

Figure 126: FDTD simulations results of the ring-to-ring power-coupling coefficient κ^2, expressed in dB, as a function of the ring-to-ring gap, when the ring waveguide width is set to 800 nm. The red and green lines represent the optimal κ^2 value required for double and triple-resonator configurations respectively.

In Tab.14 all the design parameters for the 2nd generation ring resonators with curved coupling sections are summarized for both double and triple-ring configurations.

Configuration	Parameter	Value [μm]
2-resonators	Bus-to-ring gap	0.515
	Ring-to-ring gap	0.355
	Ring Radius	8.5
	Waveguide width	0.8
	Waveguide height	0.1
3-resonators	Bus-to-ring gap	0.435
	Ring-to-ring gap	0.27
	Ring Radius	8.5
	Waveguide width	0.8
	Waveguide height	0.1

Table 14: Recap of the deign parameters for the 2nd generation double and triple-ring filters with curved coupling sections.

For what regards the 2nd generation racetrack-based filters, we decided to increase the bus-racetrack gap from the original value of 200 nm to 250 nm, both to reduce the modal mismatch in the coupling section, and to relax the fabrication tolerances. During the analysis of the 1st generation devices in fact, we found out that some areas of the wafer, such as the 200-nm gap, were not fully etched, resulting in a small layer of Si being present between the waveguides, which could completely compromise the resulting filter transfer function. An increase of the bus-racetrack gap implied the necessity

to increase the length of the coupling section too and, consequently, to reduce the racetrack bend radius, in order to keep the FSR requirement satisfied. A new set of FDTD simulations was therefore performed in order to find the new values of bend radius for the double and triple-racetrack configurations respectively, required to achieve the correct power-coupling coefficient κ^2 (see Tab.8). Simulations results are reported in Fig.127, where it can be seen that the optimal bend radius was found to be 3.6 µm for the double-racetrack structure, and 2.44 µm for the triple-resonator structure. After having evaluated the optimal bend radius, the last parameter which had to be determined was the racetrack-to-racetrack gap. Two separate sets of FDTD simulations were carried out for the double and triple-resonator filters (as they are characterized by a different bend radius), whose results are reported in Fig.128. It can be seen that the optimal racetrack-to-racetrack gap was found to be 460 nm for both of the analyzed topologies.

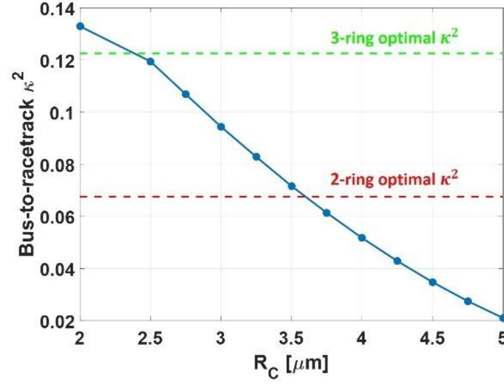

Figure 127: FDTD simulations results of the bus-to-racetrack power-coupling coefficient κ^2 as a function of the racetrack bend radius R_C, when the bus-to-racetrack gap is set to 250 nm. The red and green lines represent the optimal κ^2 value required for double and triple-resonator configurations respectively.

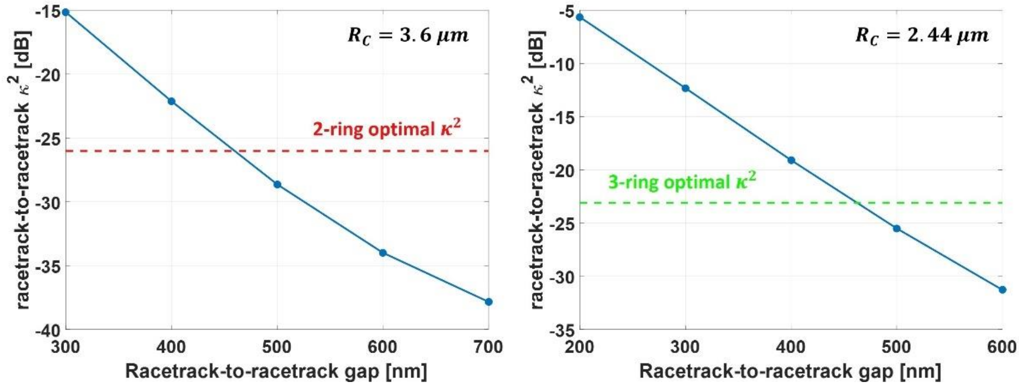

Figure 128: FDTD simulations results of the racetrack-to-racetrack power-coupling coefficient κ^2, expressed in dB, as a function of the racetrack-to-racetrack gap for double-resonator (left) and triple-resonator (right) configurations. The red and green lines represent the required optimal κ^2 value.

In Tab.15 all the design parameters for the 2nd generation racetrack resonators are summarized for both double and triple-ring configurations.

Configuration	Parameter	Value [μm]
2-resonators	Bus-to-resonator gap	0.250
	Resonator-to-resonator gap	0.460
	Bend Radius	3.6
	Coupling length	8.16
	Waveguide width	0.5
	Waveguide height	0.22
3-resonators	Bus-to-resonator gap	0.250
	Resonator-to-resonator gap	0.460
	Bend Radius	2.44
	Coupling length	11.15
	Waveguide width	0.5
	Waveguide height	0.22

Table 15: Recap of the deign parameters for the 2nd generation double and triple-ring filters with curved coupling sections.

4.6 Experimental characterization of 2nd gen. filters

Following to the previously described design activity, a new set of chips carrying the 2nd generation of integrated filters was fabricated at CEA-Leti Si-Photonics foundry, employing the same fabrication process which has already been described in paragraph 4.3. The devices were implemented using the same uniform GCs for input/output coupling previously employed for the 1st generation devices, and the experimental characterization was carried out using the same setup and the same procedure reported in paragraph 4.4.1. For what regards the tuning efficiency, as the characterization of the 1st generation of integrated filters revealed that the heaters were relatively fragile and they often cracked for values of injected current bigger than 10 mA, in the 2nd generation design we decided to test two different heaters configuration, the first one being thinner and overlaying only the silicon waveguide (as in the 1st gen.), the second one instead being wider and overlaying a bigger region of silicon oxide, as shown in Fig.129.

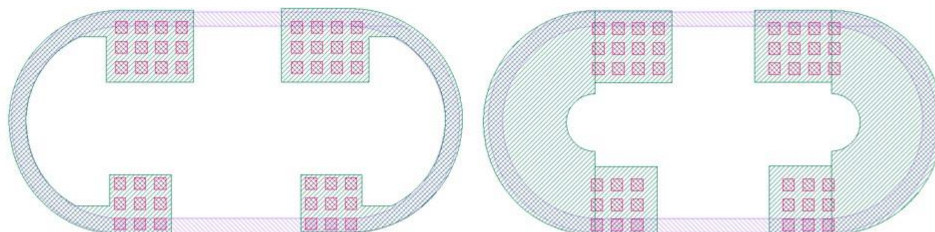

Figure 129: Different configurations of heaters used for 2nd generation of integrated filters. Left: first configuration having thin heaters which only overlay the silicon waveguide. Right: second configuration having bigger heaters, which overlay a wide area of silicon oxide.

An example of the fibre-to-fibre transmission (at the drop port) of the double racetrack filter configuration (with thin heaters), is shown in Fig.130, for different values

of the electrical power dissipated into the heaters. The results of the electrical tuning measurement for the relevant devices are shown in the following Figures. The wavelength shift with respect to the first tuned configuration is reported as a function of the total electrical power dissipated in the heaters.

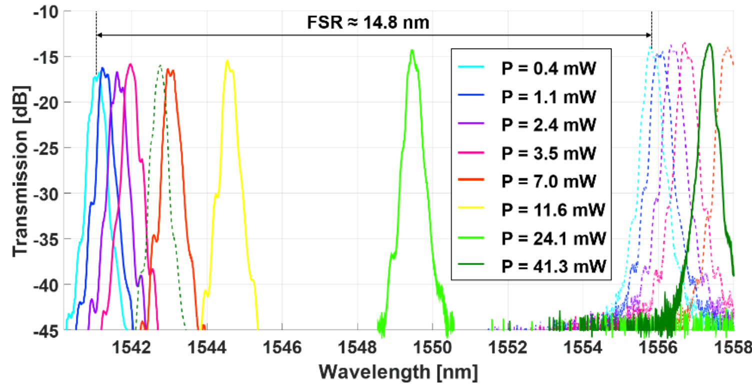

Figure 130: Fibre-to-fibre transmission of the double racetrack resonator filter, with thin heaters, for different values of electrical power dissipated into the heaters.

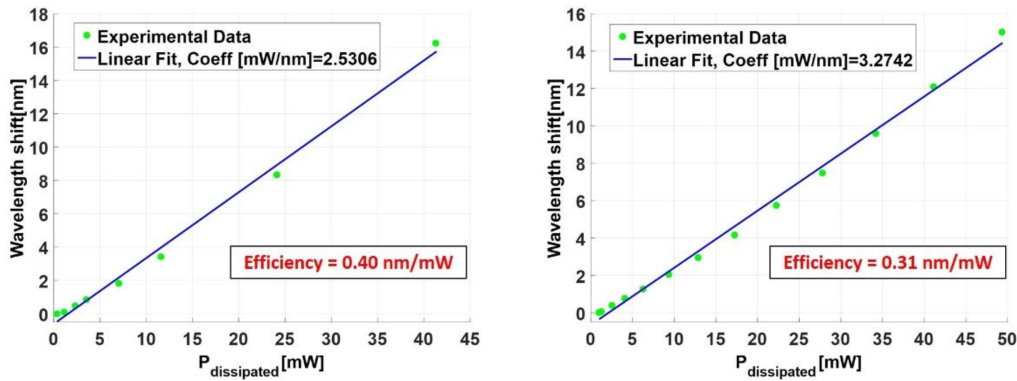

Figure 131: Electrical tuning characteristic for the double racetrack resonator device, with thin heaters (left) and with wide heaters (right). The green circles represent the experimental data, while the blue line is the best linear fit.

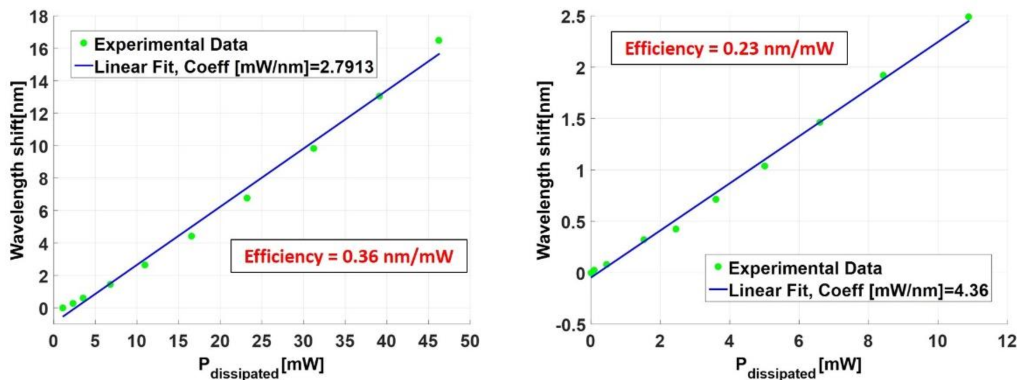

Figure 132: Electrical tuning characteristic for the triple racetrack resonator device, with thin heaters (left) and with wide heaters (right). The green circles represent the experimental data, while the blue line is the best linear fit.

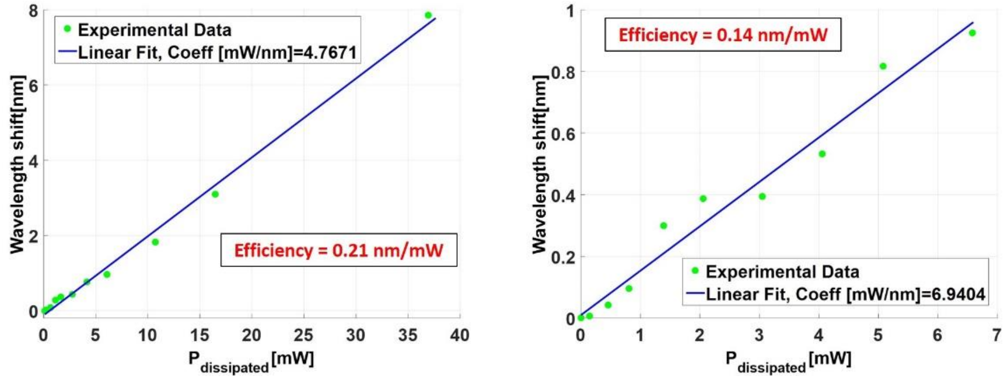

Figure 133: Electrical tuning characteristic for the double ring resonator device, with thin heaters (left) and with wide heaters (right). The green circles represent the experimental data, while the blue line is the best linear fit.

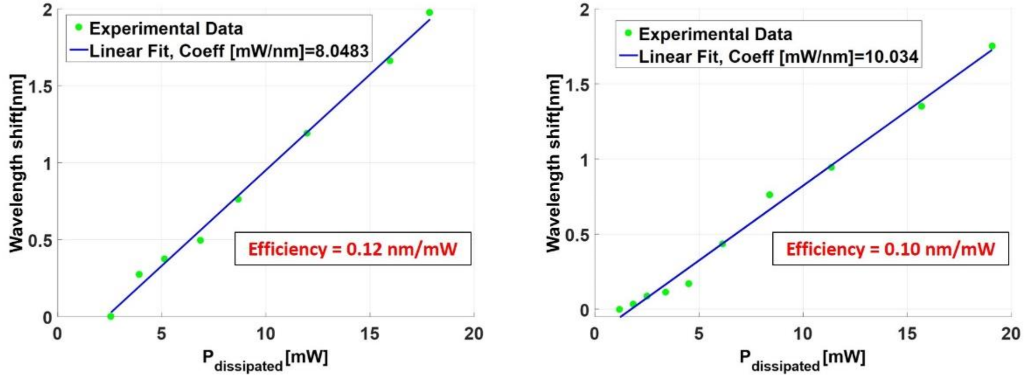

Figure 134: Electrical tuning characteristic for the triple ring resonator device, with thin heaters (left) and with wide heaters (right). The green circles represent the experimental data, while the blue line is the best linear fit.

As expected, the wider heaters exhibited a lower resistance, but the increased width made them able to support higher values of injected current (even > 30 mA) without breaking. The thinner heaters instead showed a lower “threshold” current value of $\approx$ 15 mA, which is anyway 5 mA bigger than the one reported for the 1st generation devices (probably due to improvements in fabrication process). On the other side, the tuning efficiency of the wider heaters is systematically worse than that of the structures with thin heaters, in all of the analyzed structures: this can be associated to the fact that the temperature increase produced by the larger heaters takes place also in silica regions where there is less interaction with the propagating optical beam, thus heating up chip areas that are not relevant for filter tuning. Taking into account only the tuning efficiency of the thin electrical-heaters, and comparing the results obtained in the 1st and 2nd generation devices, it can be seen that the efficiency was greatly improved for the racetrack-based devices (from 0.33 to 0.40 nm/mW for the double-resonator configuration, and from 0.18 to 0.31 nm/mW for the triple-resonator configuration), while it was reduced for the ring-based devices (from 0.28 to 0.12 nm/mW

for the triple-ring configuration). The reason for this reduction can be attributed to the ring radius increase (from 6 µm to 8.5 µm) which led to a bigger heating volume [129, 130]. It is however interesting to note that, thanks to heater damage-current threshold increase, we managed to increase the maximum achievable tuning-range with respect to the 1st generation devices (which was limited to a few nm), obtaining a value of 8 nm for the double-ring configurations, and > 16 nm for the racetrack-based devices. A useful metric to define the tuning efficiency of the implemented filters is the amount of dissipated electrical power required to shift the filter resonance wavelength over an entire FSR (thus achieving a 2π phase shift), divided by the number of resonant elements of the filter. The mW/FSR/resonator efficiency is reported, together with the measured FSR, in Tab.16, for all the analyzed filter configurations employing thin heaters, and in Tab.17 for different resonator-based filters reported in the literature.

Structure type	**2-racetrack**	**3-racetrack**	**2-ring**	**3-ring**
FSR [nm]	14.8	15.2	13.8	13.7
2π Efficiency [mw] (per resonator)	18.7	14.1	32.9	36.7

Table 16: Recap of the FSR and the power value required to shift the resonance wavelength over an entire FSR (divided by the number of the filter resonators) for all of the analyzed filter configuration carrying thin heaters.

Description	**Heaters type**	**WG. Cross-section [nm x nm]**	**FSR [nm]**	**2π Eff.[mw] (per resonator)**	**Ref.**
Lateral air trenches (channel WG)	Ti	450 x 250	19	**21**	[131]
Undercut etch (channel WG)	Ti	450 x 250	11.5/ 6.4	**2.4**	[132]
Back etch (ridge WG)	doped silicon slab	360 x 300 (slab height = 150 nm)	0.97	**3.9**	[130]
Undercut etch (ridge WG)	NiSi	500 x 220 (slab height = 110 nm)	12.5	**4.9**	[133]
Channel WG	Ti	800 x 100	16	**≈42**	[134]
Ridge WG	doped silicon slab	360 x 300 (slab height = 150 nm)	8	**89**	[135]
Channel WG (1 racetrack)	p-Si (lateral heater)	450 x 220	11.35	**74**	[136]
Channel WG (2 racetracks)	p-Si (lateral heater)	450 x 220	11.35	**51**	[136]
Channel WG (1 ring)	Ti	425 x 220	18.4	**54.1**	[129]
Channel WG (5 rings)	Ti	425 x 220	18.4	**36.8**	[129]
Channel WG (2 rings)	Ti	600 x 105	16	**53.6**	[128]
Channel WG	(not specified)	450 x 220	20	**363.6**	[137]

Table 17: Summary of the tuning electrical power (mW per FSR per resonator) of different resonator-based filters reported in the literature. The state-of-the-art results (all obtained by means of undercut or back etching techniques) are highlighted with green background.

Comparing the results of Tab.16 with that of Tab.17, it can be seen that the experimentally derived tuning power per FSR of our filters is still higher than that of the state-of-the-art devices reported in literature, where lateral air trenches (obtained by means of anisotropic etching) and undercuts (obtained by means of SF_6 isotropic dry etching) were used to obtained suspended resonators, thermally isolated from the Si substrate [132, 133], or where anisotropic hydroxide wet back-side etch was used to directly remove the Si substrate underneath the optical resonator [130]. Both of these techniques allowed to achieve tuning powers per FSR < 5 mW, with a record of 2.4 mW reported in [132]. However, the performances of our filters in terms of tuning power per FSR are excellent if compared to other resonator-based filters reported in literature without the use of undercut or back-etch techniques [129, 134, 135, 136, 137, 128], with a power consumption (per FSR per resonator) reduction of 71,8% with respect to [136] and of 60.9% with respect to [129], when considering the racetrack configuration. The filter thermal efficiency can also be furtherly optimized by performing additional simulations of the interaction between the propagating optical mode and the current induced temperature gradient, taking into account both the particular implemented geometry and the detailed specifications of the fabrication process.

After measuring the tuning efficiency of the fabricated devices, we evaluated their insertion losses, defined as the ratio between the maximum of the through channel spectrum immediately close to the resonance, and the maximum of the drop channel spectrum. Measurements were carried out at different current values in order to make clear if thermal effects could affect the loss mechanism. Fig.135 shows a superimposition of the spectra measured at the through port, and at the drop port, for a single racetrack filter (which was included in the final chip design as a test structure). The maxima of both spectra are marked, and the difference between these two values (expressed in dB) is considered as the filter insertion loss.

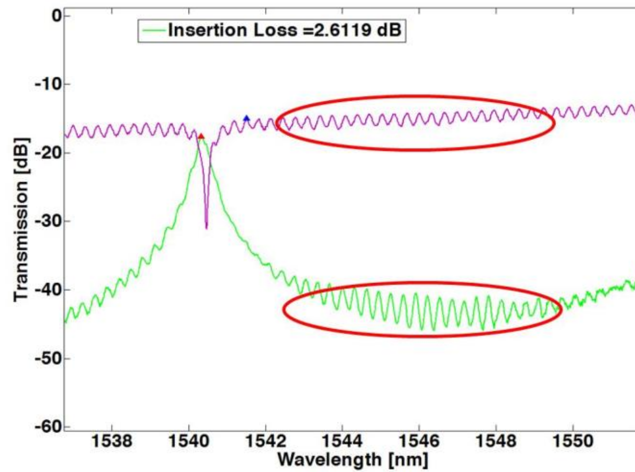

Figure 135: Superimposition of the drop spectrum and the through spectrum for a single racetrack filter. The maxima of both spectra are marked. The red ovals evidence the presence of a parasitic amplitude ripple on both the drop and through outputs.

From Fig.135, it can be clearly observed the presence of a parasitic amplitude ripple, both on the through and the drop transmission spectra. The period of the oscillation is compatible with a parasitic Fabry-Perot cavity having a length similar to that of the filter bus waveguide, indicating that spurious back-reflections take place in correspondence of the input/output GCs, whose reflectivity was probably increased because of fabrication imperfections. The same amplitude ripple was also observed on the transmission function of the double and triple-resonator filter configurations, as shown in Fig.136-137.

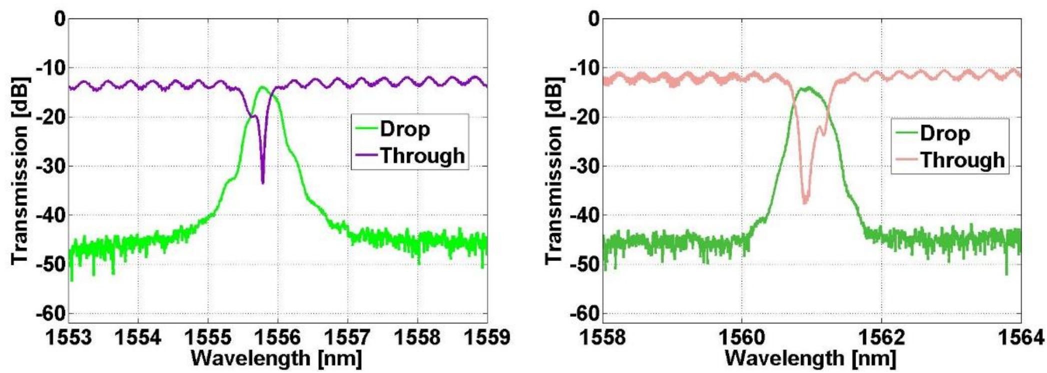

Figure 136: (left) OSA-acquired drop and through spectra for a double-racetrack filter. (right) OSA-acquired drop and through spectra for a triple-racetrack filter.

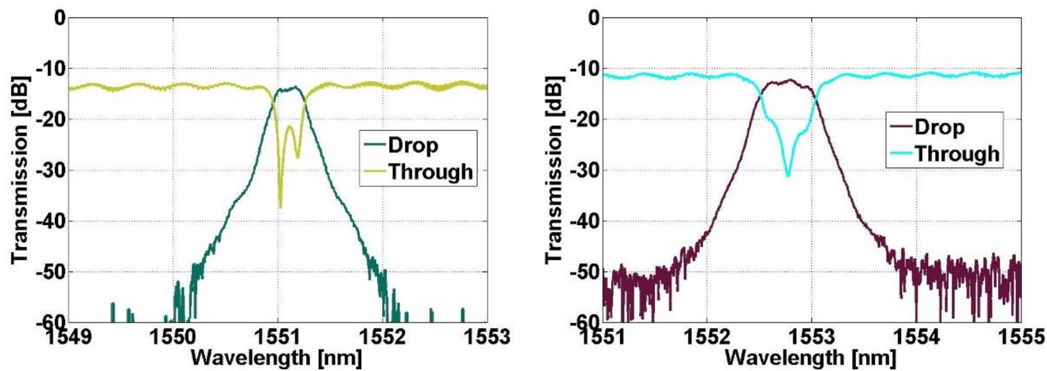

Figure 137: (left) OSA-acquired drop and through spectra for a double-ring filter. (right) OSA-acquired drop and through spectra for a triple-ring filter.

As both the drop and the through spectra were distorted by the superimposition of the resonant modes pattern of the parasitic Fabry-Perot cavity, it became very difficult to tune each resonator resonance, and to reach a situation where the correct filter shape was achieved while having the maximum of the "real" drop transmission function exactly superimposed with a maximum of the resonant modes pattern. Because of that, insertion loss measurements results, repeated for different injected current values, exhibit a quite large variation of about ± 0.3 dB. It was in any case possible to assess that no significant trend in the optical loss with respect to the injected current, was observed (as it can be seen in Fig.138, where the insertion loss measured for one

of the double-ring filter, is plotted as a function of the power dissipated in the electrical-heaters), meaning that thermal effects do not affect the losses.

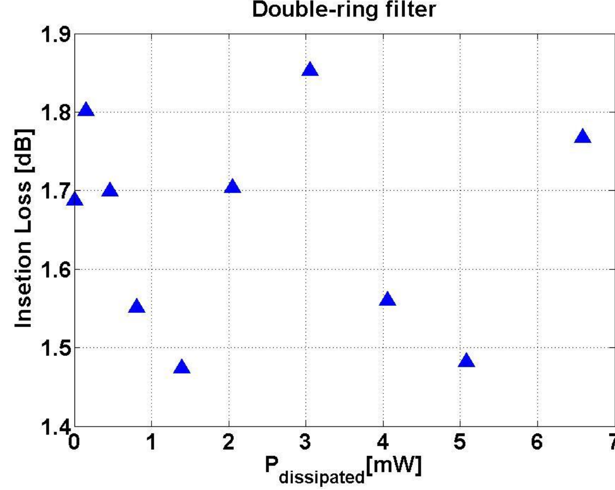

Figure 138: Insertion loss values measured over a double ring filter for different values of electrical power dissipated into the heaters. The variation of the measured values is due to the presence of an amplitude parasitic ripple. No significant trend is observed as a function of the injected electrical power.

The best values of insertion loss obtained for each of the characterized filter, are reported in Tab.18.

Structure type	**Structure 1 Ins. Loss [dB]**	**Structure 2 Ins. Loss [dB]**	**Structure 3 Ins. Loss [dB]**	**Structure 4 Ins. Loss [dB]**
2-racetrack	1.9	3.1	2.5	2.9
3-racetrack	3.3	4.2	4.8	3.5
2-ring	0.8	1.7	1.3	1.5
3-ring	1.2	1.4	1.7	1.6

Table 18: Best values of insertion loss obtained from the analysis of all of the implemented filter topologies. Measurements were carried out on a single chip, where 4 replicas of each filter structure were fabricated.

From Tab.18, it is possible to observe that the performance of the racetrack structures slightly deteriorated, compared to that measured on the 1st generation devices (around 1 dB worse), and this may be partially due higher round-trip losses caused by the reduction of the curvature radius. Conversely, a big improvement was obtained, thanks to the new design, on the ring-based structures, whose "previous generation" losses were around 4.6 dB, for both double and triple resonators structures. It's also very important that, for many of the analyzed ring filters, the measured insertion loss was very close to the project FABULOUS specification (Insertion Loss $<$ 1dB), with a best-performing device showing an Insertion Loss equal to 0.8 dB. The obtained

results were confirmed by measurements on different chips; Tab.19 shows, for example the best results obtained, for each kind of structure, on a different chip.

Structure type	2-racetrack	3-racetrack	2-ring	3-ring
Ins. Loss [dB]	2.2	3.5	1.5	1.6

Table 19: Recap of the best loss values between through channel and drop channel, for all the double configurations and triple configurations of filters analyzed on a second chip.

As a last step of our characterization, we analyzed the spectral characteristics of the filters, in order to compare them with the required project-specifications. For this reason, we analyzed all the OSA-acquired drop-port spectra, by using Matlab script, in order to evaluate the -3dB bandwidth, the -20dB bandwidth, and the suppression ratio of the adjacent channels (100 GHz away from the wavelength resonance peak). An example, evaluated for a double ring filter, is shown in Fig.139. As already mentioned in the previous paragraph, the superimposition of a parasitic pattern of resonant modes over the “real” drop-port spectrum, strongly modify its spectral characteristics, thus leading to variations in the values of -3 dB bandwidth, -20 dB bandwidth and adjacent channels suppression, obtained from measurements made with different values of injected current. The –3dB and –20 dB bandwidth variation was measured to be $\approx$ 3 GHz. In order to overcome this problem, the spectral analysis was carried out over all of the drop-port traces, acquired for each structure at different injected current values, and the mean value of the spectral parameter of interest was considered as the reference one. The obtained results, shown in Tab.20 and in Tab.21, recap respectively, the -3 dB bandwidth and the -20 dB bandwidth values, evaluated for all the double- and triple-resonator structures. Tab.22 and Tab.23 recap respectively the left adjacent channel suppression and the right adjacent channel suppression.

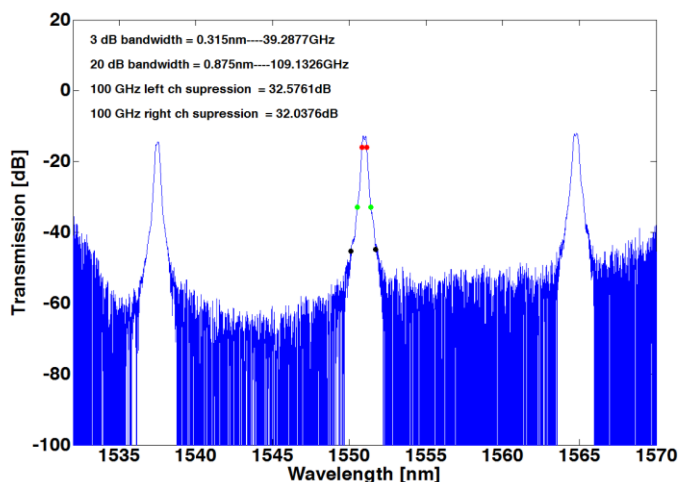

Figure 139: Drop-port spectrum for a double ring filter; the -3dB band is marked in red, the -20 dB band is marked in green and the wavelength-position of the adjacent channels is marked in black.

-3 dB Bandwidth [GHz]				
Structure type	**Structure 1**	**Structure 2**	**Structure 3**	**Structure 4**
2-racetrack	37	37	40	39
3-racetrack	46	44	54	50
2-ring	35	35	39	39
3-ring	66	62	59	66

Table 20: Recap of -3 dB bandwidth values of all the double and triple resonator filters.

-20 dB Bandwidth [GHz]				
Structure type	**Structure 1**	**Structure 2**	**Structure 3**	**Structure 4**
2-racetrack	118	115	131	117
3-racetrack	117	121	132	125
2-ring	96	95	109	108
3-ring	133	122	123	133

Table 21: Recap of -20 dB bandwidth values of all the double and triple resonator filters.

Left channel suppression [dB]				
Structure type	**Structure 1**	**Structure 2**	**Structure 3**	**Structure 4**
2-racetrack	31	30	28	32
3-racetrack	38	35	34	36
2-ring	33	35	30	31
3-ring	34	34	33	32

Table 22: Recap of the adjacent left channel suppression values of all the double and triple resonator filters.

Right channel suppression [dB]				
Structure type	**Structure 1**	**Structure 2**	**Structure 3**	**Structure 4**
2-racetrack	29	29	26	35
3-racetrack	31	31	28	30
2-ring	32	33	31	30
3-ring	29	32	36	36

Table 23: Recap of the adjacent right channel suppression values of all the double and triple resonator filters.

From the results reported in Tab.20-23, it can be seen that the modified design of the 2nd generation filters allowed to obtain a consistent reduction of the -20 dB bandwidth for all of the employed resonator topologies, with respect to their 1st generation counterparts. The best result was obtained by the double-ring resonators, which satisfied, or were in any case extremely close, to the FABULOUS target of achieving a -20 dB bandwidth $<$ 100 GHz. For the other types of the structure, the obtained results were still quite distant from the value. Nevertheless, this was compensated by

the excellent results recorded for the adjacent channels suppressions (both left and right), which exceed the objective threshold of 30 dB, for the vast majority of the analyzed filters. It can be noticed that the new design also led to a reduction of the measured -3 dB bandwidth with respect to the 1st generation devices: whereas in triple-resonator filters the -3 dB bandwidth requirement (-3 dB > 40 GHz) was fully satisfied, for the double-resonator filters the measured bandwidth was found to be slightly less than the required value.

4.7 Stand-alone packaged device

Based on the previous experimental analysis, we thought that the double-ring resonators could represent the best compromise in terms of insertion losses, spectral characteristics and tuning efficiency. In order to demonstrate the possibility to effectively employ the Si-integrated filter as a "stand-alone" device in a conventional fibre-optic communication system, one of the fabricated chip was packaged by *Tyndall* using their standard Si-Photonics packaging technique [138]. The PIC was epoxy-bonded to a standard Tyndall PCB, as shown in Fig.140, with a thermistor and a thermoelectric-cooler (TEC) inserted between the PCB and aluminum mount in order to stabilize the sample temperature.

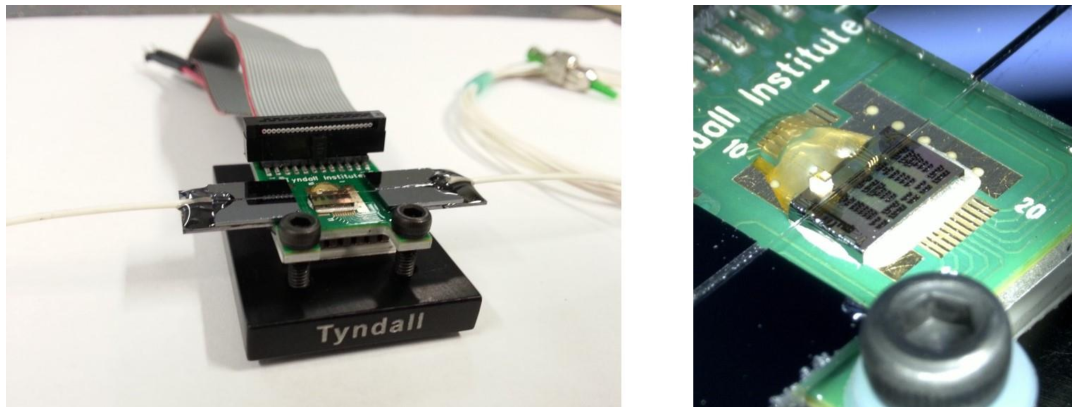

Figure 140: (left) Photograph of the PIC carrying the integrated double-ring resonator, packaged over a standard Tyndall PCB. Optical input/output to the "packaged" device is provided by means of standard FC/APC fibre connectors. (right) Detail of the PIC packaged on the PCB.

Two single-mode optical fibres were used to couple the input and drop port GCs of the double-ring resonator, as shown in Fig.141(left), where an optical micrograph of the packaged PIC is reported. An "horizontal" coupling scheme was employed, as schematically shown in Fig.141(right). Angled-polished fibres (with a 40° cutting angle) were epoxy-bonded to the chip (with an index-matching medium), coming in parallel to the chip surface: the light propagating into the fibre undergoes a total internal reflection at the fibre/air polished interface, so that it can be nearly-vertically coupled

to the Si-integrated grating coupler. The PIC electrical pads were also wire-bonded to the PCB, so as to allow current injection into the electrical heaters.

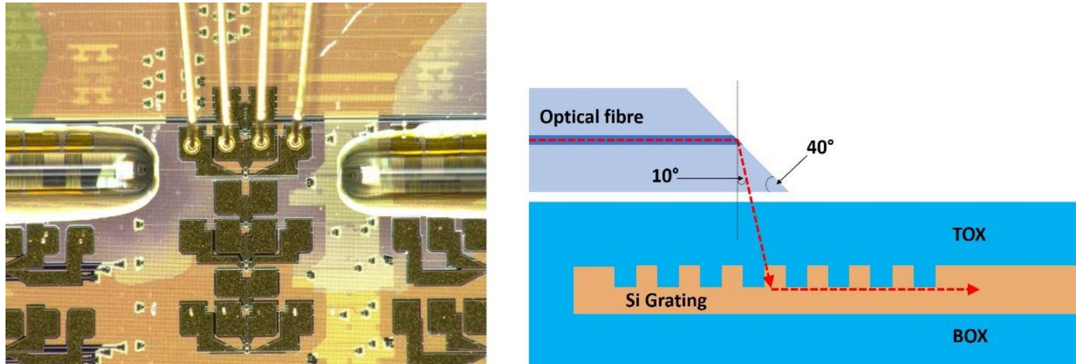

Figure 141: (left) Optical micrograph of the packaged double-ring integrated filter. Cleaved single-mode fibres were used to horizontally couple the input and drop port GCs. Wire-bonding was used to connect the PIC electrical pads to the PCB. (right) Schematic representation of a horizontal coupling scheme between an angle-polished (40° cutting angle) single-mode fibre and a Silicon integrated grating coupler.

In Fig.142 an example of the fibre-to-fibre transmission of the filter is shown, for different values of current injected into the heaters.

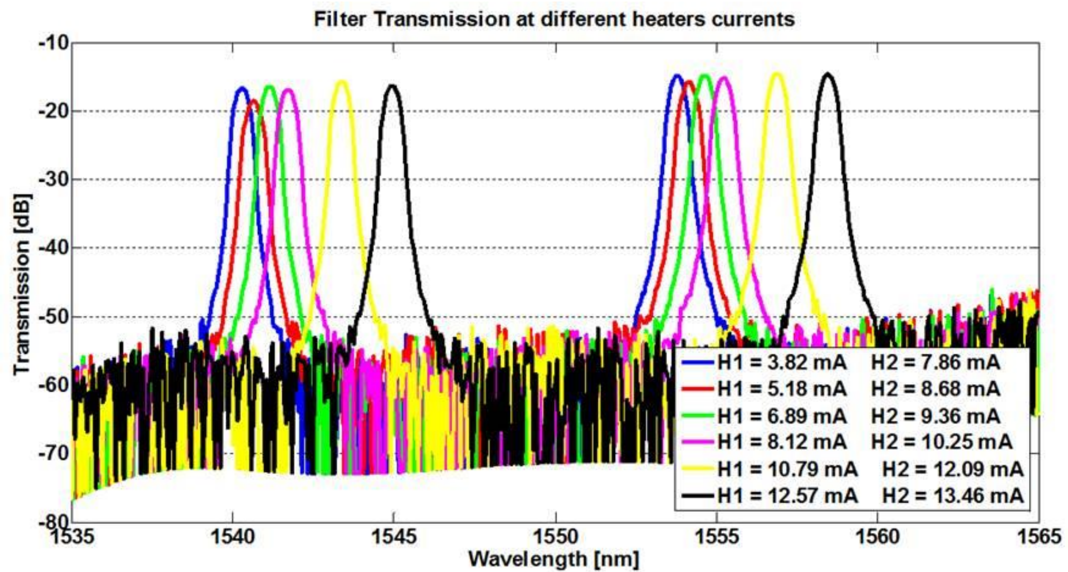

Figure 142: Fibre-to-fibre transmission of the packaged double-ring filter, for different values of current injected into the heaters.

5 Hybridly integrated III-V on Si semiconductor optical amplifiers

This chapter will focus on III-V material devices hybridly integrated on Silicon wafers in order to achieve optical amplification. The first paragraph will give a brief overview of the possible approaches to III-V on Silicon integration, describing some of the devices which have already been reported in the scientific literature. After that, the structure of the semiconductor optical amplifiers (SOAs) designed for the integration in the FABULOUS ONU will be described, and a brief report of the experimental characterization that we carried out over one of the packaged FABULOUS SOA sample will be reported. The gain properties of the integrated SOA will be analyzed, in order to outline which grade of performance can be achieved, and how severely they can be affected by the integration and packaging process.

5.1 Current approaches for light generation and amplification in Silicon Photonics

Silicon, owing to its indirect band-gap nature, is a very poor material for the implementation of active optical devices. One possible way to overcome this limitation and to obtain Silicon-based light emitters and amplifiers, is to exploit stimulated Raman scattering (SRS). Silicon is in fact characterized by a very large Raman scattering coefficient (several orders of magnitude larger than that of silica, which is commonly employed for fibre Raman amplifiers), and this fact allowed to demonstrate both CW net optical gain [139] and CW lasing action [140] based on SRS in SOI waveguides. A schematic representation of the integrated Silicon Raman laser described in [140], is shown in Fig.143.

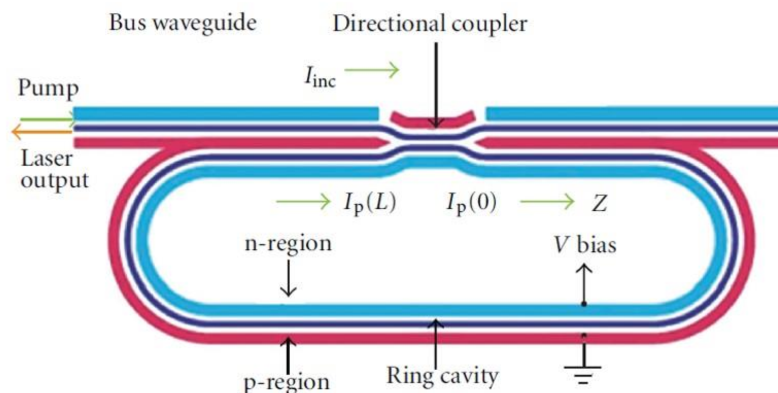

Figure 143: Schematic representation of the Silicon Raman ring laser reported in [140]. A reveres-bias p-i-n structure was implemented in the Silicon rib waveguide, in order to reduce the lifetime of TPA-induced carriers.

The Silicon Raman laser reported in [140] was constituted by a 3 cm long racetrack resonator, implemented using a rib SOI waveguide with large geometrical dimensions (waveguide width = 1.5 µm, waveguide height = 1.55 µm, rib height = 0.7 µm). A directional coupler was used for the in/out coupling of the Raman pump and of the Raman-generated laser signal, and a p-i-n junction was implemented along the waveguide rib in order to remove the TPA-induced free carriers, thus reducing the losses. Laser emission at $\lambda = 1686$ nm was observed when launching into the resonator a pump beam at $\lambda = 1550$ nm, demonstrating a pump power threshold of 20 mW, a slope efficiency close to 28% and a maximum output power of 50 mW when applying a 25 V reverse bias across the p-i-n junction. The same type of waveguide, embedding a p-i-n, junction, was used to demonstrate an optical amplification gain > 3 dB in a 4.8 cm long structure, for a pomp power ≈ 700 mW and a reverse bias voltage of 25V [139]. Despite having been successfully used for the implementation of Silicon-based optical sources and amplifiers, two main factors limit the practical effectiveness of SRS:

i. The narrow bandwidth of Silicon Raman gain spectrum (≈ 1.2 nm), which limits the application of SRS based amplifier only to single-channel operation.
ii. The optical pumping scheme, which involves the necessity to couple an-externally generated pump beam to the Silicon integrated chip.

A very promising alternative to Silicon SRS for the integration of optical sources and amplifiers on a Si-substrate, is the so-called "hybrid integration" of III-V direct band-gap semiconductors, such as GaAs and InP, which allows to exploit the III-V materials excellent properties in terms of high optical gain, broad gain spectrum, and electrical pumping mechanisms. The main technological obstacle for hybrid integration is represented by the crystalline lattice mismatch between Si and GaAs or InP, which is about 4.1% and 8.1% respectively, and by the difference in thermal expansion coefficient, which is about 120.4% and 76.9% respectively, thus preventing the possibility to employ standard epitaxial growth techniques to grow III-V layers on Silicon with low concentrations of lattice defects.

To overcome this limitation, the most commonly employed and most mature approach to integrate III-V materials on Silicon is the wafer-bonding technique. The process starts with two different wafers, which are pre-processed in two separate foundries: the first is a standard SOI wafer, which already contains all the required Si-based passive and active optical components (waveguides, filters, modulators, etc.) and that has already been planarized by CMP techniques, while the second is a III-V material wafer, where gain layers and a sacrificial "etch stop" layer have already been created by means of epitaxial deposition processes. Dies are cut from the III-V wafer, and then bonded on top of the SOI wafer waveguides, with the optical active layers down. Different techniques can be used to bond the III-V die, such as direct bonding and adhesive bonding. In direct bonding the surface of the SOI wafer and of the III-V die

are directly put in contact with each other, without the use of any adhesive material in between. Traditional wafers direct-bonding usually requires performing a high-temperature (> 600 °C) annealing process, thus making it not suitable for III-V on Si integration, owing to the thermal expansion coefficient mismatch between the two materials, which would create excessive strain. Advanced processes have been therefore developed, such as "O_2 plasma-assisted" wafer bonding (also known as molecular bonding) [141], which leads to the formation of a very thin SiO_2 layer between the III-V and the Si wafers, and can be performed using a low temperature (≈ 300 °C) annealing step. Alternatively, the adhesive bonding approach can be used: in this case the adhesive material must be chosen in order to guarantee a sufficiently small and well-controlled thickness and an adequate transparency of the bonding layer, as well as a low process temperature. The most commonly employed adhesive material is benzocyclobutene (BCB); the BCB-based wafer bonding approach is more tolerant to surface planarity imperfections with respect to molecular bonding, and allows to obtain a bonding layer with thickness < 50 nm, even if it unfortunately exhibits a low thermal conductivity [142]. After being bonded to the SOI wafer, either by molecular or adhesive bonding, the substrate of the III-V die is etched down to the sacrificial layer, so that standard planar processing techniques can be then used to define the structure of the active device.

An example of a hybridly integrated III-V SOA on a SOI chip was demonstrated by H. Park et al. [143] in 2007; a cross-sectional schematic of the proposed device and a SEM (scanning electron microscopy) image of the fabricated device, are shown in Fig.144.

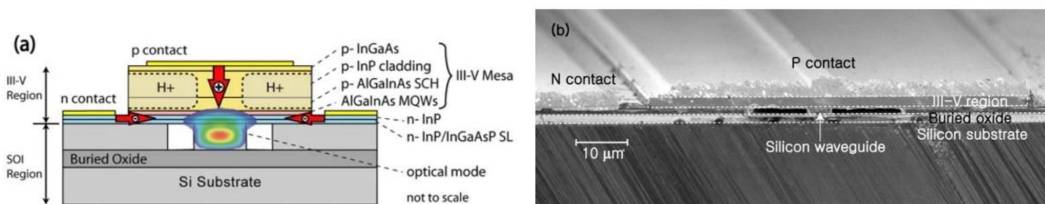

Figure 144: Cross sectional schematic (left) and SEM image (right) of the III-V SOA hybridly integrated on a SOI wafer reported in [143].

The hybridly integrated SOA reported in [143] was obtained by O_2 plasma-assisted direct bonding of a InP die over a SOI substrate, where a Si strip waveguide (width = 2 μm, height = 0.76 μm) had previously been manufactured using a RIE technique. The III-V die gain section was composed by 8 AlGaInAs quantum wells (QWs), stacked between two n and p doped AlGaInAs layers, in order to obtain a separate confinement heterostructure (SCH). RIE was used to define the amplifier mesa, and proton (H+) implantation on the two sides of the p-type mesa was performed to create a 4 μm wide current channel in order to prevents lateral current spreading. As it can

be seen in Fig.144(left), the optical mode remains mostly confined in the Si strip waveguide, with a modal overlap of 74%, and only evanescent coupling takes place with the III-V active waveguide, where there is only a 3.4% overlap of the mode with the QWs. Using lensed-fibres to butt-couple the SOI chip, the fibre-to-fibre gain of the integrated SOA was measured to be about 3 dB, while the on-chip gain (evaluated excluding fibre-to-chip losses) was estimated to be around 13 dB. The same type of hybridly integrated III-V structure, with the addition of a pair of integrated DBR mirrors in order to create a Fabry-Perot cavity, was used in [144] to demonstrate an integrated laser device, having a current threshold of 65 mA and a maximum output power of 11 mW.

A different approach in order to achieve a better overlap of the optical mode with the active III-V waveguide, and therefore an increase of the obtained optical gain, was first reported by Ben Bakir et al. in [145], where an hybridly integrated Fabry-Perot laser was demonstrated. In this case the optical coupling between the SOI rib waveguide and the III-V active waveguide, rather than being evanescent as in [143], is instead achieved by an adiabatic conversion of the optical mode propagating in the SOI waveguide, thanks to the use of adiabatic tapers which linearly widen the length of the SOI rib from 0.7 µm to 1.1 µm over a length of 120 µm. A schematic top-view and side-view of the adiabatic tapers implemented in [145], are shown in Fig.145: thanks to this approach a coupling efficiency of 97% between the Si waveguide and III-V active waveguide was estimated.

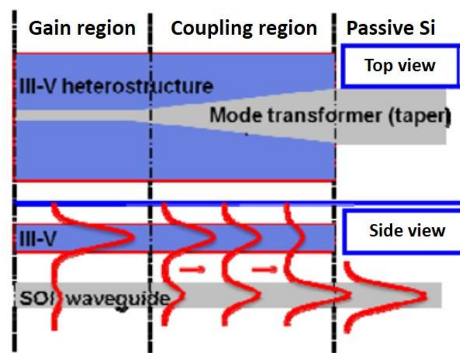

Figure 145: Top and side views of the tapered Si rib waveguide, showing the transfer of the optical supermode from the upper active waveguide to the lower silicon waveguide [145].

It is also important to mention that new technologies, such as transfer-printing and advanced epitaxial growth processes, are recently emerging as valid alternatives to wafer bonding for achieving hybrid integration of III-V materials on Silicon. Transfer printing is basically a pick-and-place technique, in which thin-film III-V stacks having micrometer-size (usually referred as coupons) are transferred from a III-V substrate to a target SOI wafer. Elastomeric stamps are used, which allow to transfer many coupons in a parallel way, thus making transfer-printing a suitable technique for high-volume production. After the coupon has been printed, standard planar fabrication processes

are used to define the active devices, similarly to wafer-bonding. However, the very small size of the printed coupons with respect to the dies used in wafer-bonding (which are usually millimer-sized) allows to avoid the wasting of precious III-V material during the etching process, while at the same time giving the possibility to integrate, on the same SOI chip, coupon transferred from different III-V substrates. Transfer-printing has already been demonstrated to be an effective technique for the integration on Silicon of both III-V based LEDs [146] and Fabry-Perot lasers [147].

On the other hand, direct epitaxial growth of III-V materials on Silicon has recently made lots of improvements and has drawn constantly increasing attention from many scientific research group worldwide, also pushed by the renewed interest of the CMOS industry regarding the possibility to use III-V materials, which are characterized by very large carrier mobility, as the gate material for next generation transistors [148, 149]. As previously discussed, the lattice constant mismatch represents the main obstacle for III-V material epitaxial growth on Silicon, as the grown III-V layer would present a high concentration of dislocations, which would behave as non-radiative recombination centers, thus limiting the achievable radiative quantum efficiency. Moreover, the different polarity of Silicon and III-V materials would lead to the formation of the so called anti-phase boundaries (APBs), which, similarly to dislocations, could act as non-radiative defects. These problems can in theory be mitigated by growing very thick buffer layers, which allows for a gradual variation of the lattice constant. However, thick buffer layers are incompatible with integration with silicon waveguides, and they also require very long growth time, which usually translates into high fabrication costs. Recently two interesting approaches have been demonstrated to reduce the buffer layer thickness while at the same time also reducing the detrimental effects of dislocations. The first approach is based on the introduction of quantum-dots based strained-layer superlattices (SLSs) in the buffer layer, which basically act as filters for the dislocations, preventing them from reaching the III-V active layers. Using this approach, very high-quality III-V material can be grown over the buffer layer; in [150] for example, a III-V on Si CW laser was demonstrated with a room temperature output power exceeding 105 mW. The second approach was instead demonstrated by Z. Whang et al. in [151]: in this case, starting from a pure <001> Si wafer, a wet chemical etch was used in order to expose the <111> crystal planes of the wafers, thus obtaining a V-groove structure, which was covered with a high-quality SiO_2 layer, and then filled by an InP buffer layer deposited by means of a metal–organic chemical vapor phase epitaxy (MOVPE). Thanks to the V-groove sidewalls crystalline orientation, APBs were suppressed, and the defects remained confined in a narrow 20 nm thick layer near the Si-InP interface, without affecting the bulk of the material. The growth was carried on until InP completely filled the trench: after that the wafer was planarized by CMP, and active layers (such as InGaAs) were grown on top of it. Using this approach, lasing action was demonstrated from the epitaxially grown samples, with a threshold pump power of 22 mW.

5.2 III-V on Si SOAs for FABULOUS Project

As previously discussed in Chapter 1, amplification stages are required on both arms of the Si-based FABULOUS reflective ONU, in order to guarantee an adequate power budget for the upstream signal, which is generated by modulating the received CW seed, and then relayed from the ONU to the OLT. These optical amplifiers are implemented as III-V based SOAa, directly integrated over the ONU Si-PIC.

A first generation of hybridly-integrated III-V on Si SOAs was fabricated by *III-V Lab*, using molecular bonding of InP dies over a patterned and planarized SOI wafer, having a native Silicon thickness equal to 440 nm. The gain section was composed by 6 InGaAsP QWs, sandwiched between two InGaAsP layers with different composition, so as to form a separate confinement heterostructure. In order to process the III-V material and define the active waveguide, 405 nm h-line photolithography and RIE were used [152]. Finally, the active wave guide was encapsulated using BCB (for passivation and to prevent lateral current spreading) and Au electrical contacts were deposited. In Fig.146 a schematic cross-section and a SEM image of the fabricated structure (which has also been used for the implementation of laser sources [153]) are shown.

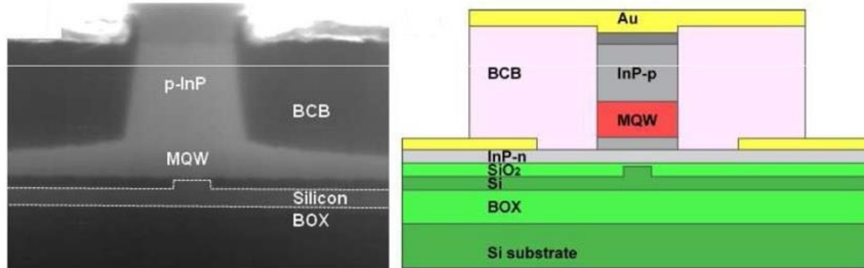

Figure 146: (left) SEM image of the fabricated III-V on Si SOA. White lines are used to mark the borders of the SOI rib waveguide. (right) Schematic cross-section of the proposed device [153].

Coupling between the Silicon Rib waveguide and the active III-V waveguide was achieved employing a double-taper structure, as shown in Fig.147.

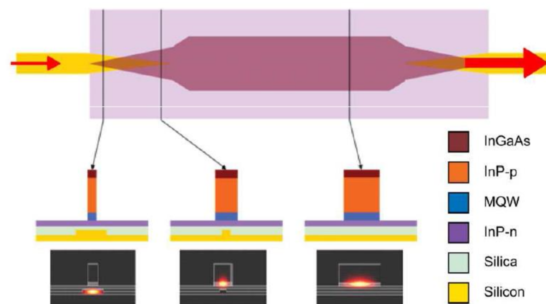

Figure 147: Top and cross-sectional views of the coupling structure of the hybrid SOA with representative mode profiles in three cross-sections [153].

This coupling configuration is conceptually similar to the one used in [145] (where only the Silicon rib waveguide was actually tapered), and allows to obtain an overlap of the optical mode with the QWs of about 10% [152], thus definitely greater than the 3.4% mode overlap reported in [143], where evanescent field coupling was employed.

Some of the fabricated samples, having length of the active waveguide equal to 1.1 mm, were packaged by *Tyndall*, in a modified butterfly package, with the inclusion of a TEC element for temperature control. Coupling between the optical fibres and the SOI chip was achieved by means of uniform 1D-GCs defined at the input/output of the Silicon rib waveguide, employing a horizontal coupling scheme with angle-polished fibres (the same coupling configuration previously described in paragraph 4.7).

5.3 Packaged SOA experimental characterization

We performed an experimental CW characterization of one of the previously described packaged SOA, using the setup shown in Fig.148.

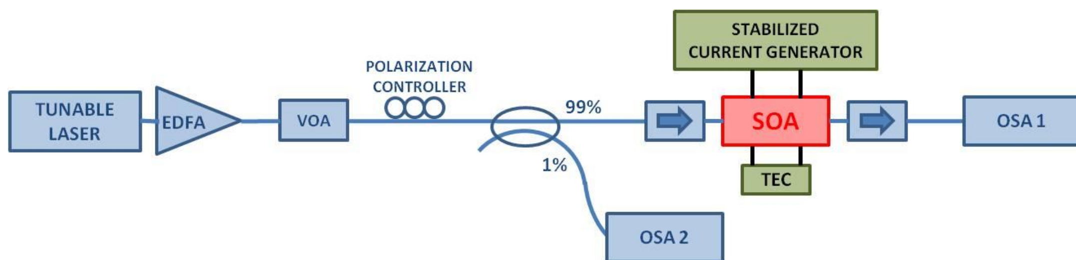

Figure 148: Experimental setup used for the packaged SOA characterization.

An external-cavity semiconductor tunable laser (with a maximum output power of 8 dBm at $\lambda = 1550$ nm) was used as the optical source, amplified by an erbium-doped fibre amplifier (EDFA) in order to increase the maximum level of optical power injectable in the device under test (the maximum output power of the employed EDFA was 30 dBm at $\lambda = 1550$ nm). The tunable laser was set to its maximum level of output power, in order to saturate the gain of the EDFA, and a variable optical attenuator (VOA) was used to control the amount of optical power effectively launched into the SOA. After that, a fibre polarization controller was used to adjust the polarization state of the seed signal (as both the Silicon GCs and the SOA quantum wells were optimized for TE polarized input light), followed by a fibre tap splitter with a 99/1 power splitting ratio. The 1% of the signal was sent to a first optical spectrum analyzer (OSA) in order to monitor the level of the input power, whereas the remaining 99% was launched into the SOA. Optical isolators were inserted immediately before and after the SOA, in order to avoid possible back-reflections towards the optical source, while the amplified output signal from the SOA was collected and recorded by means of a second OSA. A stabilized current generator was employed to feed the SOA, in order to create the population inversion required to achieve optical gain, while the device temperature T was stabilized using a thermos-electric cooler (TEC). This was

required as the SOA behavior is characterized by a strong thermal dependency (Arrhenius dependency [154]), which leads to a gain reduction when increasing T. By acquiring the optical power levels at the SOA input fibre (P_{in}) and at the SOA output fibre (P_{out}), the optical gain G can be simply calculated as:

$$G[dB] = \; P_{out}[\text{dBm}] - P_{in}[\text{dBm}] \tag{70}$$

We threated the SOA as a “black box”, meaning that all the losses originated by the coupling between the fibres and the grating couplers, and between the Si waveguide and the active material waveguide, were included in the calculated gain G.

A first set of measurement was carried out in order to evaluate the SOA gain G, as a function of P_{in} for different values of the injected electrical current I, while stabilizing the device temperature to 20 °C. Measurements results are reported in Fig.149, where the wavelength of the input signal was set to $\lambda = 1550.08$ nm, and I was varied from 50 mA to 80 mA.

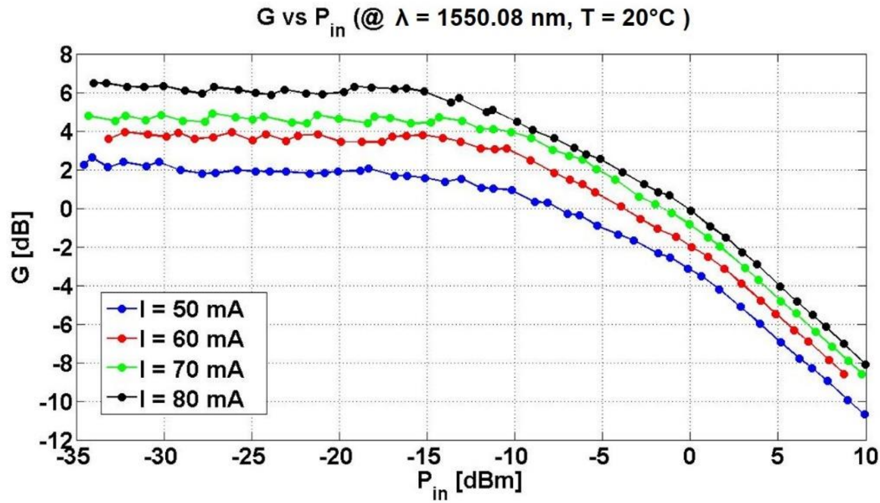

Figure 149: Optical gain G as a function of the fibre input optical power P_{in} at $\lambda = 1550.08$ nm and $T = 20$ °C. The different colors of the curves, refer to the electrical current values used to feed the SOA.

Fig.149 shows the classical gain saturation behavior, typical of III-V semiconductor amplifiers, as a function of the input optical power. The un-saturated gain was found to vary from 2.0 dB up to 6.2 dB, when increasing the driving current from 50 mA to 80 mA, whereas the input saturation power (which define the input power level at which the optical gain drops by 3 dB) was extracted to be around -5.2 dBm.

When repeating the same type of measurements with a slight variation of the input signal wavelength λ however, we observed a consistent variation of the measured un-saturated gain; this is, for example, shown in Fig.150, where the gain curves as a function of P_{in}, obtained for a driving current $I = 80$ mA, are reported when λ equals 1550.08 nm or 1550.06 nm.

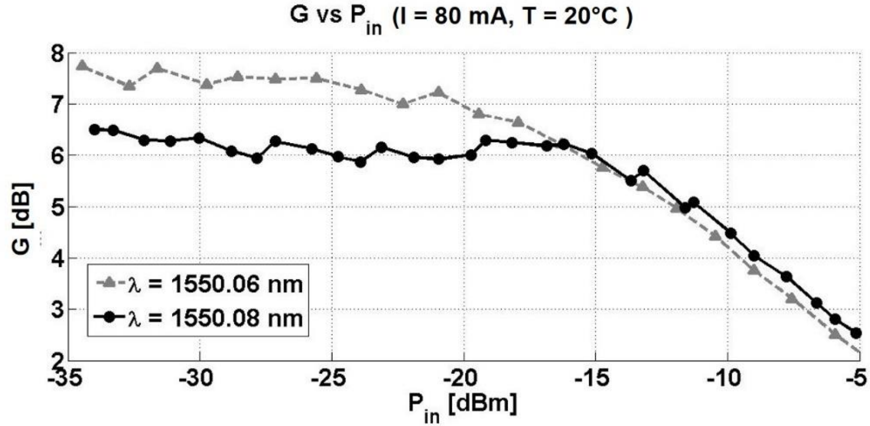

Figure 150: Optical gain G as a function of the fibre input optical power P_{in} at I = 80 mA and T = 20 °C. The grey curve with triangles represent a measurement carried out using an input signal wavelength λ = 1550.06 nm, while the black curve with dots represent a measurement carried out using an input signal wavelength λ = 1550.08 nm.

In order to better understand the reason for this variation, we decided to evaluate the dependency of the un-saturated optical gain over the input signal wavelength λ. The obtained results are reported in Fig.151, where the SOA driving current I was set to 75 mA, and the optical input power P_{in} was kept fixed to -15 dBm.

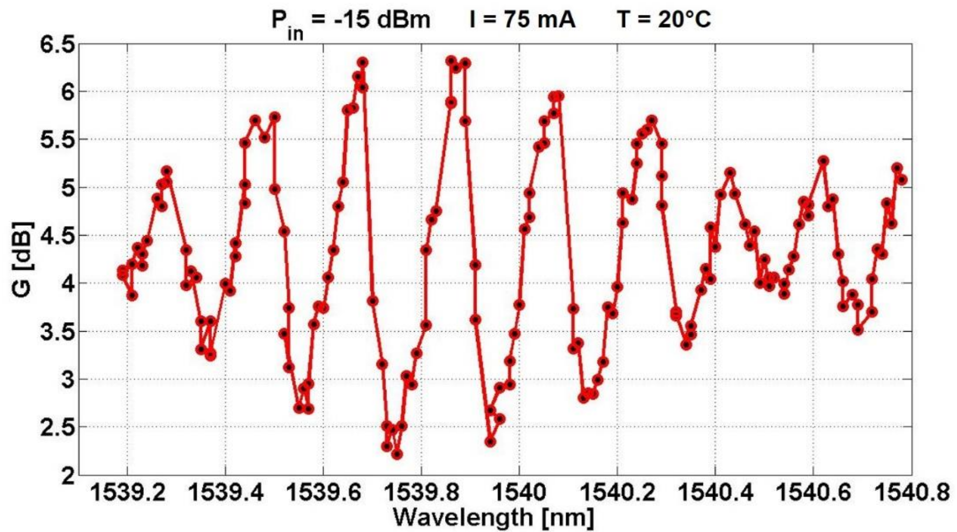

Figure 151: Un-saturated gain as a function of the optical wavelength λ, for I = 75 mA, P_{in} = -15 dBm, and T = 20 °C. A strong amplitude ripple is superimposed on the gain curve, with maximum amplitude ≈ 4 dB, and period $\Delta\lambda \approx 0.2$ nm.

As it can be seen from Fig.151, the un-saturated gain of the analyzed sample exhibits a strong amplitude ripple, having a maximum amplitude ≈ 4 dB. As the SOA ASE emission is directly proportional to the optical gain [154], the same amplitude oscillation observed on the gain spectrum can be found on the ASE spectrum, as it is shown in Fig.152.

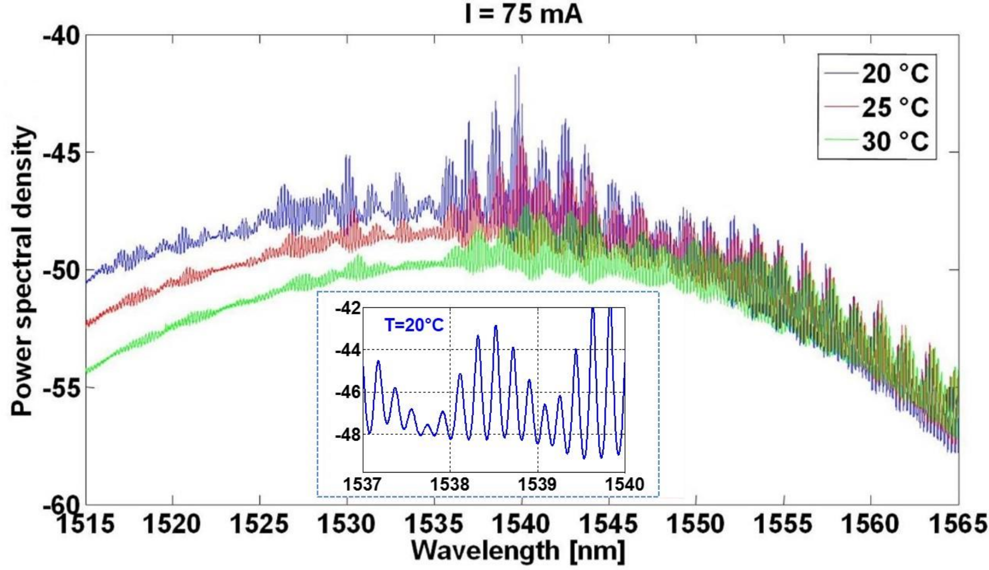

Figure 152: OSA acquired (resolution = 0.01 nm) ASE spectra of the analyzed SOA obtained for a driving current I = 75 mA, and for T = 20 °C (blue curve), 25 °C (red curve), and 30 °C (green curve). A temperature increase leads to a red-shift of the ASE spectrum, and to a reduction of the ripple amplitude, due to optical gain reduction. The inset show a detail of the ASE spectrum at T = 20 °C, which matches the gain ripple observed in Fig.151.

From Fig.152 it can be noticed that the amplitude ripple is composed by the superimposition of two oscillations, having period $\Delta\lambda$ respectively equal to 0.2 nm and 1.3 nm. These values are compatible with the FSRs of parasitic Fabry-Perot cavities having length similar to that of the Silicon waveguide and of the active material waveguide respectively. We therefore believe the ripple to be originated by spurious back-reflections taking place in correspondence of the Si-grating couplers and of the Si/III-V tapers, which generates a pattern of resonant longitudinal modes into the SOA.

When a narrow-bandwidth signal is launched into the SOA, the resulting optical gain will strongly vary according to the relative spectral position of the signal wavelength with respect to the peaks of the resonant mode pattern. Therefore, if the wavelength of the input signal is initially set so as to match the wavelength of one of the resonant mode pattern maxima, an increase of the injected current will lead, because of the FCD effect, to a spectral shift of the resonance pattern, thus preventing the signal from experiencing the maximum achievable optical gain (as we previously reported in Fig.150). To overcome this limitation, we performed a new set of measurement, in order to evaluate the un-saturated gain G (for P_{in} = -25 dBm) as a function of the driving current I: this time the wavelength of the input signal was finely tuned near λ = 1550 nm for every increment of the current I, so as to be sure to keep the signal aligned with one the maxima of the resonance pattern. Measurements results are reported in Fig.153, where it can be seen that a considerable gain of 10.7 dB was obtained, for I = 120 mA.

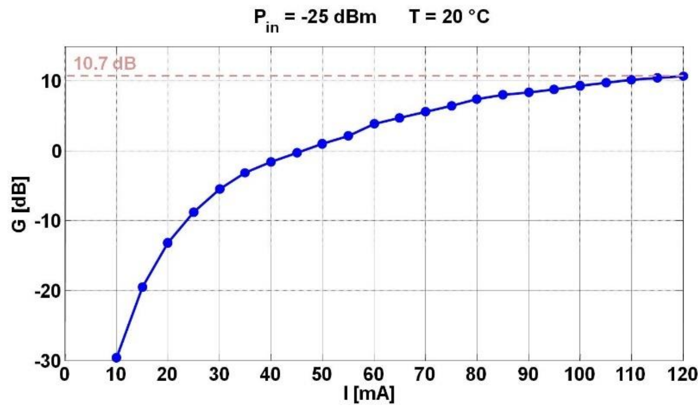

Figure 153: Un-saturated optical gain as a function of the driving current I, for an optical input power P_{in} = -25 dBm. At every I increment, the wavelength of the input signal was finely tuned near 1550 nm in order to align it with one of the maxima of the resonance pattern.

It is important to mention that a spectral shift of the resonant modes pattern also takes place when, at a fixed level of feeding current I, the input optical power P_{in} is increased towards the gain saturation threshold. This is due to the fact that the carrier depletion in the active material also leads to a FCD effect, which results in a change of the optical length of the parasitic Fabry-Perot cavity. This can be easily observed for high values of the feeding current, as it is for example shown in Fig.154, where I = 120 mA. In this case, we initially set the wavelength of the laser signal so as to be aligned with a maximum of the resonance pattern, in order to maximize the un-saturated gain, and we then evaluated G as a function of P_{in}. It can be seen that, for P_{in} $>$ -20 dBm, the effective gain experienced by the signal undergoes a very rapid reduction, which is caused by the “artificial” superimposition of the material gain saturation, and of the resonance modes pattern shift. When the pattern shift is equal to its FSR, the input signal finds itself newly aligned with one of the cavity mode, so that the optical gain is apparently increased (as it can be seen when P_{in} is comprised between -5 dBm and -2.5 dBm). When the input power P_{in} is further increased instead, the optical gain starts to decrease again.

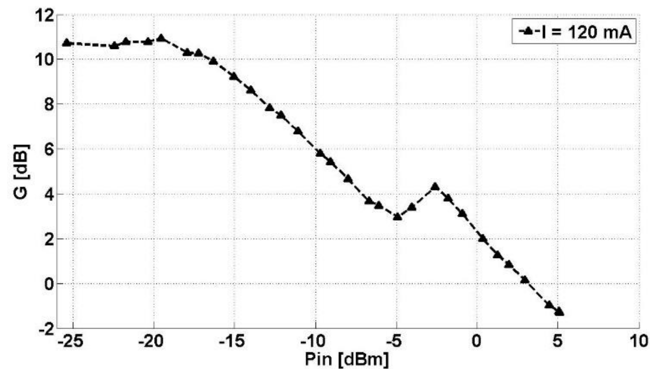

Figure 154: Optical gain G as a function of the input optical power P_{in}, for a driving current I = 120 mA.

The last measurement that we performed on the packaged SOA, was done in order to evaluate the noise factor (NF), an important parameter which basically describes how much the signal-to-noise ratio (SNR) of a signal is degraded after amplification, because of the amplifier ASE emission. The NF factor can be calculated as:

$$NF(\lambda) = \frac{2P_{ASE,||}}{h\nu \ G(\lambda)B_0} \tag{71}$$

Where $h\nu$ is the photon energy, $G(\lambda)$ is the optical gain, $P_{ASE,||}$ is the optical power of the ASE emission, co-polarized with the amplified signal, and B_0 is the detection bandwidth (expressed in Hz), corresponding the wavelength-resolution of the OSA-acquired spectra. Measurements were carried out using the setup previously described in Fig.148, but without the EDFA amplifier, so as to reduce the noise contribution at the input of the SOA. The laser output optical power was set to its maximum value, and the power input to the SOA was then varied using a VOA, in order to guarantee a constant optical signal-to-noise ratio (OSNR) for the input signal. An example of a OSA-acquired spectrum (with a 0.1 nm resolution) is shown in Fig.155(left). It can be seen that the ASE power spectral density (both the ASE and the amplified signal are TE-polarized because of the Silicon GCs) is again characterized by the same amplitude ripple previously observed in the other measurements, originated by the longitudinal resonant modes pattern. To overcome this problem, we applied a moving average filter (with an averaging-window length of 1 nm) to the output spectra, and we then evaluated the ASE power spectral density at a distance of 1.5 nm to the right of the amplified signal (as marked by the arrow in Fig.155(left).

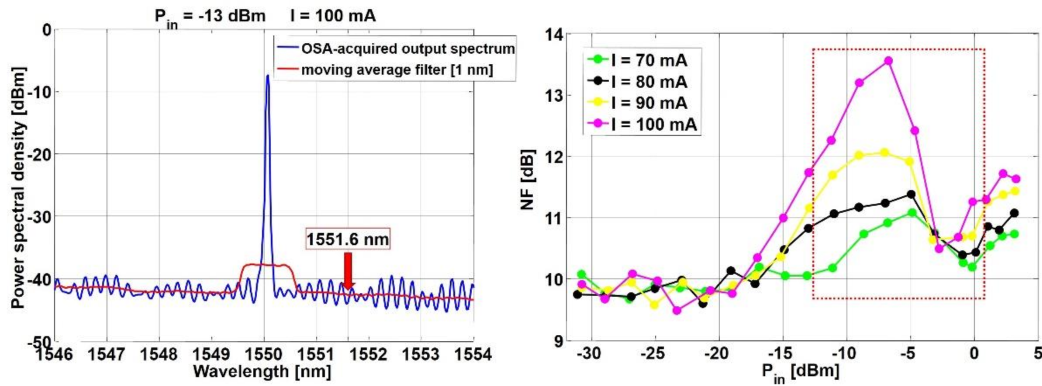

Figure 155: (left) Example of a OSA-acquired output spectrum (with a 0.1 nm resolution), where both the amplified signal and the ASE emission spectra, characterized by a parasitic amplitude ripple, can be observed (blue trace). In order to smooth the ripple, a moving average filter (with a 1 nm averaging window) was applied to the output spectrum (red trace), and the ASE power spectral density was evaluated at a distance of 1.5 nm from the amplified signal central wavelength. (right) NF (expressed in dB) as a function of P_{in}, for different values of the feeding current I. The wavelength of the input signal is initially aligned, for low values of P_{in}, with one peak of the resonant mode pattern.

The NF was calculated as a function of the optical input power P_{in}, and the wavelength of the input signal was initially carefully aligned, in the vicinity of 1550 nm, to one peak of the longitudinal resonance pattern (for the lowest value of P_{in} employed). Measurements were then repeated, using the same strategy, for different values of the feeding current (from 70 mA up to 100 mA). The resulting NF (expressed in dB) is reported in Fig.155(right). It can be seen that the measured NF is comprised between 9.5 dB and 10 dB for low levels of P_{in}, and, as expected by theory [155], it reduces when P_{in} is increased, due to gain saturation. The strange non-monotonic behavior, which is highlighted in the red frame of Fig.155(right), gets more evident for high values of I, and can be explained by the fact that, when P_{in} is increased towards the material gain saturation threshold, the wavelength shift of the resonant mode pattern leads to an apparent faster reduction of the signal gain (as it has been previously shown in Fig.154), thus affecting and "over-boosting" the resulting NF value.

As a concluding remark, we can claim that the analyzed SOA is characterized by a very high fibre-to-fibre gain (10.7 dB at $I = 120$ mA), as it has also been confirmed by measurements carried out on other samples of the same SOA device [152]. A direct comparison can be made with the SOA reported in [143], where the measured fibre-to-fibre gain was only about 3 dB: this proves the efficacy of the double-taper coupling configuration, which, compared to the evanescent field coupling configuration, allows the optical mode to experience a much better overlap with the III-V QWs, thus experiencing higher optical gain. It is also important to mention that the fibre-to-fibre gain can be further increased by reducing the fibre-to-GC loss, and the loss between the Si and the III-V waveguide. Regarding the NF, the values that we measured for the unsaturated regime (9.5-10 dB) are very close to the one reported by Park et al. (10-11 dB) for the evanescent-coupling SOA [143]; these values are however still quite far from the values that can be achieved in state-of-the-art III-V SOAs with reduced noise, where NF can even be < 4.5 dB [156, 157]. It must be noticed however that the performances of our SOA are severely affected by a high-amplitude (≈ 4 dB) spectral modulation of the amplifier gain, induced by spurious back-reflections, which can result in a distortion of modulated signals spectrum. This problem can be even worse in polarization-diversity architecture such as the FABULOUS ONU, where the optical power input to each SOA can vary in a broad range of possible values, according to the polarization of the input signal. Variations of the input optical power can in fact leads to FCD effects in the III-V waveguide, resulting in a spectral-shift of the spurious cavity longitudinal modes pattern, and consequently, in big variation of the gain and the noise factor experienced by the signal. This shows that improvements and optimizations in the fabrication and packaging processes, are required in order to suppress spurious back-reflections and maximize the hybridly-integrated SOAs performances.

Conclusions

The objective of this PhD activity has been the theoretical analysis and experimental characterization of high-performing Silicon-based optical components, conceived for integration in a multi-function photonic integrated circuit (PIC).

During my investigations 5 aspects were mainly considered:

1. The optimal design and characterization of high-efficiency 1D Grating couplers.
2. The characterization of 2D grating couplers (based on an already available design).
3. The study of the performance exhibited by height reduced Si-waveguides as a function of their width.
4. The design and characterization of integrated optical filter based on micro-ring resonators and with extremely low losses.
5. The characterization of semiconductors-based (III-V) optical amplifiers for Si-PIC

Regarding the first research line, we aimed at achieving efficient optical coupling between standard single-mode fibres and PICs. We proposed a novel simple design strategy for achieving a highly-efficient 1-D diffractive grating coupler (GC), based on the simultaneous linear apodization of both the grating fill-factor and the grating period. This allows to conveniently vary the grating effective index along the light direction of propagation into the grating, while at same time ensuring the respect of the Bragg condition in each section of the grating. We performed a complete set of 2D-FDTD simulations, taking into accounts Silicon-on-Insulator (SOI) platforms with different thicknesses of the Silicon layer, and exploring different combinations of etch depth and linear apodization factor. Different grating parameters were analyzed, such as the coupling efficiency (CE), the directionality, and the reflectivity. When employing a 260 nm Silicon thick SOI and using a 160 nm deep etch, we theoretically demonstrated an extremely high CE of 83% (-0.8 dB). We also showed a consistent improvement in directionality (+10%) and reflectivity (-5%) for our apodized design with respect to the uniform grating approach, highlighting the absolute necessity to optimize the etching depth. Test structures were fabricated at the *University of Southampton* and then experimentally characterized. We reported an average CE of -1.1 dB and an average 1-dB bandwidth of 38.8 nm for samples fabricated in different chips, with a best-performance device showing a record-high CE of -0.9 dB. This is, to our knowledge, the highest experimental result ever reported for a 1-D grating coupler implemented without the aid of a substrate-embedded back-reflector.

We then experimentally evaluated the performances of a photonic crystal based 2D-GC, implemented in a standard 220 nm Silicon thick SOI platform, and able to handle both the orthogonal polarization states of light incoming from a single-mode optical fibre. The design of the photonics crystal was previously optimized by researchers in the *Physics Department* of the *University of Pavia*, showing a maximum theoretical CE of -3.2 dB. We designed a set of test structures which were fabricated by *CEA-Leti*, and we then performed an experimental characterization of the fabricated samples by means of a vertical coupling setup, achieving a CE of -4.4 dB (with a 1-dB bandwidth of 33 nm) for the device including the taper, and a CE of -3.75 dB for the taper-less configuration. Differences between the experimental and theoretical results can be ascribed to fabrication imperfections and to the presence of non-optimal tapers. Furthermore, additional sets of measurements were performed, to assess the grating-coupler tolerances.

The third activity was dedicated to the reduction of propagation losses in Silicon optical waveguides with sub-micrometer dimensions. We carefully investigated the performance of height-reduced (100nm instead of 220nm) Silicon optical waveguides. We designed a set of test structures which were fabricated by *CEA-Leti*, employing Reactive Ion Etching (a fully CMOS-compatible process) to lower the waveguide height from 220 nm (the initial Si-thickness on the wafer) to 100 nm. Experimental data demonstrated a significant reduction of propagation losses which passed from about 3 dB/cm for standard waveguides (500x220 nm) to $\approx$ 1.8 dB/cm for 825x100 nm waveguides. We were also able to extract the group index and group velocity dispersion values for all of the implemented waveguide geometries, employing Mach-Zehnder interferometric structures. Results showed a lower group index value for reduced height waveguides with respect to the standard ones, as expected because of lower modal confinement, and anomalous group velocity dispersion, which can be tailored from $\approx$ -8130 ps/(nm·km) to $\approx$ -3900 ps/(nm·km) by increasing the waveguide width from 500 nm to 800 nm. The obtained high values of group velocity dispersion, combined with the excellent performances in terms of propagation loss, suggests that reduced height waveguides could find a suitable application in integrated devices for fibres dispersion compensation.

Thanks to the careful analysis and characterization of height-reduced waveguides, we also took advantage of their delicate modal confinement and low propagation loss to obtain optical-resonator filters characterized by low insertion loss and WDM compatible spectral characteristics (3-dB bandwidth $>$ 40 GHz, 20-dB bandwidth $<$ 100 GHz). During the design stage we explored the possibility to employ a different number of cascaded resonators, and to use different resonator topologies as well as different coupling configurations. As a final result of the design activity, we implemented two different filter configurations: ring-based resonators employing curved coupling sections and reduced height waveguides (100 nm), and racetrack-based resonators employing standard (500x220 nm) waveguides. Different test chips were fabricated (by

CEA-Leti) and then characterized in our labs. We assessed both the linear and non-linear optical properties of the filters. As a result of the characterization, we observed that, by using 2 cascaded ring resonators with optimized geometrical parameters, an insertion loss of 0.8 dB and a 3-dB bandwidth of 95 GHz were achieved. The use of reduced height waveguides was also found to beneficial for reducing the effect of non-linear impairments, as it allowed for a higher threshold-power with respect to standard waveguides.

As a final part of this work, we addressed the problem of the integration of III-V materials on Silicon to implement optical amplifiers. We performed a complete CW characterization of the gain properties of a quantum-well (QW) semiconductor optical amplifier (SOA), which was hybridly-integrated, using a molecular bonding technique, on a Silicon chip by *III-V Lab*, and then packaged by *Tyndall*. We reported a non-saturated gain of 10.7 dB, for a feeding current of 120 mA, an input saturation power of about -5.2 dBm and a non-saturated noise-figure (NF) comprised between 9.5-10 dB. These values highlight that the integrated SOA performance is obviously lower than that achievable by stand-alone components, but it is in any case better than that demonstrated by the hybridly-integrated SOAs previously reported in literature.

Appendix A

FABULOUS upstream transmission experimental results

Different upstream transmission experiments were performed by the partners of FABULOUS Project, both using discrete optical components to emulate the FABULOUS ONU architecture, in order to demonstrate the feasibility of the proposed network architecture, and also using a first prototype of the Silicon based ONU, where only the 2D-GC and the MZM where integrated on the PIC.

The discrete ONU was implemented following a scheme similar to the one reported in Fig.10, thus including a PBS and a customized $LiNbO_3$ MZM, offering individual access to both the electrodes and characterized by an electro/optical bandwidth of 12 GHz. Nevertheless, only a single bidirectional SOA was included, placing it out of the ONU loop and before the PBS, rather than having one SOA on each of the branches of the loop (as shown in Fig.10). A first set of experiment was carried out targeting an aggregate capacity of 32 Gb/s over a single wavelength, serving 32 different ONUs with a 1 Gb/s capacity per user. Only 2 discrete ONUs were implemented, while the Amplified-Spontaneous-Emission (ASE) interference produced by the remaining 30 devices, which were not physically implemented, was emulated via a noise-loading mechanism. The ODN for the experimental measurements was composed by a 37 Km long portion of the metropolitan optic fibre network of the city of Turin, and a variable optical attenuator (VOA) to change the ODN loss. A CW signal at the wavelength λ of 1550 nm and with a launch power of +9 dBm was used as the optical seed. A 16-QAM modulation format was used for each electrical subcarrier, adopting a square-root raised cosine shaping with a 0.1 roll-off factor. Each FDMA channel carried 300 Mbaud, with a 20% FEC overhead, thus requiring an electrical bandwidth of 330 MHz per user and, as no guard-band was foreseen between adjacent channels, an overall electrical bandwidth of 11 GHz to accommodate all of the 32 supported users. The system was optimized by a careful optimization of the MZM modulation index and of the spectral position of each electrical subcarrier (to reduce the negative effects of second and third electrical harmonic components), and by an optimization of the SOA biasing current. The performances of the network were then evaluated in terms of the Bit-error-rate (BER) received at the OLT as a function of the ODN loss. Measurements were carried out adopting an “offline” approach, thus using a real-time oscilloscope to emulate the OLT. Considering that the FEC hard-decoding scheme is able to correct the incoming US data stream up to a BER of 10^{-2}, the maximum tolerable ODN loss was found to be 31.5 dB (when using a MZM modulation index of 20%) [59], thus being compliant with the requirements of standard NG-PON2.

A second set of experiments was then carried out using the same setup previously described, but including 5 discrete ONUs (instead of 2), while simulating the effect of the remaining 27 ONUs via noise-loading. The position of the electrical subcarriers of

the 5 ONUs was set in order to maximize the electrical interference experienced by one of the channel, chosen to be the channel under test (CUT); to do that the remaining 4 channels were organized in order to have 2 channels adjacent to the CUT, and 2 channels generating a second harmonic component over the electrical bandwidth of the CUT. BER measurements showed that the maximum tolerable ODN loss was, in this case, 31 dB [60]. Beside the single wavelength transmission, also the WDM operation of the FABULOUS architecture was tested. To do that, 4 seed wavelengths (1549.32, 1550.12, 1550.92 and 1551.72 nm) were launched across the ODN with a launching power of +9 dBm, and a discrete ONU, with the enclosure of WDM filters, was used to generate the CUT over one of these wavelengths. A reflective electro-absorption modulator (R-EAM) was then used to generate 7 more electrical channels (placed in order to surround the CUT), both on the wavelength under test and on the remaining 3 wavelengths. BER measurements showed that no penalty was introduced by WDM operation with respect to single-wavelength [60], as it can be seen in Fig.156.

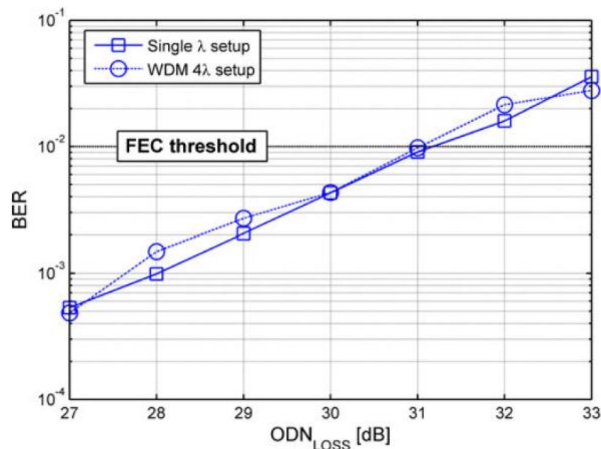

Figure 156: BER of the US 16-QAM signal, measured at the OLT as a function of ODN loss for single-wavelength transmission and for WDM operation. The threshold is set by the maximum incoming BER that the implemented FEC code is able to accept [60].

Finally, the performances of the partially-integrated Silicon based ONU were evaluated. The integrated ONU and a discrete-components ONU (the same used for the previously described experiments) were connected to an ODN composed by 25 km of standard SMF and a VOA to increase at will the ODN loss. Only single-wavelength operation was performed, using a CW seed with central wavelength λ of 1550.92 nm and +9 dBm of launching power. System performances were again evaluated in terms of the BER received at the OLT as a function of the ODN loss, using both an “offline” approach (the same used for the discrete ONU testing, with a FEC BER threshold of 10^{-2}) and a “real-time” approach, based on the use of FPGAs, both at the OLT and ONU sides, where a FCE algorithm with a 10-4 outage threshold was implemented. Initially a 16-QAM modulation with a 300 MBaud speed was unsuccessfully tested, as the received BER at the OLT was 10^{-3} without any extra attenuation applied to ODN.

A more robust QPSK modulation was then adopted, even if this brought the US bit-rate per user to drop from 1 Gbps (the project target value) to 500 Mbps. Using this modulation format, the maximum tolerable ODN losses were measured to be 24 dB in offline processing, and 21 dB in real time processing [62], as shown in Fig.157. These values are definitely lower than the ones measured for the discrete-components ONU, due to high fibre-to-fibre loss of the PIC, which was measured to be about 30 dB. This highlights the importance of the implementation of hybrid integrated III-V on Silicon SOAs in the next generation of FABULOUS integrated ONU, in order to increase the optical power budget and consequently increase the supported ODN loss range.

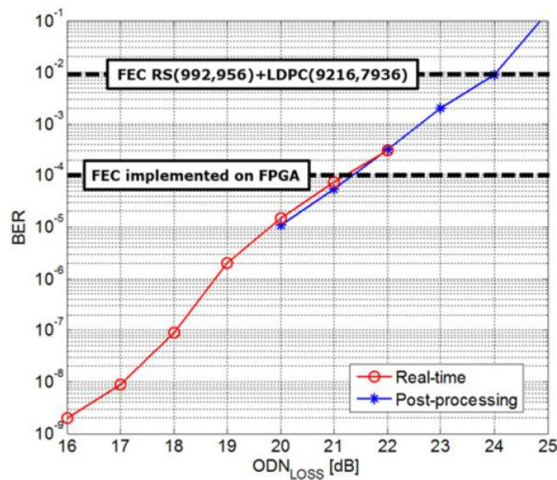

Figure 157: BER of the US QPSK signal generated by the integrated ONU, measured at the OLT as a function of ODN loss in real-time (red trace) and in post-processing (blue trace). The FEC incoming BER threshold is 10^{-4} in real time, and 10^{-2} in post-processing.

Appendix B

Scientific production

Peer reviewed journal publications

1. **R. Marchetti**, V. Vitali, C. Lacava, I. Cristiani, G. Giuliani, V. Muffato, M. Fournier, S. Abrate, R. Gaudino, E. Temporiti, L. Carroll and P. Minzioni, "Low-Loss Micro-Resonator Filters Fabricated in Silicon by CMOS-Compatible Lithographic Techniques: Design and Characterization," MDPI Appl. Sciences 7 (2), 174–185 (2017).

2. **R. Marchetti**, V. Vitali, C. Lacava, I. Cristiani, B. Charbonnier, V. Muffato, M. Fournier, and P. Minzioni, "Group-velocity dispersion in SOI-based channel waveguides with reduced-height," Opt. Express 25(9), 9761–9767 (2017).

3. S. Straullu, P. Savio, G. Franco, R. Gaudino, V. Ferrero, S. Bernabé, M. Fournier, V. Muffato, S. Menezo, B. Charbonnier, E. Temporiti, D. Baldi, G. Minoia, M. Repossi, L. Carrol, J. Lee, P. O'Brien, **R. Marchetti**, G.-H. Duan, F. Saliou, and S. Abrate, "Demonstration of a Partially Integrated Silicon Photonics ONU in a Self-Coherent Reflective FDMA PON," J. Light. Technol. 35(7), 1307–1312 (2017).

4. **Riccardo Marchetti**, Cosimo Lacava, Ali Khokhar, Xia Chen, Ilaria Cristiani, David J Richardson, Graham T. Reed, Periklis Petropoulos, and Paolo Minzioni, "High-efficiency grating-couplers: demonstration of a new design strategy", Sci. Rep. 7(16670) 1-8 (2017).

International conference publications

1. C. Lacava, **R. Marchetti (speaker)**, G. Giuliani, M. Fournier, S. Menezo, S. Messaoudene, and P. Minzioni, “Impact of waveguide cross section on nonlinear impairments in integrated optical filters for WDM communication systems,” CLEO Europe 2015, 21-25 June 2015, Munich, Germany (CI-P.8).

2. C. Lacava, M.J. Strain, V. Pusino, **R. Marchetti**, P. Minzioni, M. Sorel, and I. Cristiani, “Highy Nonlinear AlGaAs Waveguides for Broadband Signal Generation,” CLEO Europe 2015, 21-25 June 2015, Munich, Germany (CD-P.4).

3. C. Lacava, L. Carrol, A. Bozzola, **R. Marchetti**, P. Minzioni, I. Cristiani, M. Fournier, S. Bernabe, D. Gerace, and L. C. Andreani, “Design and characterization of low-loss 2D grating couplers for silicon photonics integrated circuits,” SPIE Photonics West 2016, 13-18 February 2016, San Francisco, United States (9752-30).

4. C. Lacava, **R. Marchetti**, V. Vitali, I. Cristiani, G. Giuliani, M. Fournier, S. Bernabe, and P. Minzioni, “Reduced nonlinearities in 100-nm high SOI waveguides,” SPIE Photonics West 2016, 13-18 February 2016, San Francisco, United States (9753-37).

5. S. Straullu, P. Savio, G. Franco, R. Gaudino, S. Bernabé, M. Fournier, V. Muffato, S. Menezo, B. Charbonnier, E. Temporiti, D. Baldi, G. Minoia, M. Repossi, L. Carrol, J. Lee, P. O’Brien, **R. Marchetti**, G. Duan, F. Saliou, and S. Abrate, “Demonstration of a Partially Integrated Silicon Photonics ONU in a Self-Coherent Reflective FDMA PON,” ECOC 2016 (Post Deadline), 18-22 September 2016, Düsseldorf, Germany.

6. **R. Marchetti (speaker)**, V. Vitali, C. Lacava, I. Cristiani, G. Giuliani, L. Adelmini, M. Fournier, and P. Minzioni, “Low-Loss Integrated Ring-Resonators Filters Realized by CMOS Fabrication Process,” CLEO Europe 2017, 25-29 June 2017, Munich, Germany (CI-P.2).

7. **R. Marchetti**, C. Lacava, A. Khokhar, I. Cristiani, D. Richardson, P. Petropoulos, and P. Minzioni, (2017, July). Reflector-less Grating-Coupler with a-0.9 dB Efficiency Realized in 260-nm Silicon-On-Insulator Platform. OSA Advanced Photonics Congress 2017, 24-27 July 2017, New Orleans, United States. (pp. ITu1A-2).

Bibliography

[1] S. M. Sze, Physics of semiconductor devices, New York: J. Whiley and Sons, 1981.

[2] G. E. Jellison Jr and F. A. Modine, "Optical absorption of silicon between 1.6 and 4.7 eV at elevated temperatures," *Appl. Phys. Lett.,* vol. 41, no. 2, pp. 180-182, July 1982.

[3] K. D. Hirschman, L. Tsybeskov, S. P. Duttagupta and P. M. Fauchet, "Silicon-based visible light-emitting devices integrated into microelectronic circuits," *Nature,* vol. 384, no. 6607, pp. 338-341, Nov 1996.

[4] G. Franzò, F. Priolo, S. Coffa, A. Polman and A. Carnera, "Room-temperature electroluminescence from Er-doped crystalline Si," *Appl. Phys. Lett.,* vol. 64, no. 17, pp. 2235-2237, Feb. 1994.

[5] L. Pavesi, L. Dal Negro, C. Mazzoleni, G. Franzò and F. Priolo, "Optical gain in silicon nanocrystals," *Nature,* vol. 408, no. 6811, pp. 440-444, Nov. 2000.

[6] H. Philipp and E. Taft, "Optical Constants of Silicon in the region 1 to 10 eV," *Phys. Rev. Lett.,* vol. 120, no. 1955, pp. 37-38, Oct. 1960.

[7] F. Bianco, E. Borga, A. Yeremian, B. Dierre, K. Fedus, P. Bettotti, A. Pitanti, R. Pierobon, M. Ghulinyan, G. Pucker, M. Cazzanelli and L. Pavesi, "Second-order susceptibility $\chi(2)$ in Si waveguides," in *Group IV Photonics (GFP), 2011 8th IEEE International Conference on. IEEE*, 2001.

[8] B. Chmielak, M. Waldow, C. Matheisen, C. Ripperda, J. Bolten, T. Wahlbrink, M. Nagel, F. Merget and H. Kurz, "Pockels effect based fully integrated, strained silicon electro-optic modulator," *Opt. Express,* vol. 19, no. 18, pp. 17212-17219, Aug. 2011.

[9] S. A. Clark, B. Culshaw, E. J. C. Dawnay and I. E. Day, "Thermo-optic phase modulators in SIMOX material," in *Proc. SPIE*, 2000.

[10] R. Soref and B. R. Bennet, "Electrooptical effects in silicon," *IEEE J. Quantum Electron.,* vol. 23, no. 1, pp. 123-129, Jan. 1987.

[11] L. Yin and G. P. Agrawal, "Impact of two-photon absorption on self-phase modulation in silicon waveguides," *Opt. Lett.,* vol. 32, no. 14, pp. 2031-2033, July 2007.

[12] G. P. Agrawal, Nonlinear fiber optics, Academic press, 2007.

[13] C. Manolatou and M. Lipson, "All-Optical Silicon Modulators Based on Carrier Injection by Two-Photon Absorption," *J. Lightwave Technol.,* vol. 24, no. 3, pp. 1433-1439, Mar. 2006.

[14] V. R. Almeida, C. A. Barrios, R. R. Panepucci and M. Lipson, "All-optical control of light on a silicon chip," *Nature,* vol. 431, no. 7012, pp. 1081-1084, Oct. 2004.

[15] C. Lacava, M. J. Strain, P. Minzioni, I. Cristiani and M. Sorel, "Integrated nonlinear Mach Zehnder for 40 Gbit/s all-optical switching," *Opt. Express,* vol. 21, no. 18, pp. 21587-21595, Sept. 2013.

[16] Q. Xu and M. Lipson, "All-optical logic based on silicon micro-ring resonators," *Opt. Express,* vol. 15, no. 3, pp. 924-929, Feb. 2007.

[17] M. J. Strain, C. Lacava, L. Meriggi, I. Cristiani and M. Sorel, "Tunable Q-factor silicon microring resonators for ultra-low power parametric processes," *Opt. Lett.,* vol. 40, no. 7, pp. 1274-1277, Apr. 2015.

[18] R. A. Soref and J. P. Lorenzo, "Single-crystal silicon: a new material for 1.3 and 1.6 µm integrated-optical components," *Electron. Lett.,* vol. 21, no. 21, pp. 693-694, Oct. 1985.

[19] G. Abstreiter, "Engineering the future of electronics," *Physics World,* vol. 5, no. 3, pp. 36-39, Mar. 1992.

[20] R. A. Soref, "Silicon-based optoelectronics," *Proceedings of the IEEE,* vol. 81, no. 12, pp. 1687-1706, 1993.

[21] G. K. Celler, "Silicon-on-insulator films by oxygen implantation and lamp annealing," *Solid State Technology,* vol. 30, no. 3, pp. 93-98, 1987.

[22] B. N. Kurdi and D. G. Hall, "Optical waveguides in oxygen-implanted buried-oxide silicon-on-insulator structures," *Opt. Lett.,* vol. 13, no. 2, pp. 175-177, Feb. 1988.

[23] M. Bruel, "Process for the production of thin semiconductor material films". Patent US5374564 (A), 20 12 1994.

[24] Y. Bogumilowicz, A. Abbadie, V. Klinger, L. Benaissa, P. Gergaud, D. Rouchon, C. Maurois, C. Lecouvey, N. Blanc, C. Charles-Alfred, A. Drouin, B. Ghyselen, A. Wekkeli, F. Dimroth and V. Carron, "Realization and characterization of thin single crystal Ge films on sapphire," *Semicond. Sci. Technol.,* vol. 28, no. 3, p. 035013, Feb. 2013.

[25] A. Rickman, G. T. Reed, B. L. Weiss and F. Namavar , "Low-Loss Planar Optical Waveguides Fabricated in SIMOX Material," *IEEE Photonics Technol. Lett.,* vol. 4, no. 6, pp. 633-635, June 1992.

[26] J. Schmidtchen, A. Splett, B. Schüppert, K. Petermann and G. Burbach, "Low loss singlemode optical waveguides with large cross-section in silicon-on-insulator," *Electron. Lett.,* vol. 27, no. 16, pp. 1486-1488, Aug. 1991.

[27] R. A. Soref, J. Schmidtchen and K. Petermann, "Large Single-Mode Rib Waveguides in GeSi-Si and Si-on-SiO2," *IEEE J. Quantum Electron.,* vol. 27, no. 8, pp. 1971-1974, Aug. 1991.

[28] S. P. Chan, C. E. Png, S. T. Lim, G. T. Reed and V. M. N. Passaro, "Single-Mode and Polarization-Independent Silicon-on-Insulator Waveguides With Small Cross Section," *J. Lightwave Technol.,* vol. 23, no. 6, pp. 2103-2111, June 2005.

[29] Y. A. Vlasov and S. J. McNab, "Losses in single-mode silicon-on-insulator strip waveguides and bends," *Opt. Express,* vol. 12, no. 8, pp. 1622-1631, Apr. 2004.

[30] W. Bogaerts, R. Baets, P. Dumon, V. Wiaux, S. Beckx, D. Taillaert, B. Luyssaert, J. Van Campenhout, P. Bienstman and D. Van Thourhout, "Nanophotonic Waveguides in Silicon-on-Insulator Fabricated With CMOS Technology," *J. Light. Technol.,* vol. 23, no. 1, pp. 401-412, Jan. 2005.

[31] V. R. Almeida, Q. Xu, C. A. Barrios and M. Lipson, "Guiding and confining light in void nanostructure," *Opt. Lett.,* vol. 29, no. 11, pp. 1209-1211, June 2004.

[32] Q. Xu, V. R. Almeida, R. R. Panepucci and M. Lipson, "Experimental demonstration of guiding and confining light in nanometer-size low-refractive-index material," *Opt. Lett.,* vol. 29, no. 14, pp. 1626-1628, July 2004.

[33] C. Koos, P. Vorreau, T. Vallaitis, P. Dumon, W. Bogaerts, R. Baets, B. Esembeson, I. Biaggio, T. Michinobu, F. Diederich, W. Freude and J. Leuthold, "All-optical high-speed signal processing with silicon organic hybrid slot waveguides," *Nat. Photonics,* vol. 3, no. 4, pp. 216-219, Mar. 2009.

[34] J. Matres, C. Lacava, G. C. Ballesteros, P. Minzioni, I. Cristiani, J. M. Fédéli, J. Martí and C. J. Oton, "Low TPA and free-carrier effects in silicon nanocrystal-based horizontal slot waveguides," *Opt. Express,* vol. 20, no. 21, pp. 23838-23845, Oct. 2012.

[35] H. Yang, L. Fan, A. Jin, Q. Luo, C. Gu and Z. Cui, "Low-energy electron-beam lithography of ZEP-520 positive resist," in *Nano/Micro Engineered and Molecular Systems, 2006. NEMS'06. 1st IEEE International Conference on (pp. 391-394). IEEE*, 2006.

[36] M. Sugawara, Plasma Etching: Fundamentals and Applications, Oxford Science Publication, 1998.

[37] L. Vivien, J. Osmond, J.-M. Fédéli, D. Marris-Morini, P. Crozat, J.-F. Damlencourt, E. Cassan, Y. Lecunff and S. Laval, "42 GHz p.i.n Germanium photodetector integrated in a silicon-on-insulator waveguide," *Opt. Express,* vol. 17, no. 8, pp. 6252-6257, Apr. 2009.

[38] K. Hammani, M. A. Ettabib, A. Bogris, A. Kapsalis, D. Syvridis, M. Brun, P. Labeye, S. Nicoletti, D. J. Richardson and P. Petropoulos, "Optical properties of silicon germanium waveguides at telecommunication wavelengths," *Opt. Express,* vol. 21, no. 14, pp. 16690-701, Jul. 2013.

[39] C. Lacava, S. Stankovic, A. Z. Khokhar, T. Dominguez Bucio, F. Y. Gardes, G. T. Reed, D. J. Richardson and P. Petropoulos, "Si-rich Silicon Nitride for Nonlinear Signal Processing Applications," *Scientific Reports,* vol. 7, no. 22, pp. 1-13, Feb. 2017.

[40] D. Taillaert, P. Bienstman and R. Baets, "Compact efficient broadband grating coupler for silicon-on-insulator waveguides," *Opt. Lett.,* vol. 29, no. 23, pp. 2749-2751, Dec. 2004.

[41] B. Ben Bakir, A. Vazquez de Gyves, R. Orobtchouk, P. Lyan, C. Porzier, A. Roman and J.-M. Fedeli, "Low-Loss (< 1 dB) and Polarization-Insensitive Edge Fiber Couplers Fabricated on 200-mm Silicon-on-Insulator Wafers," *IEEE Photonics Technol. Lett.,* vol. 22, no. 11, pp. 739-741, June 2010.

[42] G. F. R. Chen, J. R. Ong, T. Y. L. Ang, S. T. Lim, C. E. Png and D. T. H. Tan, "Broadband Silicon-On-Insulator directional couplers using a combination of straight and curved waveguide sections," *Scientific Reports,* vol. 7, no. 7246, pp. 1-8, Aug. 2017.

[43] Y. Zhang, S. Yang, A. E.-J. Lim, G.-Q. Lo, C. Galland, T. Baehr-Jones and M. Hochberg, "A compact and low loss Y-junction for submicron silicon waveguide," *Opt. Express,* vol. 21, no. 1, pp. 1310-1316, Jan. 2013.

[44] X. Wang, W. Shi, H. Yun, S. Grist, N. A. F. Jaeger and L. Chrostowski, "Narrow-band waveguide Bragg gratings on SOI wafers with CMOS-compatible fabrication process," *Opt. Express,* vol. 20, no. 14, pp. 15547-15558, July 2012.

[45] W. Bogaerts, P. Dumon, D. Van Thourhout, D. Taillaert, P. Jaenen, J. Wouters, S. Beckx, V. Wiaux and R. G. Baets, "Compact Wavelength-Selective Functions in Silicon-on-Insulator Photonic Wires," *IEEE J. Sel. Top. Quantum Electron.,* vol. 12, no. 6, pp. 1394-1401, Dec. 2006.

[46] R. Marchetti, V. Vitali, C. Lacava, I. Cristiani, B. Charbonnier, V. Muffato, M. Fournier and P. Minzioni, "Group-velocity dispersion in SOI-based channel waveguides with reduced-height," *Opt. Express,* vol. 25, no. 9, pp. 9761-9767, Apr. 2017.

[47] W. Bogaerts, P. DeHeyn, T. VanVaerenbergh, K. DeVos, S. K. Selvaraja, T. Claes, P. Dumon, P. Bienstman, D. VanThourhout and R. Baets, "Silicon microring resonators," *Laser Photon. Rev.,* vol. 6, no. 1, pp. 47-73, Jan. 2012.

[48] G. T. Reed, G. Mashanovich, F. Y. Gardes and D. J. Thomson, "Silicon optical modulators," *Nature Photon.,* vol. 4, pp. 518-526, Sept. 2010.

[49] D. J. Thomson, F. Y. Gardes, J.-M. Fedeli, S. Zlatanovic, Y. Hu, B. P. P. Kuo, E. Myslivets, N. Alic, S. Radic, G. Z. Mashanovich and G. T. Reed, "50-Gb/s Silicon Optical Modulator," *IEEE Photonics Technol. Lett.,* vol. 24, no. 4, pp. 234-236, Feb. 2012.

[50] J. Hu, X. Sun, A. Agarwal and L. Kimerling, "Design guidelines for optical resonator biochemical sensors," *J. Opt. Soc. Am. B,* vol. 26, no. 5, pp. 1032-1041, May 2009.

[51] M. Iqbal, M. A. Gleeson, B. Spaugh, F. Tybor, W. G. Gunn, M. Hochberg, T. Baehr-Jones, R. C. Bailey and L. C. Gunn, "Label-Free Biosensor Arrays Based on Silicon Ring Resonators and High-Speed Optical Scanning Instrumentation," *IEEE J. Sel. Top. Quantum Electron.,* vol. 16, no. 3, pp. 654-661, Mar. 2010.

[52] A. Z. Subramanian, E. Ryckeboer, A. Dhakal, F. Peyskens, A. Malik, B. Kuyken, H. Zhao, S. Pathak, A. Ruocco, A. De Groote, P. Wuytens, D. Martens, F. Leo, W. Xie, U. D. Dave, M. Muneeb, P. Van Dorpe, J. Van Campenhout, W. Bogaerts, P. Bienstman, N. Le Thomas, D. Van Thourhout, Z. Hens, G. Roelkens and R. Baets, "Silicon and silicon nitride photonic circuits for spectroscopic sensing on-a-chip," *Photon. Res.,* vol. 3, no. 5, pp. B47-B59, Oct. 2015.

[53] J. K. Doylend, M. J. R. Heck, J. T. Bovington, J. D. Peters, L. A. Coldren and J. E. Bowers, "Two-dimensional free-space beam steering with an optical phased array on silicon-on-insulator," *Opt. Express,* vol. 19, no. 22, pp. 21595-21604, Oct. 2011.

[54] A. A. Trusov, I. P. Prikhodko, S. A. Zotov, A. R. Schofield and A. M. Shkel, "Ultra-High Q Silicon Gyroscopes with Interchangeable Rate and Whole Angle Modes of Operation," in *Sensors, 2010 IEEE (pp. 864-867). IEEE*, Nov. 2010.

[55] J. Capmany and D. Novak, "Microwave photonicscombines two worlds," *Nat. Photonics,* vol. 1, no. 6, pp. 319-330, 2007.

[56] S. Schneider, M. Lauermann, P.-I. Dietrich, C. Weimann, W. Freude and C. Koos, "Optical coherence tomography system mass-producible on a silicon photonic chip," *Opt. Express,* vol. 24, no. 2, pp. 1573-1586, Jan. 2016.

[57] "40-Gigabit-capable passive optical networks (NG-PON2): Definitions, abbreviations and acronyms," ITU-T Recommendation G.989, Oct. 2015.

[58] FABULOUS - Project ID 318704 "Abstract from Description of Work", "http://www.fabulous-project.eu/sites/default/files/DoW_Abstract.pdf," [Online].

[59] S. Straullu, P. Savio, J. Chang, V. Ferrero, A. Nespola, R. Gaudino and S. Abrate, "Optimization of Reflective FDMA-PON Architecture to Achieve 32 Gb/s Per Upstream Wavelength Over 31 dB ODN Loss," *J. Light. Technol.,* vol. 33, no. 2, pp. 474-480, Jan. 2015.

[60] S. Abrate, S. Staullu, A. Nespola, P. Savio, J. Chang, V. Ferrero, B. Charbonnier and R. Gaudino, "Overview of the FABULOUS EU Project: Final System Performance Assesment With Discrete Components," *J. Light. Technol.,* vol. 34, no. 2, pp. 798-804, Jan. 2016.

[61] A. Narasimha, S. Abdalla, C. Bradbury, A. Clark, J. Clymore, J. Coyne, A. Dahl, S. Gloeckner, A. Gruenberg, D. Guckenberger, S. Gutierrez, M. Harrison, D. Kucharski, K. Leap, R. LeBlanc, Y. Liang, M. Mack, D. Martinez, G. Masini, A. Mekis, R. Menigoz, C. Ogden, M. Peterson, T. Pinguet, J. Redman, J. Rodriguez, S. Sahni, M. Sharp, T. J. Sleboda, D. Song, Y. Wang, B. Welch, J. Witzens, W. Xu, K. Yokoyama and P. De Dobbelaere, "An Ultra Low Power CMOS Photonics Technology Platform for H/S Optoelectronic Transceivers at less than $1 per Gbps," in *Optical Fiber Communication Conference. Optical Society of America*, 2010.

[62] S. Straullu, P. Savio, G. Franco, R. Gaudino, V. Ferrero, S. Bernabé, M. Fournier, V. Muffato, S. Menezo, B. Charbonnier, E. Temporiti, D. Baldi, G. Minoia, M. Repossi, L. Carroll, J. Lee, P. O'Brien, R. Marchetti, G.-H. Duan, F. Saliou and S. Abrate, "Demonstration of a Partially Integrated Silicon Photonics ONU in a Self-Coherent Reflective FDMA PON," *J. Light. Technol.,* vol. 35, no. 7, pp. 1307-1312, Apr. 2017.

[63] S. Abrate, R. Gaudino, G. Giuliani, E. Temporiti, P. O'Brien, G.-H. Duan, S. Menezo and B. Charbonnier, "Silicon Photonics and FDMA-PON: Insights From the EU FP7 FABULOUS Project," in *Optical Fiber Communications Conference and Exhibition (OFC), 2015. IEEE*, 2015.

[64] S. Menezo, B. Charbonnier, G. Beninca De Farias, D. Thomson, P. Grosse, A. Myko, J. M. Fedeli, B. Ben Bakir, G. T. Reed and A. Lebreton, "Reflective Silicon Mach Zehnder Modulator With Faraday Rotator Mirror effect for self-coherent transmission," in *Optical Fiber Communication Conference and Exposition and the National Fiber Optic Engineers Conference (OFC/NFOEC), 2013. IEEE*, 2013.

[65] S. Menezo, E. Temporiti, J. Lee, O. Dubray, M. Fournier, S. Bernabé, D. Baldi, B. Blampey, G. Minoia, M. Repossi, A. Myko, S. Messaoudène, L. Carroll, S. Abrate, R. Gaudino, P. O'Brien and B. Charbonnier, "Transmitter Made up of a Silicon Photonic IC and its Flip-Chipped CMOS IC Driver Targeting Implementation in FDMA-PON," *J. Light. Technol.,* vol. 34, no. 10, pp. 2391-2397, May 2016.

[66] R. Marchetti, C. Lacava, A. Khokhar, I. Cristiani, D. J. Richardson, P. Petropoulos and P. Minzioni, "Reflector-less grating-coupler with a -0.9 dB efficiency realized in 260-nm silicon-on-insulator platform," in *Integrated Photonics Research, Silicon and Nanophotonics (pp. ITu1A-2). Optical Society of America*, 2017.

[67] C. Lacava, L. Carroll, A. Bozzola, R. Marchetti, P. Minzioni, I. Cristiani, M. Fournier, S. Bernabe, D. Gerace and L. C. Andreani, "Design and characterization of low-loss 2D grating couplers for silicon photonics integrated circuits," in *Proc. of SPIE Vol (Vol. 9752, pp. 97520V-1)*, March, 2016.

[68] T. Tsuchizawa, K. Yamada, H. Fukuda, T. Watanabe, J.-i. Takahashi, M. Takahashi, T. Shoji, E. Tamechika, S.-i. Itabashi and H. Morita, "Microphotonics Devices Based on Silicon Microfabrication Technology," *IEEE J. Sel. Top. Quantum Electron.,* vol. 11, no. 1, pp. 232-240, Jan. 2005.

[69] M. Papes, P. Cheben, D. Benedikovic, J. H. Schmid, J. Pond, R. Halir, A. Ortega-Moñux, G. Wangüemert-Pérez, W. N. Ye, D.-X. Xu, S. Janz, M. Dado and V. Vašinek, "Fiber-chip edge coupler with large mode size for silicon photonic wire waveguides," *Opt. Express,* vol. 24, no. 5, pp. 5026-5038, Feb. 2016.

[70] H.-L. Tseng, E. Chen, H. Rong and N. Na, "High-performance silicon-on-insulator grating coupler with completely vertical emission," *Opt. Express,* vol. 23, no. 19, pp. 24433-24439, Sep. 2015.

[71] R. Harrington, Time-harmonic electromagnetic fields, New York: McGraw-Hill, 1961.

[72] F. Olyslager, Electromagnetic waveguides and transmission lines, Oxford univ.press, 1999.

[73] R. Orobtchouk, A. Layadi, H. Gualous, D. Pascal, A. Koster and S. Laval, "High-efficiency light coupling in a submicrometric silicon-on-insulator waveguide," *Appl. Opt.,* vol. 39, no. 31, pp. 5773-5777, Nov. 2000.

[74] S. K. Selvaraja, D. Vermeulen, M. Schaekers, E. Sleeckx, W. Bogaerts, G. Roelkens, P. Dumon, D. V. Thourhout and R. Baets, "Highly efficient grating coupler between optical fiber and silicon photonic circuit," in *Conference on Lasers and Electro-Optics (p. CTuC6). Optical Society of America*, 2009.

[75] W. S. Zaoui, A. Kunze, W. Vogel, M. Berroth, J. Butschke, F. Letzkus and J. Burghartz, "Bridging the gap between optical fibers and silicon photonic integrated circuits," *Opt. Express,* vol. 22, no. 2, pp. 1277-1286, Jan. 2014.

[76] Y. Ding, C. Peucheret, H. Ou and K. Yvind, "Fully etched apodized grating coupler on the SOI platform with -0.58 dB CE," *Opt. Lett.,* vol. 39, no. 18, pp. 5348-5350, Sept. 2014.

[77] F. Van Laere, G. Roelkens, M. Ayre, J. Schrauwen, D. Taillaert, D. Van Thourhout, T. F. Krauss and R. Baets, "Compact and Highly Efficient Grating Couplers Between Optical Fiber and Nanophotonic Waveguides," *J. Lightwave Technol.,* vol. 25, no. 1, pp. 151-156, Jan. 2007 .

[78] G. Roelkens, D. Van Thourhout and R. Baets, "High efficiency Silicon-on-Insulator grating coupler based on a poly-Silicon overlay," *Opt. Express,* vol. 14, no. 24, pp. 11622-11630, Nov. 2006.

[79] D. Vermeulen, S. Selvaraja, P. Verheyen, G. Lepage, W. Bogaerts, P. Absil, D. Van Thourhout and G. Roelkens, "High-efficiency fiber-to-chip grating couplers realized using an advanced CMOS-compatible Silicon-On-Insulator platform," *Opt. Express,* vol. 18, no. 17, pp. 18278-18283, Aug. 2010.

[80] S. Yang, Y. Zhang, T. Baehr-Jones and M. Hochberg, "High efficiency germanium-assisted grating coupler," *Opt. Express,* vol. 22, no. 25, pp. 30607-30612, Dec. 2014.

[81] M. Fan, M. A. Popović and F. X. Kärtner, "High Directivity, Vertical Fiber-to-Chip Coupler with Anisotropically Radiating Grating Teeth," in *Conference on Lasers and Electro-Optics/Quantum Electronics and Laser Science, Technical Digest (CD) (Optical Society of America, 2007), paper CTuDD3*, 2007.

[82] Y. Tang, Z. Wang, L. Wosinski, U. Westergren and S. He, "Highly efficient nonuniform grating coupler for silicon-on-insulator nanophotonic circuits," *Opt. Lett.,* vol. 35, no. 8, pp. 1290-1292, Apr. 2010.

[83] X. Chen, C. Li, C. K. Y. Fung, S. M. G. Lo and H. K. Tsang, "Apodized Waveguide Grating Couplers for Efficient Coupling to Optical Fibers," *IEEE Photonics Technol. Lett.,* vol. 22, no. 15, pp. 1156-1158, Aug. 2010.

[84] L. He, Y. Liu, C. Galland, A. E. J. Lim, G. Q. Lo, T. Baehr-Jones and M. Hochberg, "A High-Efficiency Nonuniform Grating Coupler Realized With 248-nm Optical Lithography," *IEEE Photonics Technol. Lett.,* vol. 25, no. 14, pp. 1358-1361, July 2013.

[85] M. H. Lee, J. Y. Jo, D. W. Kim, Y. Kim and K. H. Kim, "Comparative Study of Uniform and Nonuniform Grating Couplers for Optimized Fiber Coupling to Silicon Waveguides," *J. Opt. Soc. Korea,* vol. 20, no. 2, pp. 291-299, Apr. 2016.

[86] A. Bozzola, L. Carrol, D. Gerace, I. Cristiani and L. C. Andreani, "Optimising apodized grating couplers in a pure SOI platform to -0.5 dB coupling efficiency," *Opt. Express,* vol. 23, no. 12, pp. 16289-16304, Jun. 2015.

[87] Z. Zhu and T. G. Brown, "Full-vectorial finite-difference analysis of microstructured optical fibers," *Opt. Express,* vol. 10, no. 17, pp. 853-864, Aug. 2002.

[88] E. D. Palik, Handbook of optical constants of solids (Vol. 1-3), Academic press, 1998.

[89] Y. Ding, H. Ou and C. Peucheret, "Ultrahigh-efficiency apodized grating coupler using fully etched photonic crystals," *Opt. Lett.,* vol. 38, no. 15, pp. 2732-2734, Aug. 2013.

[90] J. H. Song, F. E. Doany, A. K. Medhin, N. Dupuis, B. G. Lee and F. R. Libsch, "Polarization-independent nonuniform grating couplers on silicon-on-insulator," *Opt. Lett.,* vol. 40, no. 17, pp. 3941-3944, Sept. 2015.

[91] W. S. Zaoui, A. Kunze, W. Vogel and M. Berroth, "CMOS-Compatible Polarization Splitting Grating Couplers With a Backside Metal Mirror," *IEEE Photonics Technol. Lett.,* vol. 25, no. 14, pp. 1395-1397, July 2013.

[92] J. Zhang, J. Yang, H. Lu, W. Wu, J. Huang and S. Chang, "Subwavelength TE/TM grating coupler based on silicon-on-insulator," *Infrared Phys. and Technol.,* vol. 71, pp. 542-546, July 2015.

[93] X. Chen and H. K. Tsang, "Polarization-independent grating couplers for silicon-on-insulator nanophotonic waveguides," *Opt. Lett.,* vol. 36, no. 6, pp. 796-798, Mar. 2011.

[94] G. Roelkens, D. Vermeulen, S. Selvaraja, R. Halir, W. Bogaerts and D. Van Thourhout, "Grating-Based Optical Fiber Interfaces for Silicon-on-Insulator Photonic Integrated Circuits," *IEEE J. Sel. Top. Quantum Electron.,* vol. 17, no. 3, pp. 571-580, June 2011.

[95] R. Halir, P. Cheben, S. Janz, D.-X. Xu, Í. Molina-Fernández and J. G. Wangüemert-Pérez, "Waveguide grating coupler with subwavelength microstructures," *Opt. Lett.,* vol. 34, no. 9, pp. 1408-1410, May 2009.

[96] D. Taillaert, H. Chong, P. I. Borel, L. H. Frandsen, R. M. De La Rue and R. Baets, "A Compact Two-Dimensional Grating Coupler Used as a Polarization Splitter," *IEEE Photonics Technol. Lett.,* vol. 15, no. 9, pp. 1249-1251, Sept. 2003.

[97] W. Bogaerts, D. Taillaert, P. Dumon, D. Van Thourhout, R. Baets and E. Pluk, "A polarization-diversity wavelength duplexer circuit in silicon-on-insulator photonic wires," *Opt. Express,* vol. 15, no. 4, pp. 1567-1578, Feb. 2007.

[98] F. Van Laere, W. Bogaerts, P. Dumon, G. Roelkens, D. Van Thourhout and R. Baets, "Focusing Polarization Diversity Grating Couplers in Silicon-on-Insulator," *J. Lightwave Technol.,* vol. 27, no. 5, pp. 612-618, Mar. 2009.

[99] S. Pathak, M. Vanslembrouck, P. Dumon, D. Van Thourhout and W. Bogaerts, "Compact SOI-based polarization diversity wavelength de-multiplexer circuit using two symmetric AWGs," *Opt. Express,* vol. 20, no. 26, pp. 493-500, Dec. 2012.

[100] J. Zou, Y. Yu and X. Zhang, "Single step etched two dimensional grating coupler based on the SOI platform," *Opt. Express,* vol. 23, no. 25, pp. 32490-32495, Dec. 2015.

[101] L. Carroll, D. Gerace, I. Cristiani, S. Menezo and L. C. Andreani, "Broad parameter optimization of polarization-diversity 2D grating couplers for silicon photonics," *Opt. Express,* vol. 21, no. 18, pp. 21556-21568, Sept. 2013.

[102] L. Carroll, D. Gerace, I. Cristiani and L. C. Andreani, "Optimizing polarization-diversity couplers for Si-photonics: reaching the -1dB coupling efficiency threshold," *Opt. Express,* vol. 22, no. 12, pp. 14769-14781, Jun. 2014.

[103] Z. Nong, Y. Luo, S. Gao, H. Huang, S. Yu and X. Cai, "Low-loss Two-dimensional Grating Coupler on SOI Platform with Bonded Metal Mirror," in *CLEO: QELS_Fundamental Science (pp. JW2A-143). Optical Society of America*, 2017.

[104] F. P. Payne and J. P. R. Lacey, "A theoretical analysis of scattering loss from planar optical waveguides," *Opt. Quantum Electron.,* vol. 26, no. 10, pp. 977-986, Oct. 1994.

[105] D. Marcuse, "Mode conversion caused by surface imperfections of a dielectric slab waveguid," *Bell Syst. Tech. J.,* vol. 48, no. 10, pp. 3187-3215, Dec. 1969.

[106] L. Pavesi and D. J. Lockwood, Silicon Photonics II: Components and Integration, Springer, 2011.

[107] P. Dumon, W. Bogaerts, V. Wiaux, J. Wouters, S. Beckx, J. Van Campenhout, D. Taillaert, B. Luyssaert, P. Bienstman, D. Van Thourhout and R. Baets, "Low-Loss SOI Photonic Wires and Ring Resonators Fabricated With Deep UV Lithography," *IEEE Photonics Technol. Lett.,* vol. 16, no. 5, pp. 1328-1330, May 2004.

[108] K. K. Lee, D. R. Lim, L. C. Kimerling, J. Shin and F. Cerrina, "Fabrication of ultralow-loss Si/SiO2 waveguides by roughness reduction," *Opt. Lett.,* vol. 26, no. 23, pp. 1888-1890, Dec. 2001.

[109] J. Cardenas, C. B. Poitras, J. T. Robinson, K. Preston, L. Chen and M. Lipson, "Low loss etchless silicon photonic waveguides," *Opt. Express,* vol. 17, no. 6, pp. 4752-4757, Mar. 2009.

[110] T. Barwicz and H. Haus, "Three-dimensional analysis of scattering losses due to sidewall roughness in microphotonic waveguides," *J. Lightwave Technol.,* vol. 23, no. 9, pp. 2719-2732, Sept. 2005.

[111] T. Barwicz, M. A. Popović, F. Gan, M. S. Dahlem, C. W. Holzwarth, P. T. Rakich, E. P. Ippen, F. X. Kärtner and H. I. Smith , "Reconfigurable silicon photonic circuits for telecommunication applications," in *Proc. SPIE (Vol. 6872, p. 68720Z)*, 2008.

[112] F. Morichetti, A. Canciamilla, C. Ferrari, M. Torregiani, A. Melloni and M. Martinelli, "Roughness Induced Backscattering in Optical Silicon Waveguides," *Phys. Rev. Lett.,* vol. 104, no. 3, pp. 033902(1)- 033902(4), Jan. 2010.

[113] E. Dulkeith, F. Xia, L. Schares, W. M. J. Green and Y. A. Vlasov, "Group index and group velocity dispersion in silicon-on-insulator photonic wires," *Opt. Express,* vol. 14, no. 9, pp. 3853-3863, Apr. 2006.

[114] A. C. Turner, C. Manolatou, B. S. Schmidt, M. Lipson, M. A. Foster, J. E. Sharping and A. L. Gaeta, "Tailored anomalous group-velocity dispersion in silicon channel waveguides," *Opt. Express,* vol. 14, no. 10, pp. 4357-4362, May 2006.

[115] L. Zhang, Q. Lin, Y. Yue, Y. Yan, R. G. Beausoleil and A. E. Willner, "Silicon waveguide with four zero-dispersion wavelengths and its application in on-chip octave-spanning supercontinuum generation," *Opt. Express,* vol. 20, no. 2, pp. 1685-1690, Jan. 2012.

[116] A. Yariv, "Coupled-Mode Theory for Guided-Wave Optics," *IEEE J. Quantum Electron.,* vol. 9, no. 9, pp. 919-933, Sept. 1973.

[117] H. A. Haus, W. P. Huang, S. Kawakami and N. A. Whitaker, "Coupled-Mode Theory of Optical Waveguides," *J. Lightwave Technol.,* Vols. LT-5, no. 1, pp. 16-23, Jan. 1987.

[118] R. Marchetti, V. Vitali, C. Lacava, I. Cristiani, G. Giuliani, V. Muffato, M. Fournier, S. Abrate, R. Gaudino, E. Temporiti, L. Carroll and P. Minzioni, "Low-Loss Micro-Resonator Filters Fabricated in Silicon by CMOS-Compatible Lithographic Techniques: Design and Characterization," *MDPI Applied Sciences,* vol. 7, no. 2, pp. 174-185, Feb. 2017.

[119] R. Marchetti, V. Vitali, C. Lacava, I. Cristiani, G. Giuliani, L. Adelmini, M. Fournier and P. Minzioni, "Low-loss integrated ring-resonator filters realized by CMOS fabrication process," in *The European Conference on Lasers and Electro-Optics (p. CI_P_2). Optical Society of America*, 2017.

[120] C. Lacava, R. Marchetti, G. Giuliani, M. Fournier, S. Menezo, S. Messaoudene and P. Minzioni, "Impact of waveguide cross section on nonlinear impairments in integrated optical filters for WDM communication systems," in *The European Conference on Lasers and Electro-Optics (p. CI_P_8). Optical Society of America*, 2015.

[121] C. Lacava, R. Marchetti, V. Vitali, I. Cristiani, G. Giuliani, M. Fournier, S. Bernabe and P. Minzioni, "Reduced nonlinearities in 100-nm high SOI waveguides," in *Proc. SPIE (Vol. 9753, p. 975313)*, Mar. 2016.

[122] T. E. Murphy, J. T. Hastings and H. I. Smith, "Fabrication and Characterization of Narrow-Band Bragg-Reflection Filters in Silicon-on-Insulator Ridge Waveguides," *J. Lightwave Technol.,* vol. 19, no. 12, pp. 1938-1942, Dec. 2001.

[123] C. Klitis, G. Cantarella, M. J. Strain and M. Sorel, "High-extinction-ratio TE/TM selective Bragg grating filters on silicon-on-insulator," *Opt. Lett.,* vol. 42, no. 15, pp. 3040-3043, Aug. 2017.

[124] M. J. Strain, S. Thoms, D. S. MacIntyre and M. Sorel, "Multi-wavelength filters in silicon using superposition sidewall Bragg grating devices," *Opt. Lett.,* vol. 39, no. 2, pp. 413-416, Jan. 2014.

[125] J. Buus, M.-C. Amann and D. J. Blumenthal, Tunable Laser Diodes and Related Optical Sources, 2nd Edn., John Wiley & Sons, Inc., 2005.

[126] X. Wang, W. Shi, R. Vafaei, N. A. F. Jaeger and L. Chrostowski, "Uniform and Sampled Bragg Gratings in SOI Strip Waveguides With Sidewall Corrugations," *IEEE Photonics Technol. Lett.,* vol. 23, no. 5, pp. 290-292, Mar. 2011.

[127] X. Wang, W. Shi, S. Grist, H. Yun, N. A. F. Jaeger and L. Chrostowski, "Narrow-Band Transmission Filter using Phase-Shifted Bragg Gratings in SOI Waveguide," in *Photonics Conference (PHO), 2011 IEEE (pp. 869-870). IEEE*, 2011.

[128] M. S. Dahlem, C. W. Holzwarth, A. Khilo, F. X. Kärtner, H. I. Smith and E. P. Ippen, "Reconfigurable multi-channel second-order silicon microring-resonator filterbanks for on chip WDM systems," *Opt. Express,* vol. 19, no. 1, pp. 306-316, Jan. 2011.

[129] P. Chen, S. Chen, X. Guan, Y. Shi and D. Dai, "High-order microring resonators with bent couplers for a box-like filter response," *Opt. Lett.,* vol. 39, no. 21, pp. 6304-6307, Nov. 2014.

[130] J. E. Cunningham, I. Shubin, X. Zheng, T. Pinguet, A. Mekis, Y. Luo, H. Thacker, G. Li, J. Yao, K. Raj and A. V. Krishnamoorthy, "Highly-efficient thermally-tuned resonant optical filters," *Opt. Express,* vol. 18, no. 18, pp. 19055-19063, Aug. 2010.

[131] P. Dong, W. Qian, H. Liang, R. Shafiiha, N.-N. Feng, D. Feng, X. Zheng, A. V. Krishnamoorthy and M. Asghari, "Low power and compact reconfigurable multiplexing devices based on silicon microring resonators," *Opt. Express,* vol. 18, no. 10, pp. 9852-9858, May 2010.

[132] P. Dong, W. Qian, H. Liang, R. Shafiiha, D. Feng, G. Li, J. E. Cunningham, A. V. Krishnamoorthy and M. Asghari, "Thermally tunable silicon racetrack resonators with ultralow tuning power," *Opt. Express,* vol. 18, no. 19, pp. 20298-20304, Sept. 2010.

[133] Q. Fang, J. Song, X. Luo, L. Jia, M. Yu, G. Lo and Y. Liu, "High Efficiency Ring-Resonator Filter With NiSi Heater," *IEEE Photonics Technol. Lett.,* vol. 24, no. 5, pp. 350-352, Mar. 2012.

[134] F. Gan, T. Barwicz, M. A. Popović, M. S. Dahlem, C. W. Holzwarth, P. T. Rakich, H. I. Smith, E. P. Ippen and F. X. Kärtner, "Maximizing the Thermo-Optic Tuning Range of Silicon Photonic Structures," in *IEEE Photonics in Switching*, 2007.

[135] X. Zheng, I. Shubin, G. Li, T. Pinguet, A. Mekis, J. Yao, H. Thacker, Y. Luo, J. Costa, K. Raj, J. E. Cunningham and A. V. Krishnamoorthy, "A tunable 1x4 silicon CMOS photonic wavelength multiplexer/demultiplexer for dense optical interconnects," *Opt. Express,* vol. 18, no. 5, pp. 5151-5160, Mar. 2010.

[136] P. De Heyn, J. De Coster, P. Verheyen, G. Lepage, M. Pantouvaki, P. Absil, W. Bogaerts, J. Van Campenhout and D. Van Thourhout, "Fabrication-Tolerant Four-Channel Wavelength- Division-Multiplexing Filter Based on Collectively Tuned Si Microrings," *J. Lightwave Technol.,* vol. 31, no. 16, pp. 2785-2792, Aug. 2013.

[137] A. Le Liepvre, R. Brenot, G. H. Duan, S. Olivier and S. Maho, "Fast Tunable Silicon Ring Resonator Filter For Access Networks," in *Optical Fiber Communications Conference and Exhibition (OFC), IEEE*, 2015.

[138] L. Carroll, J.-S. Lee, C. Scarcella, K. Gradkowski, M. Duperron, H. Lu, Y. Zhao, C. Eason , P. Morrissey, M. Rensing, S. Collins, H. Y. Hwang and P. O'Brien, "Photonic Packaging: Transforming Silicon Photonic Integrated Circuits into Photonic Devices," *MDPI Applied Sciences,* vol. 6, no. 12, pp. 426-446, Dec. 2016.

[139] R. Jones, H. Rong, A. Liu, A. W. Fang and M. J. Paniccia, "Net continuous wave optical gain in a low loss silicon-on-insulator waveguide by stimulated Raman scattering," *Opt. Express,* vol. 13, no. 2, pp. 519-525, Jan. 2005.

[140] H. Rong, S. Xu, Y.-H. Kuo, V. Sih, O. Cohen, O. Raday and M. Paniccia, "Low-threshold continuous-wave Raman silicon laser," *Nat. Photonics,* vol. 1, pp. 232-237, Apr. 2007.

[141] A. W. Fang, H. Park, Y.-h. Kuo, R. Jones, O. Cohen, D. Liang, O. Raday, M. N. Sysak, M. J. Paniccia and J. E. Bowers, "Hybrid silicon evanescent devices," *Materials today,* vol. 10, no. 7, pp. 28-35, Aug. 2007.

[142] G. Roelkens, A. Abassi, P. Cardile, U. Dave, A. De Groote, Y. De Koninck, S. Dhoore, X. Fu, A. Gassenq, N. Hattasan, Q. Huang, S. Kumari, S. Keyvaninia, B. Kuyken, L. Li, P. Mechet, M. Muneeb, D. Sanchez , H. Shao, T. Spuesens, A. Z. Subramanian, S. Uvin, M. Tassaert, K. Van Gasse, J. Verbist, R. Wang, Z. Wang, J. Zhang, J. Van Campenhout, X. Yin, J. Bauwelinck, G. Morthier, R. Baets and D. Van Thourhout, "III-V-on-Silicon Photonic Devices for Optical Communication and Sensing," *MDPI Photonics,* vol. 2, no. 3, pp. 969-1004, Sept. 2015.

[143] H. Park, A. W. Fang, O. Cohen, R. Jones, M. J. Paniccia and J. E. Bowers, "A Hybrid AlGaInAs–Silicon Evanescent Amplifier," *IEEE Photonics Technol. Lett.,* vol. 19, no. 4, pp. 230-232, Feb. 2007.

[144] A. W. Fang, B. R. Koch, R. Jones, E. Lively, D. Liang, Y.-H. Kuo and J. E. Bowers, "A Distributed Bragg Reflector Silicon Evanescent Laser," *IEEE Photonics Technol. Lett.,* vol. 20, no. 20, pp. 58-60, Oct. 2008 .

[145] B. Ben Bakir, A. Descos, N. Olivier, D. Bordel, P. Grosse, E. Augendre, L. Fulbert and J. M. Fedeli, "Electrically driven hybrid Si/III-V Fabry-Pérot lasers based on adiabatic mode transformers," *Opt. Express,* vol. 29, no. 11, pp. 10317-10325, May 2011.

[146] A. De Groote, P. Cardile, A. Z. Subramanian, A. M. Fecioru, C. Bower, D. Delbeke, R. Baets and G. Roelkens, "Transfer-printing-based integration of single-mode waveguide-coupled III-V-on-silicon broadband light emitters," *Opt. Express,* vol. 24, no. 13, pp. 13754-13762, June 2016.

[147] J. Justice, C. Bower, M. Meitl, M. B. Mooney, M. A. Gubbins and B. Corbett, "Wafer-scale integration of group III–V lasers on silicon using transfer printing of epitaxial layers," *Nature Photonics,* vol. 6, no. 9, pp. 610-614, Sept. 2012.

[148] C. Merckling, N. Waldron, S. Jiang, W. Guo, N. Collaert, M. Caymax, E. Vancoille, K. Barla, A. Thean, M. Heyns and W. Vandervorst, "Heteroepitaxy of InP on Si(001) by selective-area metal organic vapor-phase epitaxy in sub-50 nm width trenches: The role of the nucleation layer and the recess engineering," *J. Appl. Phys.,* vol. 115, no. 2, pp. 1-6, Jan. 2014.

[149] N. Waldron, C. Merckling, L. Teugels, P. Ong, S. A. U. Ibrahim, F. Sebaai, A. Pourghaderi, K. Barla, N. Collaert and A. V.-Y. Thean, "InGaAs Gate-All-Around Nanowire Devices on 300mm Si Substrates," *IEEE Electron Device Lett.,* vol. 35, no. 11, pp. 1097-1099, Nov. 2014.

[150] S. Chen, W. Li, J. Wu, M. Tang, S. Shutts, S. N. Elliott, A. Sobiesierski, A. J. Seeds, I. Ross, P. M. Smowton and H. Liu, "Electrically pumped continuous-wave III–V quantum dot lasers on silicon," *Nature Photonics,* vol. 10, pp. 307-311, Mar. 2016.

[151] Z. Wang, B. Tian, M. Pantouvaki, W. Guo, P. Absil, J. Van Campenhout, C. Merckling and D. Van Thourhout, "Room-temperature InP distributed feedback laser array directly grown on silicon," *Nature Photonics,* vol. 9, pp. 837-842, Oct. 2015.

[152] P. Kaspar, G. de Valicourt, R. Brenot, M. A. Mestre, P. Jennevé, A. Accard, D. Make, F. Lelarge, G.-H. Duan, N. Pavarelli, M. Rensing, C. Eason, P. O'Brien, S. Olivier, S. Malhouitre, C. Kopp, C. Jany and S. Menezo, "Hybrid III–V/Silicon SOA in Optical Network Based on Advanced Modulation Formats," *IEEE Photonics Technol. Lett.,* vol. 27, no. 22, pp. 2383-2386, Nov. 2015.

[153] G.-H. Duan, C. Jany, A. Le Liepvre, A. Accard, M. Lamponi, D. Make, P. Kaspar, G. Levaufre, N. Girard, F. Lelarge, J.-M. Fedeli, A. Descos, B. Ben Bakir, S. Messaoudene, D. Bordel, S. Menezo, G. de Valicourt, S. Keyvaninia, G. Roelkens, D. Van Thourhout, D. J. Thomson, F. Y. Gardes and G. T. Reed, "Hybrid III–V on Silicon Lasers for Photonic Integrated Circuits on Silicon," *IEEE J. Sel. Top. Quantum Electron.,* vol. 20, no. 4, pp. 158-170, Aug. 2014.

[154] N. K. Dutta and W. Qiang , Semiconductor optical amplifiers, World scientific, 2013.

[155] H. Venghaus and N. Grote, Fibre Optic Communication: Key Devices, Springer, 2017.

[156] K. Morito and S. Tanaka, "Record high saturation power (+ 22 dBm) and low noise figure (5.7 dB) polarization-insensitive SOA module," in *Optical Amplifiers and Their Applications (p. TuC2). Optical Society of America*, 2005.

[157] K. Morito, S. Tanaka, S. Tomabechi and A. Kuramata, "A broad-band MQW semiconductor optical amplifier with high saturation output power and low noise figure," *IEEE Photonics Technol. Lett.,* vol. 17, no. 5, pp. 974-976, May 2005.